Proceedings of the Second Japan-China Seminar on

Solar Physics

1993 July 6-8, Sagamihara

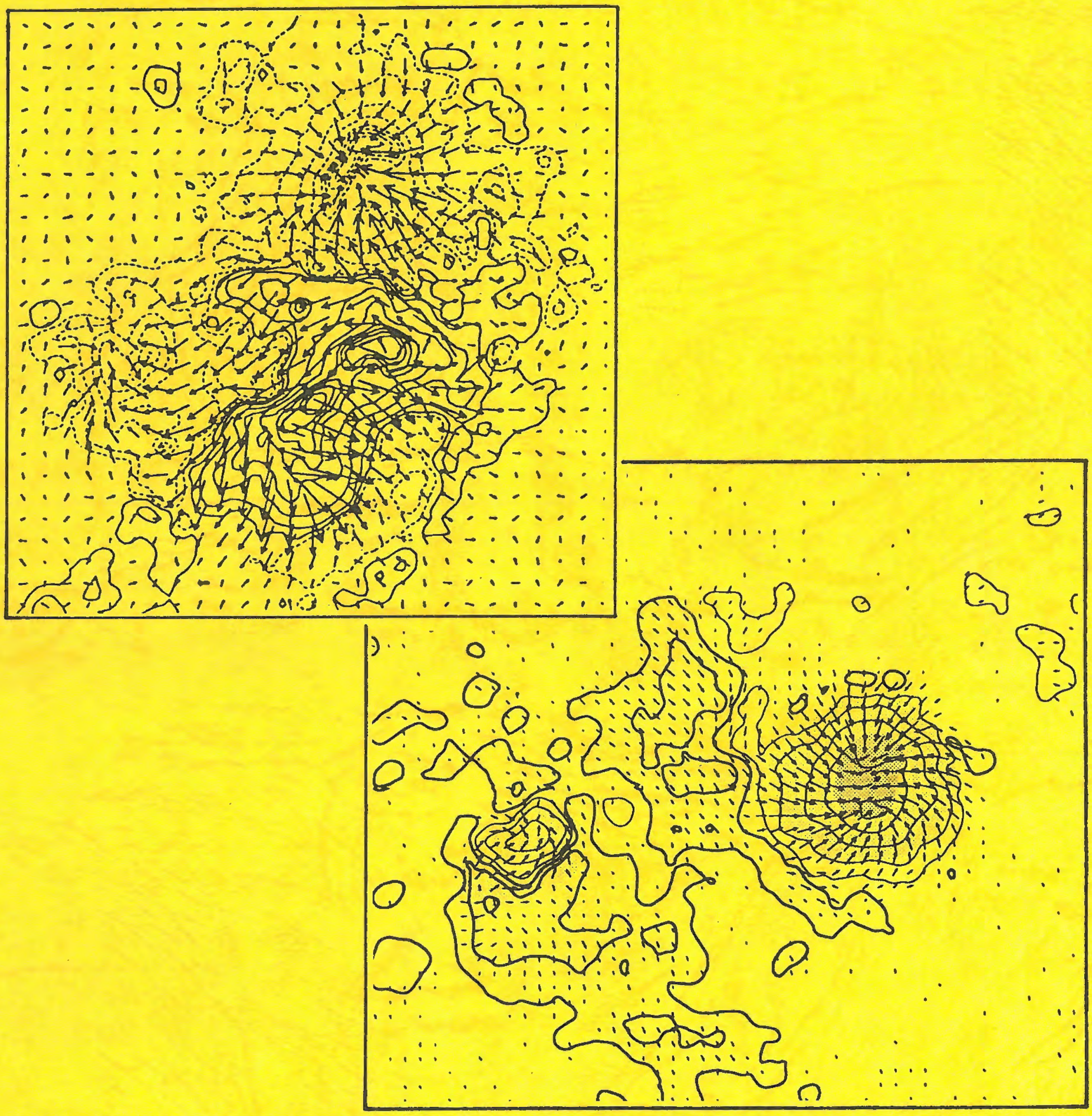

edited by T.Sakurai, T.Hirayama, and G.Ai

National Astronomial Observatory of Japan

Proceedings of the Second Japan-China Seminar on

Solar Physics

1993 July 6-8, Sagamihara

Sponsored by the Ministry of Education, Science and Culture
under the International Scientific Research Program
Grant No. 04044170 (T.Hirayama)

edited by T.Sakurai, T.Hirayama, and G.Ai

National Astronomial Observatory of Japan
Mitaka, Tokyo 181

March, 1994

Preface

The second Japan-China Seminar on Solar Physics was held in Sagamihara, Japan, on July 6-8, 1993. It was organized by National Astronomical Observatory of Japan (NAOJ).

Nineteen Chinese (sixteen of them from the mainland of China, two from Taiwan and one from U.S.A.) and more than 30 Japanese solar physicists attended this Seminar. The Chinese participants had an interesting time both in the sessions and outside. We were honoured to visit the ISAS YOHKOH Operation and Analysis Center, Mitaka and Norikura Observatories, Nobeyama Radio Observatory of NAOJ, and Hida Observatory of Kyoto University. The instruments of these organizations, in particular the Solar-A, have provided many important data for not only the Japanese but also all of the solar physicists in the world.

This meeting was very successful. Many significant observational results and valuable discussions had been reported by the Japanese participants. By these great achievements, the Japanese solar physicists have established their important position on solar physics in the world, and their research work is very conducive to the development of solar physics. On the other hand, the Chinese astronomers also introduced the new progress of Chinese solar physics made in these years.

This Seminar is the second one of the series. It played an important role in promoting scientific exchange and collaboration between Japanese and Chinese astronomers, as the first one had done. And it also had provided an excellent opportunity for the solar physicists of the two countries to meet and get to know each other better and closer.

Here I would like to express our thanks to Japanese Government for providing our official support. Special thanks are given to Prof. Hirayama, Prof. Sakurai, Prof. Hiei, Prof. Makita who made a great contribution for the success of the seminar. We also thank Dr. K. Ichimoto, H. Miyazaki, T. Okamoto, and many other Japanese participants and friends for their kind help.

As everyone knows, there is a long history in cultural exchange between China and Japan. I hope that more Japanese astronomers come to participate in the next Seminar on Solar Physics held in China.

Guoxiang Ai
Beijing Astronomical Observatory

◇ ◇ ◇

This proceedings is an outcome of the second Japan-China Seminar on Solar Physics, held in Sagamihara on July 6-8, 1993. This series of seminars is supported by a bilateral research program. The Japanese side is supported by the Ministry of Education, Science and Culture under a grant provided to T. Hirayama. The Chinese side is supported by the Academy of Sciences and the National Natural Science Foundation of China, with the leadership of Ai Guoxiang. The first seminar was held in 1991 in Kunming, and the research topics presented there were summarized in the proceedings published in 1993.

The collaboration in solar physics between the two countries was initiated almost ten years ago, as a research program co-sponsored by the Chinese Academy of Sciences and

Japanese Society for the Promotion of Sciences. At that time the Japanese solar scientists were working on the data from the Hinotori satellite, and Huairou Observatory was its very initial phase of instrument development. Ten years later, solar physics has flourished in China. The Huairou magnetograph, the Solar Tower of Nanjing University, and other facilities as well have been producing excellent data. In Japan we have Yohkoh satellite, the Nobeyama radio heliograph, and the Solar Flare Telescope at Mitaka. This series of cooperative research program is really timely, and all the participants enjoyed new pieces of data and lively discussions at the meeting.

The main topics of this workshop were the studies of three active regions, namely NOAA 7260, 7270, and 7321. These active regions were selected because they were particularly active ones in 1992, and good observational data were obtained in the observatories both in China and in Japan, as well as with the Yohkoh satellite. In addition to the studies of these active regions, more general research topics in solar physics, both observational and theoretical, were also presented. The official language of the workshop was (broken) English, and communications by using Kanji characters were found to be useful in many cases. The atmosphere of the Japan-China workshops are slightly different from other internatiolnal meetings. It was surprising that the person most fluent in Chinese among non-Chinese participants is Dr. Alphonse Sterling!

We would like to thank Prof. Ai and all the Chinese participants for making this meeting so sucessful. Sometimes the processing of visa applications were slow and additional action was necessary to expedite these procedures. We thank Prof. Yoshihide Kozai, the director of our observatory, in helping us for this. The participation of Dr. H. Wang from U.S.A. was made possible by the donation from the family of Shingo Nagasawa, the late director of the Norikura Observatory. We are grateful to the local organizers Kazunari Shibata, Kiyoshi Ichimoto, Yoshinori Suematsu, Tetsuya Watanabe, Hideaki Miyazaki, Tomizo Okamoto, Issei Sano, Toshiko Iyama, Noriko Irie, and Hideko Nishino; without their efforts the meeting might not have proceeded as smoothly as it actually did.

Tadashi HIRAYAMA and Takashi SAKURAI
National Astronomical Observatory of Japan
January 31, 1994

Table of Contents

Session 1: Observatory Reports (Chairman: Mitsugu MAKITA)

Solar Observations of Purple Mountain Observatory
Jianqi YOU 1

Solar Observation Instruments at Yunnan Observatory
Bairong ZHANG, Youji DING, and Rufeng LI 6

Solar Optical Instruments at the National Astronomical Observatory of Japan
Takashi SAKURAI 11

Hida Observatory of Kyoto University
Hiroki KUROKAWA 17

H-alpha Telescope in Hiraiso and Future Plan
Maki AKIOKA 22

The Development of Imaging Spectrograph in the Solar Tower of Nanjing University
Y.R. HUANG, C. FANG, Z.G. ZHU, Y.Z. XUE, and X.F. GAO 28

Session 2: General Topics (Chairman: Heqi ZHANG)

Microwave, Hα and Hard X-Ray Observations of the 1992 June 26 C7.3 Solar Flare
Haimin WANG 33

Fe XXV Temperatures in Flares Determined from the Yohkoh BCS Experiment
Alphonse C. STERLING 37

Time Development of an X-Class Flare on 1992 June 28
Hiroshi NAKAJIMA, Shinzo ENOME, Kiyoto SHIBASAKI, Masanori NISHIO, Toshiaki TAKANO, Yoichiro HANAOKA, Chikayoshi TORII, Yasuhiko SHIOMI, Hideaki SEKIGUCHI, Takeshi BUSHIMATA, Susumu KAWASHIMA, Noriyuki SHINOHARA, Yoshihisa IRIMAJIRI, Hideki KOSHIISHI, and Yong-Seok CHOI 40

Changes of Vector Magnetic Field during Powerful Flares in Active Region NOAA 6659 on June 6, 1991
Hongqi ZHANG 42

The Development of Magnetic Shear
Jingxiu WANG 48

Recent Classifications of Solar Flares
Jialong WANG 54

A Peak-to-Peak Correlation between Spikes and X-Ray Bursts during Type IV Bursts
Zhiguo XIA 59

Energy Distribution of Energetic Electrons in the Source of an Especially Great Radio Microwave Burst
Renyang ZHAO 65

Emission Mechanism of a Specific Solar Radio Microwave Burst
Renyang ZHAO 70

The Frequency Drift in Spike Radiation Observed on May 10, 1991
Renyang ZHAO, Shengzhen JIN, and Qirang QI 76

A Brief Analysis of Microwave FS Events Observed by BAO in 1991
Qijun FU and Bin ZHAO 81

The Features of Spikes Received at 2545 and 2645 MHz Frequencies
Shengzhen JIN and Xiaocong LI 87

The Reversion of Polarization Sense of Spikes Observed on May 16, 1991
Shengzhen JIN, Renyang ZHAO, Xiaocong LI, and Qirang QI 93

The Analysis of Solar Data at 2.84GHz on May 16, 1991
Leping ZHENG and Yuying LIU 97

Diagnostics of Non-Thermal Processes in Chromospheric Flares: I. Hα and Ca II K-Line Profiles of an Atmosphere Bombarded by Hecta keV Electrons
C. FANG, J.C. HENOUX, and W.Q. GAN 102

Diagnostics of Non-Thermal Processes in Chromospheric Flares: II. Hα and Ca II K-Line Profiles of an Atmosphere Bombarded by Hecta keV Protons
J.C. HENOUX, C. FANG, and W.Q. GAN 103

Stability of Lundquist Field and Prominence Exposing Helical-Like Patterns
Aoao XU, Guiping WU, and Heqi ZHANG 104

Development of the Fast Reconnection Mechanism in a Sheared Field
Masayuki UGAI 110

Constructional Design of the Nine Channel Lyot Filter
Ting LI, Yingyi CHU, Liqing ZHU, and Haitian LU 116

High Resolution Image Recovery by Speckle Interference Method in Huairou's 60cm Telescope
Yuanyong DENG, Guoxiang AI, and Bin ZHANG 122

Some Schemes of Space Solar Telescope
Guoxiang AI 128

Session 3: NOAA 7321 (Chairman: Haimin WANG)

Coordinated Observations of Solar Active Regions (NOAA 7260, 7270 and 7321) at Beijing Astronomical Observatory
Guoxiang AI, Hongqi ZHANG, Qijun FU, and Jialong WANG 135

Observational Results of an Active Region (NOAA 7321) on October – November, 1992
Hongqi ZHANG, Guoxiang AI, and Tongjiang WANG 141

Observations of the Magnetic Field Structure in NOAA 7321 Using the Solar Flare Telescope
Shingo KAWAKAMI 147

Optical and X-Ray Observations of the X9 Flare on 2nd Nov. 1992
Kiyoshi ICHIMOTO, Takashi SAKURAI, Flare Telescope and Norikura Teams 151

Hard X-ray Images at the Flare on 1992 October 27
Tatsuo TAKAKURA 157

Evolution of Radio Features in a Flare Productuve Active Region NOAA 7321
Masanori NISHIO, Tatsuo TAKAKURA, Shinzo ENOME, Hiroshi NAKAJIMA, Kiyoto SHIBASAKI, Toshiaki TAKANO, Yoichiro HANAOKA, Yong-Seok CHOI, and Hideki KOSHIISHI 161

Hα and Soft X-Ray Activities in NOAA 7321 Region during 26–28 October, 1992
Yoshinori SUEMATSU and Nobuyuki TANAKA 165

Session 4: NOAA 7260 (Chairman: Bairong ZHANG)

An Overview of Active Region 7260
Jianqi YOU 169

A purely Polarized Radio Source Associated with NOAA 7260
Kiyoto SHIBASAKI, Shinzo ENOME, Hiroshi NAKAJIMA, Masanori NISHIO, Toshiaki TAKANO, Yoichiro HANAOKA, Chikayoshi TORII, Hideaki SEKIGUCHI, Susumu KAWASHIMA, Takeshi BUSHIMATA, Noriyuki SHINOHARA, Hideki KOSHIISHI, and Yasuhiko SHIOMI 175

A Flare of 1992 Aug.17 23:58 UT
Masaaki TAKAHASHI, Jun-ichi SAKAI, Tetsuya WATANABE, Taro SAKAO, Takeo KOSUGI, Takashi SAKURAI, Shinzo ENOME, Saku TSUNETA, Nariaki NITTA, Hugh S. HUDSON, and Shizuyo HASHIMOTO 176

Hard X-ray Images at the Flare on 1992 August 17
Tatsuo TAKAKURA 182

The Numerical Analysis on Characteristics of Plasma Temperature Variation about the Aug. 17, 25:58UT, 1992 Flare
Jie ZHAO, Jun-ichi SAKAI, and B. CHARGEISHVILI 187

Active Region Transient Brightenings in NOAA 7260
Toshifumi SHIMIZU 193

X-ray Activity in Coronal Loops and Its Photospheric/Chromospheric Counterparts
Takashi SAKURAI, Kazunari SHIBATA, Kiyoshi ICHIMOTO, and Masao TAKATA 198

Session 5: NOAA 7270 (Chairman: Takashi SAKURAI)

NOAA 7270: A Brief Report of Observations
Mingchan WU 203

Emerging Flux Regions and Surge Activities in NOAA 7270
Hiroki KUROKAWA, Reizaburo KITAI, Yasuhiro FUNAKOSHI, Yoshihiro NAKAI, Kiyoshi ICHIMOTO, Kazunari SHIBATA, and Hongqi ZHANG 209

Flares on September 6, 1992
Reizaburo KITAI, Hiroki KUROKAWA, Yasuhiro FUNAKOSHI, Yoshihiro NAKAI, Kazunari SHIBATA, Kentaro YAJI, Nariaki NITTA, and Yohkoh Team and NOAJ Flare Telescope Team 215

Flares on Sept.6, 1992 in NOAA 7270: SXT Observations and Comparison with H-Alpha and HXT Observations
Kazunari SHIBATA, Nariaki NITTA, Reizaburo KITAI, Hiroki KUROKAWA, Kentaro YAJI, Takashi SAKURAI, and Hongqi ZHANG 220

Flares in the Region NOAA 7270 Observed with the Nobeyama Radioheliograph
Yoichiro HANAOKA 226

Meterwave Solar Radio Emission from NOAA 7260
Shin-ichi WATARI, Takeshi ISOBE, and Yohkoh SXT Team 230

BCS Spectra from Flares on 6th September 1992
Takako KATO, Tomoto Fujiwara, and Yohkoh BCS Group 236

Epilogue

A Poem by Jingxiu WANG 241

List of Participants 243

The manuscripts of the following talks were not available.

Yohkoh Satellite
Yoshiaki OGAWARA

Nobeyama Radio Observatory, National Astronomical Observatory of Japan
Shinzo ENOME

Solar Instuments in Taiwan
Wenlung LAN and Zhigang WU

Interplanetary Consequences of Coronal Disturbances Observed with YOHKOH SXT
Takashi WATANABE, Yukio KOZUKA, Masamitsu OHYAMA, Masayoshi KOJIMA, and the Yohkoh Team

The 110-Year Periodic Modulations of Solar Luminosity, Solar Cycle, and Solar Differential Rotation
Hirokazu YOSHIMURA

Quadrupolar magnetic configuration of filaments and flares
Yutaka UCHIDA

Alignment of Radio, Soft X-ray, and Hard X-ray Emissions in Impulsive Phase of the Flare of August 17-18, 1992
Shinzo ENOME

Hard X-Ray Flares of Active Region NOAA 7270
Kentarou YAJI

Session 1: Observatory Reports

Solar Observation of Purple Mountain Observatory

Jianqi You
Purple Mountain Observatory, Nanjing, China, 210008

Abstract

At Purple Mountain Observatory, six telescopes are used specially for solar observations. Among them, three radio telescopes (9.4 GHz, 2.7 GHz and 35 GHz respectively) are for daily patrol observation. The 8 inch refractor works both for daily sunspot drawing and large sunspot group photography, while the solar spectrograph for solar spectra and spectroheliogram at HeI 10830 and the fine structure telescope at Ganyu station for Hα and white light aim only to those active regions of interest. The main data available for the active regions 7260, 7270 and 7321 are also listed in this paper.

1. Introduction

At Purple Mountain Observatory, 7 telescopes are specially devoted to solar observations. Among them, the 14 cm chromospheric telescope for the whole disk patrol observation did not work last year, for its photograph system was being reformed. Therefore in the text, I give a brief decription about the other 6 instruments and also the data obtained with those facilities.

2. Instruments and Observations

(1) The fine structure telescope The telescope made by Nanjing Astronomical Instrument Factory was installed at Ganyu Station in 1990. The station is located ~300 km to the north of Nanjing,where we have more clear days and better seeing than in Nanjing. The telescope consists of two vacuum tubes with 26 cm lens objectives, one for white light and another for Hα. The images at the focal plane are 30 cm and 8.5 cm in diameter and are photographed with Kodak 5460 and 2415 films (35 mm) respectively. The Hα filter was designed to have two pass bands, 0.24A and 0.46A, for selecton and can be tuned to 0, ±0.5A, ±1A, ±1.5A within 30s (Liu *et al.* 1990). This telescope is not for routine use, only for active regions of special interest. The active regions, 7260 and 7321 happened to be the candidates and fortunately a series of flares, including the large limb flare on November 2 were obtained.

(2) Solar spectrograph The 40 cm horizontal telescope and the multi-band spectrograph was put into operation in 1967 (The Solar Telescope Research and production Group, 1975). The solar image is about 11.2 cm and spectra at 9 wavelengths(Hα .....H∞ ,H+K, D and Mgb) can be taken simultanously on plates. Resently the spectrograph was upgraded in some respects. For instance, a slit-jaw system with a DayStar filter (0.5A, 2″) was attached. Meanwhile we began to extend the observation wavelength to near infrared with solid state detectors, first an one dimension Reticon (1024S) system (Wang *et al.*. 1987) and then a CCD camera instead (You *et al.*.). Another innovation which attempted to replace the plates with films failed to complete for some unexpected reasons. Consequently multi-wavelength spectra are not available at present. Last

Fig.1 Limb flare (H)

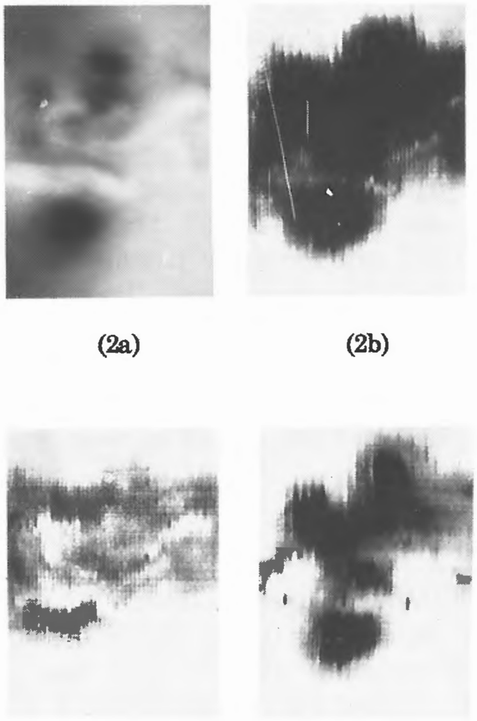

(2a) (2b)

(2c) (2d)

Fig.2 Decreasing phase of a flare Oct.27,1992 0052UT
(2a) H α
(2b) HeI 10830—I
(2c) HeI 10830—I/Ic
(2d) Ic (10820 A)

Fig.3 Profiles of HeI 10830 of bright parts (1,2) and the undisturbed background(3)

October the CCD system was just being adjusted and some test observations in HeI 10830 were taken.

The solar image scanning is performed by rotating the second mirror of the coelostat with 1.8″/step. A TM860 CCD camera (11x11.5μ, 590x800 pixels) works at the first order of grating (10x10 cm, 600 grooves/mm). In order to match the resolution of CCD, a lens system is inserted between the camera lens and CCD so that the dispersion may be reduced to 4.17 A/mm and the spacial resolution perpendicular to the dispersion is about 0.34″/pixel. The video output is led to an image processor, Imaging Technology 151, and a PC microprocessor is used to acquire the image data. For saving memory and time, usually for each picture, we fetch two windows, 10830.3±1A and 10820±0.35A (continuum). In general, it takes 5—6 minutes for a two–dimensional HeI 10830 spectra of 3′x 3′. The spectroheliograms of various off–band as well as the profiles can, at the same time, be obtained. Further processing such as dark and flat field corrections were made afterward. Two image spectra at HeI 10830 were taken on AR 7321 and one of them on Oct. 27 was at its decreasing phase of a M1/1N flare.

From figure 1, some results can be summarized:

(a) Though the observation was made almost 30 minutes after the flare maximum, some parts in HeI 10830 still appeared bright. All the bright parts occurred in the penumbra of spots.

(b) The bright features in HeI 10830 coincide on a whole with those in Hα, but some differences could be noticed between Hα and HeI and between the images of different off–band HeI as well.

(c) For checking the bright regions at HeI 10830, we plot their profiles in figure 3. The HeI 10830 appears to be a emission profile for the brightest region in I/Ic, while the faint ones still keep absorption, but shallower than the undisturbed region nearby. The appearances obtained here confirm our previous conclusions (You *et al.*, 1993).

(3) 20 cm equatorial The 20 cm refractor, made by Zeiss, is mainly used for daily sunspot drawing. Sometimes photographs were made with an amplified

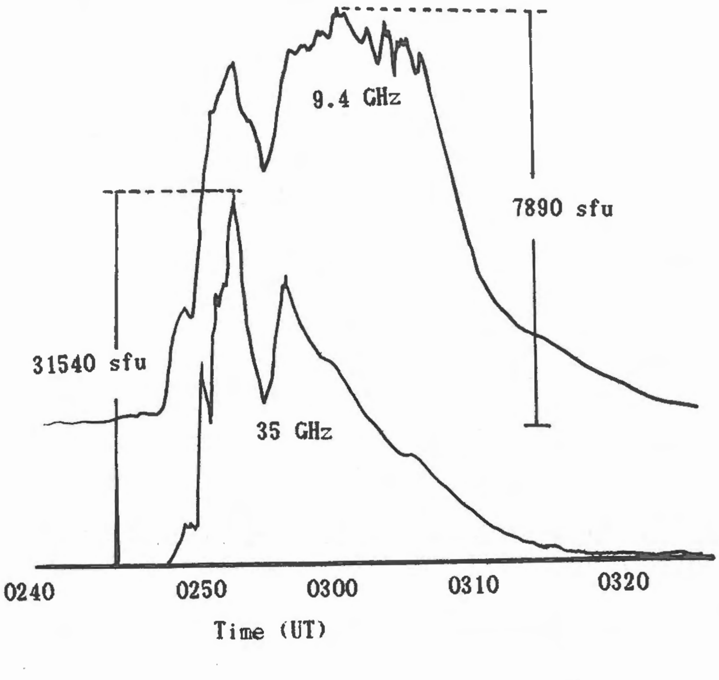

Fig.4 The solar radio burst on Nov.2, 1992

system, but only for those large sunspot groups. The image is 30 cm at focal plane and a 135 camera is used for photograph. From Aug.17 to Aug.22, 1992, we obtained many photos of AR 7260 with ~1″.

(4) Radio telescopes There are 3 radio telescopes, 2.7 GHz, 9.4 GHz and 35 GHz in frequency, used for routine observation. The first two sample every 10 ms regularly, but only 1/100 data are reserved except the radio bursts. An outstanding burst was observed at all these three frequencies on Nov. 2, 1992 (figure 4). This impulse emission came from AR 7321, 10° behind the west limb. This event was characterized by its two peaks and some subsecond intensity fluctuation around its peak.

Finally the observations of AR 7260, 7270 and 7321 made at PMO are briefly listed in table 1 for reference.

Table 1 Observations of AR 7260, 7270 and 7321 made at PMO

Active region	Date 1992	H_α Time(UT)	Flare	White light Time(UT)	HeI 10830 Time(UT)	flare	Radio burst
7260	Aug.17	0059–0341		0236–0334			
				0635–0705			
	18	0131–0158		0612–0656			
		0240					
	19			0257–0320			
				0628–0738			
	20	0645–0837	2	0149–0327			
				0615–0700			
	21	0254–0317	2	0227–0259			
	22			0120—124			
	23	0748–0836	1				
	24	0058–0153					
		0306–0317	1				
		0654–0703					
7270	Aug.30						1
	Sept.4						1
	Sept.5						1
	Sept.6						3
	Sept.7						2
7321	Oct.25				0055		
	Oct.27	0153–0721			0052	1	1
	Oct.28						1
	Oct.30	0026–0620					
	Oct.31	0107–0647					
	Nov.1	0105–0741					
	Nov.2	0420–0531	1				1

Acknowledgements

Thanks due to Dr. C.J.Wang, Misses F.Y.Xu, B.Q.Li and Z.Y.Fan for their help in the preparation of this paper.

References

Liu, Q., Seng, R., Fan, Z., Song, M., Hu, F., Liu, G., He, F., Mao, W., Hua, J. and Wang, Y. 1990, *Publ. of Purple Mountain Observatory*, 9, 218.

The Solar Telescope Research and Production Group 1975, *Acta Astronomica Sinica* 16, 225.

Wang Chuanjin, Lu Jing, Ni Zhiren, You Jianqi and Fan Zhongyu 1987, *Acta Astronomica Sinica,* 28, 101.

You Jianqi, Wang Chuanjin, Lu Jing and Fan Zhongyu, *Acta Astronomca Sinica,* in press.

You Jianqi, Wang Chuanjin and Fan Zhongyu 1993, *Proceedings of the First China –Japan Seminar on Solar Physics,* ed. G.X.Ai, E.Hiei, Y.J.Ding and Z.X.Ling. (Ton Dar Institude, Kunming), P148.

Solar Observation Instruments at Yunnan Observatory

ZHANG Bai-rong, DING You-ji, and LI Ru-feng

Yunnan Observatory, P.O.Box 110, Kunming, 650011, China

Abstract

Beside the telescopes used for solar rotine observation, two new instruments were installed since 1991. A brief introduction is presented.

I, The telescopes used for solar routine observation at Yunnan Observatory are as followings.

1, White light sunspot drawing and photography with a 5 inch refractor.

2, H_α flare patrol with a 14 cm refractor. $\Delta\lambda=0.5$ A.

3, 26 cm binocular vacuum telescopes with one tube work on H_α band and another on white light.

4, Horizontal telescope and multi-band spectrograph with 40 cm coelostats and 30 cm primary mirror.

5, A group of solar radio telescopes. The working wavelengths of these telescopes are at 7. 5 cm, 10. 7 cm, 15 cm, and 21 cm respectively. Beside a radio acoustic-optical spectrograph is working at 230-300 MHz with a 10 m dish antenna. The time-resolution of the receivers of these telescopes are about 1 ms.

II, Two instruments were installed since the first Japan-China Solar Physics Workshop in Kunming , 1991 , and now are in testing and calibrating.

1, Specta-spectroheliograph and scanning Stokes polarimeter. A telescope consisting of spectra-spectroheliograph (SSHG) and Stokes polarimeter (SP) , which was made in Nanjing Astronomical Instrument Factory, has been installed at Yunnan

Observatory. Fig 1 is the optical system of the telescopes. The part SSHG can be used to scan two lines simultaneously from 3600A to 11000A by rotating the grating, with a spectral resolution 1.2A/mm and a spatial resolution up to 1–2″.

When the polarimeter package enters the light way, the scanning of magneto-sensitive line will yield profiles of all four Stokes parameters orderly by mechanical modulation. The SSHG, SP and observing system are computer cotrolled. The parameters of the optical system is as follows.

(1),Telescope

Objective:—500 mm aperture
—cervit mirror
—focal length 12.5 m

Image size :—solar diameter 116 mm

Entrance slit:—length 14.4 mm

(2),Spectrograph

Grating: —630 lines/mm,size 320x300 mm
—blaze 22° 17′
—focal length 12.5 m
—average dispersion 0.8 mm/A
—solar image : 116 mm, 125 mm

Spatial resolution: —solar image 0.5″
—spectrum 1–2″

Scanning time for an AR: 20 S

(3),Polarimeter package

Content: —Three quarter wave plates (2,3,4 see Fig 2) and an empty window 1 and a Richion prism 5.

Mechanical modulation :

(i) 1,4(0°),5(±45°) ⟶ 1/2 (I±V)
(ii) 2(0°),4(0°),5(±45°) ⟶ 1/2 (I±U)
(iii) 3(45°),4(0°),5(±45°) ⟶ 1/2(I±Q)

(4),Electronic system

Computer system —AST/386

CCD array —size 6 mm x 6 mm

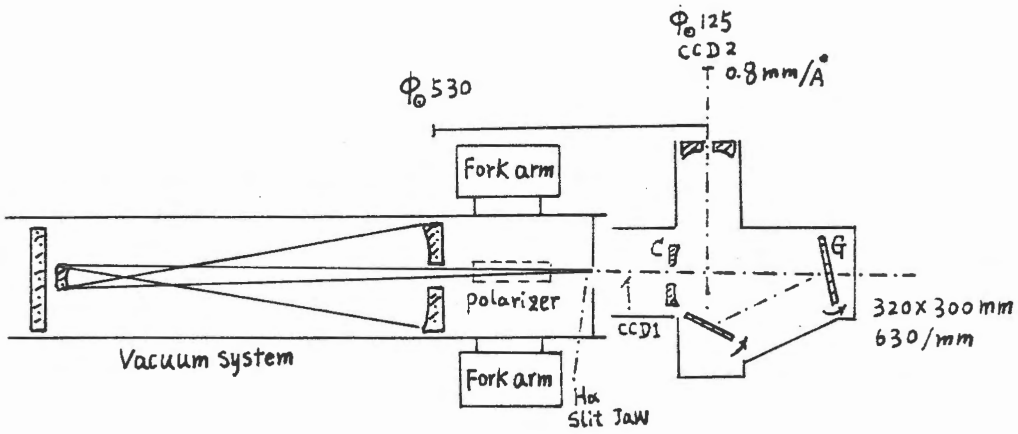

Fig 1, The optical system of the SSHG telescope

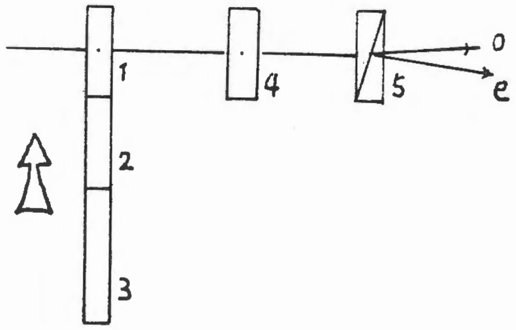

Fig 2, The polarimeter package

—pixel 512 x 512
—sensitivity 0.2 lux

2, Photometric solar seismograph

According to a cooperative agreement between the University of Arizona and Yunnan Observatory,a photometric solar seismograph was installed at Yunnan Observatory in 1991, and was put into testing operation in last year. The instrument was developed by SCLERA, the Santa Catalina Laboratory for Experimental Relativity by Astrometry, lead by prof H.A.Hill.

The seismograph is used to observe solar oscillations by determining changes in the intensity of the continuum on the solar disk with a spatial resolution of about 50 arcsec.

The optical system of the instrument consist of a coelostat, a primary mirror and a detector system, as shown in Fig 3. Sunlight passes through a window to the 20 cm diameter coelostat mirror and then to the primary with an aperture of 7.0 cm and a focal length of 200 cm. After the sunlight passes through the primary focus, two solar image are formed in the optical system. One of them has a diameter of 19 mm for measurement at the disk center and the other has 28 mm for measurement at the solar limb.

The solar images are scanned across three diode of Ge 1 x 16 pixel at 0.55 μ m and across a second set of Ge array at 1. 6 μ m. In front of each linear array is a mask which is designed to yield to a spatial resolution approximately 3° / pixel for two orthogonal directions in the heliocentric coordinates. Scanning is utilized to give a coverage of ±90° in the longitude and ±60° in the latitude.

The operating system and data acquisition system of the telescope are controlled with a Masscomp 5500 on-line computer. The signals received by the detectors are sampled every 50 msec with a 12-bit A/D system and the A/D signals for a given location on the solar disk are filtered by a digital triangle filter with a width of 16 sec. This output of the tringle filter is sampled every 4 sec and recorded. This data-acquisition system can produce 31 mbytes of data in 10 hours, and the data is recorded on 1/4-inch cartrige type. The data are exchanged between Yunnan Observatory and SCLERA.

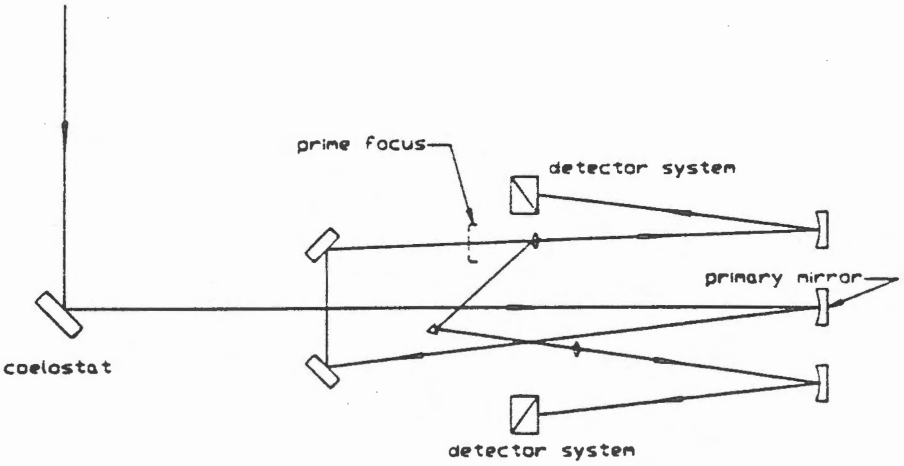

Fig 3, The optical system of the photometric solar seismograph

Solar Optical Instruments at the National Astronomical Observatory of Japan

Takashi Sakurai

National Astronomical Observatory, Mitaka, Tokyo 181

Abstract

This article describes solar optical instruments of the National Astronomical Observatory of Japan.

1. Introduction

Optical instruments which are currently being operated at the National Astronomical Observatory of Japan for solar observations are reviewed in the following. The instruments are located at the Mitaka campus and at two stations; Norikura and Okayama. Okayama Observatory is a facility for both night time and solar observations.

2. Mitaka Campus

2.1. Sunspot Observation

Routine observations of sunspots have been conducted since 1938, by using a 20cm refractor made by Zeiss (figure 1). Sketches (solar image diameter = 24cm) and white light photographic observations of sunspots are made daily. Solar differential rotation and meridional circulation were studied by using these data (Kambry and Nishikawa 1990; Kambry et al. 1991; Yoshimura and Kambry 1993).

2.2. Hα Flare Patrol

Hα flare patrol observations have been carried out since 1957, with a 14cm refractor equipped with a birefringent filter made by Cecasi, France. Photographs were usually taken at 30 second intervals. In 1991, a system for automatic detection and subsequent light curve plotting of flares was introduced (figure 2). This system is made of a 4cm objective lens, a Halle Hα filter, and a CCD camera. The video signal from the CCD is digitized in a personal computer. In normal operation, a full disk image is taken every one minute. When a flare is detected, images of a limited area around the flaring region are taken at a rate of one frame per second. The pixel size corresponds to 4$''$ on the sun. A cross-comparison of measurements between the new system and the old photographic system has been conducted, and a satisfactory performance of the new video system was confirmed. In May 1992, the old photographic Hα flare patrol was replaced by the new system. Observations with this new video system is described by Suematsu and Tanaka (1994).

2.3. The Solar Flare Telescope

The main instrument at Mitaka is the Solar Flare Telescope (figure 3). The aim of the Solar Flare Telescope is to observe solar flares in four aspects, namely (1) the magnetic field, (2) the velocity field (Doppler shifts), (3) chromospheric fibril structures and flares in Hα line, and (4) growth and decay as well as motions of sunspots observed in continuum light. Initial results from this telescope are reported by Ichimoto et al. (1991, 1993) and by Sakurai et al. (1992a,b).

In order to perform the four measurements described above, we put four telescopes on a single mounting. The telescope optics and the mounting were built by Nikon. Four telescopes have the same field of view of $300'' \times 400''$, and the pixel size of CCD cameras corresponds to 0.8$''$ on the sun. Two telescopes are used to measure polarizations and Doppler shifts of spectral lines, by using birefringent filters. The other two telescopes observe the sun through wide band filters, and through a Zeiss birefringent filter for the Hα line, respectively. Hα images are recorded onto a laser video disk at a rate of one frame in ten seconds. Continuum images are recorded onto a video tape at a normal video rate, and the tape is recycled unless notable events are detected.

The birefringent filter for magnetic vector measurements, built by Nanjing Astronomical Instrument Research Center, has a pass band of 1/8 Å. The transmission peak is set at the blue wing of the Fe I 6303 Å line (Landé factor = 2.5). Circular polarizations are measured by using a KD*P modulator as a quarter-wave retarder, and a polaroid following the KD*P as an analyzer. Linear polarizations are measured in the same system by converting linear polarizations into circular polarizations. The conversion is made by quarter-wave plates in front of the KD*P modulator.

The Fe I 6337 Å line (Landé factor = 2.0) is used to measure the Doppler shift and also the longitudinal magnetic field. The birefringent filter for 6337 Å, also built by Nanjing Astronomical Instrument Research Center, has a pass band of 0.2 Å. The thickest calcite element in the filter is equipped with a KD*P crystal. By modulating the retardation of the KD*P, the transmission peak of the filter can be moved by ±0.1 Å. The difference in signals from the blue and red wings gives information on the Doppler shift of the spectral line.

Vector magnetograms and Dopplergrams are taken every 3 minutes. At the end of a full-day observing run, data of about 0.5 GB are obtained and are written to a digital audio tape.

2.4. STEP Full-Disk Magnetograph

Large-scale magnetic field distributions on the solar surface play an important role of determining the magnetic field structures in the corona and in the solar wind. As part of our observatory's contribution to the Solar Terrestrial Energy Program (STEP project), a full disk solar magnetograph was constructed (figure 4). The system of polarization measurements is similar to the Solar Flare Telescope, and uses a birefringent filter, two KD*Ps, and a CCD camera. The pixel size corresponds to 5″ on the sun. The whole system is set up on the optical bench in the observing room. A heliostat mirror system of 20cm in diameter is used to feed the sun light into the observing room. The spectral line used is that of Fe I at 5324.2 Å (Landé factor = 1.5). The heliostat and the birefringent filter were made by Nanjing Astronomical Instrument Research Center, and the imaging optics was built by Nikon. The instrument is now in the phase of test observation.

3. Norikura Coronagraph Station

At Mt. Norikura, 2800 m above sea level, three coronagraphs are in operation (figure 5). The oldest 10cm coronagraph, made in 1950 by Nikon, has been used to measure the intensities of the coronal emission line at 5303 Å. It is also used for photographic observations of coronal structures and prominences.

The 25cm coronagraph, also built by Nikon in 1971, is equipped with a spectrograph and a CCD camera, and the mapping of the sun using the Helium 10830 Å line is conducted on an almost routine basis. A single pixel of the CCD covers 1″× 0.2Å, and spectral strips of 2Å width are recorded. A raster scan of the full-disk, made of four swaths of 500″ wide, is completed in 30 minutes.

The newest 10cm coronagraph is mounted on the old 10cm coronagraph. This instrument takes digitized images of the solar corona by using four interference filters as follows:

wavelength	bandwidth
5303Å	3Å
5876Å (He D_3)	4Å
6563Å (Hα)	3Å
6630Å (continuum)	21Å

The field of view is 2600″ × 2400″. The acquisition of one set of data takes 2 minutes. The photometric accuracy of this system is about 10^{-6} times the sun-center brightness. The initial results are reported by Ichimoto et al. (1992).

4. Okayama Observatory

At Okayama, the 65cm coude-type solar telescope was built in 1967 by Nikon (figure 6). In 1982, a photoelectric vector magnetograph was installed and has been in operation since then. The spectral line used is Fe I 5250 Å (Landé factor = 3.0). The photomultipliers measure the intensity of the wing of this line (27 – 80 mÅ from the line center), which is modulated according to its polarization state by a rotating quarter-wave plate. A typical observing run of about an hour covers an area of $500'' \times 450''$ with $10''$ steps. The polarimetric accuracy of this instrument is of the order of 10^{-4} for the integration of 1 second. The maps of solar active regions taken with this vector magnetograph are published every year. Major research topics studied in the first ten years of this instrument is summarized in Makita et al. (1993).

5. Future Plans

In order to conduct systematic, long-term observations of the solar activity, we are proposing to construct the Solar Cycle Telescope. This facility is made of (a) small refractors equipped with various filters to measure the magnetic fields, velocity fields, and solar images in various wavelengths, and (b) a 1m-class telescope and a spectrograph which will be used for high precision spectroscopic observations of the sun's velocity and magnetic fields. The facility will be operated continuously over at least one solar cycle, and the accumulated data will be used for the study of the driving mechanism of the solar activity cycle. The Solar Flare Telescope, the automatic Hα flare patrol telescope, and the STEP full disk magnetograph are part of the phase (a) of this project. The next step is to automatize sunspot observations, and to initiate spectroheliographic observations of the full solar disk in Ca K and He 10830 Å lines. The phase (b) of this project aims at high dispersion spectroscopic and polarimetric observations of the full solar disk by raster scanning. For Stokes profile observations we plan to use the Fe I line at 1.56 μm. For Doppler measurements a Zeeman-insensitive line (such as Fe I 5576 Å) will be used.

References

Kambry, M.A., and Nishikawa, J. 1991, *Solar Phys.*, **126**, 89

Kambry, M.A., Nishikawa, J., Sakurai, T., Ichimoto, K., and Hiei, E. 1992, *Solar Phys.*, **132**, 41

Ichimoto, K., Sakurai, T., Yamaguchi, A., Kumagai, K., Nishino, Y., Suematsu, Y., Hiei, E., and Hirayama, T. 1991, in *Flare Physics in Solar Activity Maximum 22, Lecture Notes in Physics* **387**, eds. Y. Uchida, R.C. Canfield, T. Watanabe, and E. Hiei, Springer Verlag, p.320

Ichimoto, K., Hirayama, T., Yamaguchi, A., Kumagai, K., Tsuneta, S., Hara, H., Acton, L.W., and Bruner, M.E. 1992, *Publ. Astron. Soc. Japan*, **44**, L117

Ichimoto, K., Sakurai, T., Nishino, Y., Shinoda, K., Noguchi, M., Kumagai, K., Imai, H., Irie, M., Miyashita, M., Tanaka, N., Sano, I., Suematsu, Y., and Hiei, E. 1993, in *The Magnetic and Velocity Fields of Solar Active Regions, IAU Colloquium No.141, Astron. Soc. Pacific Conference Series* **46**, eds. H. Zirin, G. Ai, and H. Wang, p.166

Makita, M., Sakurai, T., Shibasaki, K., and Koyano, H. 1993, in *Magnetic and Velocity Fields of Solar Active Regions, IAU Colloquium No.141, Astron. Soc. Pacific Conference Series* **46**, eds. H. Zirin, G. Ai, and H. Wang, p.180

Sakurai, T., Ichimoto, K., Hiei, E., Irie, M., Kumagai, K., Miyashita, M., Nishino, Y., Yamaguchi, K., Fang, F., Kambry, M.A., Zhao, Z.W., and Shinoda, K. 1992a, *Publ. Astron. Soc. Japan*, **44**, L7

Sakurai, T., Shibata, K., Ichimoto, K., Tsuneta, S., and Acton, L.W. 1992b, *Publ. Astron. Soc. Japan*, **44**, L123

Suematsu, Y., and Tanaka, N. 1994, in this volume.

Yoshimura, H., and Kambry, M.A. 1993, *Solar Phys.*, **143**, 205

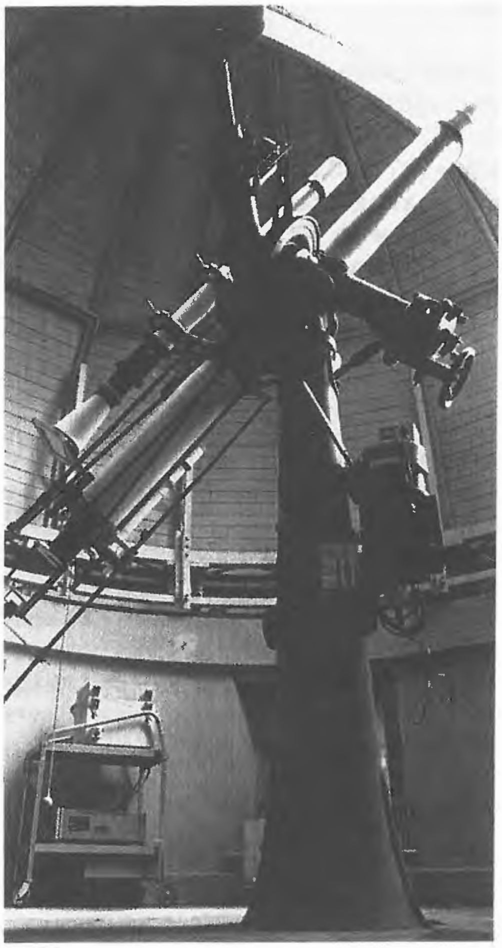

Fig. 1 The Zeiss 8-inch refractor at Mitaka.

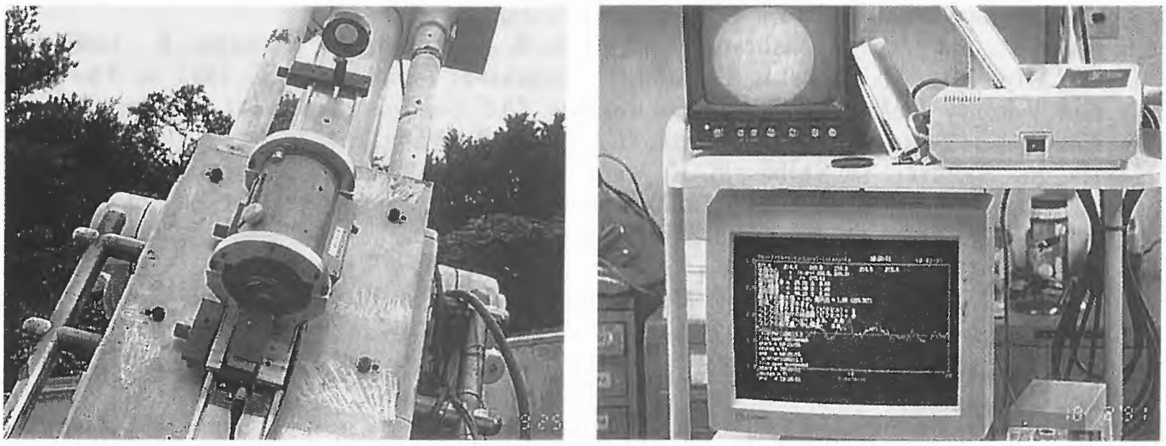

Fig. 2 The Hα flare patrol telescope (left) and the analysis system (right) at Mitaka.

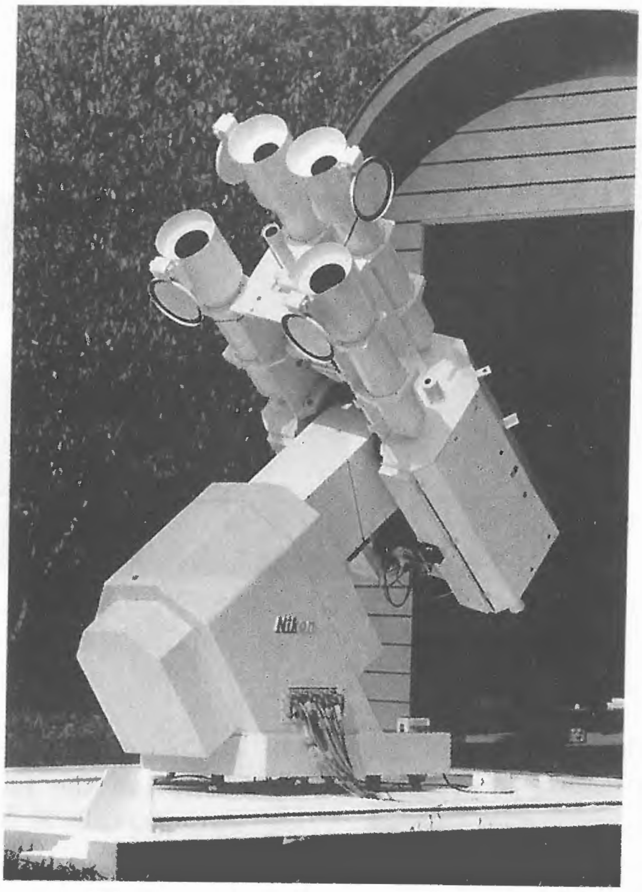

Fig. 3 The Solar Flare Telescope at Mitaka.

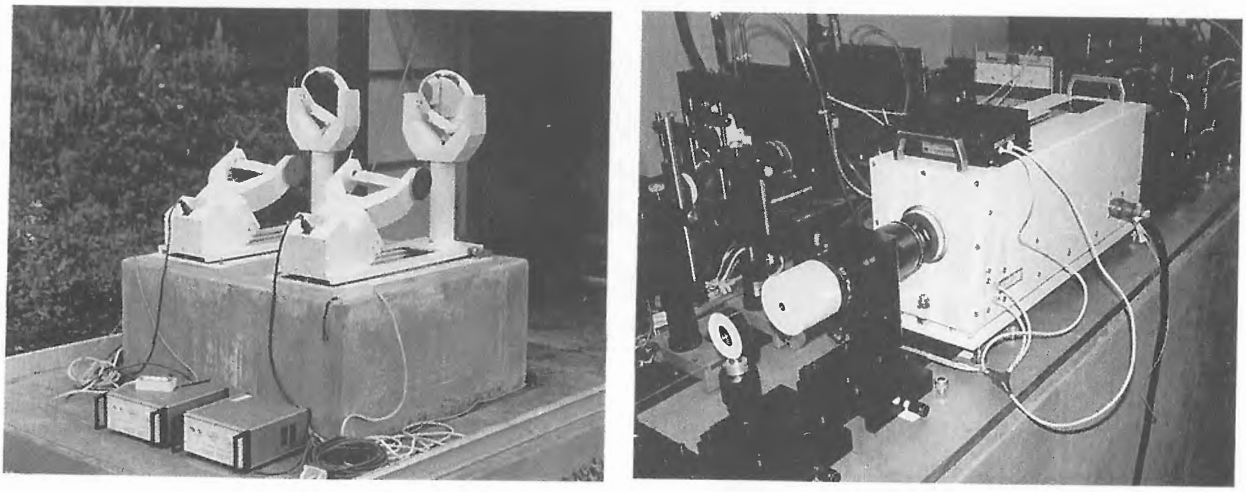

Fig. 4 The STEP full-disk magnetograph at Mitaka; the heliostat mirrors (left) and the birefringent filter (right).

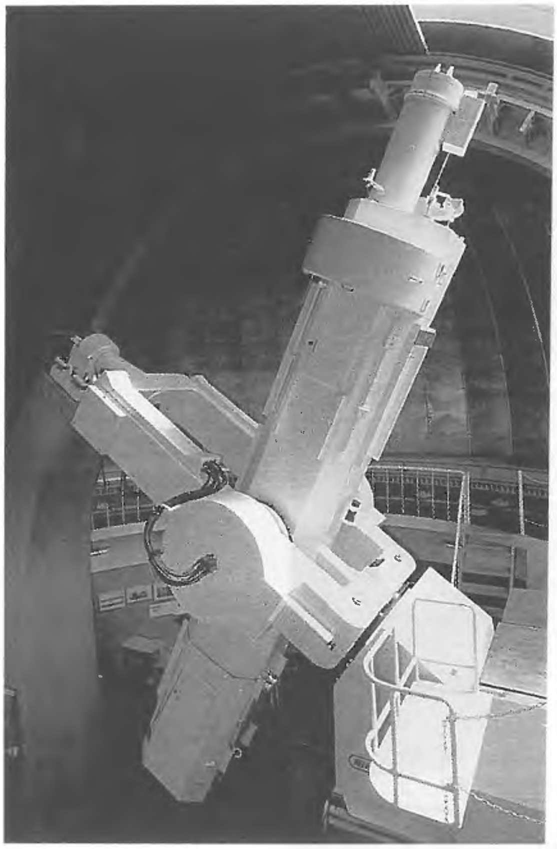

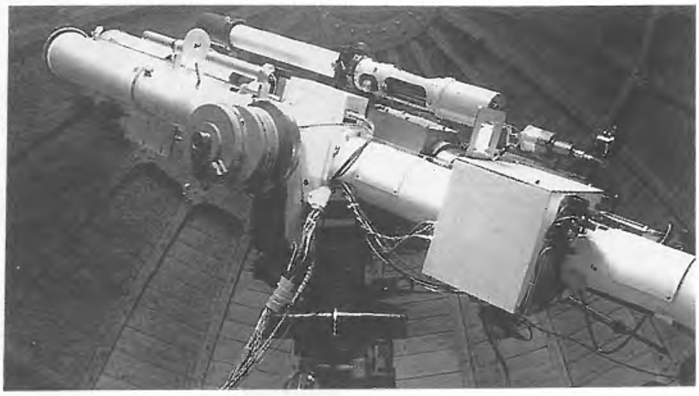

Fig. 5 The 25cm-aperture coronagraph (left) and the 10cm-aperture (right) coronagraphs at Norikura.

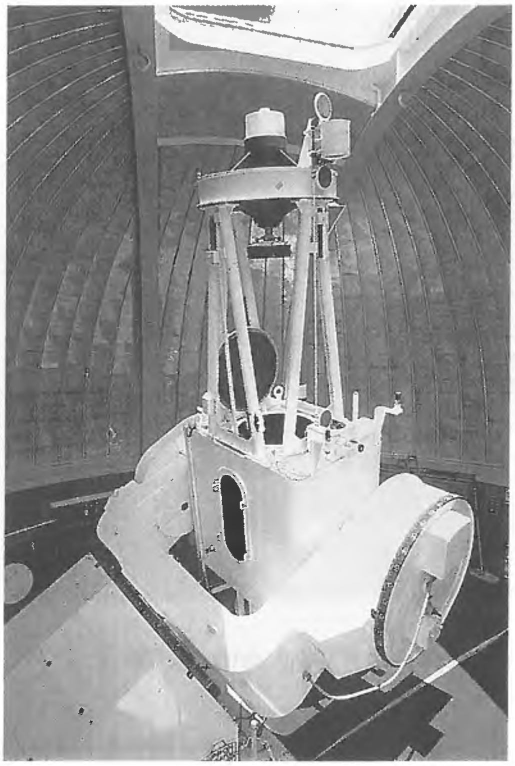

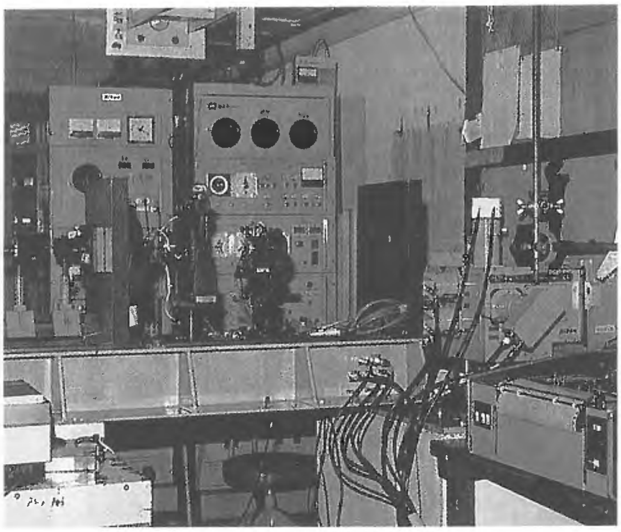

Fig. 6 The 65cm coude-type solar telescope (left) and the photoelectric magnetograph (right) at Okayama.

HIDA OBSERVATORY OF KYOTO UNIVERSITY

Hiroki KUROKAWA

Kwasan and Hida Observatories, Kyoto University, Kamitakara, Gifu 506-13

I. Introduction

Hida Observatory is affiliated with the Faculty of Science, Kyoto University and located at 137° 18′ E longitude, 36° 05' N latitude and 1276 m above sea level in the mountainous area of Hida, the northern part of Gifu prefecture. One and a quarter hours drive will bring you to the Observatory from Takayama city, which can be reached from Nagoya, a two hours ride on an express train. Here one will find the panorama of the Japan Alps which includes such mountains as Mt. Norikura at 3000 meters above sea level. This unpolluted natural environment affords significant reseach activities at Hida Observatory.

The main observational instruments are a 65-cm refracter and a 60-cm reflector for night work, and 60-cm Domeless Solar Telescope (DST) and Solar Flare Monitoring Telescope (FMT) for solar observation. The overview of the Observatory is given in Figure 1.

II. Domeless Solar Telescope (DST)

The Domeless Slar Telescope (DST) of Hida Observatory was installed in 1979 (Nakai and Hattori, 1985). The telescope is designed to attain the highest resolution that can be expected from ground-based observations and considered to be one of the most advanced in the world. In fact, the operation of the DST has provided a number of new findings on the structure of active solar phenomena. These facilities are available to guest investigators not only from all over Japan but also from other countries as well.

The DST is particulary distinguished from the ones of traditional type in the following five ways as seen in Figure 1: (1) It is placed on top of a 18-m-high tower. (2) There is no extra floor on the top of the tower. (3) It is domeless. (4) The telescope is in a vacuum. (5) The surface of the tower is cooled. An example of high reslution picture of an active region observed with the Zeiss Hα Lyot filter of 0.25 Å bandwidth is given in Figure 3 ,where the width of a spectrograph slit at the center of the picture is about 1 second of arc. An example of high resolution spectrum of chromospheri fine structures is demonstrated in Figure 4.

II. Flare Monitoring Telescope (FMT)

Fig. 1. Overview of the Hida Observatory. The Domeless Solar Telescope, the domes of the 65 cm refracter and the 60 cm reflector are standing from front to back.

Fig. 2 (a). The overview of the dome of the Flare Monitoring Telescope.

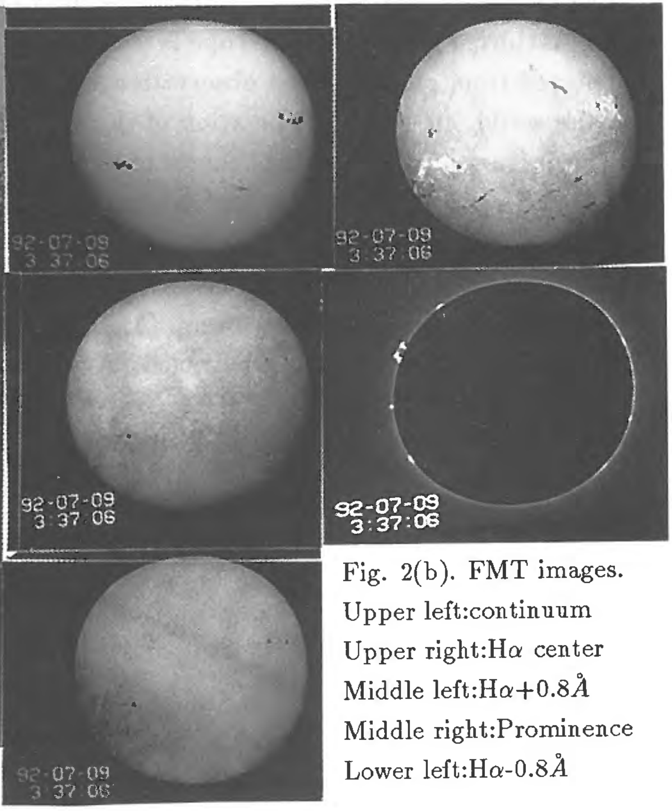

Fig. 2(b). FMT images.
Upper left:continuum
Upper right:Hα center
Middle left:Hα+0.8$\mathring{A}$
Middle right:Prominence
Lower left:Hα-0.8$\mathring{A}$

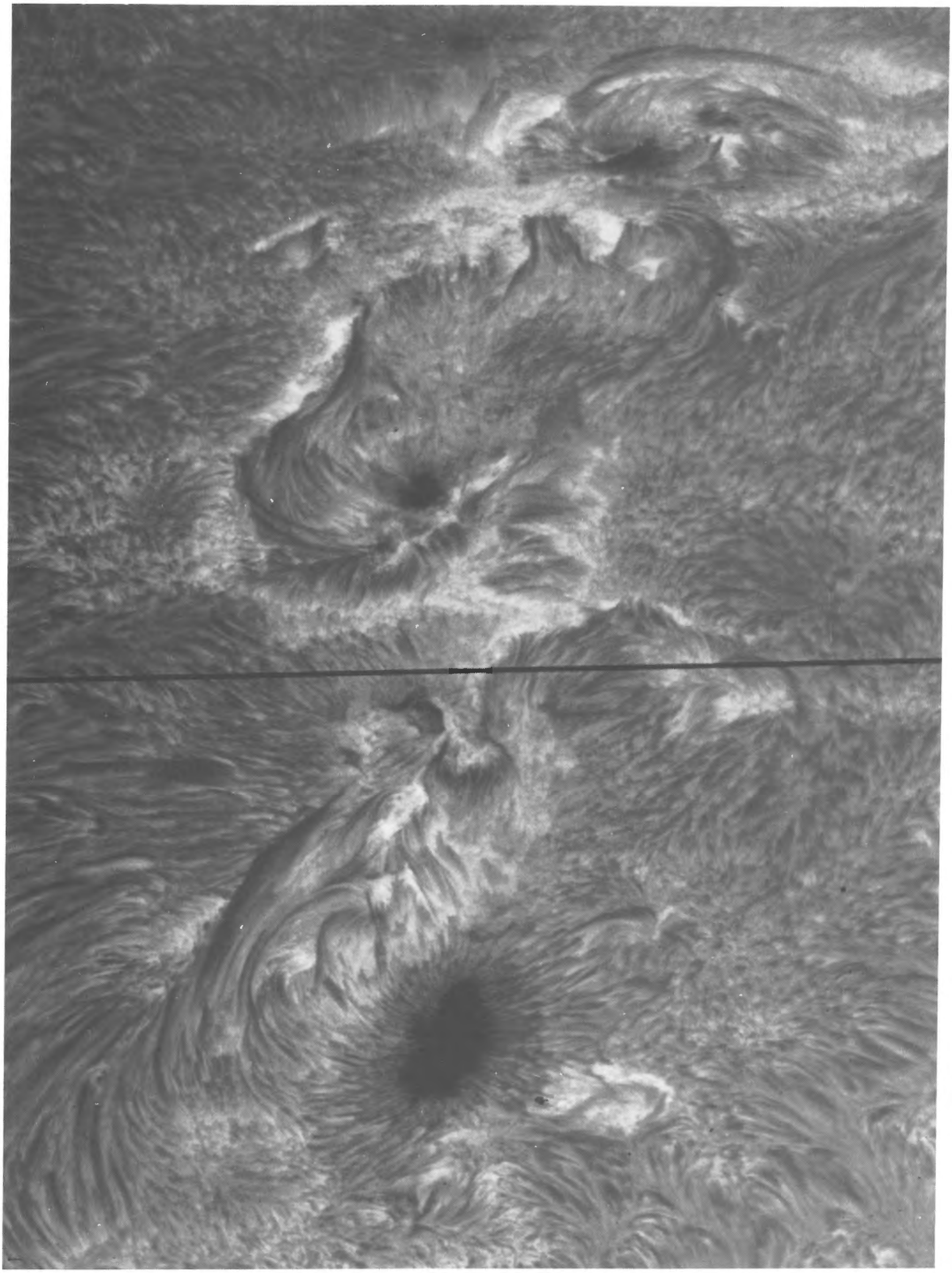

Fig. 3. An example of high resolution Hα image of an active region obtained with the Zeiss Lyot filter of Domeless Slar Telescope.

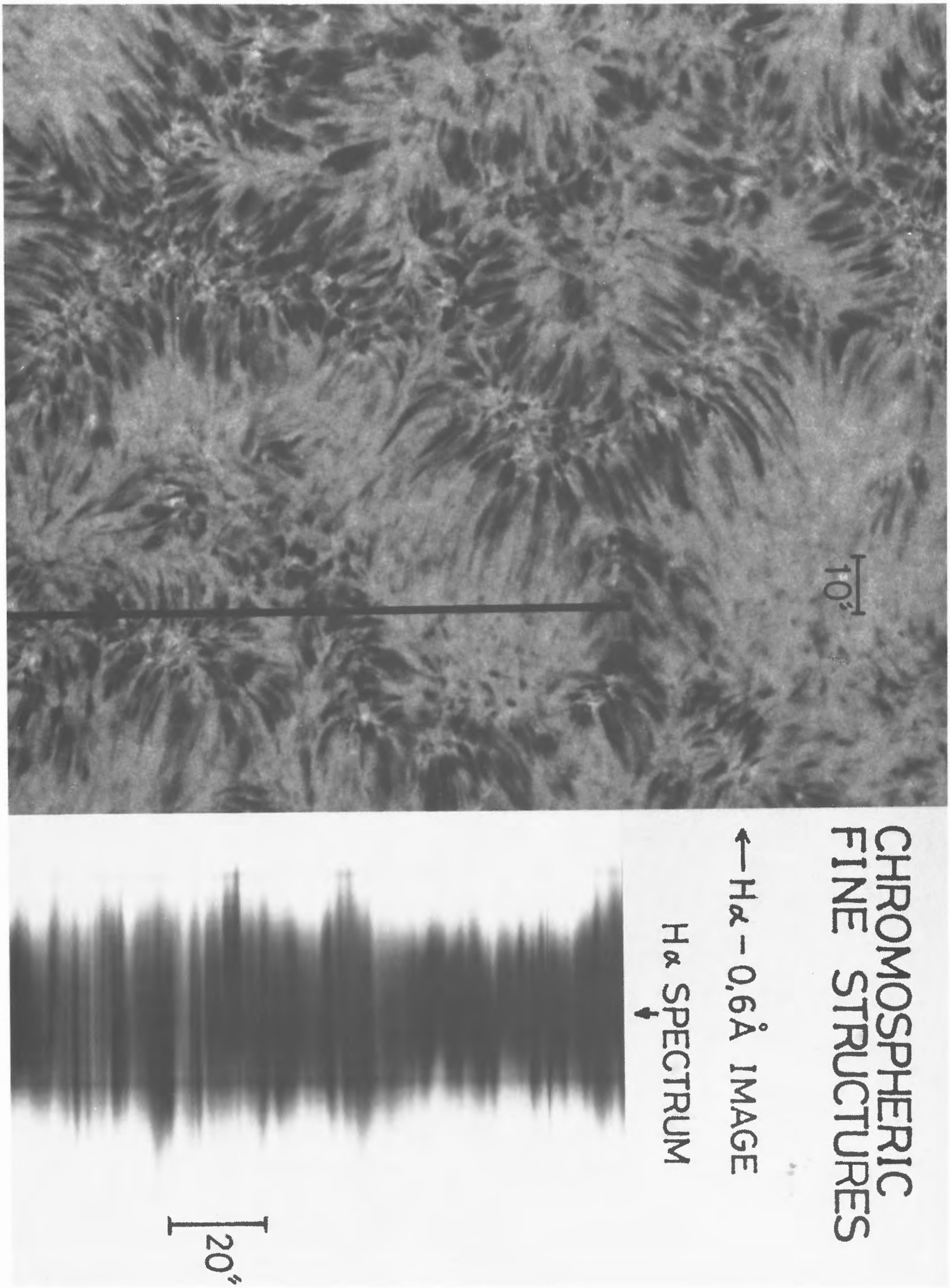

Fig. 4. An example of high resolution spectrum and filtergram of chromospheric fine structures obtained with the vertical spectrograph of DST.

The Flare Monitoring Telescope (FMT) was built to study the causal relation between solar flares, prominence eruptions, and the interplanetary and geomagnetic storms financed by the Japan STEP (Solar Terrestrial Energy Program) project (Kurokawa et al. 1992).

The overall feature of the dome of the FMT is demonstrated in Figure 2 (a). The FMT consists of six small telescopes, namely, four Full Disk Telescopes, one Prominence Telescope and one Photoelectric Guiding Telescope. They are assembles in a large fork arm which is driven with a telescope control unit. The bjective lens of each telescope is 64 mm in diameter. The four Full Disk Telescopes observe full solar images in four different wavelengths, those are, Hα line-center, Hα+0.8$\mathring{A}$, Hα-0.8 $\mathring{A}$ and continuum. The Prominence Telescope observes solar prminence outside the solar limb with two occulting cones and a Hα filter of 3$\mathring{A}$ bandwidth. These five solar images, whose examples are shown in Figure 2 (b), are continuously recorded with five CCD cameras and five time-lapse video-tape-recorders.

References

Kurokawa, H., Nakai, Y., Funakoshi, Y., Kitai, R. 1992, *STEP GBRSC NEWS* , vol.**2**, No.**2**, p.6.

Nakai, Y. and Hattori, A. 1985, *Memoirs of the Faculty of Science, Kyoto Univ.,* vol. **36**, No. **3**, p.385.

The Observatory Report

H alpha Telescope in Hiraiso and Future plan

Maki Akioka

Hiraiso Solar Terrestrial Research Center
Communications Research Laboratory
Ministry of Posts and Telecommunications
3601 Isozaki, Nakaminato-shi, Ibaraki 311-12 JAPAN

1,Intro.

Hiraiso Solar Terrestrial Research Center started the project named " Space Whether Forecast" at 1988. The purpose of this project is the comprehensive understanding of solar active phenomena and related interplanetary and geomagnetic disturbances . Its final goal is the understanding of influence of space environment for human activity in future and predict its dangerous conditions.

The current most important topic of this porject is the study of elementary process of active phenomena such as flares and the development the optical telescopes for study and prediction of solar active phenomena. The H alpha telescope for observation of surface structure and velocity field of chromosphere and filter type vector magnetograph by measuring polarization of photospheric absorption line are now under construction. The two dimensional spectrograph for multiwavelenghth observation of active phenomena and HeI 10830 heliograph will be constructed in near future. Small patrol telescopes will be also operated. These telescopes will be dedicated to study of solar flare, its prediction and patrol in colaboration with other facilities in different wavelength.

In this report, the status of H alpha telescope and observtional examples obtained during its test observation is reviewed.

2. General Specifications of telescopes

This system are developed by ourselves based on the 15cm telescope made by Zeiss. Operations for changing field of view , inserting additional optics, and adusting focus etc. can be done via Personal Computer and/or Unix Workstation. General specification of H alpha telescope are followings.

Telescope : Coude refracter of D=150mm f=2250mm (By Zeiss)
Filter : Lyot Filter with passband of 0.25 (By Zeiss)
Camera : 1/2 inch EIA camera
Pixel Size : 0.8"/pix for active region (1.2"/pix until end of June '93)
4" /pix for full disk
Guider : Photoeletric guider

The degital images are obtained by Unix workstation. Communications between Personal computer for telescope controll and imaging workstation is established by RS232 serial line. The telescope controll command are issued by workstation to PC1, and PC1 send back status to workstation. Wavelength of filter are controlled by PC 2. With PC2, the rotation angle of optical elements of Lyot filter is monitered and the motor for rotation of filter optics are controlled. PC 2 are controlled by PC 1 through serial line (Fugure 1).

The softwear for imaging and telescope controll have some useful functions. To reduce the data quantity, important part in the field of view are extracted as saving data . The seeing selection system are developed and operated to capture image with better seeing quarity. The observing sequence table can be easily programmed by using the observation supporting softwears.

3. Observation

The telescope are operated on every fine day. Usually, the target region is the same as PFI of Yohkoh/SXT. In usual case, the following data are obtained automatically.

(1) Narrow field of view mode (every or every two minutes)

The field of view is about 5 arcmin * 5 arcmin and its pixel size is 0.8"/pix. The images in H alpha center, H alpha+0.7 A, and H alpha−0.7 A are obtained every minutes or every two minutes. The continium images are also obtained.

(2)Wide field of view mode (every 30 minutes)

The field of view is about 10 arc min. and 7 arc min. Other conditions are same as narrow field of view mode.

(3)Full disk

The fulldisk in H alpha center with 4"/pix are obtained for monitoring flare and filament activities outside of primary target region.

4. Observational examples

Some observational examplesss are shown in Figure 2 – 4.

The M4/2B flare with associated surge are observed from 01UT on 23 Oct. 1993 (Figure 2) . The intermittent subflares and surge activities are observed after this event. The KPNO magnetogram shows that the isolated magnetic island of opposite polarity are located very near sunspot.

Figure 3 is the evolution of active region of NOAA 7260 and Figure 4, the evolution of NOAA 7321.

5. The future plans

(1) Filter type vector magnetograph

For the observation of magnetic field of active region, the filter type vector magnetograph is under construction. Lyot filter (FeI 6337A) and KDP elements are developed under collaboration with Dr. Li Ting at Nanjing Astronomical Research Center. The start of test observation is planned to start at around summer in 1994.

(2) Two Dimensional Spectrograph

The telescope for two dimensional spectral observation with grating or Fabry-perot filter are now planned. The purposes are detail spectral observation of initial phase of flare and filament eruption and daily monitor of coronal hole with He10830 spectroheliogram.

<Acknowledgements>

The author gratefully thanks to Drs. Y.Nakai,Y.Funakoshi at Kwasan and Hida Observatories for their various helpful comments and discussion, and Mr. J.Maekawa and M.Kamata at Carl Zeiss Co. for their kind support in maintenance work. The figures are prepared by Mrs. Okano, the secretary of Solar division of Hiraiso solar terrestrial research center.

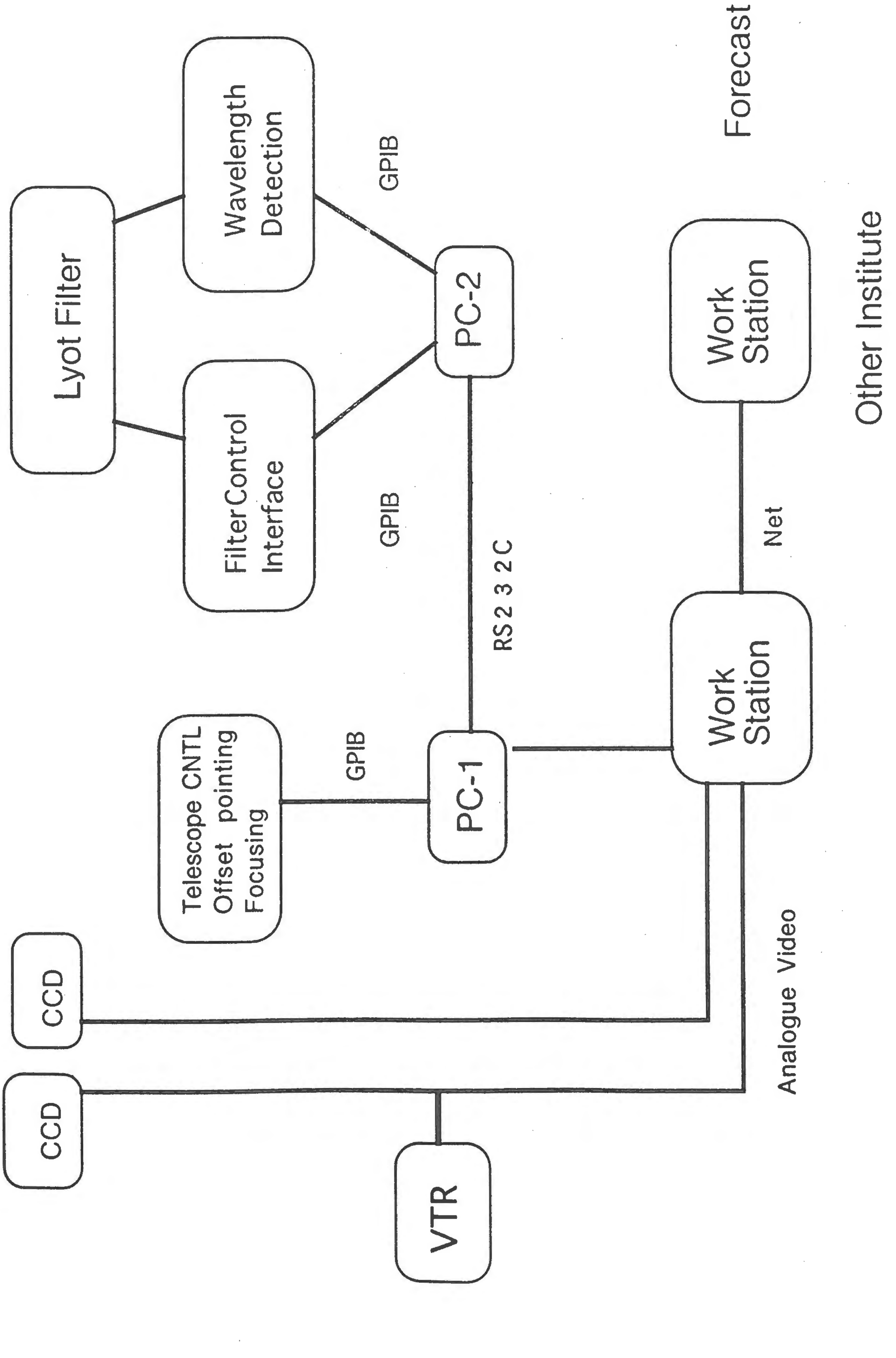
Lyot Filter
Wavelength Detection
Filter Control Interface
GPIB
GPIB
PC-2
RS232C
Forecast
Telescope CNTL
Offset pointing
Focusing
GPIB
PC-1
Work Station
Net
Work Station
Other Institute
CCD
CCD
Analogue Video
VTR

FIGURE 1

FIGURE 2

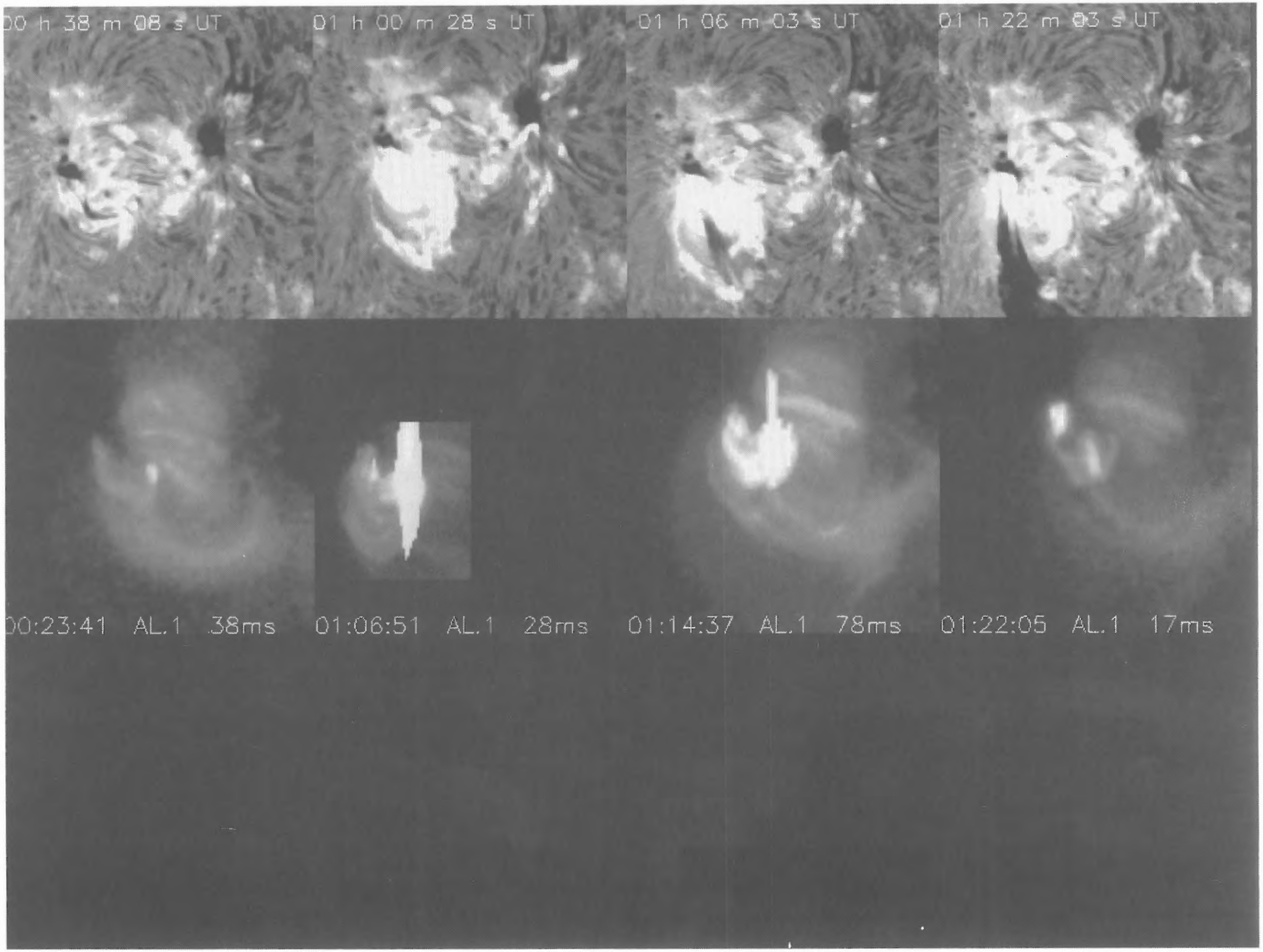
00 h 38 m 08 s UT
01 h 00 m 28 s UT
01 h 06 m 03 s UT
01 h 22 m 03 s UT
00:23:41 AL.1 38ms
01:06:51 AL.1 28ms
01:14:37 AL.1 78ms
01:22:05 AL.1 17ms

FIGURE 3

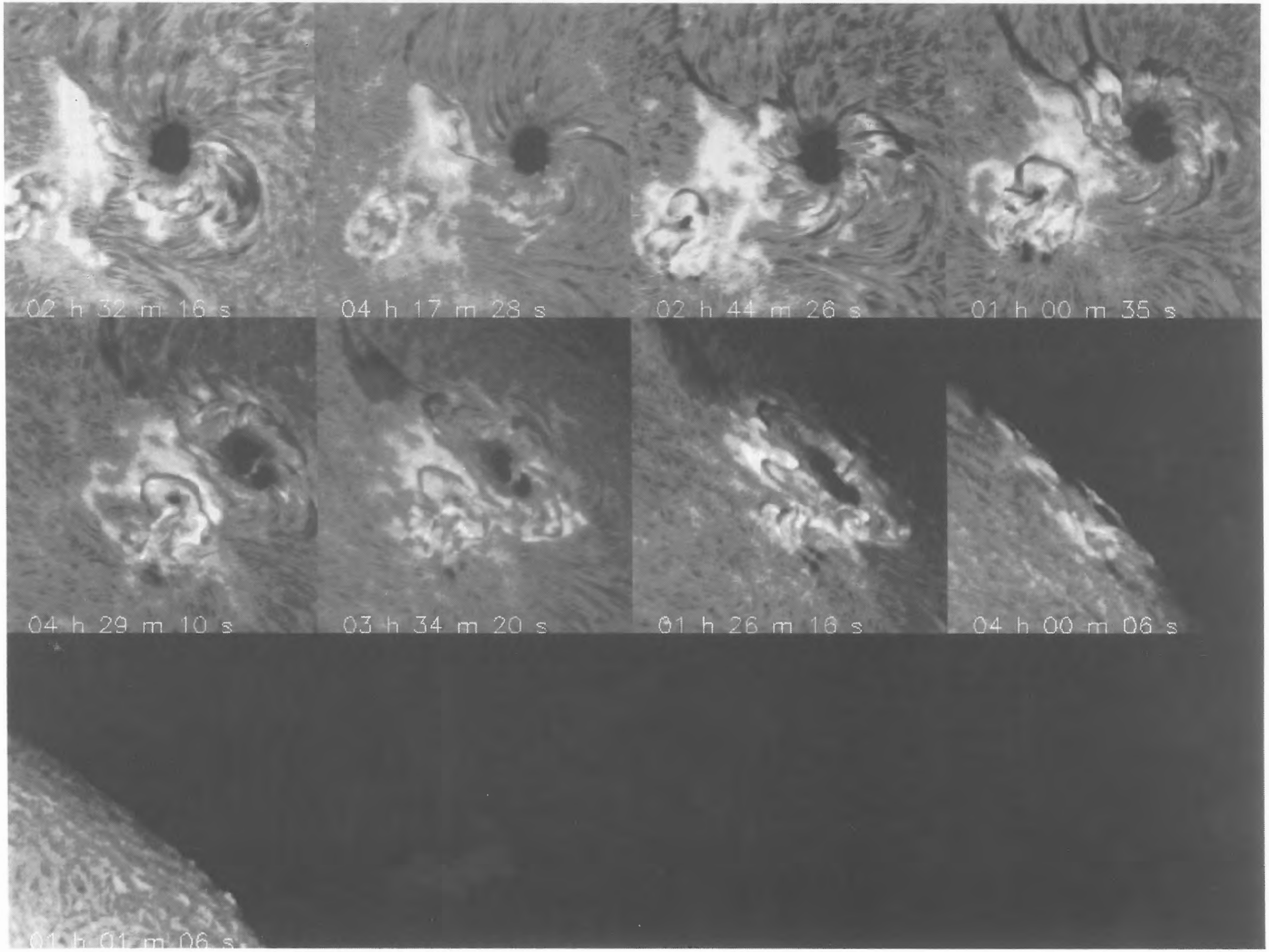
02 h 32 m 16 s
04 h 17 m 28 s
02 h 44 m 26 s
01 h 00 m 35 s
04 h 29 m 10 s
03 h 34 m 20 s
01 h 26 m 16 s
04 h 00 m 06 s
01 h 01 m 06 s

FIGURE 4

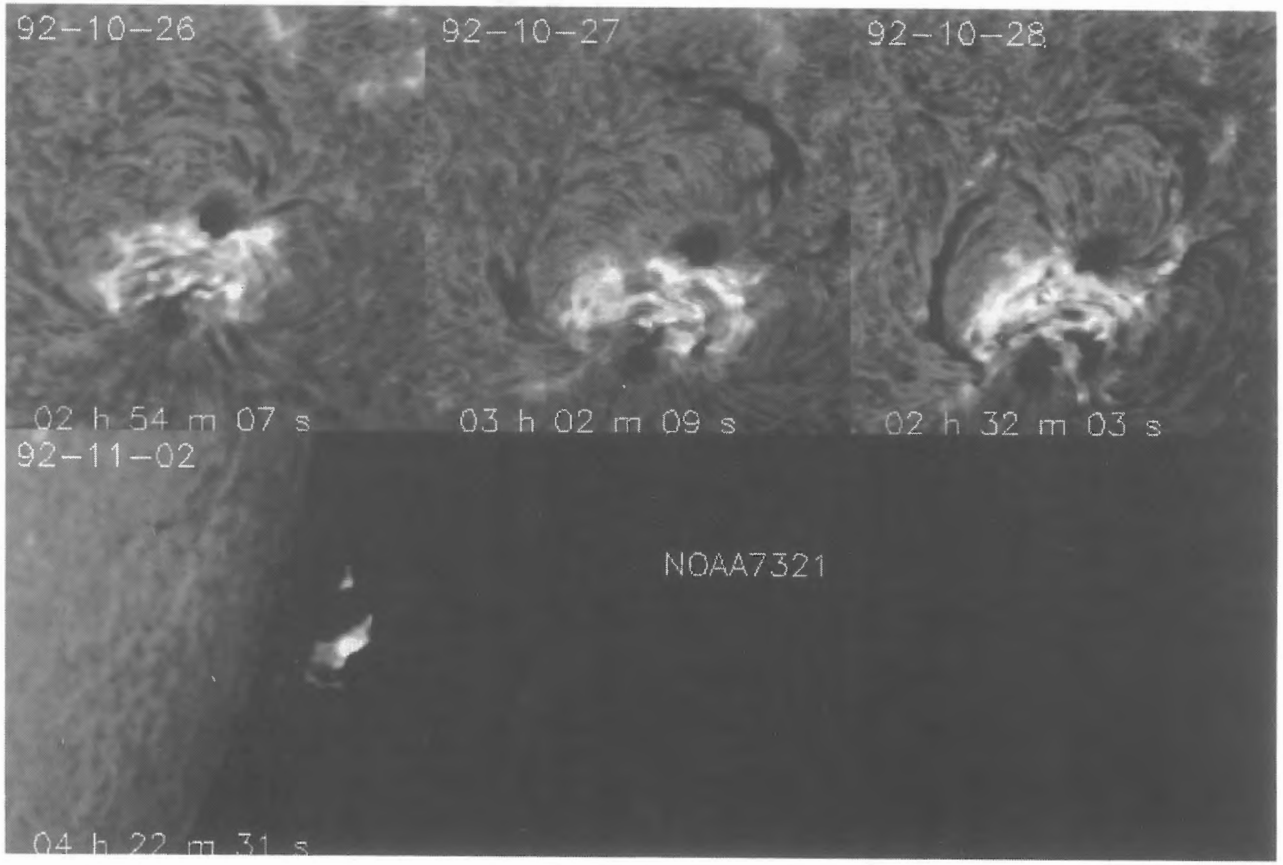
92-10-26
02 h 54 m 07 s
92-10-27
03 h 02 m 09 s
92-10-28
02 h 32 m 03 s
92-11-02
04 h 22 m 31 s
NOAA7321

The Development of Imaging Spectrograph in the Solar Tower of Nanjing University

Y. R. Huang, C. Fang, Z. G. Zhu. Y. Z. Xue, X. F. Gao
(Department of Astronomy, Nanjing University, Nanjing, China)

Abstract

This paper describes the design and the features of a imaging spectrograph which was established in the Solar Tower of Nanjing University. Some observational results obtained by the system were given.

1 Introduction

A traditional spectrograph can only obtain one dimensional spectrum of object covered by the slit of spectrograph. In order to study the physics of solar events in three-dimension space of solar atmosphere, it is needed to observe line profiles in two-dimensional field and in many wavelengths simultaneously. There are basically two kinds of way to approach this goal: one is based on using spectrograph, another is wavelength scanning with a narrow-band filter. Comparing to the filter, a spectrograph gives a high spectral resolution and a low scattering light level. Nevertheless,in the case of spectroheliograph the scanning and recording by film are too slow to observe the fast evolution of solar events. The application of CCD data acquisition gives the possibility to solve this problem. Since October 1992, by use of CCD cameras we have developed a imaging spectrograph , which can obtain the real time data of digital bidimensional spectra in the Hα and CaII K wavebands automatically and simultaneously. The foregoing description gives the details of this system.

2 Construction of the CCD system

Fig. 1 shows the scheme of the solar telescope and the imaging spectrograph system. The system includes a multichannel spectrograph, CCD cameras, an image processor, a computer, and an advanced mechanical scanning device.

The spectral resolution of the spectrograph is 130000. An image reducer is used to reduce the spectral image by a factor of 3. The CCD cameras are PULNIX TM-765 with 756(H)×581(V)

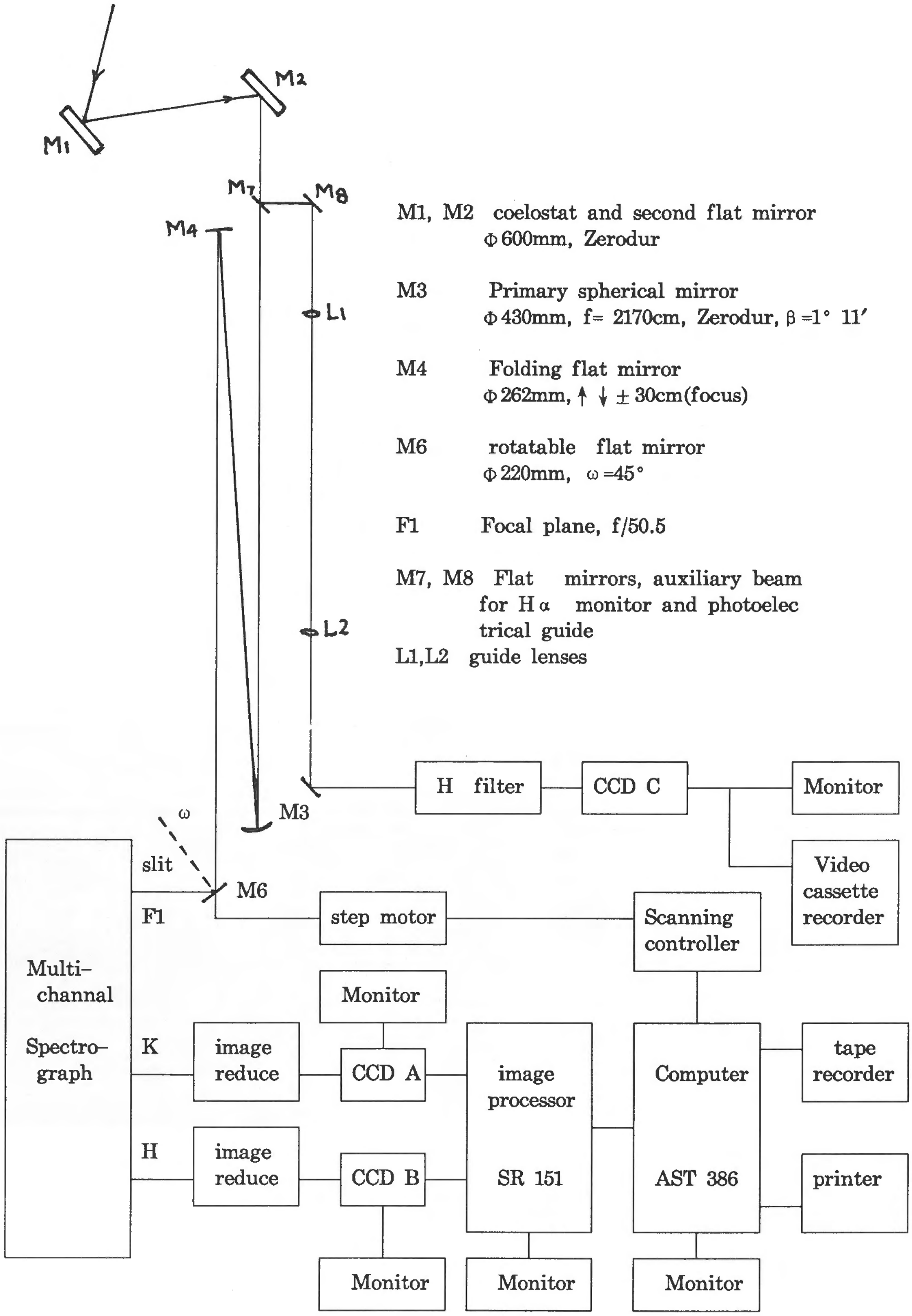

M1, M2	coelostat and second flat mirror Φ600mm, Zerodur
M3	Primary spherical mirror Φ430mm, f= 2170cm, Zerodur, β =1° 11′
M4	Folding flat mirror Φ262mm, ↑ ↓ ± 30cm(focus)
M6	rotatable flat mirror Φ220mm, ω =45°
F1	Focal plane, f/50.5
M7, M8	Flat mirrors, auxiliary beam for Hα monitor and photoelectrical guide
L1,L2	guide lenses

Fig. 1. Scheme of the solar tower of Nanjing University and the imaging spectrograph

pixels The size of each pixel is $11\mu \times 11\mu$. The image scale on the CCD is 0".732 per pixel along the direction of slit of the spectrograph. The dispersion is 0.0422 Å/pixel for Hα and 0.0541 A/pixel for CaII K respectively.

The automatic scan system makes the solar image move perpendicularly over the slit while the observation is doing. Signals from CCD cameras are amplified and digitized to 8 bit data by the image processor. A microcomputer AST386 is used for data store and scan controlling. A software package, which gives various automatic observing program, has been developed. Only 10 seconds is needed to obtain a bidimensional spectra in 10 Å wavelength region for an 1' × 2' area on the solar disk.

3 Application Examples

Using the system many bidimensinal spectra of solar events , such as flares, prominences and filaments have been recorded.

Fig. 2 shows the time variations of a flare on December 16, 1992, which were reduced from the bidimentional spectra obtained. The red-asymmetry can be seen easily from this figure.

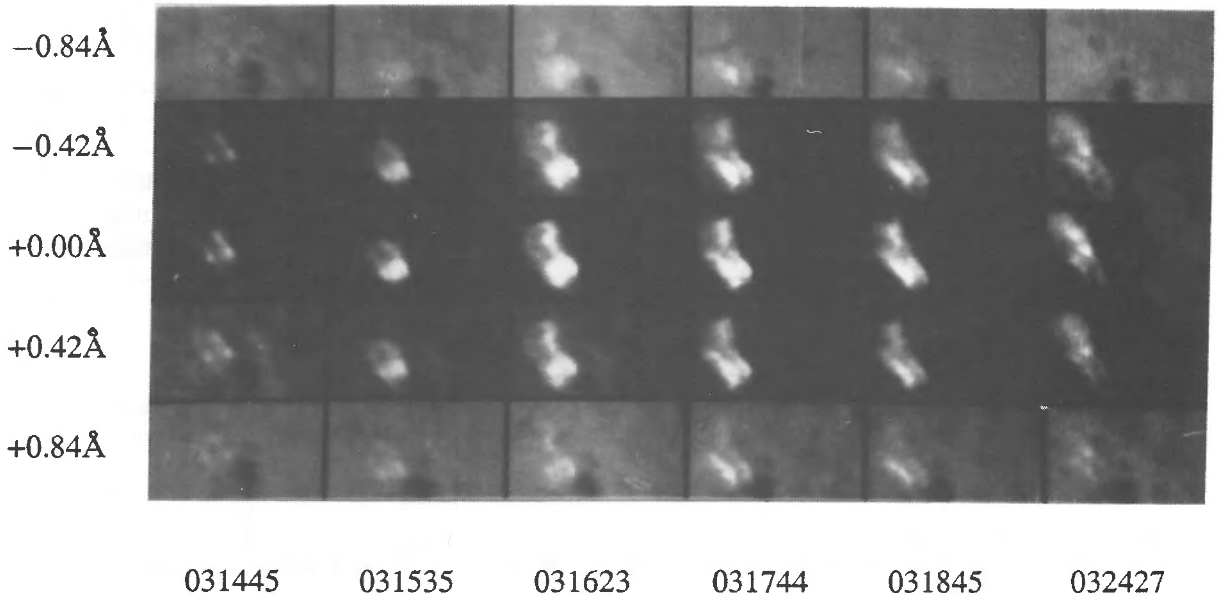

Fig. 2. Time variation of a Hα flare on December 16, 1992. Figures on the left side indicate offband raletive to the center of Hα line

Fig. 3 is the line of sight velocity field contours of the flare of Dec.,16 1992 at 03:16:23 UT, which was also reduced from the bidimensional spectra. The contours from outside to inside correspond to line of sight velocity as follows: 11.5km s^{-1}, 23.0 km s^{-1}, 32.6 km s^{-1}, 40.3 km s^{-1}. Fig. 4 is the intensity contours of the same flare at 03:16:23 UT

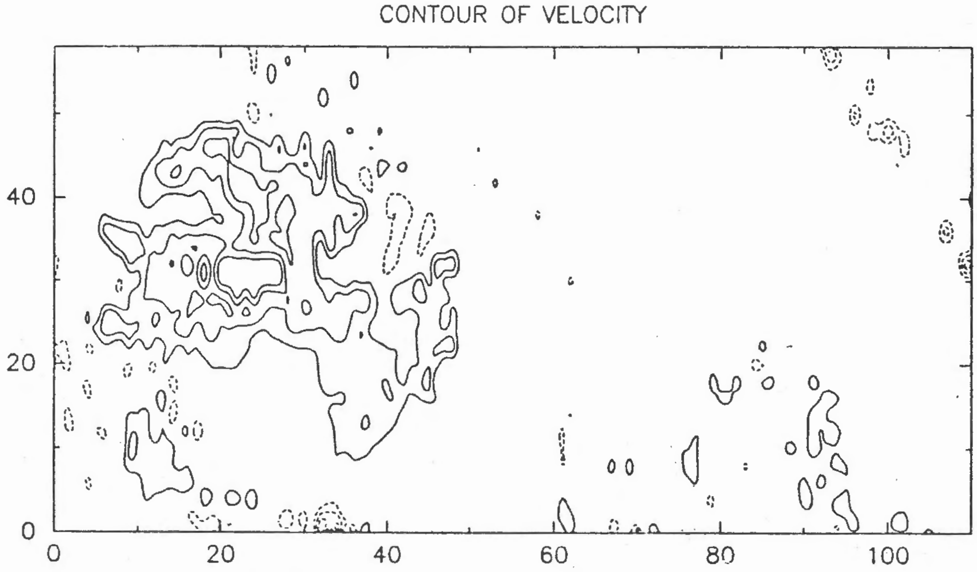

Fig. 3. Line of sight velocity contours of the flare of Dec.,16, 1992 at 03:16:23 UT, dashed lines -- blue shift, solid line -- red shift

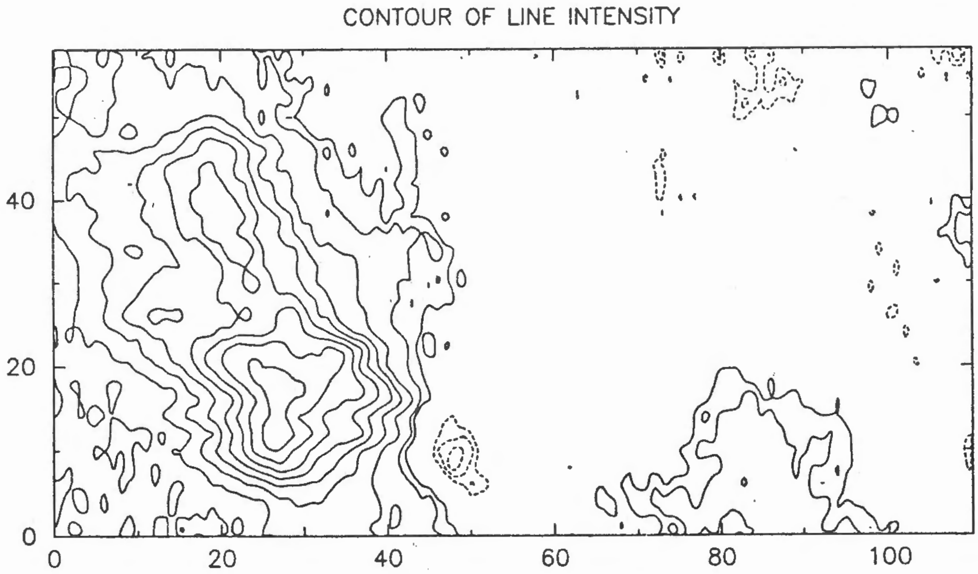

Fig. 4. Intensity contours of the same flare as shown in Fig. 3.

Session 2: General Topics

Microwave, Hα and Hard X-ray Observations of the 1992 June 26 C7.3 Solar Flare

Haimin Wang

Big Bear Solar Observatory, Caltech, Pasadena, CA91125, USA

(Extended Abstract)

Studying of solar microwave and hard X-ray is important in understanding the electron accelerations in the flare process. High temporal, spatial and spectral resolutions are vital for radio observations. In the past, microwave flares on the Sun have been studied with multi-frequency but with little or no two dimensional spatial information, (Stahli, Gary and Hurford, 1989, 1990; Wiehl et al., 1985), or high spatial resolution but little or no spectral information (e.g. VLA observation by Marsh & Hurford 1980). Since bursts may be composed of multiple sources, the spectrum obtained with poor spatial resolution may be a composition of multiple sources. On the other hand, the microwave maps may vary markedly with frequency (Dulk, Bastian & Kane, 1986), so high spatial resolution observation without spectral information could not interpret radiation mechanism. Starting from June 1991, the Owens Valley Radio Observatory (OVRO) upgraded its solar array to the 5-element array. This improved its ability to obtain high spatial (5" to 20") and spectral (45 frequencies from 1 to 18 GHz) resolution with moderate time resolution (6-12s) (Lim et al., 1993). The electrons that produced hard X-ray emissions in solar flare have long be considered as the same group which are responsible for the microwave bursts (Dennis, 1988). However, most observations of the solar flare hard X-ray have been obtained with instruments of modest or poor spectral resolution (Dennis and Schwartz 1989). The launch of the Compton Gamma Ray Observatory has make available high quality solar flare observations since April of 1991. In particular, the Burst and Transient Source Experiment (BATSE) offers dramatic a increase in sensitivity and excellent energy resolution about 10keV (Schwartz et al., 1993).

In this paper we compare the optical, microwave and BATSE observations of the June 26, 1992 C7.3 flare that occurred at 1710UT. Hα movies were obtained at Big Bear Solar Observatory. Before the onset of the flare, over-exposed Hα images show the complicated flux loop structure above the limb. Material is observed to descend along the loops towards the site where the flare occurred hours later. Using the 5-Antenna solar array at Owens Valley Radio Observatory, we obtain two dimensional maps of flare emission from 1.4 to 14 GHz. In all three temporal peaks of the microwave bursts, the maps show the same characteristics. The low frequency emission comes from the top of one bundle of the Hα loops and gradually shifts to the footpoint of the loops (the location of Hα flare) as the frequency increases. The locus of the shift of the emission peak follows the shape of an Hα surge that occurred after the flare. For each point along the locus, we create the microwave brightness temperature spectra, and compare radio derived electron distribution with that derived from the high resolution hard X-ray spectra observed by the BATSE on board the Compton Observatory. We found that the peak frequency increases as we move from loop top to the footpoint, meaning that the magnetic field increases towards the footpoint; and the high frequency slope of microwave spectra gets harder from the loop top to foot point. The microwave brightness temperature index predicted by the BATSE power-law hard X-ray spectra agrees with the observation only at the footpoint. At the loop top, the emission may be due to thermal gyrosynchrotron with a temperature of 3.5×10^7 K.

FIGURE 1

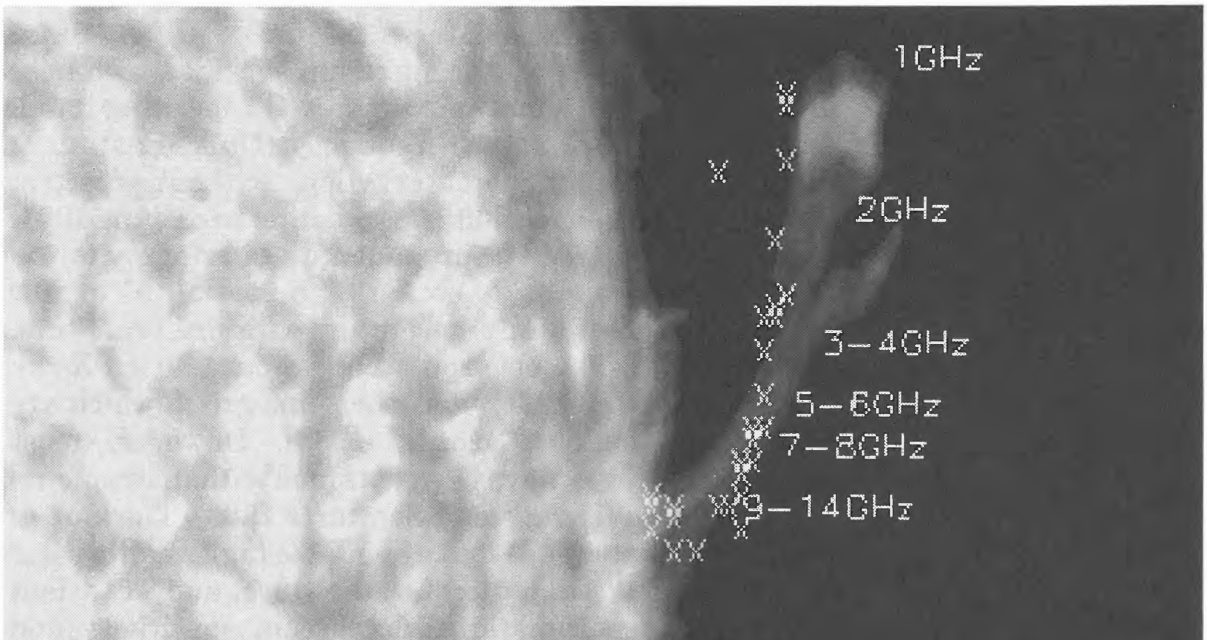

Figure 1 shows the positions of emission peaks of radio maps. The field of view of the image is 220 by 150 arcsec. The background is the Hα-0.5Å filtergram taken at 1730UT, 20 minutes after the radio bursts. The surge is clearly presented in the map. Please note that at the time of surge, there is no

FIGURE 2

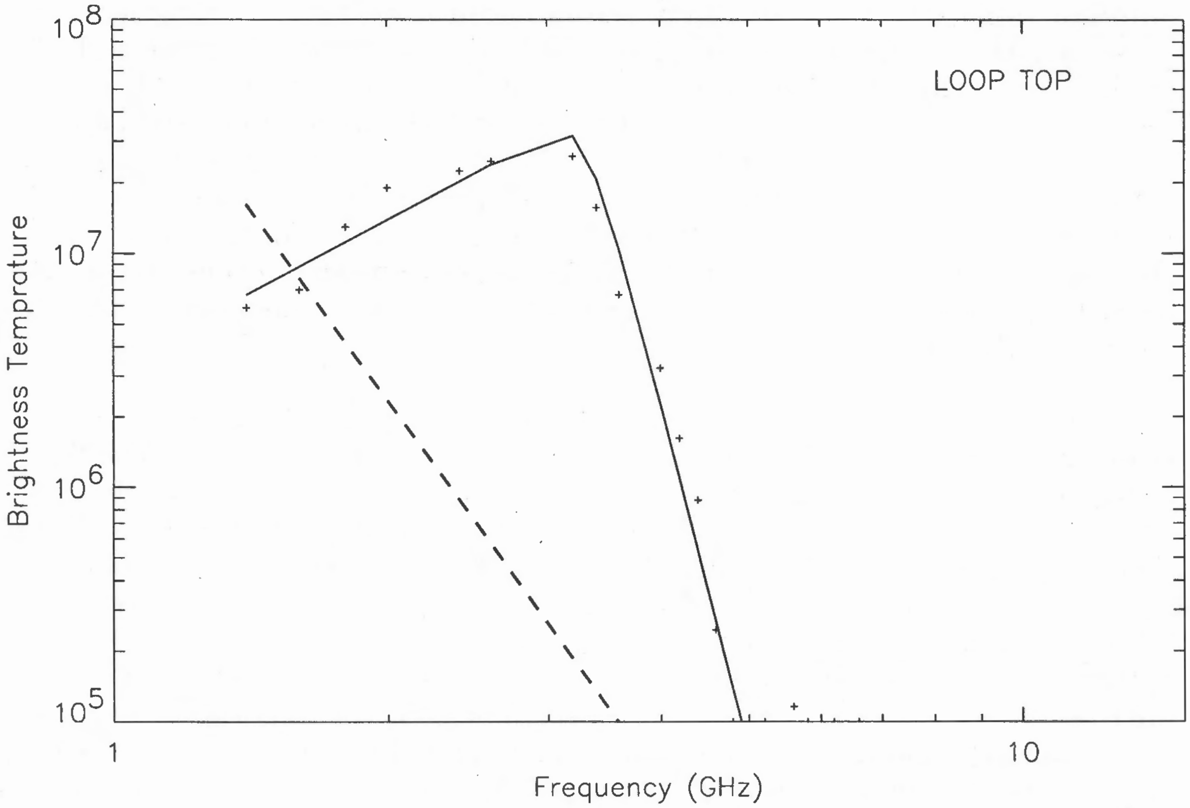
LOOP TOP
Brightness Temprature
10^8
10^7
10^6
10^5
1
10
Frequency (GHz)

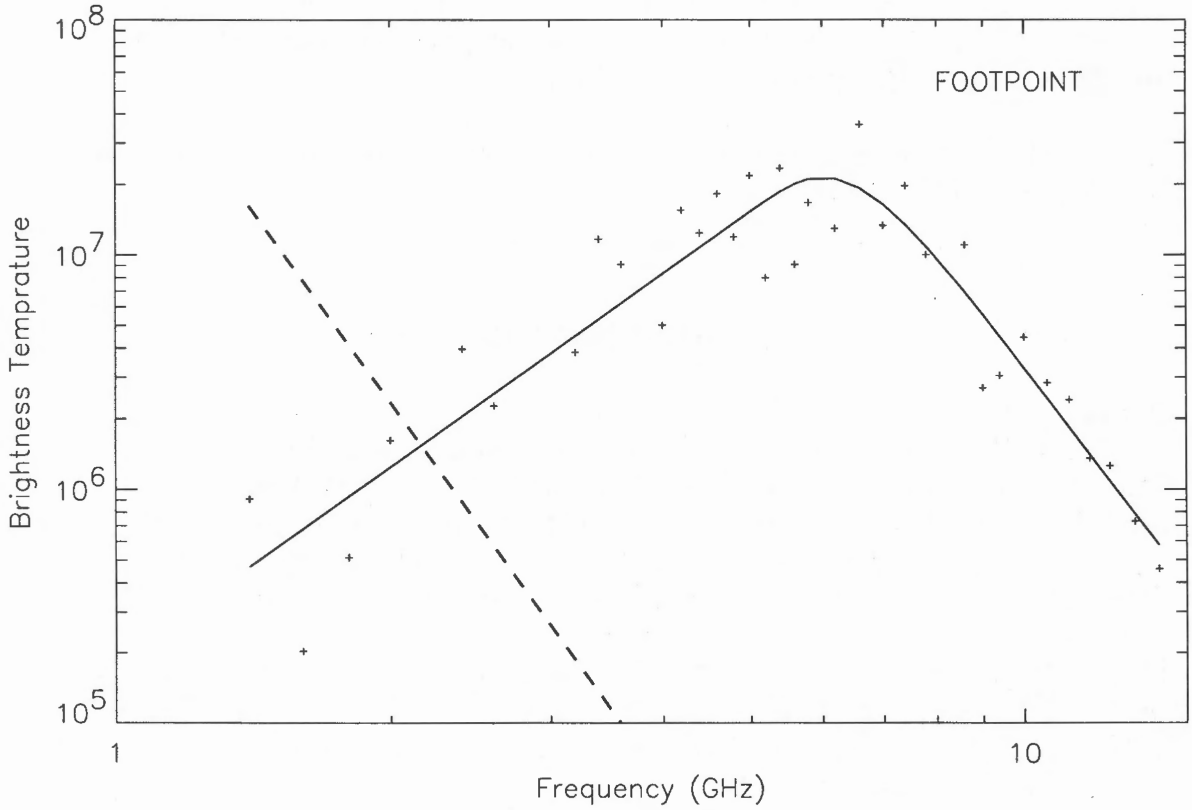
FOOTPOINT
Brightness Temprature
10^8
10^7
10^6
10^5
1
10
Frequency (GHz)

detectable microwave emission. So we are comparing two observations at different times. We show this comparison because we believe that the surge makes visible a magnetic structure that did exist during the impulsive phase of the flare. The emission peak shifts mainly towards South and sightly towards East for about 100 arcsec from 1 to 14 GHz. Most of the shift occurs between 1 and 5 GHz. The locus of the emission peaks follows the shape of the Hα surge. Likely, high energy electrons are trapped in the flux loops where the surge occurred minutes later. Low-frequency microwave emission comes from the top of the surge loop, and high-frequency emission comes from the footpoint, where the Hα brightening occurred simultaneously with the microwave bursts at 1710UT.

Figure 2a and 2b give a closer look of two typical radio brightness temperature spectra at the loop top and the footpoint respectively. The light solid line is the least-square fit of the observed spectra, developed by Stahli et al. (1989). The fitting gives peak brightness temperature, low-frequency slope, high frequency slope and turn-over frequency. Two dark dashed lines in Figure 2 reflect the predicted power index from the BATSE hard X-ray power index (photon index=3.9), assuming the radio emission is due to the power-law gyrosynchrotron. At the footpoint, the hard X-ray prediction matches with the microwave emission quite well. It is conceivable that the microwave emission from footpoint (mainly from the high frequency) and the hard X-ray emission are due to the same group of electrons. At the loop top, the brightness temperature spectra match with the shape of thermal gyrosynchrotron emission which requires the high frequency power index to be 10 and temperature to be 3.5×10^7 K, which is the temperature of a super-hot component observed by the BATSE spectra.

This work was done while the author was a Compton fellow under the NASA grant NAG5-2090.

REFERENCES

Dennis, B.R., 1988, Solar Physics, 118, 49
Dennis, B.R. & Schwartz, R.A. 1989 Solar Physics, 121, 75
Dulk, G.A., Bastian, T.S. & Kane, S.R. 1986, Ap. J., 300, 438
Lim, J., Gary, D.E. & Hurford, G.J., 1993, submitted to Ap. J.
Marsh, K.A. & Hurford, G.J., 1980, Ap.J. 240, L111
Schwartz, R.A., Fishman, G., Meegan, C., Wilson, R. & Paciesas, W., 1993, COSPA Proceedings
Stahli, M. Gary, D.E. & Hurford, G.J. 1989, Solar Physics, 120, 351
Stahli, M., Gary, D.E. & Hurford, G.J. 1990, Solar Physics, 125, 343
Wiehl, H.J., Batchelor, D.A., Crannell, C. J., Dennis, B.R. & Price, P.N., 1985, Solar Physics, 96, 339

Fe XXV Temperatures in Flares Determined from the *Yohkoh* BCS Experiment

Alphonse C. Sterling
Computational Physics Inc.
2750 Prosperity Ave., Suite 600
Fairfax, Virginia 22031 USA *

January 10, 1994

Abstract

The Bragg crystal spectrometer (BCS) experiment on board *Yohkoh* is more sensitive than similar instruments flown on earlier satellites. This increased sensitivity allows us to study flares from very early periods after onset. In this report we briefly introduce the instrument. We also describe observations of a unique flare that was well observed by both BCS and the soft X-ray telescope (SXT) on board *Yohkoh.* Studies such as these combining data from different *Yohkoh* instruments promises to vastly increase our understanding of solar flare phenomena.

1 The *Yohkoh* BCS

The Bragg crystal spectrometer (BCS) experiment on board *Yohkoh* observes the Sun in four narrow spectral bands in the soft X-ray region. These four bands cover the resonance lines and associated satellite lines of H-like iron (Fe XXVI, near 1.78 Å), He-like iron (Fe XXV near 1.85 Å), He-like calcium (Ca XIX, near 3.18 Å), and He-like sulfur (S XV, near 5.04 Å). The three highest energy channels only observe flares, while the S XV channel is capable of observing both flares and non-flaring active regions. Both iron channels share a single detector, while the calcium and sulfur channels share a second detector. The *Yohkoh* BCS is about an order of magnitude more sensitive than BCS experiments that have flown on the *P78-1, SMM,* and *Hinotori* satellites. Lang *et al.* (1992) describe the performance of the *Yohkoh* BCS.

Among the scientific objectives of the BCS is to measure thermal and non-thermal flare temperatures, bulk plasma motions, and elemental abundances. A standard procedure for measuring thermal temperatures is to use the ratio of intensities of a dielectronic recombination line to the corresponding resonance line. This ratio is well known to be temperature-sensitive. In Fe XXV spectra, appropriate lines are the Fe XXIV dielectronic line at 1.866 Å ($1s^2 2p\ ^2P_{3/2} - 1s2p^2\ ^2D_{5/2}$) and the Fe XXV resonance line ($1s^2\ ^1S_0 - 1s2p\ ^1P_1$) at 1.8499 Å. For Fe XXVI, useful lines are the Lyα lines near 1.778 Å and 1.785 Å, and the associated satellite lines in the region around 1.79 – 1.793 Å. It is also possible to estimate the Fe XXVI temperature by measuring the ratio of the intensities

---

*Current address: Institute for Space and Astronautical Science, Yoshinodai 3-1-1, Sagamihara, Kanagawa 229, Japan of the sum of the Lyα lines and the Fe XXV resonance line. Doschek *et al.* (1990) give a relationship between this ratio and Fe XXVI temperature. Flares generally have maximum Fe XXV temperatures of about 18 – 27 MK, while Fe XXVI temperatures are comparable or a little higher (e.g., Doschek 1990). There is also a category of flares that have very hot Fe XXVI spectral signatures (Lin *et al.* 1981, Tanaka 1986), as high as about 35 MK. These events are referred to as having a "superhot" component.

For the *Yohkoh* BCS, virtually all flares smaller than the GOES mid-M class produce usable spectra in all BCS channels, except Fe XXVI. Flares larger than mid-M class saturate the sensitive BCS detectors. Most flares that are large enough to generate detectable Fe XXVI spectra saturate the iron channel detector before Fe XXVI is strong enough to be detected. Only relatively small flares which have a superhot component display Fe XXVI spectra in the *Yohkoh* BCS. So far, only a small number of flares seen by *Yohkoh* satisfy these conditions. One example is an event seen on 16-Dec-1991 (Culhane *et al.* 1994). In the next section we discuss a second such event.

2 BCS Observations of the 6 Feb 1992 Flare

Around 3:12 UT on 6-Feb-1992, a flare reaching GOES class M7.6 occurred near the solar west limb. Although it was too large for continuous BCS observations, we did obtain good data throughout much of the rise phase of the event. An analysis of the Fe XXV spectra shows that the flare has a complicated Fe XXV temperature time evolution, first rising to a first maximum, then decreasing, and then increasing again, heading toward a second maximum. The first maximum is about 19 MK and occurs near 3:15 UT, and then the temperature decreases to below 18 MK, reaching a minimum at about 3:18 UT before starting to increase again. Near 3:22 UT the Fe XXV temperature is near 21 MK and still increasing, at which point the intensity of the flare saturates the BCS detectors.

This event displays a prominent Fe XXVI spectrum prior to saturation. The intensity of this spectrum is very weak or non-existent until about 3:18 UT, and it becomes strong after about 3:20 UT. The ratio of the sum of the intensity of the Lyα lines and the intensity of the Fe XXV resonance line indicates that the emitting plasma has a temperature of about 30 – 40 MK. Thus this event does indeed possess a superhot component.

Images from the *Yohkoh* soft X-ray telescope (SXT) of this event also show some interesting features. Up until about 3:20 UT, there is what appears to be one single flaring loop. Moreover, that loop is brightest in a localized region near the top of the loop. After an initial footpoint brightening, loop-top brightenings are characteristic of many flares observed by SXT (Acton *et al.* 1992, Hudson *et al.* 1994). From about 3:21 UT, what appears to be a second loop, a few arcseconds to the north of the first loop, begins to brighten. The brightening in the northern loop appears to proceed from one footpoint, and expands to fill the entire loop by about 3:26 UT. The loop-filling motion has an apparent velocity of about 200 km s^{-1}. By 3:32 UT, the intensity of the northern loop completely dominates that of the first, southernmost loop.

One possible interpretation of these observations is the following: The southern loop in the SXT images is a relatively "standard," frequently observed flare which has a maximum Fe XXV temperature of around 19 MK, no substantial Fe XXVI spectral signature, and a loop-top brightening seen in SXT images after onset. In contrast, the northern loop, which occurs later, has a maximum Fe XXV temperature in excess of 21 MK, a substantial Fe XXVI emitting component with temperatures of 30 – 40 MK, and appears to be a loop gradually filling with hot plasma in SXT images. If this interpretation is correct, this event is, to the best of our knowledge, the first of its kind ever analysed. A full report on this event, including observations from the *Yohkoh* hard X-ray telescope (HXT), will appear at a later date (Kosugi *et al.* 1994).

3 Future Prospects

Combining BCS data with observations from the *Yohkoh* SXT can give insights into flare dynamics not previously possible. In the same way, in the future work will be done combining results from all *Yohkoh* instruments. Such studies promise to further increase our understanding of solar flares.

References

Acton, L.W. *et al.* 1992, PASJ, 44 (no. 5), L71.
Culhane, J.L. *et al.* 1994, *in preparation.*
Doschek, G.A. 1990, Ap.J. (Supplement), 73, 117.
Kosugi, T. *et al.* 1994, *in preparation.*
Hudson, H.S. *et al.* 1994, *in preparation.*
Lang, J. *et al.* 1992, PASJ, 44 (no. 5), L55.
Lin, R.P. *et al.* 1981, Ap.J. (Letters), 251, L109.
Tanaka, K. 1986, PASJ, 38, 225.

Time Development of an X-Class Flare on 1992 June 28
(Extended Abstract)

Hiroshi Nakajima[1], Shinzo Enome[1], Kiyoto Shibasaki[1],
Masanori Nishio[1], Toshiaki Takano[1], Yoichiro Hanaoka[1],
Chikayoshi Torii[1], Yasuhiko Shiomi[1], Hideaki Sekiguchi[1],
Takeshi Bushimata[1], Susumu Kawashima[1], Noriyuki Shinohara[1],
Yoshihisa Irimajiri[2], Hideki Koshiishi[1,3],
and Yong-Seok Choi[1,3]

[1]Nobeyama Radio Observatory, National Astronomical Observatory, Nobeyama, Minamisaku, Nagano 384-13
[2]Communication Research Laboratory, Koganei, Tokyo 184
[3]Department of Astronomy, School of Science, University of Tokyo, Bunkyo-ku, Tokyo 113

1. Introduction

Microwave observations at high spatial resolution can provide information on acceleration and heating of electrons and magnetic field structures relevant to those electrons. In this paper, we present observations of an X-class flare (X1.8) with the Nobeyama Radioheliograph with the operating frequency at 17 GHz. The flare occurred on the west limb (N11, W90) on 1992 June 28 and was associated with intense microwave and millimeterwave emissions with duration more than 1 hour.

2. Observation

The weak plasma heating was observed during the extended preflare phase at the apparent height of 2.5×10^4 km, near and clearly separated from the microwave source in the flash phase. This preflare source is located at the higher part of a large soft X-ray loop which were able to be seen in SXT full-disk images.

The microwave weak enhancement in the pre-flash phase was initiated at the apparent height of 0.7×10^4 km around the intersection of the footpoint of the large soft X-ray loop and an adjacent arcade-like region, and then, expanded to the whole arcade-like region, resulting in an elongated, double-peak structure.

The strong microwave emission in the flash phase is essentially located around the southern part of the elongated structure seen in the pre-flash phase.

The microwave-millimeterwave spectrum in the pre-flash phase has rather a narrow bandwidth, a low turn-over frequency of 5 GHz, and a soft spectrum index of 4.1 in the high frequency part. On the other hand, the spectrum in the flash phase has a wider bandwidth extending well in the millimeterwave frequency, a higher turn-over frequency of 9 GHz, and a harder spectrum index of 2.1 with soft-hard-soft time evolution. Both spectra in the pre-flash and flash phases can be explained by gyrosynchrotron emission due to nonthermal electrons.

In the post-burst increase phase, the microwave source has an elongated structure extending along the limb showing rising motion at a speed of 3.5 km/s. This elongated microwave source, in the initial stage when the elongated structure begins to be seen, almost exactly coincides in both extension and position with the microwave source seen in the pre-flash phase.

SXT partial-frame images, available in the post-burst increase phase, show a hot post-flare loop system accompanied by rising motion with the same speed as the microwave post-burst increase source, corresponding to a cold H-alpha prominence system. The H-alpha loop system is composed of double arcades which are slightly separated in series. Corresponding to the H-alpha double arcades, the soft X-ray loop system shows a double-peak structure. Note that the double-peak structure is also seen for the microwave source in the pre-flash phase. Overlay of microwave and soft X-ray images shows that the elongated microwave structure in the post-burst increase phase roughly coincides with the corresponding soft X-ray structure, including the double peak structure, suggesting both emissions from the same thermal plasma trapped in the post-flare loop system.

3. Conclusion

The above observations suggest that there already exists in the pre-flash phase almost the same magnetic field structure as the arcade structure seen in the early post-burst increase phase. At the onset of the pre-flash phase, there is morphological evidence of loop-loop interaction which is followed by the source expansion into the whole arcade region.

The weak nonthermal emission in the pre-flash phase is followed by the much more intense and harder nonthermal emission in the flash phase. The present observations suggest that the microwave emission in the flash phase originates from a part of the same arcade structure as that in the pre-flash phase.

Changes of Vector Magnetic Field During a Powerful Flares in Active Region (NOAA 6659) on June 6, 1991

Hongqi Zhang

Beijing Astronomical Observatory,
Chinese Academy of Sciences Beijing 100080, China

Abstract

The active region of 1991 June, NOAA 6659, was the most prolific white light flare-producing region in recent history. About five white light flares were observed in the active region. We present here the observational results of photospheric vector magnetic fields of this region at the Huairou Solar Observing Station of the Beijing Astronomical Observatory and discuss the magnetic fields and the relation with the powerful (white light) flares.

After analysis of a series of monochromatic images of Stokes parameters Q, U and V with high spatial resolution, the following new phenomena observed are found that before and after powerful (white light) flares, the obvious change of vector magnetic fields occurred at the magnetic neutral line near the sites of these flares. The white light flares probably are caused by the violent motion of the photospheric lines of force.

1. Introduction

NOAA 6659 was a largest solar active region of the abnormal magnetic configuration after solar cycle 22 began. This region produced some powerful flares which include five white light flares. When the first great (white light) flare occurred in this active region at the east limb of the Sun on June 4, we arranged magnetograph observation. A series of photospheric vector magnetograms, chromospheric longitudinal magnetograms and Dopplergrams in Active Region 6659 were obtained at Huairou Solar Observing Station of the Beijing Astronomical Observatory during the international campaign of June 3 – 16, 1991.

2. Observational Data

The observations of this study were using the vector video magnetograph at the Huairou Solar Observing Station (Ai, 1987). The magnetic structures of the active region 6659 are complicated. Some magnetic gulfs and islands formed in this region. The magnetic structures of this region was a δ-configuration. The total measured field in this region was concentrated in a great central row of p-polarity spots, completely surround by f-polarity. On June 9, 1991, this active region was located near the center of the solar disk. The transverse components of the field showed the evident rotation around the main pole of negative polarity clockwise. The transverse components near the magnetic neutral line were strongly sheared and almost parallel to it in the east side of the active region.

A large number of flares were registered in X-ray. Five white light flares (WLFs) were obtained (Zhu *et al.*, 1991; Yan and Zhang, 1991; Sakurai *et al.*, 1992). Some of these flares and corresponding magnetic fields in this active region were observed at Huairou Solar Observing Station.

3 A 4B/X12 (White Light) Flare on June 6, 1991

A series of chromospheric Hβ images of 4B/X12 flare on June 6, 1991 given was obtained at Huairou Solar Observing Station. The initial sites of this flare as the thread-like pattern appeared in the middle of the active region along the magnetic neutral line at 0100 UT, then the flare ribbons separated away from the magnetic neutral line, and the Hβ post-flare loops formed and bridged over the neutral line at 0123 UT. A white light flare was observed at 0105–0108 UT at Shahe Station of Beijing Observatory (Zhu *et al.*, 1991). The emissions of the WLF were located in the ribbons of the Hβ flare. But the appearance of post-flare loops formed on Hβ images was later than the white light flare about 20 min. The end time of this flare was 0215 UT.

A series of longitudinal and transverse magnetograms of this active region is shown in Figure 1. We can see that two large-scale magnetic structures A and B of positive polarity in Figure 1 almost connected together to form a ribbon-like structure and separated the field of negative polarity near the middle area in the active region. The average width of this magnetic ribbon of opposite polarity is about $9''$. The obvious change of magnetic field appeared near the sites of white light flare. The black pieces in Figure 1 mark the sites of the white light flare. The largest changing area was located at the east side of the preceding main spot. Two large-scale magnetic structures A and B of positive polarity, discussed above, connected together to stretch over the active region then broke again twice from 0050 to 0650 UT. The evident shift of the magnetic neutral line toward the preceding main pole P occurred at 0127 UT. Perhaps, this change of magnetic neutral line was caused by following possibilities: (a) The direction of the field changed near the inversion line due to the fast winding or emerging of twisted force lines, if we consider the project effect of the magnetic field and the spatial configuration of the field in the active region; (b) The inversion or distortion of the photospheric line profile at the working wavelength of the magnetograph after the white light emission about a half hour also kept at the surrounding of patches of white light flare and it influenced the measured results of the photospheric magnetic field near sites of the white light flare. Even the second possibility exits, we also point up a fact that after the Hβ flare the longitudinal magnetic structures (0234 UT) near the sites of WLF also show more different than before one (0050 UT). At 0234 UT, a new magnetic structure $f2$ of positive polarity occurred at the connecting place of large-scale magnetic structures A and B.

Because the region on June 6 was located near the east limb of the Sun (N30, E43), the transverse components of the field contained some information of the vertical components of the field relative to the solar surface. If we compare the difference between the transverse magnetograms in Figure 1 carefully, we can find that the orientations of transverse components of the magnetic field changed in between the two sites of the white light flare near the magnetic neutral line. Transverse fields with a tendency rotated toward the direction of the connected line of WLF's sites. The largest change of the orientations of the transverse field here was about $30° - 40°$. Because the transverse magnetograms are inverted from Stokes parameters Q and U, we return to study the monochromatic images of Stokes parameters Q and U and confirm their evolution. In Figure 2, we show four couples of corresponding monochromatic images of Q and U in AR 6659 at about 0052, 0145, 0518 and 0643 UT on June 6. Near the sites of the white light flare in the vicinity of the magnetic neutral line of the active region, the structures on Q and U components changed obviously from 0050 to 0146 UT. These changes contain the intensities and polarities of Q and U components of the linear polarization light. But other structures in Q and U images were relative stable.

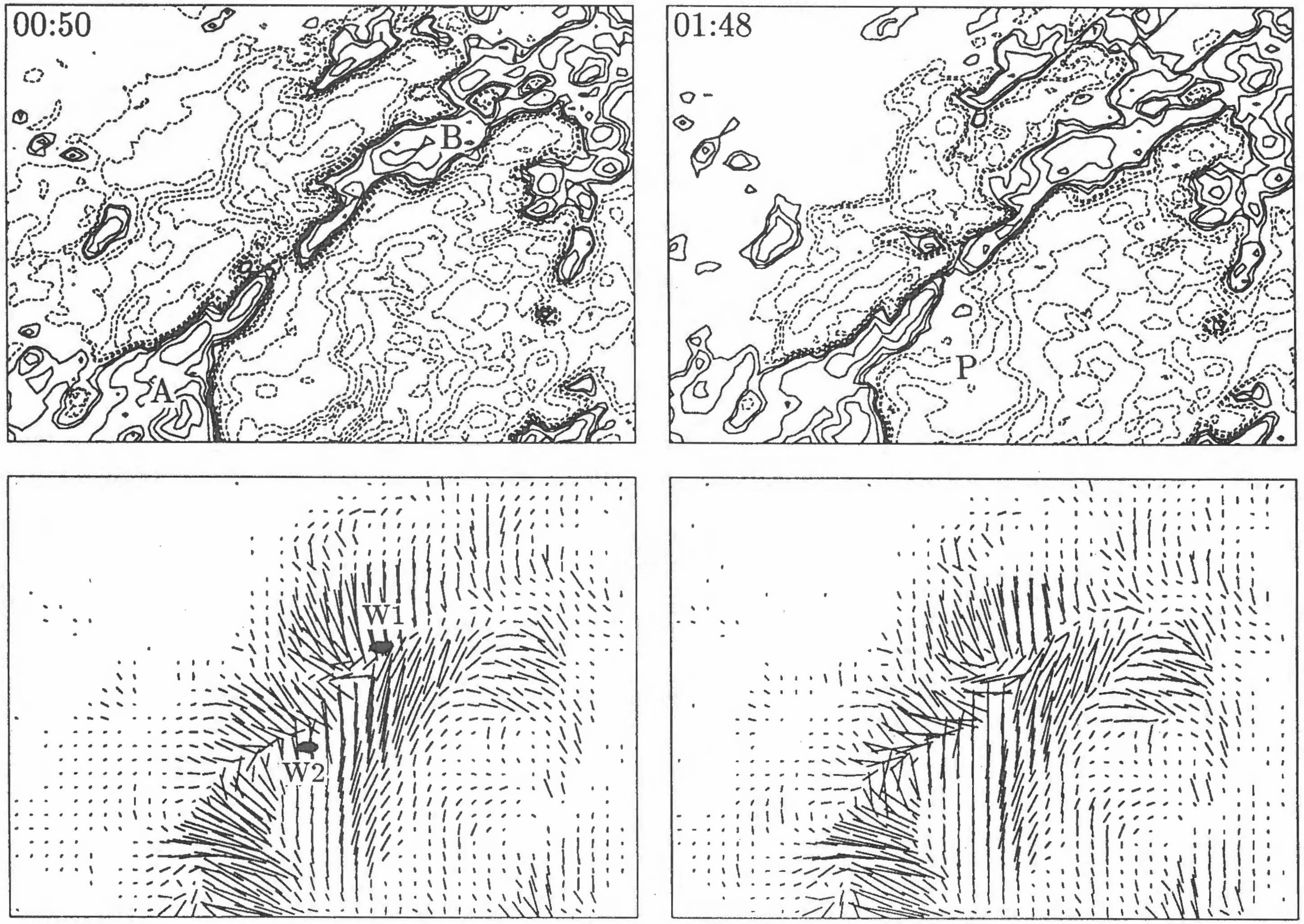

Fig. 1a. A series of photospheric longitudinal and transverse magnetograms in AR 6659 on June 6, 1991. The black structures mark the sites of the white light flare. The change of the transverse field occurred on the area between the both sites (w1 and w2) of WLF.

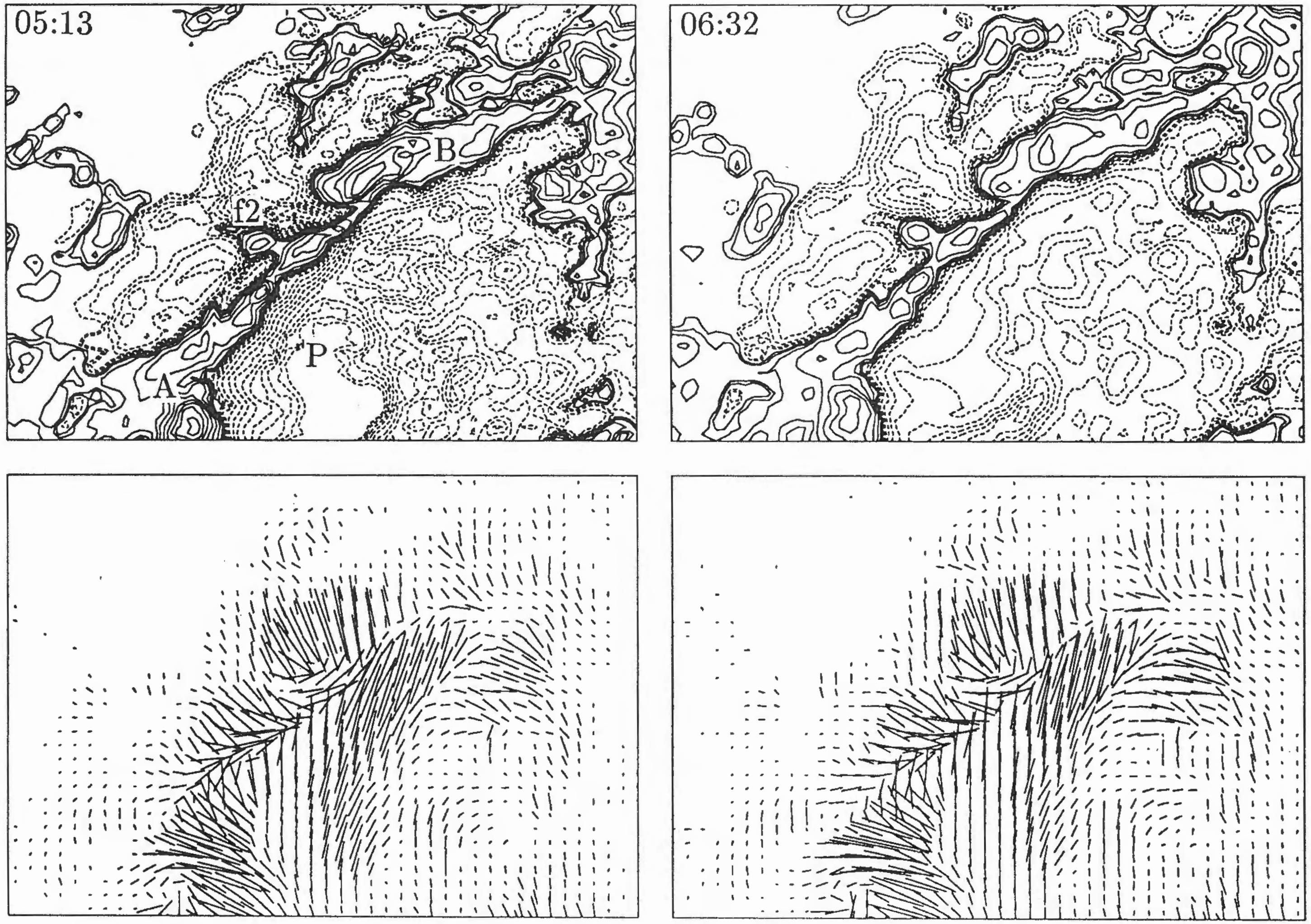

Fig. 1b.

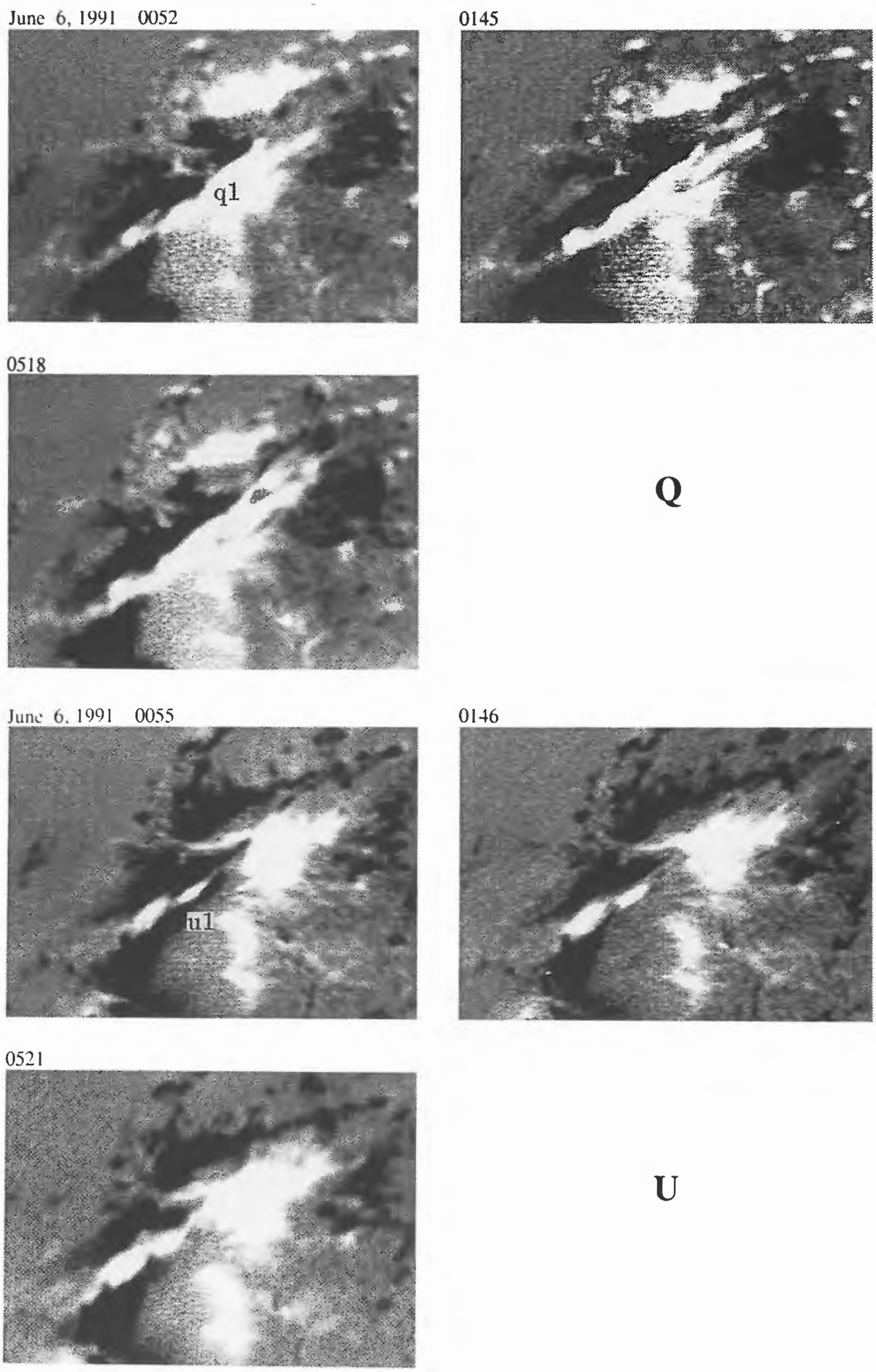

Fig. 2. A series of monochromatic images of Stokes parameters Q (a) and U (b) in AR 6659 on June 6.

We see that in the middle of the monochromatic image of Stokes parameter Q the peak $q1$ of positive polarity during this time shifted toward the east-south direction to form a ribbon-like structure, and where a structure $u1$ of negative polarity in the monochromatic image of Stokes parameter U shifted at same direction obviously while the neighbouring structures of positive polarity moved toward here gradually. According to the formulae $B_{\perp}=C_{\perp}\sqrt[4]{q^2+u^2}$ and $\varphi=0.5\mathrm{tg}^{-1}(\frac{u}{q})$, where φ is the orientational angle of the transverse component of the field, the evolution of Stokes parameters Q and U, in the middle of the active region, actually reflects the changes of the transverse magnetic field. These variations of the Q and U discussed above were consistent with the analysis of the transverse field and roughly synchronized with that of the longitudinal magnetic field before and after the WLF of June 6. This means that the changes of the field during this powerful flare did not only take place in the line-of-sight component. The powerful flare was accompanied with change of the photospheric vector magnetic field in the active region.

4. Discussion and Results

The main pole of this active region was negative and some enhanced networks of positive polarity were located around this region. Some of magnetic lines of force probably connected both structures of opposite polarities at the higher atmosphere. A series of homologous flares in AR 6659 probably was triggered by interaction between the twisted magnetic ropes and the large-scale magnetic field of the main pole near the magnetic neutral line. The former probably was new emerging flux and formed at lower atmosphere. If we compare the magnetograms of June 4, 6 and 9 and consider the perspective effect of the field in the active region on the solar disk, we can easily imagine that some of magnetic lines of force immediately connected the both sites of white light flares and bridged over the magnetic inversion line at the lower solar atmosphere. The magnetic field of high shear and gradient near curved neutral line stored the enough free energy for the trigging of a series of white light flares in this active region.

After analyses of the vector magnetograms and the relationship with powerful flares in the active region (NOAA 6659), the main results are following:

(a) Active Region 6659 was a complex region. The preceding polarity spots had more than 80 % of flux and umbra area. Large-scale magnetic field shows the polarity order inverted from the Hale-Nicholson low.

(b) The vector magnetic field of AR 6659 appeared obvious variation during the white light flares on June 6, 1991. The changes of the magnetic neutral line and the orientation of the transverse components of the field taken place near the sites of the white light flares. The observed results of flares also demonstrated that the magnetic shear increases after powerful flares.

Acknowledgements

This research was supported by the Chinese Academy of Sciences and National Science Foundation of China.

References

Ai, G. 1987, *Publ. Beijing Astron. Obs.*, 9, 27.

Sakurai, T., Ichimoto, K., Hiei, E., Irie, M., Kumagai, K., Miyashita, M., Nishino, Y., Yamaguchi, K., Geng, F., Kambry, M. A., Zhao, Z. 1992, *Publ. Astr. Soc. Japan*, 44, L7.

Yan, X. and Zhang, H. 1991, *CSGD*, 218, 40.

Zhu, C., Gao, F. and Qiao, Q. 1991, *CSGD*, 215, 78.

The Development of Magnetic Shear

Jingxiu Wang

Beijing Astronomical Observatory, Chinese Academy of Sciences

Abstract

The current concept of magnetic shear is visualized from a global sense. The external linkage or compression of two sets of current-carrying magnetic loops seems to be the basic topology of sheared magnetic field. Internal twisting of magnetic lines of force has not been incorporated into the shear presentation. As a fully three-dimensional phenomenon, more efforts are crucially needed to understand the characteristics of magnetic shear in the higher atmosphere.

Two modes of shear creation are suggested. One is named as *Tanaka mode* according to which the strong sheared field emerges from below the photosphere. The other is the *generation mode* in which the interaction between plasma motion and the magnetic field is responsible for the local changes of shear status.

1 Introduction

The concept of magnetic shear has occupied a central position in the study of flare-associated changes in the magnetic field since early of 1970's (Zirin and Tanaka, 1973). Particularly after the introduction of a quantitative measure of magnetic shear by Hagyard et al.(1984), the shear observation has become one of the most important aspects in flare research. However from physical sense, what is meant and what kind of magnetic topology is implied by the term of magnetic shear, and what causes the changes of the shear status? On the other hand, from observational point view, how could we describe the magnetic shear more accurately? All these questions are addressed in this paper with the purpose to provide possible guidance for further studies in this working area.

2 Topology of Sheared Magnetic Field

The magnetic shear was first recognized from the morphology of H_α fibrils or filaments, which were in alignment with the magnetic neutral line in flare studies (Zirin and Tanaka, 1973). A quantitative measure of magnetic shear was suggested then by Hagyard et al.(1984). They defined the angular shear, $\Delta\phi$, on the photosphere as the azimuth difference between the observed vector field and a potential field which shares the line-of-sight field with the observed one. The following studies were almost entirely concentrated on the angular shear on the magnetic neutral line. Intrinsically, the shear is represented by a bundle of strong transverse field, or a sets of flux loops aligned with the magnetic neutral line. However, the magnetic neutral line, in fact, is specified by

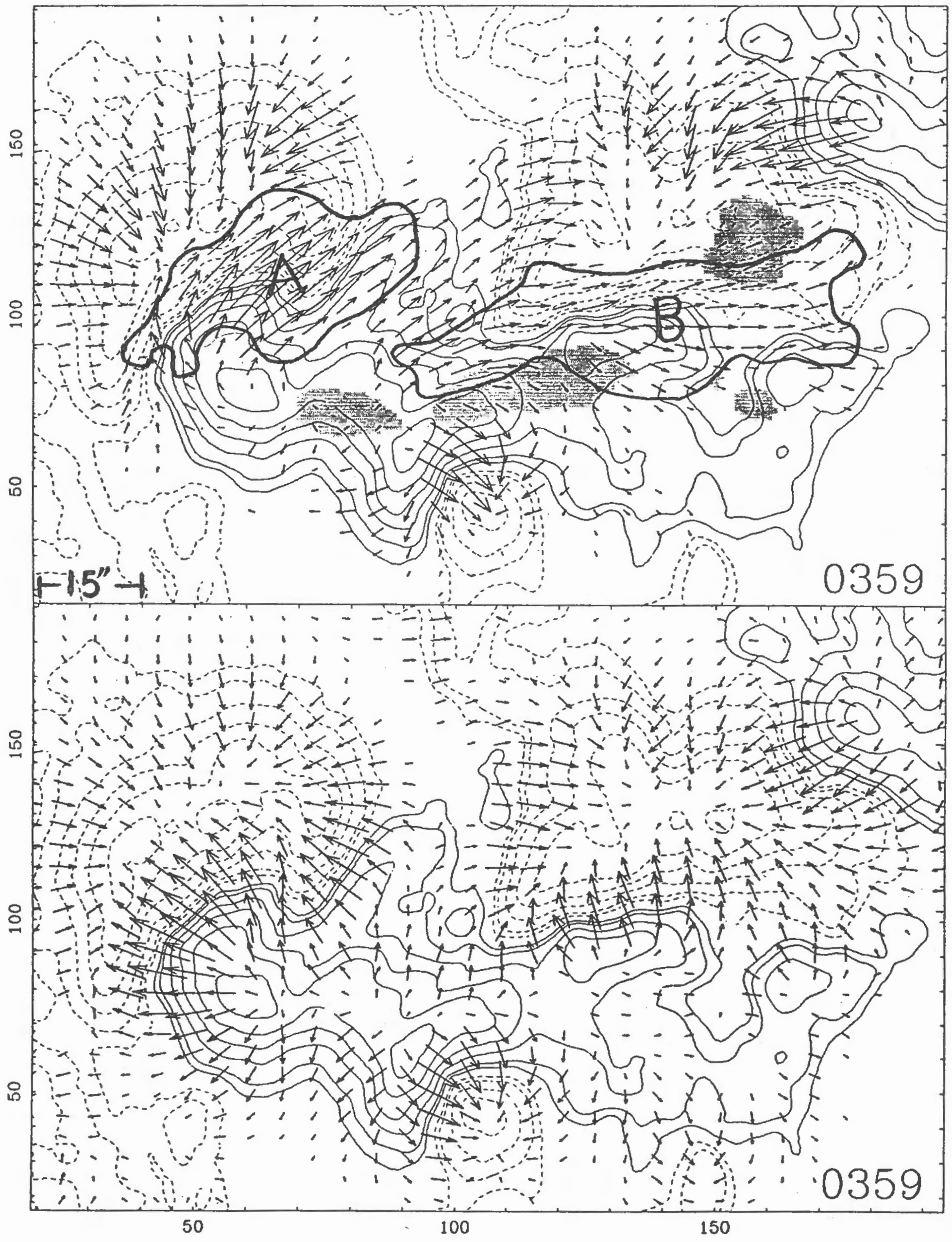

Fig.1 An example of strong sheared field in AR 6233. The upper part is the observed vector magnetogram with removed ambiguity in field azimuth. Line-of-sight field is represented by isogauss contours with solid (dashed) lines for positive (negative) polarity. The transverse field is represented by arrows with length proportional to the relative field strength. The lower part is the corresponding potential field. Two strong sheared zones 'A' and 'B' are shown by thick contours.

the global distribution of line-of-sight magnetic field. Therefore, the magnetic shear is basically visualized from a global sense. As a fact of matter, the internal twisting of magnetic line of force has been ignored in the shear presentation. Magnetic field is a vector field. In a narrow sense, the term of shear commonly means that either some external forces have pushed the vector away from the the status of minimum stress to some new status in a certain volume, or some discontinuity has been created in a certain scope of the vector field. Thus, the real shear angle of the vector magnetic field should be that suggested by Lü et al.(1993), while the angular shear of Hagyard et al.(1984) is merely its projection on the photosphere. The deviation from the minimum stress, or the discontinuity of the magnetic field, clearly indicates that currents are flowing in a certain volume of the vector magnetic field.

In Figure 1, a typical example of strong sheared field in AR 6233 is shown by observed vector magnetogram (upper part) and the corresponding potential configuration (lower part). The line-of-sight component is presented by isogauss contours with solid (dashed) lines for positive (negative) polarity, the transverse component is presented by arrows with length proportional to the relative field strength. Two strong shear zones 'A' and 'B' are marked by thick contours indicating the sites of higher free magnetic energy (Wang et al., 1993). Flare ribbons of a 1M flare is superposed as grey patches. Now the question is what we really observed in the case for the strong shear zones. In the example 'B', the strong transverse field lines are aligned with the main neutral line. This can only means that currents are flowing from the northern side of the zone 'B' – the negative field area, into the southern side – the positive field area. The vertical current deduction has supported this speculation exactly (Wang et al., 1993). However, we know that anti-parallel to the currents there must be magnetic lines of force-free field. Moreover, the low-lying magnetic loops of strong shear zone 'B' themselves might be current-carrying as well. Hence, we actually observed the linkage of two sets of current carrying loops in this example. The strong shear zone 'A' could interpreted in the same way. The external linkage of current-carrying loops appears to be the basic topology of strong sheared field.

This example shows that shear takes place in a fully three-dimensional domain in a certain volume of the vector field. However, so far, only the shears on the photosphere have been studied. Even two-dimensional mapping of magnetic shear is rare in the solar literature. No information on the shear development in the vertical extent, or, in the higher atmosphere has been extracted seriously. For this, we suggest that to study the shear development in the higher atmosphere is of greatest importance, and Yohkon soft X-ray images are extremely useful for this study. With regard to the analysis of vector magnetogram on the photosphere, two-dimensional mapping of the magnetic shear is necessary for getting accurate information on the shear development.

3 Shear development

3.1 Observations

Observational studies have shown that the magnetic shear can be created by the following ways.

(1) Shear motion of magnetic footpoints with opposite polarity on both sides of the magnetic neutral line;
(2) Collision of opposite polarity fields from two independent magnetic loops, particularly between new emerging flux to old flux loops;
(3) Emergence of strong sheared field directly from below the photosphere;
(4) Flux cancellation which may convert the line-of-sight field to the transverse field in some cases.

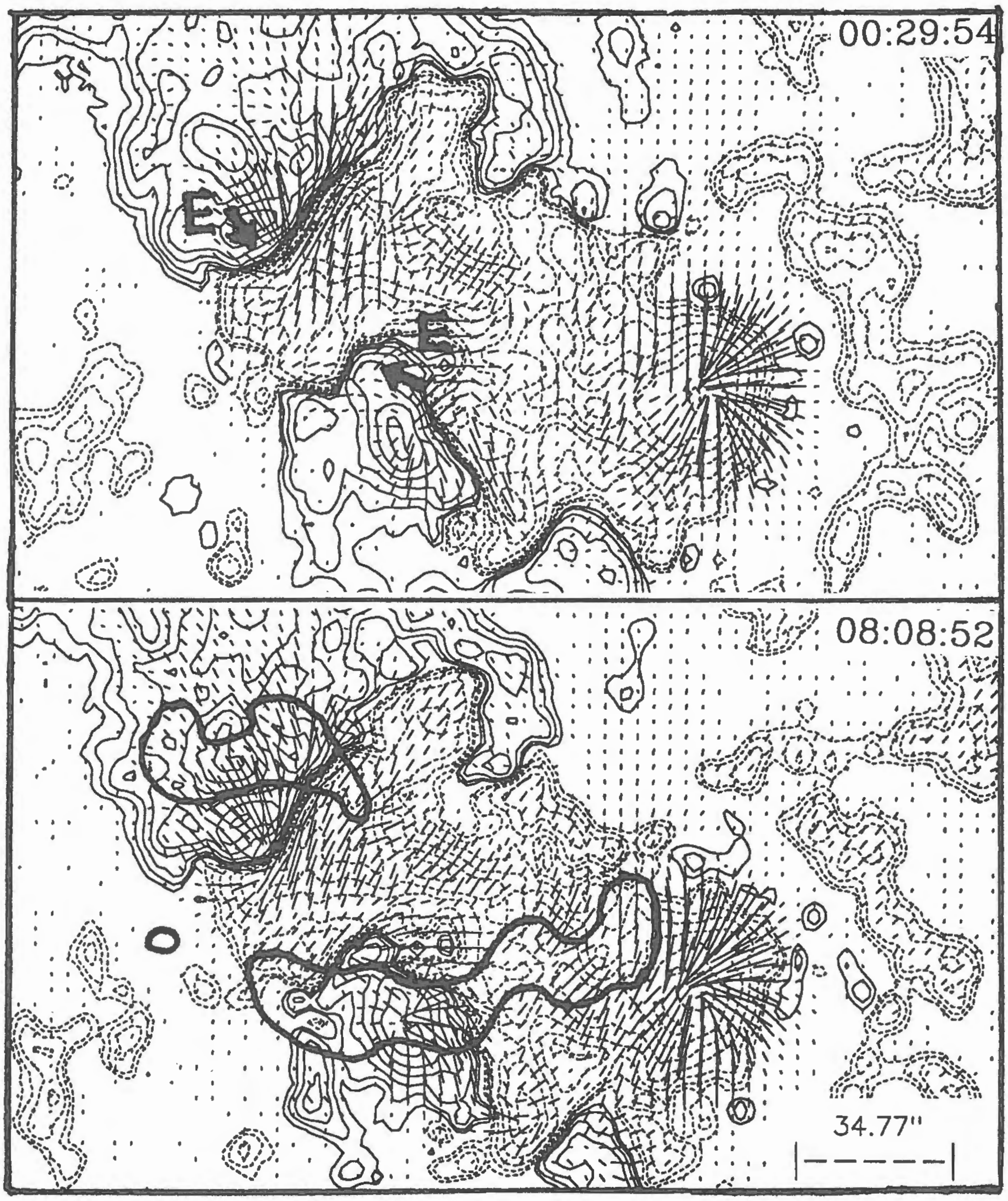

Fig.2 An example of shear development by collision of new EFRs with preexisting flux loops. EFRs are marked by a letter 'E', collision motion is indicated by arrows.

Excellent examples of category (1) are found in Wang et al. (1991) for AR 5395; Typical examples for category (2) is shown by Gaizauskas and Harvey (1986) and Ai et al.(1991); Tanaka (1991) and Kurokawa (1991) present convincing examples for category

(3); while Martin and Livi (1991) demonstrate the fourth category. Complicated cases including somehow the combination of any two or all above categories are also not uncommon.

In Figure 2, an example of shear development by collision of new EFR (emerging flux region) loops with pre-existing magnetic loops in AR 6089 is shown by Huairou vector magnetograms. The earliest signature of these EFRs may traced back to June 9. The EFR positions are marked by letter 'E', the collision motion is seen at two pieces of neutral line and indicated by arrows in the first panel. It was not until the positive pole crushed into the pre-existing negative flux on June 10 that obvious magnetic shear appeared at these two pieces of neutral line. Shear strengthening can even be found in the interval between taking the two magnetograms in the figure. A major flare appears around 07:12 UT on June 10, which is shown by thick contours in panel 2.

3.2 An analytical discussion

In a previous paper(Wang, 1992), we have demonstrated that magnetic shear can be approximately described by the non-potential character of a force-free field. The force-free factor α, or the normalized current helicity would be a measure of magnetic shear. The temporal evolution of α can be analytically expressed as

$$\frac{d\alpha}{dt} = \frac{1}{B^2}\nabla \cdot \mathbf{G} + \mathbf{V} \cdot \nabla\alpha, \tag{1}$$

where, $\mathbf{G} = \frac{\partial \mathbf{B}}{\partial t} \times \mathbf{B}$. The first term on the right represents the local generation of the shear, and $\mathbf{G}$ serves as the source function of magnetic shear. The second term on the right is the shear transportation caused by the non-uniformity of α in space. It is noticed that the Ohmic diffusion is capable of changing the shear status by virtue of $\frac{\partial \mathbf{B}}{\partial t}$. When Ohmic diffusion is ignored, the generation term appears as

$$\frac{\partial\alpha}{\partial t} = \frac{1}{B^2}\nabla \cdot \{[\nabla \times (\mathbf{V} \times \mathbf{B})] \times \mathbf{B}\}. \tag{2}$$

For not missing the generality, assume the $\mathbf{B} = B\mathbf{e}_z$, then

$$\frac{\partial\alpha}{\partial t} = \frac{\partial}{\partial z}(\frac{\partial V_y}{\partial x} - \frac{\partial V_x}{\partial y}) + \frac{1}{B_z^2}(V_y\frac{\partial}{\partial x} - V_x\frac{\partial}{\partial y})\frac{\partial B_z^2}{\partial z} + \frac{1}{B_z^2}[\frac{1}{2}(\frac{\partial V_y}{\partial x} - \frac{\partial V_x}{\partial y}) + \frac{\partial}{\partial z}(V_y - V_x)]\frac{\partial B_z^2}{\partial z} \tag{3}$$

This equation shows that the gradients of velocity and/or magnetic fields are decisive factors for shear generation. For instance, the first term on the right is the z derivative of *curl*$\mathbf{V}$, which indicates that as long as there is curly motion, the shear status may be altered no matter the motion is sheared, or collided.

For the flare study, the total shear evolution in an active region is more relevant. If the region is isolated from other regions, then the only open surface of the magnetic field would be the photosphere. Thus

$$\iiint_V \frac{d\alpha}{dt} \cdot dv = -\iint_{photos.}[\frac{B_\perp^2}{< B^2 >}\frac{d\phi}{dt} + \alpha V_z] \cdot ds \tag{4}$$

Where, ϕ is the field azimuth, $B_\perp$ is the transverse field on the photosphere, and $< B^2 >$ is some medium value of B^2 in the integration volume. Shear is generated by the plasma motion which either makes the vector field rotate to the sheared configuration, or transports the shear through the open surface. For the convenience, we may divided the shear changes into two modes: the generation mode represented by the first term and the migration mode represented by the second term. Tanaka is the first author who clearly stated that the sheared field was emerged from below the photosphere. Therefore we suggest to name the second mode as Tanaka mode.

4 Concluding Remark

In this discussion, we have suggested that the magnetic shear represents an external linkage of current-carrying magnetic loops. Both observations and analytical deductions show that shear is created by either the local generation from interaction of plasma motion and the magnetic field, or the transportation of strong sheared field directly from below the photosphere.

REFERENCES

Ai,G., Zhang,H., Li,W., Li,J., and Chen,J.: 1991, *Chinese Scien. Bull.*, **36**, 1275.

Gaizauskas,V. and Harvey,K.L.: 1986, *Adv. Space Res.*, **6(6)**, 17.

Hagyard,M.J., Smith Jr.,J.B., Teuber,D. and West,E.A.: 1984, *Solar Phys.* **91**, 115.

Kurokawa,H: 1991, *Adv. Space. Res.*, **11(5)**, 233.

Lü,Y., Wang,J. and Wang,H.: 1993, *Sol. Phys.* (in press)

Martin,S.F. and Livi,S.H.B.: 1992, *Lect. Notes, Phys*, **399**, 33.

Tanaka,K: 1991, *Sol. Phys.*, **136**, 133.

Wang,H., Tang,F., Zirin,H., and Ai,G.: 1991, *Ap. J.*, **380**, 282.

Wang,J: 1992, *Acta Astrophysica Sinica*, **12**, 134.

Wang,J, Shi,Z., Wang,H., Lü,Y.: 1993, Submitted to *Ap.J.*

Zirin,H. and K.Tanaka: 1973, *Solar Phys.* **32**, 173.

Recent Classifications of Solar Flares

Jia – Long Wang

Beijing Astronomical observatory, Beijing 100080 *P. R. China*

Abstract

A review on solar flare classifications proposed recently is given firstly in the first part of this paper. Then a new classification of solar flares, based on optical, radio and X-ray observations of flares, is proposed in the second part. The classification tries to reflect temporal process and spacial structure of a flare with the optical, radio and X-ray observational data obtained at different phases of a solar flare. The first one of the three letters used in the classification is decided by the spacial relation of the hard X-ray source with the H_α source in the early phase of the flare classified. The second letter is decided by the temperature of the X-ray source around the peak phase of the flare and the third letter of the classification is decided by the configuration of the relevant magnetic field in the late phase of the flare.

1. Introduction

Great progresses of solar flare observations and studies have been made since 70s of this century, in particular of the spatial observation of flares. These progresses have greatly changed our traditionary conception of a solar flare which was established mainly based on optical observation, and have given us a completely new idea of what a solar flare should be according to ground-based and space - based observations in multi-energy-bands. Now, we know that a flare is a time process with a three dimensional spatial structure radiating various emissions in a certain temporal order, although we do not quite know the mechanism of a flare in detail, yet. A number of classifications of solar flares (e. g. Pallavicini et al. 1977; Ohki et al., 1983; and Tanaka, 1983) have been proposed recently along with these progresses. The proposed classifications, in principle, well reflect the progresses of solar flare study made in various periods of time, on one hand. On the other hand, it is obvious that we should have a multi-energy-bands classification of flares instead of a single-band or a simple classification of flares, by which we may appropriately describe the time process and the spatial structure of a flare. In the first part of this paper a brief review of the recently proposed classifications of flares is given. Then in the second part, a new classification based on multi-bands observations is proposed. Finally we simply discuss the flare classifications in the third part of this paper.

2. Review of the Recently Proposed Flare Classifications.

Švestka (1976) divided solar flares into two kinds in his book, Solar Flares, published in 1976. One kind of flares is called low temperature flares, the other one is called high temperature flares. Actually, his high temperature flares mainly are the high temperature sources emitting radio, X-ray and other energetic emissions while low temperature flares mainly are the low temperature sources of the flares emitting optical emissions. Based on soft X-ray imaging observations of 43 limb flares by satellite Skylab Pallavicini et al. (1977) grouped flares as compact flares, bright point-like flares and large and extended flares firstly. Then they simplified their three groups of flares into two groups, low and compact flares and high, extended and low density flares. Thus, the density of flares is the critical parameter in Pallavicini′s classification.

In 1980s, hard X-ray imaging of solar flares was successfully carried out by satellites such as SMM and Hinotori. This supplied a good condition to the study of energetic part of flares. Using the hard X-ray images of flares obtained by satellite Hinotori, Ohki et al. (1983)classified hard X-ray bursts as two types: (a) flares with impulsive time profiles and low positions. and (b) flares with gradual time profiles and high positions. That flares are grouped as impulsive and gradual is of considerable significance but it is found that some flares have a moving source from low position at early phase to a high position at late phase (Wang et al. , 1987).

A widely quoted classification (types A, B and C) of flares was proposed by Tanaka (1983) and discussed by Tsuneta (1984), which was mainly based on the different characteristics of flares in hard X-ray images, spectra and flux variabilities. Some radio properties of flares of different classes of this classification were mentioned when Tanaka (1987) reviewed the impact of X-ray observations from Hinotori satellite on solar flare research. In this classification, hot thermal flares especially with Fe XXVI line emissions are defined as type A, impulsive flares emitting from the extended low corona including the footpoints and with softening spectra are defined as type B, and gradual-hard flares especially with a high source and hardening spectra are defined as type C flares. No doubt, this classification is a good summary of the very successful Hinotori observation, but it is faced the ununiqueness problem as pointed out by de Jager and Svestka (1985) and Nitta et al. (1989). Meanwhile, Takakura et al. (1984). analyzed Hintori data and argued that a burst might be a combination of some among the components including impulsive component, gradual component, thermal component, quasi-thermal component and hot thermal component. This idea is obviously more physics. However, it seems to be not convenient to use in realistic and morphological applications.

In a discussion of physical aspects of the prediction of solar flares with solar activity forecasters. Sturrock (1984) divided flares into 7 types considering mainly filament activities and magnetic configurations before a flare. These 7 types of flares are $\overline{F}N$, $\overline{F}C$, $\overline{F}O$, $F\overline{E}C$, $F\overline{E}O$, FEC, and FEO respectively, where F means no filament, F～filament, E～filament eruption but no ejection, E～filament ejection, N～no current sheet, C～closed current sheet and O～open current sheet. Surely this is a more theoretical classification of flares. Actually, till now we can not directly measure the feature of a current sheet on the sun just before a flare. Since the complicacy of classifying flares and every classification of flares has its own weak points, Švestka (1986) persisted his suggestion that flares should be simply divided into two categories, dynamic flares and confined flares. This classification appears to be too simple to use in applied aspects and subclassifications have to be developed. In 1989, Bai and Sturrock (1989) reviewed solar flare classifications with an emphasis on energetic flares, and proposed a new classification of flares. Flares are classified as thermal hard X-ray flares, non-thermal hard X-ray flares, impulsive gamma-ray/interplanetary proton flares, gradual gamma-ray/interplanetary proton flares and quiet filament eruption flares. A possible problem for the practical use of this classification might be the serious dependence of the interplanetary proton measurement on the interplanetary condition.

3. A New Multi-Energy-Bands Classification of Flares.

Observational base of the classification: optical (H_α) radio (dynamic spectrum) and hard and soft X-ray observations.

Purpose of the classification: trying to reflect the recently ground-based and space-based observational results of flares and give physical differences of different types of flares.

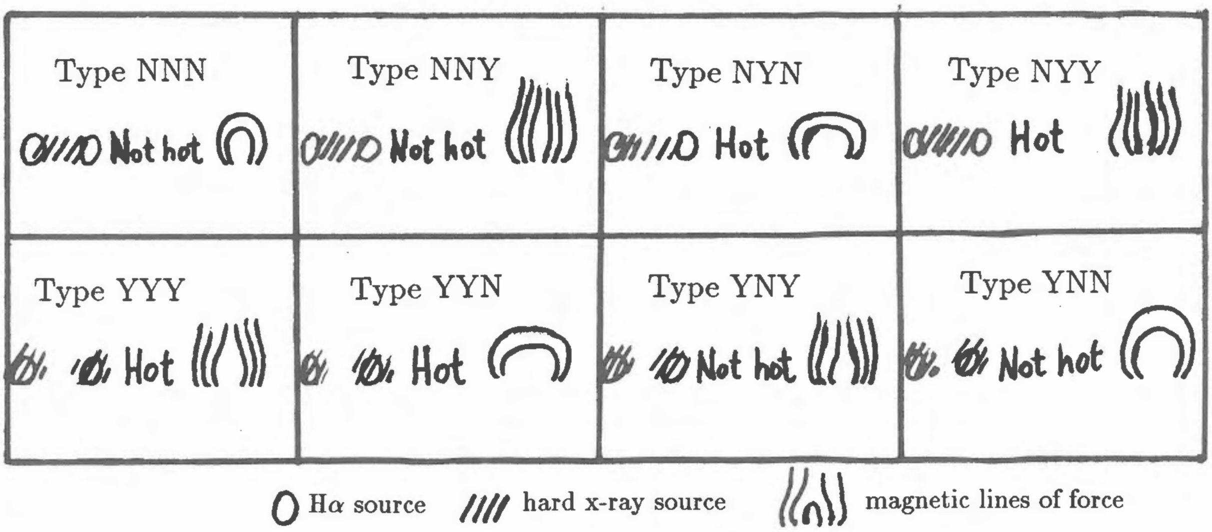

Fig. 1 Illustration of the multi-bands classification of solar flares.

Method of the classification: We use a group of three letters to classify flares. We use the first letter of the letter group to reflect the spatial structure of the flare in the early phase. If the hard X-ray source of the flare is low near the chromosphere or the normal projection of the main hard X-ray source is coincident with the H_α patch of the flare in the early phase, we take Y as the first letter. Otherwise, put N as the first letter. The second letter is used to reflect the thermal status of the plasma of the flare in its peak phase. If Fe XXVI line emissions are observed from the flare around the peak phase, we take Y as the second letter. Otherwise N should be the second letter. The third letter is used to reflect the magnetic configuration of the flare in its late phase. It has been known for a long time that proton flares have a close relation with an open magnetic field and a type VI radio burst. So we put Y as the third letter if the flare is accompanied by a radio type VI burst in it late phase. Otherwise the third letter is taken as N.

Thus, all of flares is classified into eight types as illustrated in Figure 1. Obviously, every certain flare would belong to a certain type and flare such as the flare on 1980 May 21 which is thought to have simultaneously properties of type B and C (de Jager and Svestak, 1985) and the flare on 1982 February 3 which is thought to have simultaneously properties of type A, B, and C, (Nitla et al., 1989) can easily be classified in our classification.

4. Discussion

From what we reviewed above we can see that the progress of flare classifications goes along with the progress of solar flare observation and study and that any parameter or a combination of parameters of flares can be used as a criterion of a classification but only a multi-bands classification might be able to reflect the complicated process of a flare and to show the physical differences between flares.

This work is supported by the NNSF of China throngh Program 49391400.

References

Bai, T , and sturrock, P. A. 1989, *Ann. Rev. Astron. Astrophys*, **27**, 421.
De Jager, C, and Svestka, Z. 1985, *Solar Phys*, **100**, 435.
Nitta, N, Kiplinger, A. L. and Kai, K, 1989, *Astrophys.* J, **337**, 1003.
Ohki, K. , Takakurk, T. , Tsuneta, S. , and Nilla, N. 1983, *Solar Phys*, **86**, 301.
Pallavisini, R. , Serio, S. and Vaiana, G,S. 1977, *Solar phys*, J, **216**, 108.
Sturrock, P, A. 1987, *Artificial Satellite*, **22**, 57.
Svestka, Z. 1976, *Solar Flares* (D, Reidel Publ, Co, Dordrecht).
Svestka, Z. 1986, in *The Lower Atmosphere of Solar Flares*, ed, by D, FNeidig, National Solar Obs, N. M. , US, p. 332.
Takakura, T. , Tanaka, K. and Hiei, E. 1984, *Adv*, *Space Res*, **4**, No, 7,143.
Tanaka, K, 1983, in *Activity in Red-Dwarf Stars*, IAU Coll. 71. ed. by P. B. Bgrne and M. Rodono, p. 307.
Tanaka, K. 1987, *PASJ*, **39**, 1.
Tsuneta, S. 1984, in *Active Phenomena in the Outer Atmosphere of the Sun and Stars*, ed. by J-C. Pecker and Y. Uchida, Obs. de Paris, Meudon, p. 234.
Wang, J. L. et al. ,1987, *Solar Phys.* ,**108**, 169.

A Peak—to—Peak Correlation between Spikes and X—Ray Bursts during Type IV Bursts

Xia Zhiguo

Yunnan Astronomical Observatory,Chinese Academy of Sciences,Kunming

Abstract

We present a peak- to-peak comparison between the hard X— ray burst and spikes during type IV bursts.16 type IV bursts were analized in which there were 31 groups of spikes. The close correlation indicates that they both are excited by electron beam. The spike and HXR not only occur in impulsive phase, but also occur during type IV burst. Electron beams(type III bursts, spikes,HXR)may appear many times during a large flare.

1. Introduction

In a evolution of a solar flare,energetic particles accelerated by magnetic field interact with the solar atmosphere producing a series of observational phenomena such as X-ray events, radio bursts and Hα -flares. These phenomena occur at a different height of solar atmosphere,however they often associate each other.

There is a very close relation between hard X-ray and microwave bursts. The numerous books and articles review the subject[1] [2].The emission mechanism for most microwave bursts is gyrosynchrotron emission. The emisson is produced by mildly relativistic electrons (100 kev~few Mev) . It seems that most microwave emisson is excited by the higher-energe electrons of the same electron population which produces the hard X-rays.

H. Nakajima et. al[3] obtained simultaneous imaging observations of the sun at microwave and hard X-rays with high resolutions. They found that the microwave sources are displaced from the hard X-ray sources.Maybe when electron beams produced by acceleration process propagate over solar atmophere, they produce different wavelenths radiation at different site. K. Kai[4] discussed the problem of a common origin of HXR and microwave. Detailed analyses suggest that hard X-rays and microwaves are emitted from nearly co-spatial sources due to electrons streaming down to the chromosphere. Many workers studied the timing delay between HXR and microwave bursts. Cornell et al.(1984)summarizes the analysed results:the microwaves are delayed with respect to the hard X-rays. Kaufmann(1983) and Takakura(1983) obtained similar resuts.The typical delay is around 0.2s.

Many researchers carried out studies of relation between HXR and associated metric type Ⅲ bursts[5] [6] [7] . It is noted that upward drifting metric type Ⅲ bursts were delayed in comparison to HXR bursts by about 0.5 to 1s. It is suggested that HXR and type Ⅲ bursts have a common origin. M. R.Kundu[8]reported that type Ⅲ bursts which were associated with impulsive Hard X-rays, were observed to great heights (3.1 $R_{\circ}$ from disk center at 28 MHz) . The location of the type Ⅲ burst resource indicates that electron acceleration occurs over a region which covers a wide range of magnetic field lines. Kundu also find wide separation between type Ⅲ sources associated with a group of hard X-ray bursts, the separation amounts to ~ 7×10^5 km. Somtimes there is a close relation between HXR,Radio burst and Hα -flare, it implies the electron beam travel for along distances.

A. O. Benz, M.J.Aschwanden et al.have carried out studies of relationship between decimetric spikes and HXR bursts[9].

T. Takakura [11] reported the time delays of 5s to 10s between the peaks of solar hard X-ray burst and microwave burst at 17 GHz.In most cases,the time delays are one second or less, H. S.Sawant identifies this result,but the delays of five seconds or more have been detected in some exceptional cases in intense bursts. The long time delay should be attributed to expansion of optically thick individual radio sources. The delay at the highest frequency (17 GHz) can be ascribed at least partly to the hardening of electron spectrum resulting in a temporal increase in the electron number.The delay can reach 5~10s.

2. Correlation of spikes with HXR during type Ⅳ burst

Many workers previously studied the correlation between spikes, type Ⅲ and HXR burst.The close correlation implies that energetic electron is a probable exciter of them. When M. J. Aschwanden and A. O. Benz studied a correlation of solar decimetric radio bursts with X-ray flares, they excluded a long lasting type Ⅳ bursts. Type Ⅳ burst usually occures after the impulsive phase and lasts for a long time. The correlation of spikes with HXR peaks during type Ⅳ bursts has not yet been considered carefully before. We analyzed 16 type Ⅳ bursts in which there are 31 clusters of spikes.

2.1) Data selection and statistic result

There is a complete list of decimetric millisecond spikes during 1977-1989 at the astronomical institute of ETH in zurich.This list contains 164 spike clusters.Dennis provided the HXR catalog, it contains a total of 12672 bursts. Comparing the two lists, chose out events with overlap duration, then compared their time profile in detail. Their maximum was separately examined,note them with ts and tx.(ts-tx)is the delay between HXR and millisecond spike cluster. If (ts—tx) is positive, it means spikes occur after HXR burst. If the time difference between spike peak and HXR peak is less than 5s, i. e. $|\Delta t|<5$s, we classify it as "peaks in correlation". The 13 clusters of spikes belong to this class. For the rest (18 clusters) , the time difference is from 6s to 59s. In which 12 clusters of spikes occured before HXR bursts, only 6 clusters occured after HXR bursts. Perhaps the reason for the result is: HXR source often is generated at foot of loop(sometimes HXR appear at top of loop) , therefore spikes at long decimetric band often occur at the upper corona. Multiple electron beams may be generated during one flare. One of electron beams excites HXR event, others excites spikes cluster. There are the different distances between spikes sources and HXR sources, maybe this is one of the reasons why the delay has various numbers,from 0.2s to 59s.

2. 2)Gereral characteristics of type Ⅳ burst

Type Ⅳ burst is a flare-related continuum emission at meter wavelengths. It is a background for our studing subject. Type Ⅳ bursts can be divided into four distinct classes.

Early flare continuum (FCE) is generated during the flash phase of the solar flare,always in association with type Ⅲ burst.

Type Ⅳ burst is associated with polar cap absorption events which are caused by 10 to 100 Mev protons. Protons are initially accelerated in the microwave emitting region. The FCE events have stronger correlations with high fluxes of both protons and microwaves.

At the impulsive phase of a flare electrons are accelerated to energies ≤100 kev in a few seconds(type Ⅲ burst, impulsive microwave bursts, hard X- ray bursts).Type Ⅱ-Ⅳ bursts as well as the slower X-ray events, all come later in the flare. The impulsive phase of the flare corresponds to sub- relativistic electrons. After the impulsive phase, the flux slowly increase again and remains high for over an hour,in which the high energy particles involved. Sometimes spikes, type Ⅲ burst and HXR occured during a type Ⅳ burst. The characteristics have been used as evidence, it implies that there are multiple electron beams during a large flare.

2.3) Flare 80/04/06

We discuss a typical event as follows:

HXR emission(26-78kev,ISEE-3)started at 1420 UT,a maximum peak occurred at 142630 UT. An Hα flare of importance N was from 1423 UT to 1521 UT (N11, E 12) . The HXR emission of this flare was recorded from 143340 UT to 143800 UT by SMM, the time of three peaks are separately:1434.6 UT,1435.7 UT and 1436.4 UT.OTTA reported a type 47 GB burst.It started 1420 UT,at 1435.5 UT it reached maximum.Their peak time are:1426 UT, 1435.5 UT and 1452.8 UT . The spike cluster just occurred at 1435.5 UT. WEIS reported that a type Ⅱ burst occurred during 1423.3 -1428.0 UT; a type Ⅳ burst occurred during 1424-1711 UT. At solar radio station of ETH there are two types of radio spectra: the digital spectrometer IKARUS (Its data was recorded in tape) and the analog spectrometers DAEDALUS(Its data was recorded in film) ,On both IKARUS and DAEDALUS spectrometer, the spike clusters were recorded at 1434-1438UT,and they both closely correlated with HXR. We can believe that there was the accelerated electron beam in the active region.

Fig.1 shows the time profile of a radio burst from OTTAWA at 2800 MHz.

The burst started at 14:20 UT of 80/06/04, the first peak appeared at 142435UT. The second flux peak locaded at 1427.5 UT Fig.2 shows a type Ⅲ G burst associated with HXR, it occurred during 1420-1422, this should be during a impulsive phase of the flare. Following the impulsive phase, a type II--Ⅳ burst appeared, It is a sign of a energetic process. There is a very typical spikes that closely correlated with HXR at 1434--1436 UT in Fig.3. The spikes overlap on background radiation with longer duration. There are two subclusters of spikes(subclusters a and b) . We noted the durations of increased background with Tba and Tbb. Tba and Tbb increased with frequency increase, and the end points of spike clusters on each frequency appeared a shift to high frequency. It is shown that the motion direction of exciter is from acceleration region to chromosphere.

The evolution of radio radiation on a frquency domain may show the propagation process of electron beam in solar atmosphere. At 143400--143500, i.e.at a interval of burst a, there is a burst of longer duration (few seconds) at 425-464 MHz; there is a spike cluster at 586--652 MHz ; the end of the spike cluster drifts to higher frequency at 817--913 MHz. At 143500--143600 UT, i.e.at a interval of burst b, there is no burst at 425--464 MHz and 586--652 MHz; there is a spike cluster at 817--913 MHz and the end of the cluster also drifts to higher frequency.

During rise time of the radio maximum peak i. e. at 1434-1436, HXR and spike clusters coevolutely occurred. During the large flare, two electron beams occurred: 1424 UT and 1434 UT.

Acknowledgements: Thank Dr.A.O.Benz for providing the opportunity to use a lot of spectrum data made at the astronomical institute of ETH.

Reference

[1] M.R.Kundu (1982) Space Sci. Reu 32(1982), 405.
[2] S.R.Kane, Solar Flares, P.187. 1980, Boulder.
[3] H.Nakajima, Solar Physics 113(1987), 63.
[4] K.Kai, Solar Physcs 113(1987), 165.
[5] S.R.Kane, et al, Astrphys, J, 24(1980), L113.
[6] S.R.Kane, Astrophys.J.247, 1113.
[7] H.S.Sawant, Solar Physics 130(1990), 57.
[8] M.R.Kundu, Solar Physics, 79(1982), 107.
[9] A.O.Benz, Solar Physics 104(1986), 179.
[10] A.O.Benz, Astron Astrophys 109(1982), 305.
[11] T.Takakura, Solar Physics 89(1983), 379.

Fig.1 The time profile of a radio burst at 14:20 UT of 80/06/04

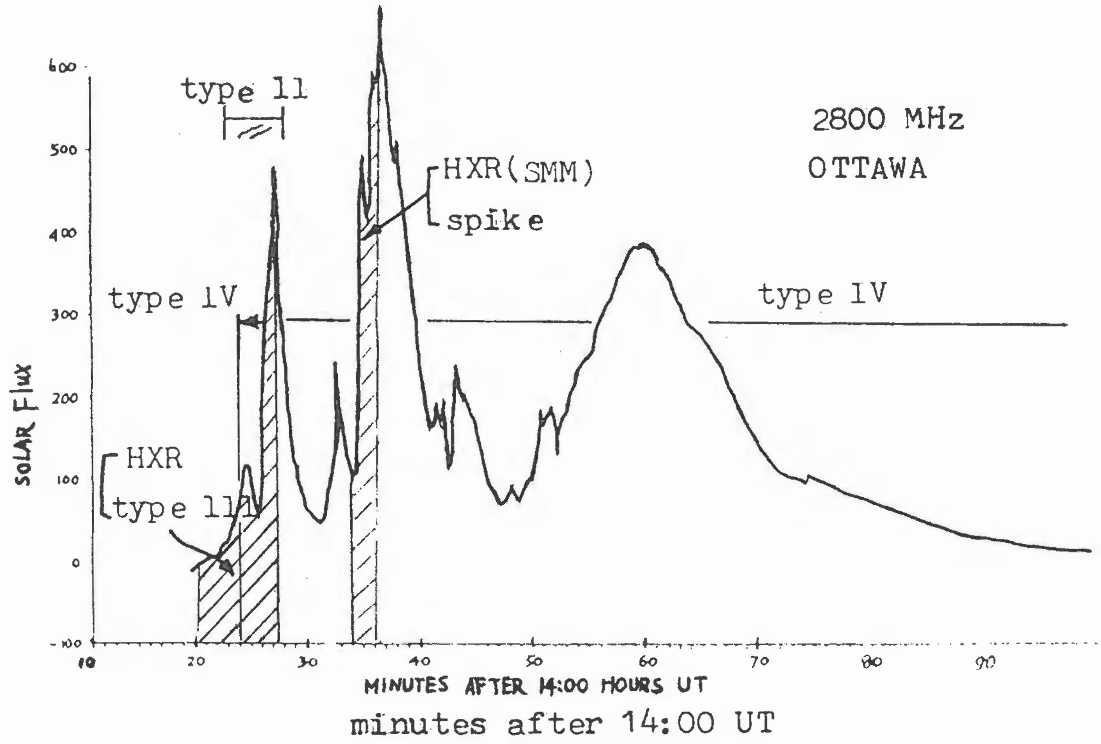

Fig.2 A type 111 G burst associated with HXR

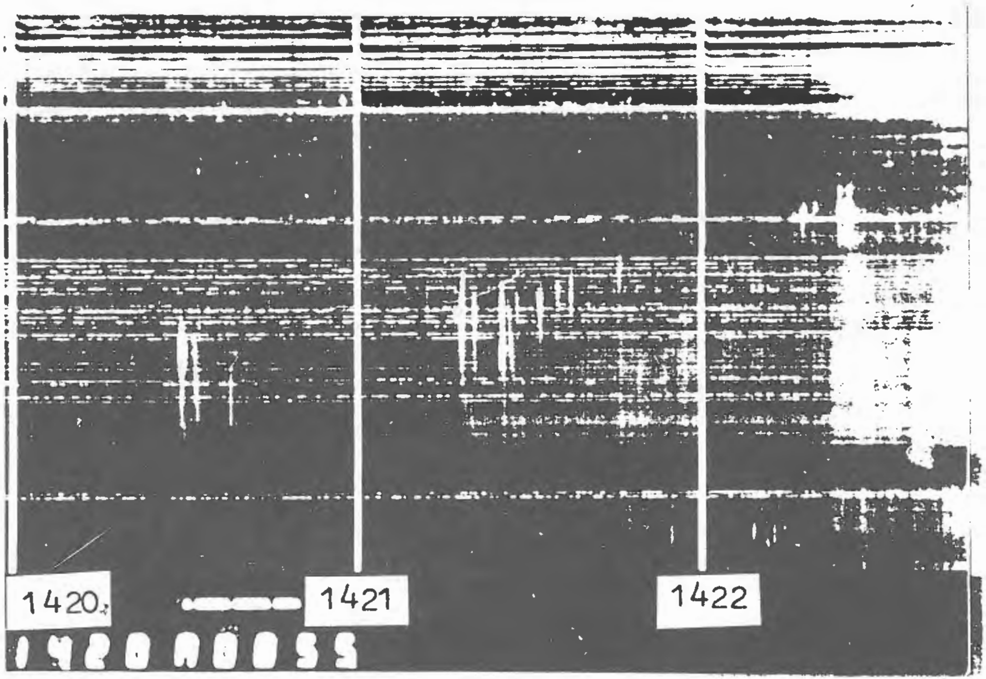

Fig. 3 Two clusters of spikes(a and b)associated with HXR

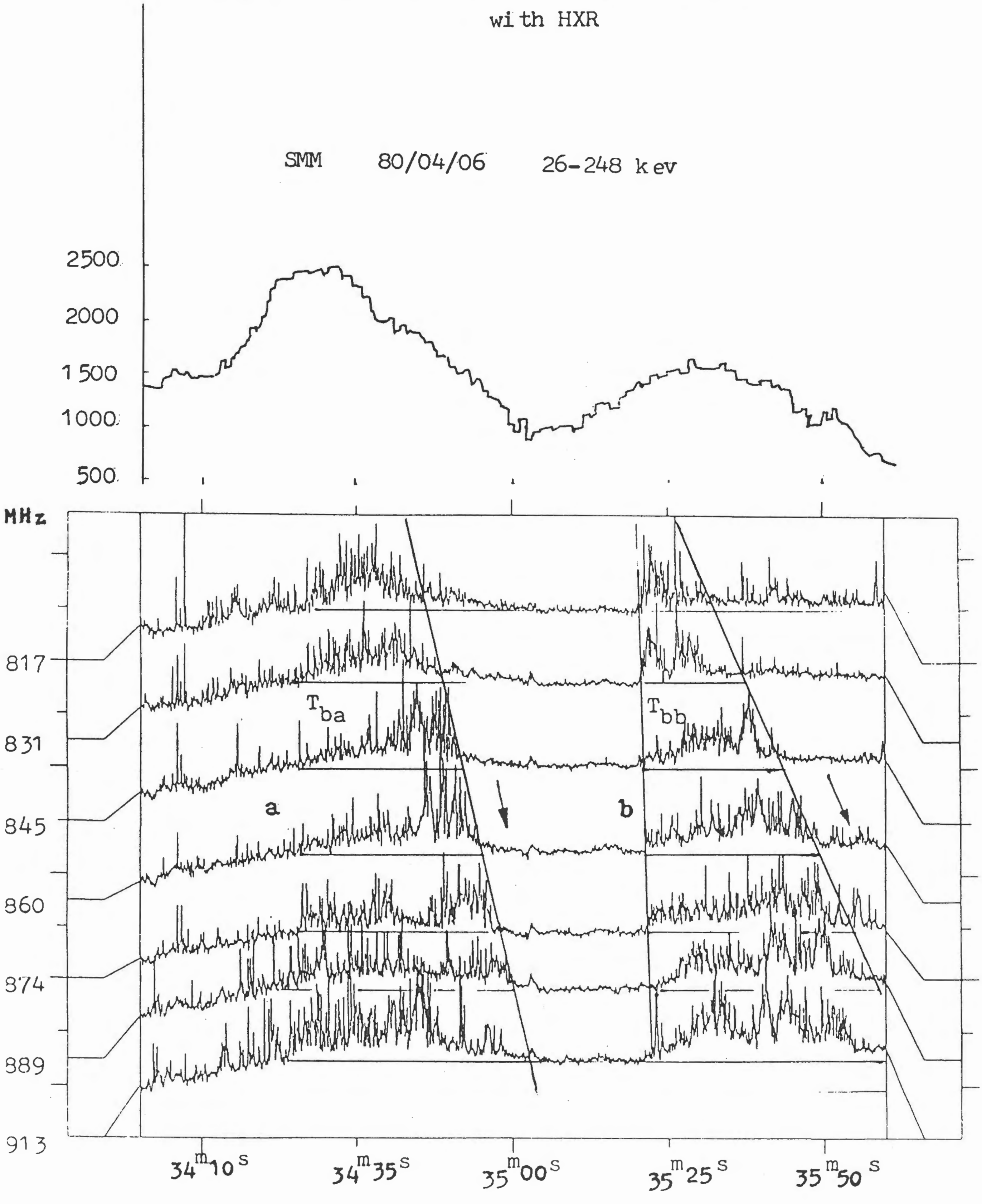

Energy Distribution of Energetic Electrons in the Source of an Especially Great Radio Microwave Burst

Ren-yang ZHAO

Beijing Observatory , Academia Sinica , Beijing , China

Abstract

By using the data of an especially great solar radio microwave burst occurring at 1700 UT on 30 October 1992 in a "very active" active region NOAA/USAF Region 7321, on the basis of the theoretical emission mechanism of nonthermal gyro-synchrotron radiation, we have derived the energy distribution of energetic electrons in the source region of the burst and made a simple analysis.

1. Introduction

In general, solar radio microwave bursts arise from the low corona in the closed magnetic fields of active regions. An important type of microwave burst is the impulsive burst that occurs during the flash phase of flares, when the rate of energy release is highest and their profiles are remarkably similar to those of impulsive hard X-ray bursts. The radiation mechanism for the impulsive bursts is gyro-synchrotron emission from the electrons that are trapped in the loops of energy $\simeq 0.1$ to $1MeV$, spiralling in a magnetic field of $B \simeq 100$ to $500Gauss$, and emitting at harmonic numbers ≈ 10 to 50 of the gyro-frequency (Dulk,1985; Zhao, Magun and Schanda, 1990). The spectra of microwave impulsive bursts usually have a single maximum at the peak frequency ν_{peak} ($5000MHz \le \nu_{peak} \le 10GHz$) and the burst sources are optically thick below ν_{peak} and optically thin above ν_{peak} (Dulk et al., 1985). But it is not clear what the energy distribution of the energetic electrons is; possibilities include a near-Maxwellian of $T_e \approx 10^8$ to 10^9K, a power law of energy spectral index $\delta \approx 3$ to 7, or a multicomponent distribution with different volumes at different effective temperature (Dulk,1985).

During the most active time of the "very active" active region NOAA/USAF Region 7321, there is an especially great radio microwave burst to be observed at 7 frequencies on October 30,1992. This burst has an impulsive and complex profile with a double-peak structure at the frequency of 2800 MHz (cf. Figure 1). There may be a considerably important significance in the researching of the burst and the active region, because its intensity is extremely high. In the present paper, therefore,we have simply and theoretically researched the energy distribution of energetic electrons in the source region of the burst.

2. Data of the Burst

The especially great burst occurred on October 30, 1992 in the "very active" active region NOAA / USAF Region 7321. The start times of the burst at 7 frequencies (1415, 2695, 2800, 4995, 8800, 9500, and 15400 MHz) are within 1656-1701 UT,the maximum times are within 1748-1751 UT, and the durations are within 116-195 minutes. The types of the burst at 7 frequencies are 49GB or 47GB. The peak flux densities of the burst are 2300 SFU at 1415 MHz,5800 or 7700 SFU at 2695 MHz,5400 SFU at 2800 MHz,7700 or 10000 SFU at 4995 MHz, 8200 or 9000 SFU at 8800 MHz,7145 SFU at 9500 MHz,and 4000 or 5600 SFU at 15400 MHz (S.-G.D.,1993).

From these values of the flux density at 7 frequencies,we can obtain the spectrum of the burst at the maximum time and determine the spectral peak frequency ,ν_{peak},by means of the method of interpolation:$\nu_{peak} \simeq 6000MHz$.

The profile of the burst at $\nu = 2800MHz$ frequency is shown in Figure 1. Its major peak at 1750 UT is about 5400 SFU and minor peak at $\sim$ 1733 UT is about 4400 SFU (S.-G.D.,1992).

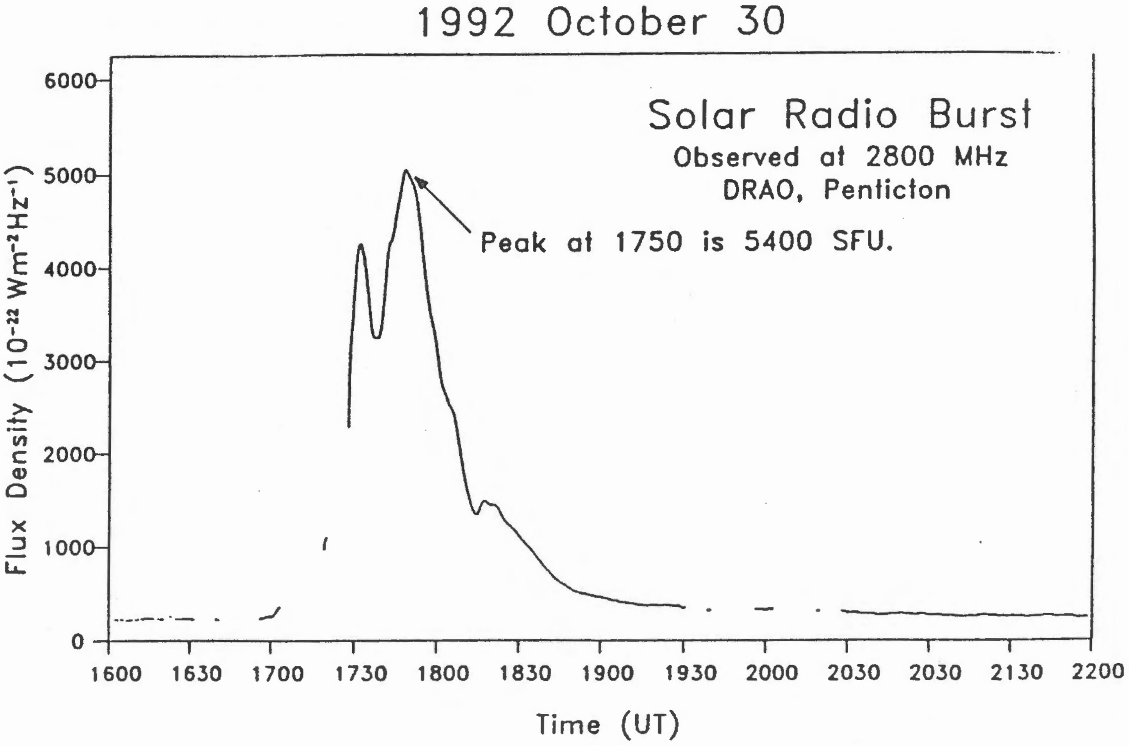

Fig.1 Solar radio burst observed at 2800 MHz, DRAO, Penticton (from S.-G.D.).

The importance and the time of start-maximum-end of the corresponding H_α are 2B and 1702-1730-2203 UT, respectively.The importance and the time of start-maximum-end of the corresponding GOES solar X-ray flare are X1.7 and 1702-1730-2203 UT, respectively (S.-G.D.,1993).

The magnetic field in NOAA/USAF Region 7321 on 30 October 1992 is very complex and strong (Ai and Zhang, 1993).

3. Theoretical Analysis

In the present paper,we try to make a simple research only for the burst at the frequency of $\nu = 2800MHz$.

In view of the profile characteristics of the burst shown in Figure 1 (for example,the extremely high intensity and the impulsive shape), it may be reasonably assumed that the burst is generated by the emission mechanism of gyro-synchrotron radiation from the nonthermal energetic electrons with a power law energy distribution (Dulk,1985; Zhao, Magun and Schanda, 1990; Zhao,1993).

The energetic electrons emitting the gyro-synchrotron radiation have an isotropic pitch angle distribution and a power-law distribution in energy (Dulk,1985):

$$n(E) = KE^{-\delta}, \tag{1}$$

where δ is the power law index of the energy distribution and K is related to N,the number of electrons per cm^3 with the energy of $E > E_0$, by the relation

$$K = (\delta - 1)E_0^{\delta-1}N. \tag{2}$$

It is assumed that the low-energy cutoff is $E_0 = 10keV = 1.6022 \times 10^{-8} ergs$, but in fact the electrons with the energy less than 50 to $100keV$ contribute very little to the radiation.

The flux density, F, of the burst source,as it is known, is related to the brightness temperature, T_b, by the relation

$$F = \frac{2k\nu^2}{c^2} \int T_b d\Omega, \tag{3}$$

where k is the Boltzmann's constant,c the speed of light,ν the radiation frequency, $d\Omega$ is a differential solid angle, and the integral is over the projected area of the source.

From the configuration of the active region,the projected dimension of the source can be taken as $L = 7 \times 10^9 cm$ corresponding to $96'' arc$. If the distribution of the brightness temperature is uniform over the source area, then the maximum radiation intensity of the major peak can be calculated by means of equation (3) from the value of flux density $F = 5400SFU$ at 1750 UT:$T_b = 1.03 \times 10^9 K$. For the sake of simplicity, the assumption of $T_b = T_{b,x} = T_{b,o}$ might be made in the present analysis, where $T_{b,x}$ and $T_{b,o}$ are the brightness temperature of the extraordinary and ordinary mode,respectively.

The burst source is optically thick for the frequency $\nu = 2800MHz$ at the maximum time of 1750 UT because $\nu < \nu_{peak}$, thus the brightness temperature approximates to the effective temperature of the emitting electrons (of course, on the supposition that T_{eff} is constant in the source region):

$$T_b \approx T_{eff}. \tag{4}$$

Through the value of T_b, therefore, the average energy of the emitting electrons can be estimated: $< E >= 88.8keV$.

For the gyro-synchrotron radiation from the electrons with the power law energy distribution,the effective temperature cab be approximately expressed by (Dulk,1985)

$$T_{eff} \approx 2.2 \times 10^9 10^{-0.31\delta}(\sin\theta)^{-0.36-0.06\delta}(\frac{\nu}{\nu_B})^{0.50+0.085\delta}, \qquad (5)$$

where θ is the viewing angle(angle between the magnetic field direction and the line of sight),ν/ν_B, the harmonic number,ν_B,the electron gyro-frequency.

The magnetic field of the active region can be assumed to be a magnetic dipole field, so the field strength can be given as follows (e.g. Zhao,1991):

$$B = \frac{[r^2 + 4(h + d_0)^2]^{1/2}}{2[r^2 + (h + d_0)^2]^2} d_0^3 B_0, \qquad (6)$$

where h is the height above the photosphere, r the distance from the central axis of the active region,d_0 the depth of the dipole below the photosphere, B_0 the magnetic field strength at the photosphere. The height of the burst source at the frequency $\nu = 2800MHz$ can be taken as $h = 4.2 \times 10^9 cm$ (e.g. Dulk,1985). According to the observations, the magnetic field strength at photosphere is about $B_0 = 3000Gauss$. The magnetic field in the source region, moreover, can be assumed to be homogeneous. By using equation (6) and taking $r = 0$ and $d_0 = 2.0 \times 10^9 cm$, thus, one can estimate the magnetic field strength in the source region: $B \approx 100Gauss$. That is to say, the harmonic number can be taken as $\nu/\nu_B \approx 10$. As for the viewing angle of the magnetic field θ, it may be suggested from the observations that $\theta \approx 50°$.

By means of equations (4) and (5) and substituting the values of T_b, θ, and ν/ν_B, therefore, one can obtain the power law index of the energy distribution: $\delta = 4$.

Besides,the peak frequency of the gyro-synchrotron radiation from the electrons with the power law energy distribution can be approximately written as (Dulk,1985)

$$\nu_{peak} \approx 2.72 \times 10^3 10^{0.27\delta}(\sin\theta)^{0.41+0.03\delta}(NL)^{0.32-0.03\delta}B^{0.68+0.03\delta}, \qquad (7)$$

where L is the scale length of the emission (i.e. dimension of the source along the line of sight) and,B,the magnetic field strength in the source region.So, from the values of $\nu_{peak} = 6000\ MHz, \delta = 4, \theta = 50°, L = 7 \times 10^9 cm$,and $B = 100\ Gauss$,using equation (7), one can obtain the number of electrons per cm^3 with $E > E_0$: $N = 6.03 \times 10^8 cm^{-3}$.If the ratio of the fast electron density to the background electron density is about 1:10-100,then the electron density in the source region of the burst is about $N_e = 6.03 \times 10^9 - 6.03 \times 10^{10} cm^{-3}$.

Finally, inserting the δ and N into equations (1) and (2), therefore, we have derived the energy distribution of the nonthermal energetic electrons in the source region at the time of the maximum radiation (the major peak of the burst):

$$n(E) = 1.81 \times 10^{21} E^{-4}, \qquad (8)$$

where energy E is in units of eV.

By using equation (8), one can calculate the number of electrons, which make predominant contributions to the gyro-synchrotron radiation, per cm^3 with the energy from $100keV$ to $2MeV$: $N(100keV < E < 2MeV) = 6.03 \times 10^5 cm^{-3}$. If the volume of the burst source is about $V \approx L^3 = 3.43 \times 10^{29} cm^3$, then the total number of these electrons in the whole burst source is about $N_{total} \approx 2.07 \times 10^{35}$.It will be seen from this that only a fraction (one thousandth) of the electrons with $E > E_0$ can play an important role in the gyro-synchrotron radiation. These electrons may be the nonthermal electrons which generate the corresponding hard X-ray burst.

As for the minor peak at ~1733 UT,if the burst source is still optically thick at this time,then the electron energy spectral index may be estimated to be $\delta = 4.4$. It follows that the electron energy spectrum at the time of the major peak is harder than the spectrum at the time of the minor peak. It may be inferred that after the minor peak there are some high-energy electrons to be injected into the source region or some low-energy electrons to be accelerated in the source region and then they generate the major peak. Those are just our tentative ideas.

4. Conclusions

The especially great radio microwave burst analysed in the present paper is an important event. On the basis of the emission mechanism of nonthermal gyro-synchrotron radiation, by using the observational data, we have derived and calculated the energy distribution of energetic electrons in the source region of the burst. The results are as follows:

1. The average energy of the emitting electrons is about: $< E > \approx 90\ keV$.
2. The energy distribution of the energetic electrons is: $n(E) = 1.8 \times 10^{21} E^{-4}$.
3. The number density of the electrons making predominant contributions to the radiation is about: $N(100keV < E < 2MeV) \approx 6.0 \times 10^5 cm^{-3}$ and the total number of these electrons in the whole burst source is about: $N_{total} \approx 2.1 \times 10^{35}$.

This work was financially supported by the Chinese Academy of Sciences and the National Science Foundation of China.

References

Ai, G. and Zhang, H. 1993, *China-Japan Workshop on Solar Physics.*

Dulk, G.A. 1985, *Ann. Rev. Astron. Astrophys.*, **23**, 169.

Dulk, G.A., McLean, D.J. and Nelson, G.J. 1985, in "*Solar Radiophysics*" (eds. D.J. McLean and N.R. Labrum), p.53 (Cambridge University Press).

Solar-Geophysical Data, 1992, No.579-Part I.

Solar-Geophysical Data, 1993, No.584-Part II.

Zhao, R.-y.,Magun,A.,and Schanda,E. 1990, *Solar Physics*, **130**, 361.

Zhao, R.-y. 1991, *Science in China (Series A)*, **34**, 969.

Zhao, R.-y. 1993, *ASP Conference Series*, **46**, 295.

Emission Mechanism of a Specific Solar Radio Microwave Burst

Ren-yang ZHAO

Beijing Observatory , Academia Sinica , Beijing , China

Abstract

Choosing a representative solar radio microwave burst, a typical burst which contains a precursor and an impulsive burst followed by a slowly decaying component, as an example, we have researched its radio emission mechanism and calculated the two important theoretical characteristic parameters, intensity and dimension, of its various sources.

1. Introduction

Although the solar radio microwave bursts are always continuum in nature, their properties, especially the spatial structure, polarization, and brightness temperature change in course of the bursts (Kundu and Vlahos, 1982). In the impulsive phase,the burst sources have a diameter varying from 10" to 1$'$ arc. The peak brightness temperatures range from $10^8 K$ to $10^9 K$. The bursts are caused by gyro-synchrotron radiation. In the post-burst phase, the burst sources appear to be a diffuse region of relatively large diameter ($> 1'$ arc). Their brightness temperatures usually lie between $10^5 K$ and $10^7 K$. The bursts are generated by bremsstrahlung and / or gyro-resonance radiation.

In the present paper, we have selected a specific and representative solar radio microwave burst, which consists of a precursor and an impulsive burst followed by a slowly decaying component, researched its emission mechanism, and calculated the intensity and dimension of its sources.

2. Example of the Radio Burst

The author observed a microwave burst occurring at the frequency $\nu = 9.395\,GHz$ on March 28, 1981 and lasting from 0523 to 0620 UT. This is a representative radio burst (cf. Figure 1.): first, beginning with a small and slowly varying precursor burst whose peak is marked by P in Figure 1; about 7 minutes later, occurring with an impulsive burst followed by a slowly decaying burst. Obviously, the latter burst component can be resolved into a gradual rise and fall burst whose peak is marked by G in Figure 1 and a superposed impulsive burst whose peak is marked by I in Figure 1.

The maximum flux density of the burst is $F = 249.0\ s.f.u.$ The flux densities of the three peaks mentioned above are tabulated in Table 1. The H_α flare corresponding to the burst started at 0535 UT, maximized at 0539 UT,and ended at 0615 UT.

Table 1. Flux Densities of the Burst Peak Moments

Burst Peaks	P	I	G
Time (UT)	0529	0535.6	0541
Flux Densities (s.f.u.)	8.0	237.4	26.6

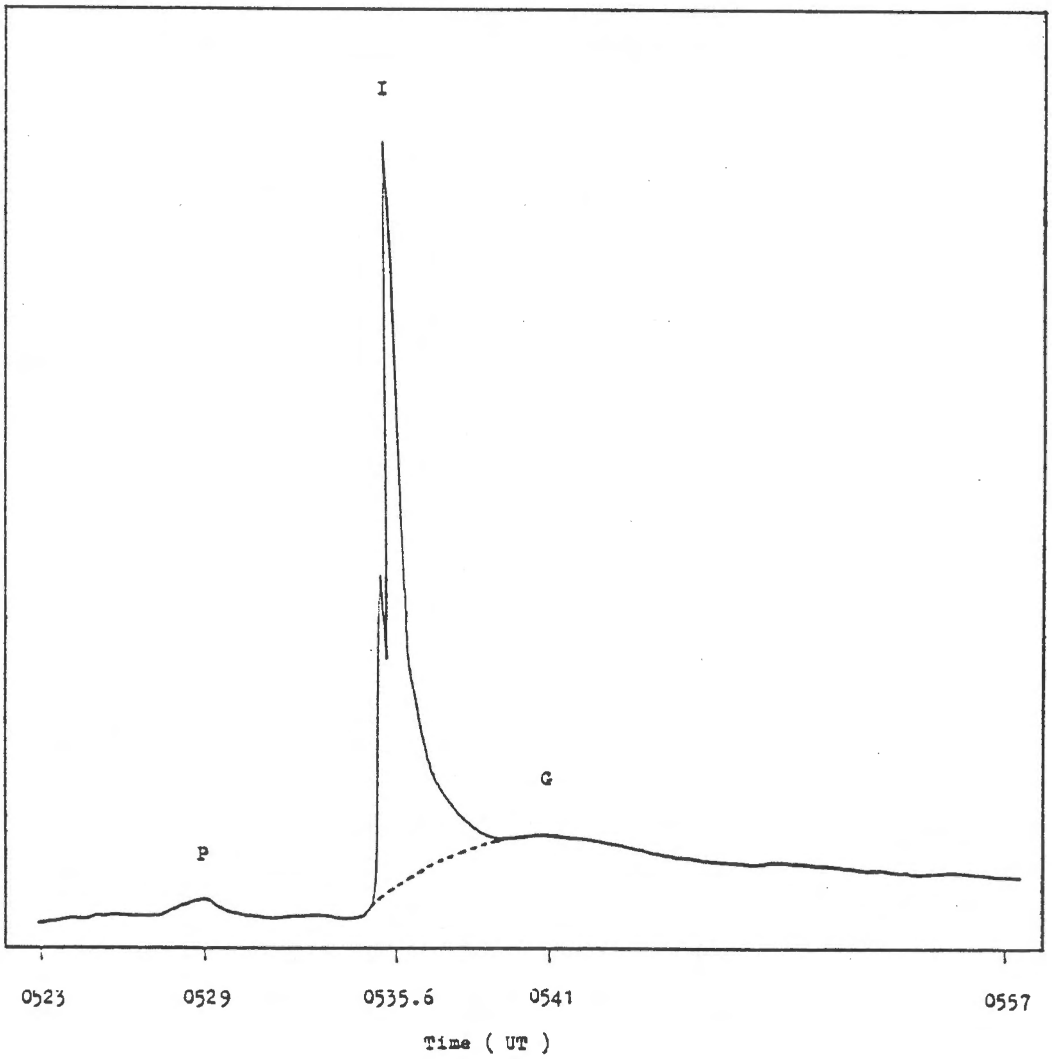

Fig.1 The radio microwave burst occurring at the frequency of 9.395 GHz on March 28, 1981.

3. Emission Mechanisms of the Radio Burst

In the present paper, it is suggested that during the pre-flare phase a small, condensed, and heated plasma volume in an active region appears as a precursor source and generates a weak and slowly varying burst (its peak is shown by P in Figure 1) at the thermal emission mechanism. During the impulsive phase of the flare some energetic particle beams are released from an acceleration region. The high energy electron beams extend throughout a certain region of the magnetic loops and form an impulsive source which produces a strong and steep burst (its peak is shown by I in Figure 1) at the emission mechanism of nonthermal incoherent gyro-synchrotron radiation. Then during the post-flare phase the moderately hot plasma volume having a large dimension becomes a post-burst source and yields a gradual rise and fall burst (its peak is shown by G in Figure 1) through the combined emission mechanism of bremsstrahlung and gyro-resonance radiation.

Because the plasma in the corona has very low density and hence the index of refraction of the medium $n_r \sim 1$, the radiative transfer equation in which the radiative intensity can be expressed by the brightness temperature can be written as

$$\frac{dT_{b,j}}{d\tau_j} = T_{eff,j} - T_{b,j}, \tag{1}$$

where the subscripts $j = x$ and o represent the parameters corresponding to extraordinary wave and ordinary wave, respectively; $T_{eff,j}$ is the effective temperature of the radiating electrons, which replaces the source function S_j, i.e.

$$\frac{k\nu^2}{c^2} T_{eff,j} = S_j = \frac{\eta_j}{\kappa_j}, \tag{2}$$

where c is the speed of light, k the Boltzmann's constant, η_j the emissivity, κ_j the absorption coefficient; and τ_j is the optical depth.

Since we only discuss the radiation of the radio source itself, we do not consider the radiation from the background source under the radio source. The solution of radiative transfer equation (1) , therefore, can be given :

$$T_{b,j} = \int_{\tau_{t,j}}^{\tau_{b,j}} T_{eff,j} \exp(-\tau_j) d\tau_j, \tag{3}$$

where $\tau_{t,j}$ and $\tau_{b,j}$ are the optical depths at the top and the bottom of the radio source, respectively.

We also consider the effects on the source radiation from the $f-f$ absorption and the gyroresonance absorption in the plasma medium above the radio source. The absorption coefficient,κ_j^{f-f} (in $c.g.s.e.$), of the $f-f$ process is (Zhao, 1991a,1993):

$$\kappa_j^{f-f} = 4(\frac{2}{\pi})^{1/2} \frac{e^6}{c^3(mk)^{3/2}} \frac{Q\lambda N^2}{T^{3/2}} F_j(v, u, \theta), \tag{4}$$

where N and T are the number density and the temperature of thermal electrons, respectively; Q is a slowly varying function of N and T; θ is the angle between the magnetic field and the wave vector $\mathbf{k}$; $v = \nu_P^2/\nu^2, u = \nu_B^2/\nu^2$. The optical depth,$\tau_{j,s}^{g-r}$ (in $c.g.s.e.$),corresponding to the absorption coefficient,$\kappa_{j,s}^{g-r}$,of the gyro-resonance process can be expressed as follows (Zhao,1991a,1993):

$$\tau_{2,1}^{g-r} = \frac{2\pi e^2 k}{(mc^2)^2} T_1 N_1 L_{B1} \lambda G(\theta_1) \tag{5}$$

and

$$\tau_{j,s\geq 2}^{g-r} = \frac{s^{2s}}{2^s s!} \frac{\pi e^2 k^{s-1}}{(mc^2)^s} T_s^{s-1} N_s L_{Bs} \lambda G_j(s, \theta_s), \tag{6}$$

where T_s, N_s, L_{Bs} and θ_s are the temperature,the density of the thermal electrons,the characteristic scale and the direction of the magnetic field in s-th gyro-resonance layer. The distributions of the electron density and the electron temperature can be obtained from the chromosphere-corona transition zone model and the corona model (e.g. Zhao, 1991b,1993).

We take the magnetic field in the active region as magnetic dipole field , then the strength B and the direction θ (i.e. $\theta = \angle(\mathbf{B}, \mathbf{k})$ of the magnetic field intensity, in the spherical coordinate (r, ξ, ϕ) can be expressed as (Takakura and Scalise, 1970):

$$B = \frac{B_0 d_0^3}{2r^3}(1 + 3\cos^2\xi)^{1/2}, \tag{7}$$

and

$$\theta = \arccos[\sin\psi \sin(\xi + \alpha)\sin\phi + \cos\psi\cos(\xi + \alpha)], \tag{8}$$

respectively, where d_0 is the depth of the dipole below the photosphere ,B_0 is the strength of the magnetic field at the photosphere and on the axis of the dipole,$\psi = \angle(\mathbf{k}, \mathbf{d})$,and $\alpha = \angle(\mathbf{B}, \mathbf{r}) = \arctan(\tan\xi/2)$. The characteristic scale of the magnetic field is

$$L_B = \mid grad\ \ln B \mid^{-1}. \tag{9}$$

It can be reasonably assumed from the observations that $B_0 = 1500\ Gauss, d_0 = 3 \times 10^9 cm$,and $\psi = 4°$ in the case of the burst.

In the present paper, we only calculate the ray in the direction from the center of the bottom of the radio source to the observer.

3.1. *Thermal Bremsstrahlung and Gyro-resonance Radiation of the Precursor Source and Post-Burst Source*

The radio radiation of a precursor and a post-burst source is generated by the combined emission mechanism of bremsstrahlung and gyro-resonance radiation from thermal electrons having a Maxwellian distribution. Now the effective temperature of radiating electrons in the radiative transfer equation is equal to the thermal electron temperature, i.e. $T_{eff} = T$. Considering the effects of the $f - f$ absorption and gyro-resonance absorption above the source, therefore, the radiation intensity can be derived from equation (3):

$$T_{b,j} = \exp[-\int_{l_t}^{l_\infty}(\kappa_j^{f-f} + \kappa_j^{g-r})dl] \int_0^{l_t} T(\kappa_j^{f-f} + \kappa_j^{g-r})\exp[-\int_l^{l_t}(\kappa_j^{f-f} + \kappa_j^{g-r})dl]dl, \tag{10}$$

where l is the length of the ray measured from the center of the source bottom along the direction of the sight line; $l_t = (h_t - h_b)/\cos\psi$, h_t and h_b are the heights above the photosphere of the source top and bottom , respectively; l_∞ is the ray length at the edge of the corona.

For the sake of simplicity, we take the height of precursor source top $h_t = 3 \times 10^9 cm$, bottom height $h_b = 5 \times 10^8 cm$. We assume the uniform electron density and temperature distributions inside the source and take $N = 10^{10}\ cm^{-3}, T = 3 \times 10^6 K$. Through numerical calculations, we obtain the radiation intensity of the precursor source: $T_b = (T_{b,x} + T_{b,o})/2 = 7.07 \times 10^5 K$.

We take the height of post-burst source top $h_t = 4.4 \times 10^9\ cm$, bottom height $h_b = 5 \times 10^8\ cm$, and the uniform distributions of electron density and temperature, $N = 5 \times 10^9\ cm^{-3}$ and $T = 5 \times 10^6 K$. Integrating the equation (10) along the line of sight, we can compute the radiation intensity of the post-burst source: $T_b = (T_{b,x} + T_{b,o})/2 = 1.32 \times 10^6 K$.

3.2. *Nonthermal Incoherent Gyro-synchrotron Radiation of the Impulsive Source*

The radio radiation of an impulsive source is generated through the emission mechanism of incoherent gyro-synchrotron radiation of nonthermal energetic electrons. We take the top height of the impulsive source $h_t = 4.40 \times 10^9 cm$ ($B = 100\ Gauss$ at the center),bottom height $h_b = 2.13 \times 10^9 cm$ ($B = 300\ Gauss$ at the center). We also assume that the energetic electrons in the source have an isotropic distribution in the pitch angle and a power law distribution in energy (Dulk,1985):

$$n(E) = (\delta - 1)E_0^{\delta-1} N E^{-\delta}, \tag{11}$$

where N is the number of electrons per cubic centimeter with energy $E > E_0 = 10\ keV$. We take $N = 4 \times 10^6 cm^{-3}$,and $\delta = 3$. Thus,when these mildly relativistic electrons gyrate in the magnetic field of $B < 300\ Gauss$,they generate the emission at harmonics $s > 12$ (s is the harmonic number, $s \approx \nu/\nu_B$).

Considering the effects of $f - f$ absorption and gyro-resonance absorption above the source,we can obtain the radiation intensity of the extraordinary wave from Eq.(3):

$$T_{b,x} = \exp[-\int_{l_t}^{l_\infty} (\kappa_x^{f-f} + \kappa_x^{g-r}) dl] \int_0^{l_t} \frac{c^2}{k\nu^2} \eta_x^{g-s} \exp[-\int_l^{l_t} \kappa_x^{g-s} dl] dl. \tag{12}$$

Because $s \approx 12$ to 39 along the integral path $l \approx 0$ to l_t, the emissivity of gyro-synchrotron radiation η_x^{g-s} and the absorption coefficient κ_x^{g-s} can be taken approximately as (Dulk,1985):

$$\eta_x^{g-s} \approx 3.3 \times 10^{-24} 10^{-0.52\delta} (\sin\theta)^{-0.43+0.65\delta} (\frac{\nu}{\nu_B})^{1.22-0.90\delta} BN, \tag{13}$$

and

$$\kappa_x^{g-s} \approx 1.4 \times 10^{-9} 10^{-0.22\delta} (\sin\theta)^{-0.09+0.72\delta} (\frac{\nu}{\nu_B})^{-1.30-0.98\delta} \frac{N}{B}, \tag{14}$$

respectively. While for the ordinary wave, the radiation intensity can be found in the form:

$$T_{b,o} = \frac{1 - r_c}{1 + r_c} T_{b,x}, \tag{15}$$

where the degree of circular polarization r_c can be expressed approximately as (Dulk, 1985):

$$r_c \approx 1.26 \times 10^{0.035\delta} 10^{-0.071 \cos\theta} (\frac{\nu}{\nu_B})^{-0.782+0.545\cos\theta} \tag{16}$$

For mildly relativistic electrons,the Razin-Tsytovich suppression effect occurs at $\nu \leq \nu_P^2/\nu_B$. While under the present circumstance of $\nu_P^2/\nu_B \leq 9.6 \times 10^8 - 2.9 \times 10^9\ Hz$

(assuming $N_e \leq 10^{10} cm^{-3}$),obviously we have $\nu > \nu_P^2/\nu_B$, therefore we can neglect the Razin-Tsytovich suppression effect.

We have calculated the radiation intensity of the impulsive source from numerical integral: $T_b = (T_{b,x} + T_{b,o})/2 = 1.02 \times 10^8 K$.

3.3. *Horizontal Dimensions of the Radio Sources*

It is well known that the relation between the radiation intensity T_b of the radio source and the flux density F observed on the Earth can be given by

$$F = \int_\Omega \frac{2k\nu^2}{c^2} T_b \cos\psi d\Omega, \tag{17}$$

where $\cos\psi\Omega$ is the solid angle of the radio source on the Earth. Assuming the uniform distribution of T_b within the solid angle of the radio source,we can calculate the horizontal dimension of the radio source from Eq. (17). From above calculated values of T_b and the values of F given in the Table 1, we can easily obtain the horizontal dimension of the precursor source $D = 4.08 \times 10^9 cm$ (i.e. 56".24 arc),impulsive source $D = 1.85 \times 10^9 cm$ (i.e. 25".51 arc) and the post-burst source $D = 5.45 \times 10^9 cm$ (i.e. 1′.25 arc).

4. Conclusions

For the radio burst observed in 0523 - 0620 UT, on March 28, 1981, at the frequency of 9.395 GHz,according to the combined emission mechanism of thermal bremsstrahlung and gyroresonance radiation, we have calculated the radiation intensity and the horizontal dimension of the precursor source and the post-burst source;while according to the emission mechanism of nonthermal incoherent gyrosynchrotron radiation,we have computed the radiation intensity and the horizontal dimension of the impulsive source. These data are listed in the Table 2.

Table 2. Characteristic Parameters at Different Peak Moments of the Radio Burst Source

Burst Source	Precursor Source	Impulsive Source	Post-burst Source
Burst Peak (time)	P (0529 UT)	I (0535.6 UT)	G (0541 UT)
Intensity T_b	$7.07 \times 10^5 K$	$1.02 \times 10^8 K$	$1.32 \times 10^6 K$
Dimension D	$4.08 \times 10^9 cm$(56".24)	$1.85 \times 10^9 cm$(25".51)	$5.45 \times 10^9 cm$(1′.25)

It can be seen from Table 2 that the various sources of the burst have their respective characteristics: At the first, a small but weaker precursor source arises. A few minutes later, a smaller but strong compact source appears. Then, after that time, a large and weak dispersed source occurs.

References

Dulk, G.A. 1985, *Ann. Rev. Astron. Astrophys.*, **23**, 169.

Kundu, M.R. and Vlahos, L. 1982, *Space Science Reviews*, **32**,405.

Takakura, T. and Scalise, E.Jr. 1970, *Solar Phys.*, **11**,434.

Zhao, R.-y. 1991a, *Science in China (Series A)*, **34**,1109.

Zhao, R.-y. 1991b, *Science in China (Series A)*, **34**,969.

Zhao, R.-y. 1993, *ASP Conference Series*, **46**,275.

The Frequency Drift in Spike Radiation Observed on May 10, 1991

Ren-yang ZHAO , Sheng-zhen JIN , and Qi-rang QI

Beijing Observatory , Academia Sinica , Beijing 100080 , China

Abstract

In this paper, we have briefly analysed the the fast frequency drift (~ 25GHz/s) characteristic in the spike radiation observed by Beijing Astronomical Observatory at the frequency band of 2545 – 2645 MHz on May 10,1991. It has been considered that the frequency drift originates from the process of down-moving of energetic electron beams along a coronal magnetic loop which form the loss-cone distributions driving the electron cyclotron maser (ECM) instability.

1. Introduction

In solar radio radiation, there are many kinds of event to have the frequency drift characteristic. For example, classical type III bursts begin at the frequency of a few hundred megahertz and then shift rapidly to lower frequencies. As it is known, in the solar atmospheric plasma, if a disturbance moves outward from the sun and at each height produces emission at the local plasma frequency $\nu_p(or\ 2\nu_p)$, then the emission shifts from high to low frequencies at a rate depending on the speed of the disturbance and whether the emission is generated at the fundamental or second harmonic (Dulk,1985).

Especially, this drift characteristic in the solar radio fast events, has also been observed recently. For example, the drift rates of the fast-drift III_{dm}-like events are very high ($\geq 2000 MHz/s$) and their value remains high up to the end frequency. This fast drift characteristic may be explained by the energetic electrons moving through the solar atmosphere having large gradients in density (Wiehl et al.,1985).

Recently, moreover, the events of microwave broadband structures with relatively low drift rates have been observed to occur more frequently. They are different from type III bursts at lower frequencies, but originate from the gyrosynchrotron emission mechanism. This frequency drift may be explained by the variations of the plasma parameters in the source, e.g. the source moving in an inhomogeneous magnetic field or the electron population varying with the time, etc.. Furthermore, similar to type II bursts, this frequency drift may be interpreted by the plasma radiation from shocks (Bruggmann et al.,1990).

The frequency drift characteristic in the spike radiation has been observed by Beijing Astronomical Observatory at the frequency band of 2545 – 2645 MHz. For instance, high drift rates up to ~ 25 GHz/s have been obtained in the spike event on May 10,1991 (Jin et al.,1991). In this paper, we make a brief analysis for the spike event.

2. Example of frequency drift

A typical spike event has been observed by Beijing Astronomical Observatory on May 10, 1991. There are some spikes in this event to exhibit an obvious time difference at the frequencies of 2545 and 2645 MHz, as it is shown in Figure 1

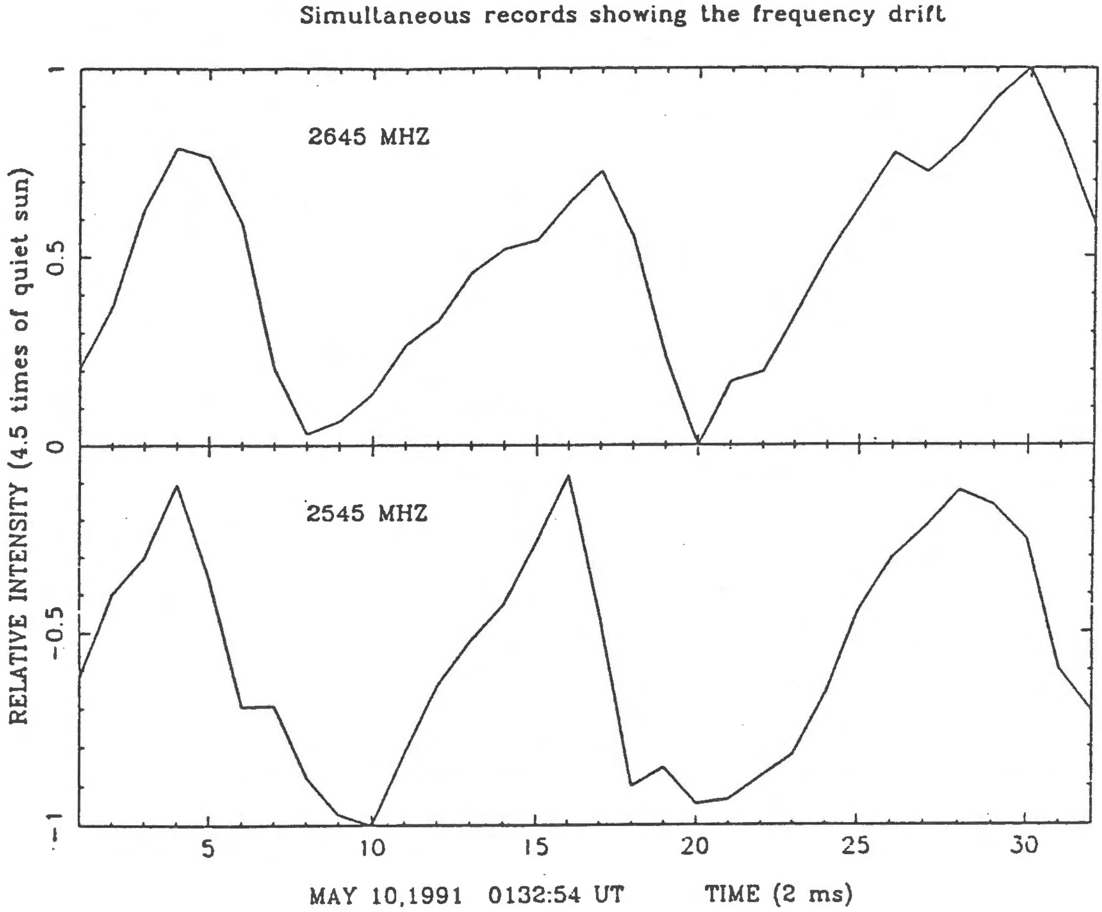

Fig.1 The frequency drift in the spike event observed on May 10,1991.

It can be seen from Figure 1 that the spikes at the 2545 MHz is about 4ms earlier than the ones at the 2645 MHz. This indicates that these spikes have a positive drift rate of about 25 GHz/sec from lower frequency to higher frequency (i.e. reverse drift).

3. Brief analysis

Nowadays, it is generally believed that spike radiation can be explained by the electron cyclotron maser (ECM) instability driven by the loss-cone distribution.The growth via ECM occurs only when the energetic electrons satisfy the wave-particle resonance condition (Dulk,1985):

$$\omega - \frac{s\Omega_e}{\gamma} - k_{\|}v_{\|} = 0 \tag{1}$$

the waves satisfy the following conditions (Winglee,1985)

$$\omega^2 \gg k_{\|}^2 c^2, \tag{2}$$

where ω is the frequency of the waves , $k_{\|}$ the wave vector component parallel to $\vec{B}$, s the harmonic number , $\Omega_e = eB/mc$ the electron cyclotron frequency , γ the Lorentz factor , $v_{\|}$ the electron velocity component parallel to $\vec{B}$, c the velocity of light . As the considered electrons are semi-relativistic ones , they can be shown that

$$0 < \frac{v^2}{c^2} \ll 1. \tag{3}$$

From equations (2) and (3) , therefore , equation (1) may be approximately taken as

$$\omega \approx s\Omega_e. \tag{4}$$

From equation (4) , one can obtain

$$\frac{d\omega}{dt} \approx \frac{se}{mc}\frac{dB}{dt}, \tag{5}$$

i.e.

$$\frac{d\nu}{dt} \approx 2.8 \times 10^6 s \frac{dB}{dt}. \tag{6}$$

we mainly take account of the emission at the second harmonic, so $s = 2$.

According to the observations (see figure 1), the frequency of the spikes drifts from 2545 MHz to 2645 MHz during the time of about 4ms, that is to say, the drift rate is about

$$\frac{d\nu}{dt} \approx 25MHz/ms.$$

Taking account of equation (6), therefore, it is clear that

$$\frac{dB}{dt} \approx 4.5Gauss/ms.$$

It will be shown from this that during the period of 4ms, the magnetic field strength in the source region of spike radiation has increased by $\sim$ 18 Gauss because of the motion of the source.

According to equation (4), the field in the radiation source at $\nu_1 = 2545MHz$ can be calculated to be

$$B_1 \approx 454Gauss.$$

It is assumed that the magnetic field is a magnetic dipole field, so the field can be written as follows (Zhao.,1991):

$$B = \frac{1}{2} d_0^3 \frac{[r^2 + 4(h + d_0)^2]^{1/2}}{[r^2 + (h + d_0)^2]^2} B_0, \tag{7}$$

where h is the height above the photosphere, r the distance from the central axis of the active region, d_0 the depth of the dipole below the photosphere. B_0 the magnetic field at the photosphere. Taking $r = 0, d_0 = 10^9 cm, B_0 = 2000 Gauss$, the height of the radiation source can be obtained

$$h_1 \approx 6.39 \times 10^8 cm$$

In the same way, when the frequency drifts to $\nu_2 = 2645 MHz$ the magnetic field in the source is about

$$B_2 \approx 472 Gauss$$

and the height of the source is about

$$h_2 \approx 6.18 \times 10^8 cm$$

Therefore, one can estimate the mean velocity of the electrons during the period 4ms:

$$v \approx 0.175c.$$

It may be concluded from the above that the energetic electron beams travel downwards at the velocity of $\sim 0.175c$, and hence produce the positive frequency drift of $\sim 25 MHz/ms$.

It is well understood that the ECM mechanism gives the radiation near the electron cyclotron frequency and its second harmonic. This process requires a kind of unstable electron distribution offering free energy for the maser. The most possible configuration is the loss-cone distribution. The energetic electron beams form the loss-cone distributions at different positions when they move downwards along the loop. Then in these unstable regions, the spike radiation is generated by maser action. Therefore, the radiation presents the positive frequency drift (i.e. reverse drift) characteristic, that is to say, the radiation frequency increases with the time.

4. Conclusions

In this paper, the frequency drift characteristic in the spike radiation observed on May 10,1991 has been briefly analysed. It has been believed that the high frequency drift rate ($\sim 25 GHz/s$) originates from the down-moving along the loop of the energetic electrons which form the loss-cone distributions driving the ECM instabilities.

This work was financially supported by the National Science Foundation of China and the Chinese Academy of Sciences.

References

Bruggmann, G., Benz, A.O., Magun, A., and Stehling, W. 1990, *Astron. Astrophys.*,**240**, 506.
Dulk, G.A. 1985, *Ann. Rev. Astron. Astrophys.*, **23** , 169.
Jin, S., Li, X., Wang, S., Ji, H., Yan, Y., and Zhao, B. 1991, *Acta Astrophysica Sinica*,**11**, 394.
Wiehl, H.J., Benz, A.O., and Aschwanden, M.J. 1985, *Solar Physics*, **95**, 167.
Winglee, R.M. 1985, *J. of Geophys. Res.*, **90**, 9663.
Zhao, R.-Y. 1991, *Science in China (Series A)*, **34**, 969.

A Brief Analysis of Microwave FS Events Observed by BAO in 1991

Fu Qijun   Zhao Bin

Beijing Astronomical Observatory, Chinese Academy of Sciences, Beijing 100080, China

Abstract

In this paper, some results of a brief analysis of microwave fine structure (FS) events registered by BAO at 2840 MHz in 1991 are presented. It has been shown that the time scales of most of FS events are between tens of msec and hundreds of msec, and the amplitudes of them are less than 200 s.f.u.

I. Introduction:

The significance of microwave msec bursts, or microwave FS events, for the diagnosis of the physical processes in solar flares and the physical conditions in plasma source region of solar flares has been recognized by solar physicists for a long time [1] [2]. The valuable qualitative observations of microwave msec bursts at 2840 MHz with a simple fast sampling equipment were made by the group of BAO from 1981 to 1983 [3] [4]. In the June of 1989, this equipment was improved and renewed. Since the August of 1990, a patrolling msec- observation with high reliability started to work. A number of microwave bursts' data with high quatity and high time resolution have been registered.

Some results obtained by statistical analyses of the data mentioned above, are presented in this paper.

II. Observations:

During the patrolling observation period of 348 days (2592 hours) in 1991, 602 microwave bursts at 2840 MHz were recorded, FS were found in 45 out of 602 bursts, and the ratio was about 7.5%. But for the observations during the interval between April of 1981 and June of 1983, this ratio was 17.5 %. Table 1 lists the whole FS events observed by BAO in 1991.For some of them, FS only appeared in one section, but for others, in more than one section. For whole 45 events, there appeared 93 sections of FS. It provides us a more completed FS event cluster of this solar maximum period. Firstly, we made analyses from some statistical features of the FS event cluster.

III. Distribution features of FS events:

1. Distribution of time scales:

For each FS section, we take the least time duration of single pulses as the time scale of the FS section Δ T. The distribution of time scale of FS section is shown in Table 2.

Table 2. Distribution of time scale

Δ T	< 10 msec	10~100 msec	100~1000 msec	1~3 s
%	3.2	20.5	46.2	30.1

2. Intensity distribution of spikes:

For each FS section we take the largest intensity of single spike as the spike intensity of the FS section ΔF. The distribution of spike intensity of FS sections is shown in Table 3.

Table 3. intensity distribution of spikes

ΔF	< 50sfu	50~ 200 sfu	200~500 sfu	> 500 sfu
%	48.3	38.2	7-9	5.6

3. Intensity dibtribution of associated microwave bursts:
The results are shown in Table 4, here Δs is the peak flux density of burst.

Table 4. Intensity distribution of associated microwave bursts

ΔS (sfu)	< 100	100~ 500	500~ 1000	1000~ 2000	≥ 2000
1) number of FS events	3	22	8	5	7
2) Distribution of FS events (%)	6.7	48.9	17.8	11.1	15.5
3) Total number of microwave bursts	500	65	15	7	10
4) Appearance rate of FS event (%)	0.6	33.8	53.3	71.0	70

Line 3 indicates the total number of microwave bursts observed by BAO in 1991. Line 4 represents the ratio of 1) to 3). It is clearly shown that the appearence ratio of FS events increases with the peak flux density of microwave bursts.

4. The relationship between FS and the phase of microwave bursts (MB):

Table 5.

phase of MB	before peak time of MB	peak time ($\pm 5^s$)	post-peak
%	38.2	19.8	42

Table 5 shows the distribution of FS sections with the phase of associated MB. It seems to be that no obvious relation between them. But it is undoubted, that the FS appearing in the phase before peak time and of peak time are stronger and more crowded.

5. The relation between FS events and H alpha flares:

Table 6. FS events Vs.Imprortance of associated flares and Vs. type of associated flares

Imp. of flare	S	1	2	3	Type of flare	F	N	B
%	13.3	37.8	33.3	11.1	%	6.7	26.7	62.2

Table 6 shows the distribution of FS events with importance of associated flare. And the flares with type B are mostly associated with FS, and most significant for research on FS phenomena.

IV. Discussion.

From the analyses mentioned above, somethings should be pointed out:

1. The change of appearance rate of FS events in different solar active cycle:

From Table 7, it seems likely, not only for fixed frequency observations but also for spectral observations, that the appearance rate of FS events in the 22nd solar maximum period is quite lower than that in 21st period. Whether, it results from the different characteristics between the 21st and 22nd solar maximum period.

2. Time scale and characteristic intensity of FS:

From Table 2, in about half of FS events, the time scale Δ T are some hundreds of msec; some tens of msec in about one fifth; and some of msec in only a few percent. These results consist with those of G *ü*del and Benz (1990) [8]. Possibly, the FS with different time scale are the manifestations of distinct kinds of fast process, such as microwave type III bursts, microwave spike emission and so on. For further analysis radio spectral observations with higher time resolution should be made.

Table 7.

Authors	Frequency (GHz)	Time period	.appearance rate of FS events (%)	references
Fu. et al.	2.84	1981-1983	17.5	[3]
Stä hli and Magun	3.2	1980-1982	13.4	[5]
Allaart, et al.	4-8.0	1982-1983	30	[6]
Brugymann	6.0-8.0	1988-1989	17.4	[7]
Fu, Zhao and Liu	2.84	1991	7.5	in this paper

From Table 3, Characteristic intensity of 86 % of FS events is less than 200 s.f.u. The largest pulse is about 2000 s.f.u. This result is quite different from that of Jin, et al (1986) [4], and Slottje (1978) [9]. Does it result from the feature of the 22 nd solar active maximum period ?

3. Intensity of associated microwave bursts:

From the first line of Table 4, almost half of FS events are in the range of 100 $\sim$ 500 s.f.u. But from the last line, it is obvious that the appearance of FS incleases quickly with intensity of associated bursts. It is only 0.6 % in the range of less than 100 s.f.u., but the rates inclease quickly up to 70 % in the range of more than 1000s.f.u.

4. Table 5 shows that the appearance of FS has no obvious relation with the phase of bursts.

But, it is undoubted, that the FS appearing around impulsive phase should be more intense. Certainly, there are some processes which can product fast FS phenomena in the declining phase of bursts. For example, tremendous change of magnetic field topology happens when small loops with rapid rising speed interact with preexisting post-flare loop system, as found by Fu, et al. (1993) [10].

This work was supported by NSF of China and the grant of Chinese Academy of Sciences.

Reference

Hudson, H. S.: 1987 Solar Phys. 113, 1.
Benz, A.: 1986 Solar Phys. 104, 99.
Fu, Q., Jin, S., Zhao, R., Zheng, L., Liu, Y., Li, X., Wang, s., Chen, Z., and Hu, C. : 1986 NASS CP-2449, 237.
Jin, S., Zhao, R., and Fu, Q. : 1986 Solar Phys. 104, 391.
Stähli, M., and Magau, A. : 1986 Solar Phys. 104, 117.
Allaart, M. A. F, Van Nieuwkoop, J., Slottje, C., and Sondaar, H.: 1990 Solar Phys. 130, 183.
Bruggmann, G., Benz, A. O., Magun, A., and Stehling, w. : 1990 Astron. Astrophys.240, 506.
Güdel, M. and Benz, A. O. : 1990 Astron. Astrophys. 231, 202.
Slottje, C.: 1978 Nature 275, 520.
Fu, Q., Li, C., Gong, Y., Li, W., Zhao, B., Shang, Q., Lu, s., and Hu, H.: 1993 Solar Phys. 143, 417.

Table 1. List of Radio Millisecond Spike Bursts (BAO 2840MHz)

NO.	Date 1991.	msec–Burst HHMMSS	msec–Burst Int SFU /%	msec–Burst time scale	sec–Burst Start (UT)	sec–Burst Max. (UT)	sec–Burst End (UT)	sec–Burst Int SFU / %
1	Jan.8	0429:57.07 -04:29:57:45	114/48	10-60ms	0357.0	0429.7	0451.0	712/299
		04:29:21 –04:30:14	30/13	2-3 s				
		04:32:32.7 -04:32:32.9	64/34	200ms				
2	Jan.25	06:50 –07:22	160/56	1-5 s	0629.0	0639E 0722D	0755.0	1123/393
		06:53:02 –06:53:42	80/28	50-600ms				
3	Jan.31	01:55:13.0 –01:55:35.2	30/8	1.5-3 s	0153.0	0204.3	0453.0	821/202
		01:58:56.6 –01:59:18	110/28	400 -800ms				
		02:00:29 –02:04:39.7	73/19	0.4-1 s				
4	Feb.6	06:46:15 –06:46:34	53/22.8	1-4 s	0644.0	0646.5	0704.0	355/153
5	Feb.8	02:48:11 –02:48:32	19/8.7	3-5 s	0236.0	0248.1	0258.0	184/85.8
6	Mar.5	02:22:50 –02:22:57	57/23	2-3 s	0218.0	0222.9	0232.0	73/29.6
7	Mar.5	06:18:37 –06:18:52	33/13.3	1.8 s	0606.0	0618.9	0631.0	88/35.4
8	Mar.6	07:41:00 –07:41:00.5	34/13.8	30 ms	0737.0	0742.6	0800.0	983/401
9	Mar.11	07:32:34 –07:33:29	22/8.5	0.5-1 s	0726.0	0733.3	0742.0	196/76.6
10	Mar.13	02:59:05 –03:04:20	130/48.6	0.5-1 s	0249.0	0302.1	0400.0	198/74
		03:00:10 –03:00:20	40/15	270 ms				
11	Mar.13	07:31:58 –07:32:48	62/23	0.5-1 s	0728.0	0732.8	0742.0	136/50.9
		07:35:58 –07:37:51	59/22.1	1.5 s				
12	Mar.19	01:57:15 –01:57:53	38/12.6	0.1 s	0156.6	0158.0	0202.0	1255/417
13	Mar.21	08:15:52.8 –08:15:55	42/15	0.5 s	0809.0	0815.5	0836.0	209/75
14	Mar.24	02:52:48 –02:53:06	47/15.6	50-100ms	0236.0	0244.2	0258.0	221/73
		02:44:05 –02:44:12	140/46	100ms-1s				
15	May.10	01:47:09 –01:47:27	270/91	50-100ms	0126.0	0147.2	0200.0	575/193
		01:54:00 –01:55:26		40 ms				
16	May.16	06:41:00 –06:49:00	900/400	50,380ms 3ms 1.5s	0631.0	0646.9	0907.0	3041 /1352
17	May.17	04:18:00 –04:21:15	84/39	2 s	0415.0	0419.7	0428.0	237/112
18	May.31	04:03:15 –04:04:17	7/3	1.5 s	0353.0	0406.1	0423.0	201/81.7
19	Jun.4	06:14:41 –06:14:48	153/50.8	30-40ms	0604.0	0614.8	0634.8	160/53.1

20	Jun.4	03:44:00 –03:46:00 03:47:52 –03:49:40		Oscil.4s Oscil.4s	0337.0	0348.2	0618D	7719 /2490
21	Jun.6	01:09:41 –01:09:41.8 02:11:58 –02:12:01 02:12:29 –02:07:09	1880/690 90/33	50 ms 50 ms –8.7 s	0051.0	0105D	0634.0	14000D /5140D
22	Jun.9	01:36:49 –01:36:54 02:11:16 –02:11:26 02:28:26 –02:28:28 02:31:56 –02:34:22 02:36:00 –02:41:20	602/206 139/47.6 55/19 213/73 290/27	50 ms 40 ms 150 ms 32 ms 60 ms	0135.0	0139.6 0239.0	0406.0	8545 /2916 4522 /1543
23	Jun.10	02:28:40.2 –02:28:42.4 02:29:00 –02:29:06 02:29:16.25 -02:29:23.65	1195/385 217/70 93/30	400 ms 40 ms 400 ms	0226.0	0228.8	0232.0	492/293
24	Jun.12	07:06:09 –07:07:06	340/104	3-6 s	0704.0	0706.3	0708.0	358/110
25	Jul.7	02:01:42 –02:04:36	142/45.2	530ms-2s	0141.0	0154.2	0230.0	1176/376
26	Jul.17	06:42:41 –06:43:03	102/52	1.7 s	0619.6	0627.6	0657.0	1000/505
27	Jul.30	07:07:07 –07:07:13 07:07:18 –07:07:20.5	20/7.8 164/64	100 ms 100 ms	0704.0	0707.5	0714.0	468/184
28	Jul.31	00:50:53 –00:51:08 00:51:22 –00:51:42	124/46 75/28	0.1-1 s 1 s	0045.0	0049.8	0141.0	743/277
29	Jul.31	03:15:37 –03:16:37	42.8/16	10-100ms	0310.0	0316.9	0320.0	32.5/12
30	Aug.2	03:12:32 –03:12:49 03:13:11 -03:13:15.49 03:15:38 –03:16:02 03:19:35.8 -03:19:49.98	79/35 30/13.3 80/38 39/17	600 ms 150 ms 150 ms 50-100ms	0301.0	0312.7	0419.0	428/187
31	Aug.3	01:22:03 –01:22:20	22/9.2	Three peaks	0120.0	0122.3	0135.0	523/216
32	Aug.5	05:28:08 –05:28:21 05:28:21 –05:29:00	40/18.9 110/50	130 ms 1 s	0528.0	0528.4	0636.0	368/174
33	Aug.25	00:52:05.7 –00:56:34	669/211	5-300 ms	0033.0	0053.1	0240.0	3440 /1085
34	Oct.27	02:08:37.4 — 02:08:59.2 –02:09:00	33/11 25/8.2	0.1 s 60 ms	0204.0	0209.3	0212.0	233/76.4

35	Oct.27	05:41:30 –05:42:20	387/127	2-3 s	0505.0	0542.2	0616.0	4454/1460
		05:42:40 –05:43:10	184/60	1 s				
		05:45:44 –05:45:50	59/19	sub-sec				
		05:51:34 –05:55:34	94/31	ten-sec				
		05:56:34 –05:58:00	146/47.9	ten-sec				
36	Oct.30	06:15:33.94 +10s	16/5	1-3 s	0600.0	0619.8	0730.0	3677/1171
		06:17:54.80 +0.5s	46/14.5	0.1-0.5s				
		06:18:54 –06:22:08	21/6.7	0.1-1 s				
		06:35:42 –06:35:50	22/7	0.5-0.8s				
		06:36:38 –06:36:41.5	52/16.6	0.1-0.3s				
		06:39:30 –06:39:51.5	23/7.3	0.1-0.3s				
37	Nov.6	04:44:38 –04:47:48	36/18	1-2 s	0440.0	0449.2	0520D	1014/515
38	Nov.10	01:26:39 –01:26:40.5	9/4	0.5 s	0118.0	0128.4 0136.7	0146.0	239/106 190/84
		01:28:20 –01:28:28	30/13	0.1-0.5s				
39	Nov.10	06:48:20.5 –06:48:22.5	26/11.6	0.3-1.0s	0646.0	0650.2	0657.0	150/66.7
		06:48:31.8 –06:48:35.8	16/7	0.1-0.2s				
		06:50:07 –06:50:13	10/4.4	1 s				
40	Nov.17	01:57:44.2 –01:57:46.1	29/16.1	0.2 s	0155.2	0158.1	0218.0	807/448
		01:57:57 –01:57:58.4	11/6.1	1.2 s				
		01:58:26 –01:58:28	23/12.8	1 s				
41	Nov.30	03:45:25 –03:45:27.5	68/38.6	0.1-0.2s	0337.0	0345.2	0355.0	321/183
		03:45:34 –03:45:36	49/27.8	0.2 s				
		03:45:59.8 –03:46:01.2	11/6.2	1.5 s				
		03:46:13.8 (peak)	11/6.2	1.5 s				
		03:46:27.8 –03:46:29.2	17.2/9.8	1.5-2.0s				
		03:47:32 –03:49:20	48/27.3	0.16-1s				
42	Dec.13	03:50:51 –03:53:21	16/6	Oscil. 16-17s	0340.0	0354.2	0430D	422/159
		03:55:12 –03:55:15.1	31/10	3 s				
43	Dec.14	01:03:49 –01:03:54.4	10/8	1 s	0045.0	0103.6	0111.0	178/68.2
44	Dec.17	06:23:52 –06:24:23	365/168	0.1-1 s	0616.0	0623.9	0640.0	576/265
45	Dec.26	06:34:11 –06:34:53	24/8	0.2-1.0s	0630.0	0634.4	0652.0	307/108

The Features of Spikes Received at 2545 and 2645 MHz Frequencies

Sheng-Zhen JIN, Xiao-Cong LI

Beijing Astronomical Observatory, Academia Sinica, Beijing 100080, China

Abstract

In this paper, some features of spike radiations and other fast fine structures of microwave bursts at 2545 and 2645MHz Frequencies, shch as the narrow bandwidth, the rapid frequency drift, the quasi- oscillation and the quick reversion of the polarization senses are introdused and discussed. We think that these features may be closely related to the electroncycrotron instability, the wave beam resonance condition,the movement of the MHD wave and the nonthermal beam in the solar corona source region.

1. Introduction

The spikes and fast fine structures(FFT) occured in solar microwave bursts are usually with very short time scales. Since 1980, they draw atentions of many solar radiophysicists. Generally, they are with very narraw radiation bandwidth ($\triangle\omega \geq 10\%$), very rapid frequency drift($df/dt \geq 10GHz$). Thy are usually modulated by some quasi-oscillation with periods in second and subsecond time scales. And the senses of polarization of the spikes are quickly reversed in short time interval.

Since June 1990, a new microwave polarimeter was put into observation at Beijing Astronomical Observatory. It received right and left hand circular polarizations (RHCP, LHCP) at 2545 and 2645 MHz frequencies. Signal from the four channels can be sampled in every 0.2 ms or 2 ms, and over one handred spikes and FFS events had been recorded(Jin et,al.,1991). Some features are demonstrated in this paper.

2. Narrow Bandwidth Radiation

Solar microwave spike and FFS radiations are known that they have very narrow bandwidth. According to Stahli and Benz(1987), at 3100 MHz frequency. the relative bandwidth of the spike radiation($\triangle\omega/\omega$) is less than 10%, and Benz(1986) at 0.1~ 2 GHz frequencies, the $\triangle\omega/\omega$ are less than 1.5%. According to the samples, we have recorded so far, it is evident that many spike and FFS emissions at 2545 and 2645 MHz are with 5% relative bandwith, and the profiles of them at different frequencies are different. Some spikes only occurred in one frequency.

Fig.1. shows the spike groups occurred at 0647 UT at 2545 and 2645 MHz , on May 16,1991. The peak flux of the spike groups at 2645 MHz is about 2.5 times $S_{\odot}$, the quiet sun flux on the same day , the duration time is about 500 ms, and it is composted of two subgroups. At 2545 MHz frequency, there are no obvious spikes recorded.

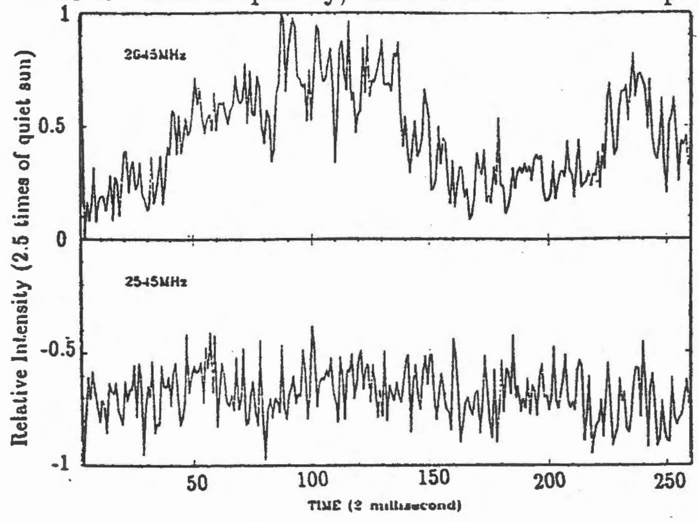

Fig. 1 The spike emission occurred at 0647 UT on May 16,1991.

Fig.2. demonstrats the spike radiations recorded at 0409 UT on January 25, 1991 , at 2545 and 2645 MHz. In the 300 ms time interval started at 0409:56 UT. The profiles of the spike, occurred at the two frequencies, are very different and there is no corresponding spike occurred at 2840 MHz frequency.

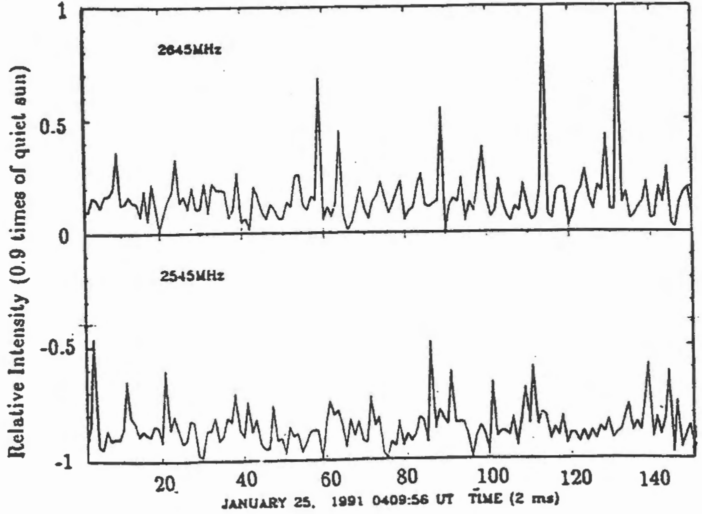

Fig. 2 The spike emission occurred on January 25, 1991.

We know that the spike emissions generally come from the electronmagnetic emission stimulated by the electron-cycrotron maser instibility under the particle wave resonance condition.

$$\omega = \gamma^{-1} s\Omega_B + k_{\|} u_{\|} \qquad (1)$$

where γ is the Lorrentz factor, s is the hamonicas of the radio wave, $k_{\|}$ is the projection on the magnetic field of the wave vector, $u_{\|}$ is projection on the magnetic field of the beam velocity, and Ω_B is the electron gyro-frequency. It is believed that the resonance condition limit the bandwidth of the spike radiations.

3. Frequency Drift

The rapid frequency drift rate of the spike and FFS events has interested many solar radiophysicists. Stahli and Benz[2] showed the frequency drift rate from-0.7GHz/s to -17GHz/s at 3100 MHz frequency. Aschwanden and Benz (1986) demonstrated the frequency drift rate from 1 GHz to 4 GHz/s, at 326 MHz and 770 MHz frequencies respectivelly.

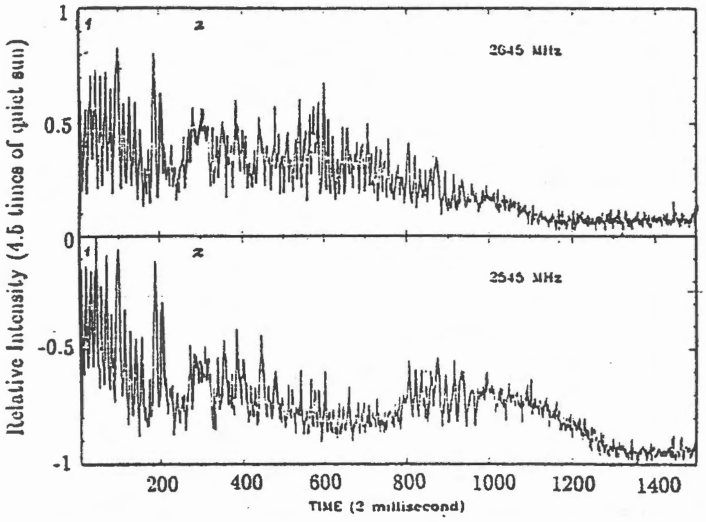

Fig. 3 The frequency drift of spike emissions occurred at 0132:54 UT on May 10,1991.

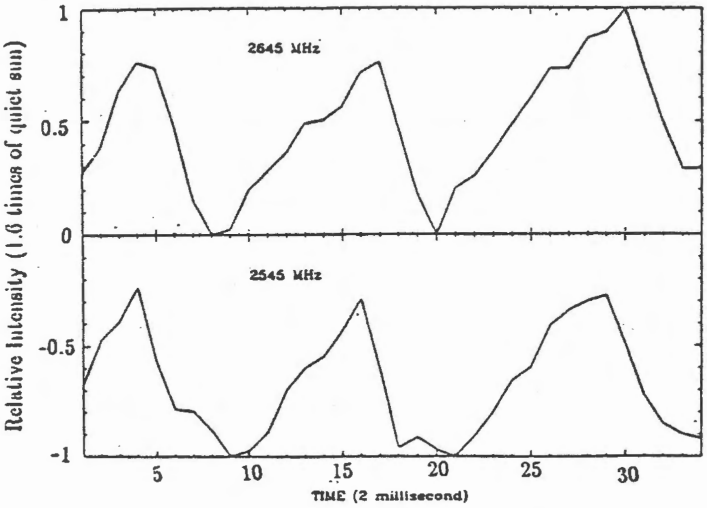

Fig. 4 The frequency drift of spike emissions occurred at 0132:02 UT on May 10,1991.

Several spikes and FFS events with rapid frequency drift have been recorded between 2545 and 2645 MHz frequencies. The frequency drift rate is about 15~ 30 GHz/s of the spike radiations. Fig.3.displys the profiles of the spikes occurred on May 10,1991. The background burst at 2545 MHz was delayed about 500 ms compared with that at 2645 MHz, the frequency drift rate is 0.4 GHz/s. The spike radiations superimposed on the backgrounds werw shown the same profile. The fine structures labeled by "1" and "2" in Fig.3. are shown in Fig.4., and Fig.5. respectivelly. It can be seen that the spikes at 2645 MHz was delayed about 6 ms compared with that at 2545 MHz in Fig.4., and the spikes at 2545 MHz was delayed about 4.0 ms compared with that at 2645 MHz in Fig.5.. The frequency drift rates are 15 GHz/s and -28 GHz/s respectivelly.

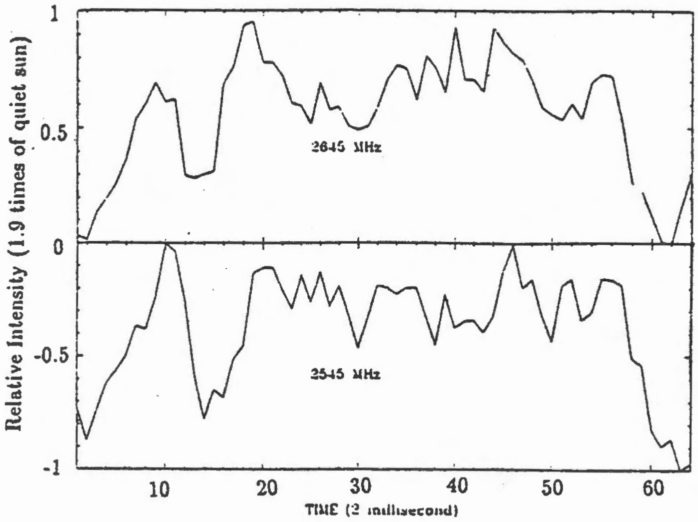

Fig. 5 The frequency drift of spike emissions occurred at 0132:55 UT on May 10,1991.

It is known that the spike and FFS radiations are depended on the interactions of particle-wave and beam-wave, stimulated by the nonthermal electron beams in the solar corona. Obviously both the direction and the time scale of the frequency drift are closely related to the direction and the velocity of the nonthermal electron beam in the source region. From Eq.1.

$$d\omega/dt = (sq/\gamma m)dB/dt - ku(sin\theta cos\alpha d\theta/dt + sin\alpha cos\theta d\alpha/dt) + kcos\alpha sin\theta du/dt \quad (2)$$

where q is the charge of a electron, m is the rest mass of a electron, S is the harmonics of the radio wave. γ is the Lorentz factor, B is the the magnetic induction in source region, k is the wave vector, u is the velocity of the nonthermal electron beam, θ is the radio angle between k and B, α is the pitch angle between u and B. Assuming that B, θ, α are unchanged, the reversion of the direction of u may lead to the reversion of the frequency drift rate. If the distribution of the electrons in the nonthermal beam is lose-cone distribution, the velocity directions of the electrons incideut and reflected may be reversed, so the directions of frequency drift rate caused by those two beams may be changed.

4. Quasi Period Oscillations.

The spike and FFS radiations usually are associated with quasi period oscillations.(Jin et al.,1989, Jin et al., 1990, Zhao et al.,1990 Fu et al 1990)The periods of this quasi-oscillations are in second or subsecond time scales. It is believed that, the quasi period oscillations of the spike and FFS events are caused by the MHD waves in the source region or the nonthermal beams modulated in the acceleration region.

Fig.6. indicats the spike groups occurred on July 30,1990. It started at 0728 UT , and it is lasted about 100 ms. The peak flux density of the spikes is about 20 times

that of the quiet sun, and it is composted of 30 individual spikes. The average period of the quasi- oscillations are about 3 ~ 5 ms. The spike groups occurred on May 10, 1991 is shown in Fig.7. The spikes started at 0132 UT, at 2645 MHz. The period of the quasi-oscillations is about 28± 2 ms.

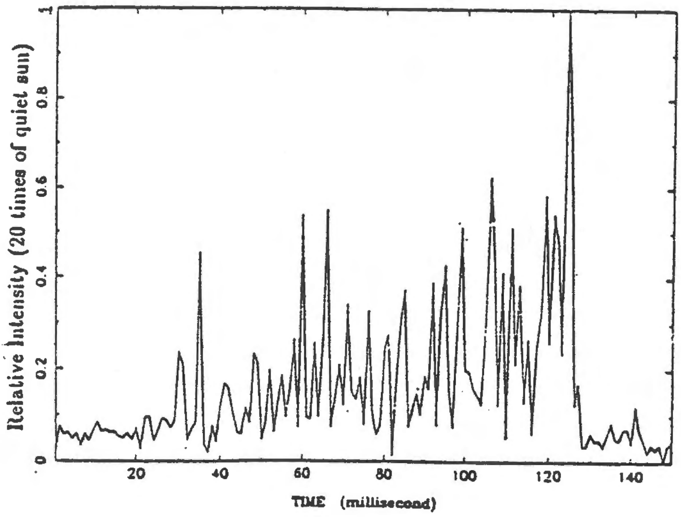

Fig. 6 The oscillation of spike emissions occurred at 0728 UT on Jyly 30,1990.

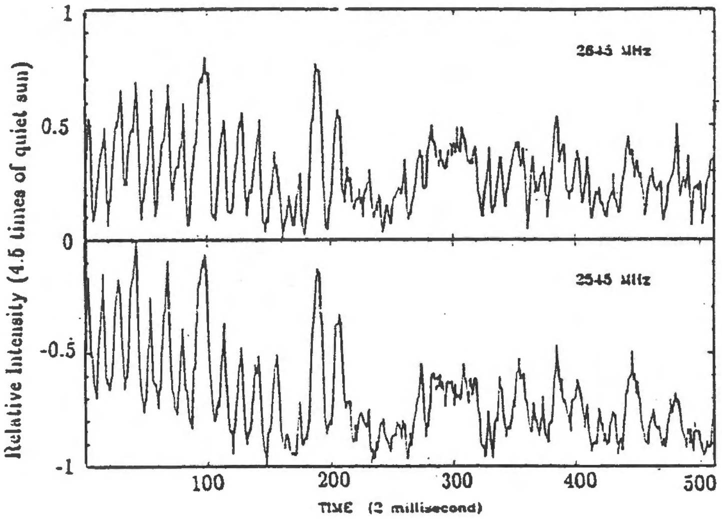

Fig. 7 The oscillation of spike emission occurred at 0132 UT on May 10, 1991

5. Reversion of the polarization senses

The quick fluctuations of the polarization sense is another characteristics of spike radiation. Gary observed the spike radiations, the polarization sense of the spikes is reversed from 86% RHCP to 23 % LHCP at 2840 MHz in 1990.(Gary,D.,et al.,1990)

An intensive solar flare associated with a microwave burst was recorded on May 16, 1991. In the peak phase of the microwave burst, a lot of spikes and FFS emissions were recorded. Fig.8. shows the polarization components of the spikes occurred at 0647 UT. The peak flux densities were about 8.5 $S_{\odot}$ of the LHLP wave and 1 $S_{\odot}$ of the RLCP wave. The polarization senses are reversed 6 times quickly and alternated. The LHCP is about 80% to 90%, and the RHCP is 30% to 40%. The average reversion time interval is 50~100 ms, and the shortest reversion time interval is about 60 ms.

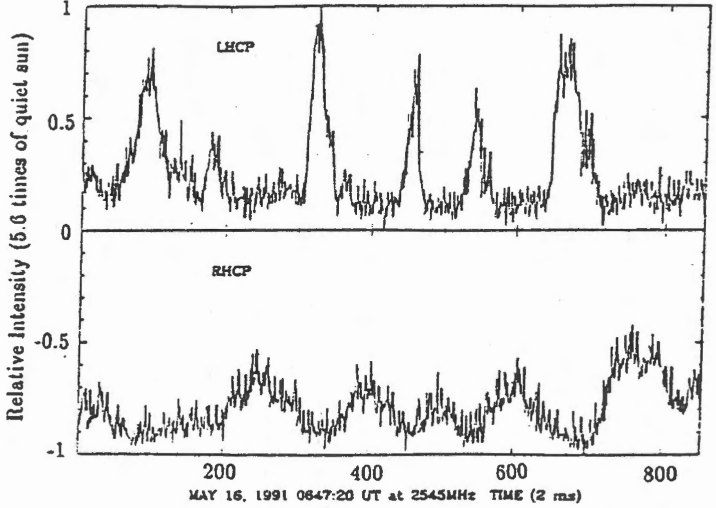

Fig. 8 The reversion of the polarization senses of the spikes occurred at 0647 UT on May 16, 1991.

The reversion of polarization sense depends on the alternation of the radiation of X mode wave and O mode wave. The mode and the frequency of the dominant radiation from the electron-cyclotron maser instability is dependant on the ratio ω_p/Ω_e(the plasm frequency to the electron-gyrofrequency). For the radiation from the corona, ω_p/Ω_e is probably from 0.1 to 2.0. When $0.3 < \omega_p/\Omega_e < 2^{1/2}$, the emission may be in the X mode at the second harmonics and when $2^{1/2} < \omega_p/\Omega_e < 3^{1/2}$, it may be in the O- mode at the second harmonics. If the ratio ω_p/Ω_e fluctuated near $2^{1/2}$, the emission mode may be alternated(Winglee,R.M.et al.,1986)

6. Discussion

The narrow bandwidth radiation, the rapid frequency drift, the quasi period oscillation and the quick reversion of the polarization senses of the spike and FFS emissions directively reflect the mechnisms and the physical conditions of the source region. These radiations are close related to the growth ratio of the electron-cyclotron maser instability stimulated by the interaction of wave-wave and wave-beam.

The futher observations and analyses are very important for the studies of the maser instibility, the interaction and resonance of the radiowave and the nonthermal beam, and the physics of source region and beam acceleration region.

References

Shenzhen Jin, Xiaocong Li et al., ,*Acta Astrophysics Sinica.*, **11**, 394.

Stahli.M.and Benz,A.O.,*Astron. Astrophys.*, **175**,271.

Benz,A.O., *Solar phys.*,**104**,99.

Aschwanden,M.J. and Benz,A.O.,*Astron. Astronphys.*, **158**,102.

Shengzhen Jin and Xiaocong Li, *ACTA Astrophysics.*, **9**,157.

Shenzhen JiN, Qijun Fu, Renyang Zhao and Chumin Hu, *Solar Phys.*,bf 130,175.

Renyang Zhao, Shengzhen Jin, Qijin Fu and Xiaocong Li *Solar Phys.*,**130**,157.

Qijun Fu,Yuanfang Gong,Shengzhen Jin and Renyang Zhao, *Solar Phys.*,**130**,161.

Gary,D., Hurford, G. and Flees,D. Bull.Am.,Astron. Soc., **22**(1990) No.2 823.

Winglee,R.M. and Dulk,G.A.,*Solar Puys.***104**,93.

The Reversion of Polarization Sense of Spikes observed on May 16,1991

Sheng-zhen JIN, Ren-yang ZHAO, Xiao-cong LI and Qi-rang QI

Beijing Observatory, Academia Sinica, Beijing 100080, China

Abstract

In this paper, the polarization reversions of the radio spikes and fine structures, superimposed on the microwave burst on May,16 1991, were introduced briefly. It may be caused by the fluctuations of plasma density and magnetic field in the source region in corona, and the fluctuation leads to the growth of the electron-cyclotron maser to control the radiation of X-mode or O-mode wave and to reverse the sense of the polarization of radio emission.

1. Introduction

It is well known that the spike emission of solar microwave radio burst often have the characteristics of high polarization and rapid sense variation of polarization. This may be explained as that spike emission is of the coherent nonthermal one and it relates closely to the magnetic field strength of the radio burst source region and the plasma density.

Since 1970s, the problem on the polarization of spike emission draws attentions of many solar radio physicists. The 100% LHCP spike emission has been observed at the frequency of 2600MHz by Slottje (1978)[1]. And Gary has also observed that the degree of polarization of spike emission changes from 26% RHCP to 83% LHCP in 370ms period at the frequency of 2840 MHz, he then gives a preliminary explanation in terms of the relation between the cutoff frequency of the second harmonic O-.X-modes and the ratio of the plasma density of background to the magnetic field strength[2].

2. Observation

On May 16, 1991, a 47GB microwave radio burst, which was associated with a optic flares on solar surface, had been observed at the frequencies of 2545 and 2645 MHz with high time resolution at Beijing Astronomical Observatory. During the peak phase of the bursts, a group of spikes had been obtained. From the observation, spike emission has been dominated by LHCP within the time scale in the main burst phase, but during $0645 - 0648UT$, the burst changes from LHCP to RHCP, the observation with a high time resolution shows complicated variations in the sense of spike polarization,especially within the 1500ms period after 0647 UT, the sense of polarization of spike emission gives six reversions continuously. In general, the LHCP value of spike emission is about 80% to 90%, and the RHCP value is about 40% to 50%, the mean time interval of reversion is about 100ms, and the shortest one is about $60ms$[3].

Figure 1 shows the time profile of the May 16, 1991 radio burst at the frequencies of 2545 and 2645 MHz, and from 0645 to 0648 UT.

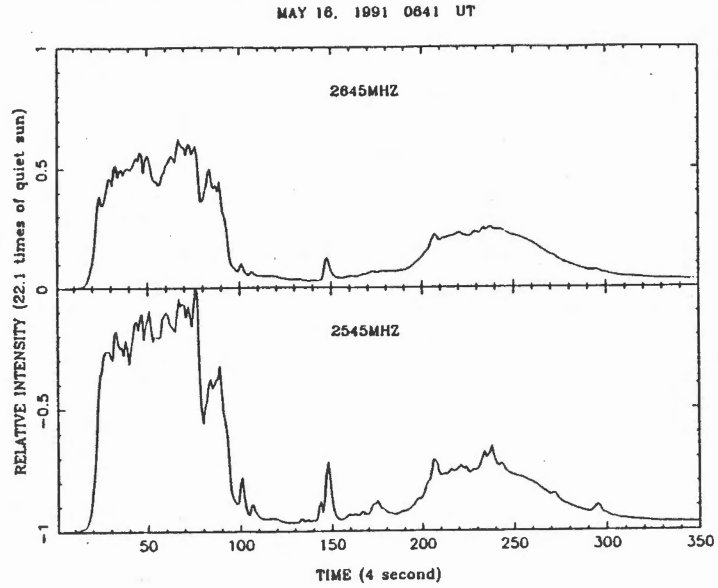

Fig. 1 The profile of the microwave burst occurred on May 16,1991.

Figure 2 is the morphological figure that shows the rapid reversions of the sense of spike polarization within the 0647 UT period. From Figure 2 we can see, during about 1000s period, the sense of spike polarization alternates between LHCP and RHCP rapidly.

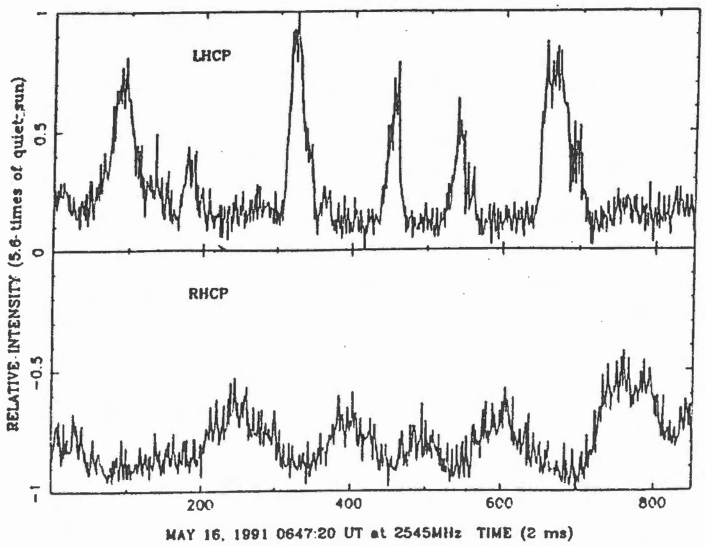

Fig. 2 The reversion of the spike polarization senses.

3. Discussion

The frequency and the waves mode of spike emission are determined by the physical background of the coronal source region. Melrose has already given their general expression in *detail*[4]. In this paper, we only discuss the electron-magnetic wave in a approximate way. Under the condition that the propagating direction get perpendicular to the magnetic field, the dispersion equations of O- and X-modes may be written as follows [5]

$$1-(\frac{ck}{\omega})^2+(\frac{\omega_p}{\omega})^2\int dv^3(\Omega\frac{\partial f}{\partial v_\perp}+k_\parallel v_\perp\frac{\partial f}{\partial v_\parallel})\frac{v_\perp J_1'^2(b)}{(\omega-\Omega/r-k_\parallel v_\parallel)}=0 \tag{1}$$

$$1-(\frac{ck}{\omega})^2+(\frac{\omega_p}{\omega})^2\int dv^3(\Omega\frac{\partial f}{\partial v_\perp}+k_\parallel v_\perp\frac{\partial f}{\partial v_\parallel})\frac{v_\parallel^2}{v_\perp}\frac{J_1^2(b)}{(\omega-\Omega/r-k_\parallel v_\parallel)}=0 \tag{2}$$

where ω_p, Ω and ω are the plasma frequency, the electron cyclotron frequency and the emitting frequency respectively; $v_\perp$ and $v_\parallel$ denote the velocity components of the nonthermal electron beams perpendicular and parallel to the magnetic field; n is the density of the nonthermal electron beams; $k_\parallel$ is the component of the electron-magnetic wavevector parallel to the magnetic field; f is the electrons distribution function in the plasma momentum space;γ is the Lorentz factor; $J_1(b).J_1'(b)$ denote the regular Bessel function and its derivative, respectively, and its variate is $b = k_\perp v_\perp/\Omega$.

From the dispersion equation, we could derive the emitting frequency of spike $\omega = \omega_r + i\Gamma, \omega_r$ is the real part, Γ is the unreal part. In fact, Γ describes the damping or growth rate of the modes against time. When $\omega_r \gg \Gamma$, we can derive the growth rates Γ_x, Γ_o of the X- and O-modes as

$$\Gamma_x=\frac{\pi^2\omega_p^2}{\omega^2}\frac{n_b}{n}\int_0^\infty dv_\parallel\int_0^\infty d^2v_\perp v_\perp^2(\Omega\frac{\partial f}{\partial v_\perp}+k_\parallel v_\perp\frac{\partial f}{\partial v_\parallel})/(\omega-\frac{\Omega}{r}-k_\parallel v_\parallel) \tag{3}$$

$$\Gamma_x=\frac{\pi^2\omega_p^2}{\omega^2}\frac{n_b}{n}\int_0^\infty dv_\parallel\int_0^\infty dv_\perp(\frac{v_\perp}{c})^2v_\parallel^2(\Omega\frac{\partial f}{\partial v_\perp}+k_\parallel v_\perp\frac{\partial f}{\partial v_\parallel})/(\omega-\frac{\Omega}{r}-k_\parallel v_\parallel) \tag{4}$$

Under the wave-particle resonant condition,

$$\omega - S\frac{\Omega}{\gamma} - k_\parallel v_\parallel = 0 \tag{5}$$

We can see that Γ_x and Γ_o will reach the maximum values. Taking the distribution function of plasma into the above equation and integrating it along the momentum space coordinate, then we will get the growth rates of Γ_x and Γ_o.

The mode, frequency and growth rate of the electron-magnetic wave of spike emission are completely determined by the physical conditions of source region (ω_p, Ω), the density. velocity of the nonthermal beams and the angle between the incidence beam velocity and the magnetic field. If we select the factor (ω_p/Ω) as the parameter, taking Γ as the function of (ω_p/Ω), and in the meantime taking account of the cutoff condition that the electron-magnetic waves propagate in the coronal region, we could get that the generation and propagation of the X-, O-modes and their harmonics of spike emission are seriously confined by the factor ω_p/Ω

$$\omega_p/\Omega < \sqrt{S(S-1)} \tag{6}$$

the condition for X-mode to propagate

$$\omega_p/\Omega < S \tag{7}$$

the condition for O-mode to propagate
where S is the harmonic number.

The source region of spike emission at the frequencies of $2.5 - 2.6GHz$ is located at the lower coronal atmosphere. The first harmonic X- and O-mode can not escape from the corona due to heavy absorption by the second and higher cyclotron resonance layers. Only the second X- and O-mode harmonics may be possible to escape from the corona and reach the earth.

When $\omega_p/\Omega \leq 1$, the emission is dominated by the first harmonic O-mode; when $1 \leq \omega_p/\Omega \leq \sqrt{2}$, the second harmonic X-mode will replace the first harmonic O-mode and govern the emission; and when $\omega_p/\Omega \geq \sqrt{2}$, the second harmonic X-mode will be quenched and the second harmonic O-mode will take the place of it. If the value of ω_p/Ω changes close to $\sqrt{2}$, the second harmonic X- and O-modes will dominate the emission alternately and then give rise to changes in the sense of polarization alternately.

At the observed frequency of 2.6 GHz and we assume that spike emission is the second harmonic radiation, then

$$\nu_p = \frac{1}{2\pi}\omega_p = (\frac{e^2 N_e}{\pi m_e})^{1/2} \doteq 9 \times 10^3 \sqrt{N_e} \ \ Hz \tag{8}$$

$$\nu_\Omega = \frac{1}{2\pi}\Omega = \frac{eB}{2\pi m_e c} \doteq 2.8 \ B \ \ MHz \tag{9}$$

where m_e is the mass of electron, e is the quantity of electron, the unit of B is Gauss. From above, we can derive the magnetic field strength ($\sim$ 500 Gauss) of the source region of the May 16, 1991 spike emission and the plasma density ($10^{10}/cm^3$).

It is well known that the disturbances will cause MHD waves ("sausage" mode), then they would create the resilient shrink of magnetic loop and the undulation of plasma density which will make the value ω_p/Ω rise and fall around $\sqrt{2}$. Furthermore, this would cause the second harmonic X- and O-modes to rule spike emission by turns, and eventually lead to the reversion of polarization of spike emission.

Acknowledgements: This work was financially supported by the National Science Foundation of China and the Chinese Academy of Sciences.

References

Slottje, C. 1978, *Nature*, **275**, 520.
Gary. 1990, *Bull. Am. Astron. Soc.*, **22**, 823.
Jin Shengzhen et. 1991, *ACTA Astrophysics Sinica*, **11**, 394.
Melrose, D.B. 1980, *Plasma Astrophysics*, Gordon and Breach, New York.
Loukas Vlahos. 1987, *Solar Physics*, **111**, 155.

The Analysis of Solar Data at 2.84 GHz on May 16,1991

Zheng Le-ping and Liu Yu-ying

Beijing Astronomical Observatory, Chinese Academy of Sciences,
Beijing 100080, China

I. The Results of Observation.

A great solar burst was observed by the radio telescope of Beijing Astronomical Observatory at 2.84 GHz on May 16,1991. It started at 0641UT, peaked at 0646.8 UT and endured for 156 minutes. Its peak flux was 3041 sfu, and it was classified as 47GB radio burst [1]. The above equipment was made in 1990. Except the analogue S-resolution records, there are three kinds of dataout processed by computer softwaves: digital S-resolution records, time constant τ=10 ms records and τ=1ms records (if some condition is satisfied). On May 16, there were two τ=1ms disk files in our hands, and their time spans add up to 16s.To make further data processing easier, we have combined the two successive disk files of τ= 1ms into a new one, ignoring the finite time interval which actually separated them. Figure 1 is the digital S-resolution record.

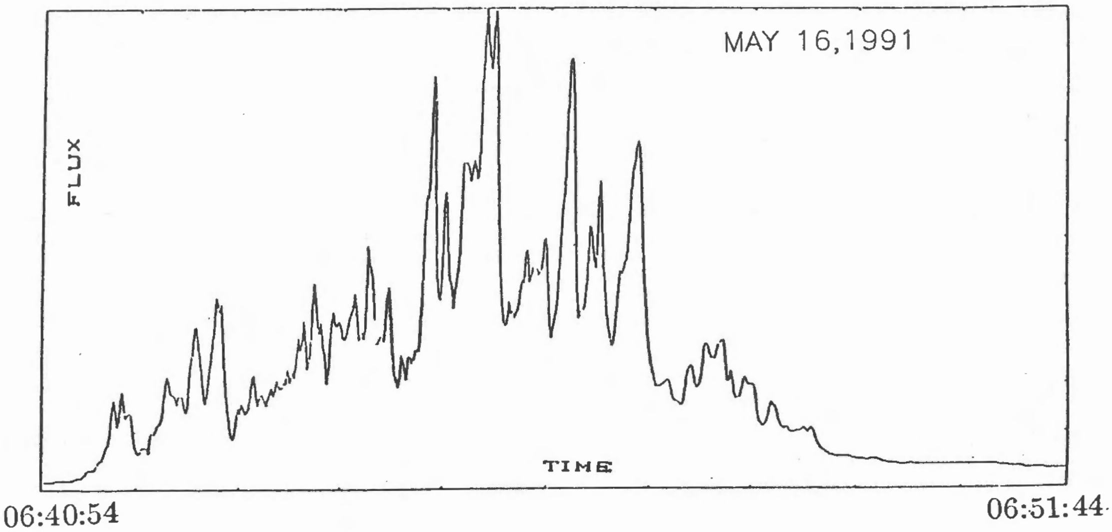

Fig. 1. The solar radio burst curve of Beijing Observatory at 2.84 GHz on May 16, 1991.

II. The Data Processing.

1. Smoothed averaging of data (or low filter).

In order to analyse data with different time constants, they must be returned to ones with a common time constant. So the data with time constant of 1ms were averaged and smoothed per 1000 points,

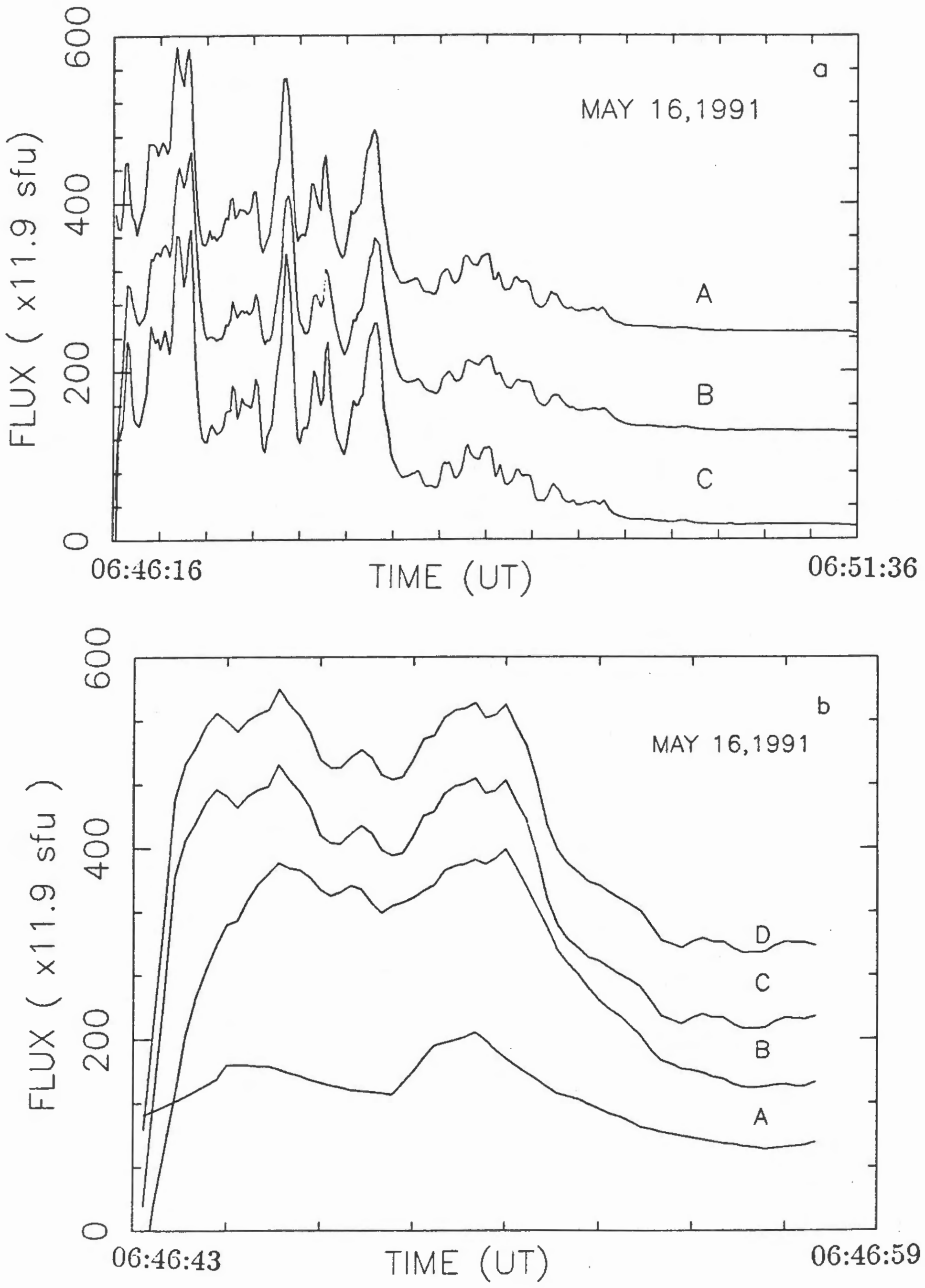

Fig. 2. The solar s-resolution records on May 16,1991 at 2.84 GHz obtained with different methods.

A: digital s-resolution record
B: RC filter of τ =10ms data
C: smoothed averaging of τ =10ms data
D: smoothed averaging of τ =1ms data

and the data with time constant of 10 ms were averaged and smoothed per 100 points. This method, by which ms-resolution data are reduced to s-resolution data, is called ‘ the simplest smoothed averaging ’[2]. It is easy to understand this kind of method processing data by considering the concept of time constants of telescopes [3]. In 1988 using this method we processed the ms-resolution data on May 16,1981 [4][5], and somebody raised a query for it [6]. So we processed new ms-resolution records by the same method as above once again to examine whether the record may be reduced to s-resolution ones or not. The result of processing is shown in Figure 2.

In Figure 2 we can see that the four (or three) s-resolution curves from observational data processed by the different methods are alike. We also compared these curves with analogue s-resolution record curves and found that they are essentially in agreement, and there is no difference in order of magnitudes. It means that the observational data with different time constants from the new receiver at 2.84 GHz are self-consistent.

2. The band-pass filter of data.

It is known that solar rapid fluctuation phenomena and s-resolution radio bursts possess different physical mechanisms; so observational record curves ought to show us that ms-resolution rapid fluctuation is superposed on the background of second-resolution solar radio bursts. Making the high-pass filter of solar ms-resolution observational data, i.e. low frequency signals were filtered out, or the signals of the s-resolution (or sub-s-resolution) background of solar bursts were deducted from the data, the rest of signals is belong to solar rapid fluctuation phenomena and noises. So we have a relation as follows:

$$\text{the original ms-resolution record}=A+B+C+D,$$

(see Figure 3.)

From the analytic result we found there is sub-second fluctuation in the data and no rapid fluctuation with the time scale lower than 100ms.

3. Comparision with the white noise

We also made a probability distribution analysis of the fluctuating flux density for A in Figure 3. The result is shown in Figure 4. From Figure 4, we see that curve A is very similar to the normal distribution curve B with r.m.s. error $\sigma = 1.8$ (i.e. the flux density is about 65 sfu).

We also made a Fourier spectrum analysis of a total of 8192 data covering 06:46:43–06:46:51 UT (see Figure 5), and found several outstanding peaks below 10 Hz in the power spectrum for $\tau = 1$ ms (curve A), indicating the existence of sub- second time scale fluctuations in the data. Furthermore, we found that a 100-1000 Hz after band-pass fliter the same dataset yield a relatively smooth power spectrum (curve B), approximating a white noise with an r.m.s. error eguivalent to a flux density of some 65 s.f.u.

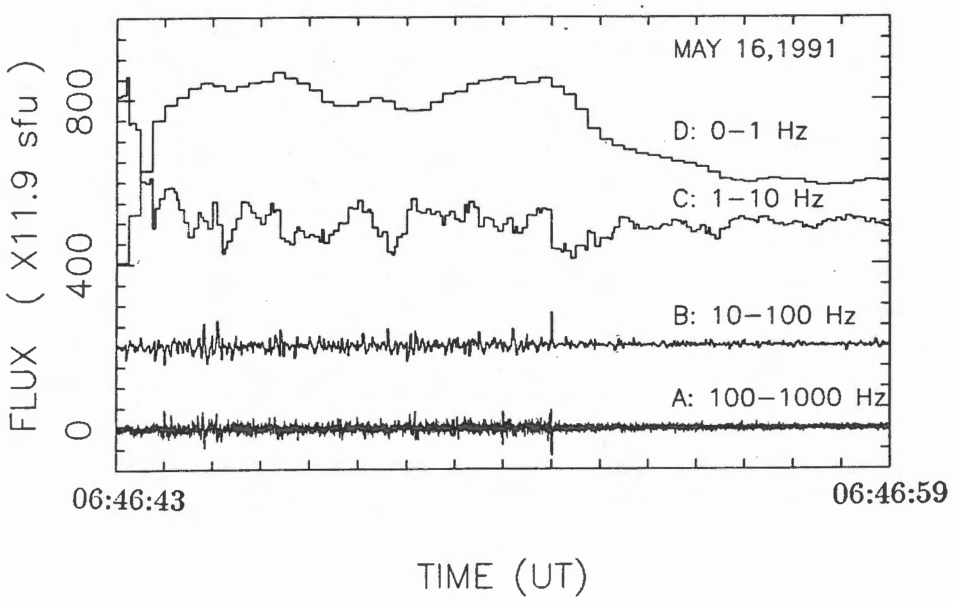

Fig. 3. The solar radio burst curves filtered with band-pass in different frequencies on May 16,1991.

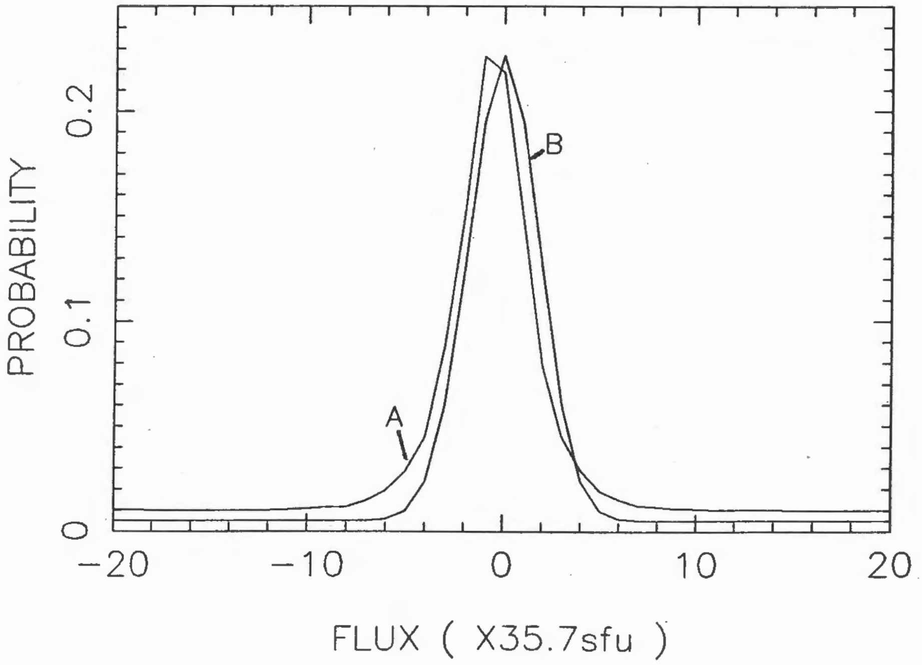

Fig. 4. The comparison between the probability distribution of various fluxes of with band-pass in 100–1000Hz on May 16,1991 (curve A) and normal distribution $P(x) = \frac{1}{\sigma\sqrt{2\pi}} \exp[-\frac{x^2}{2\sigma^2}]$ (curve B).

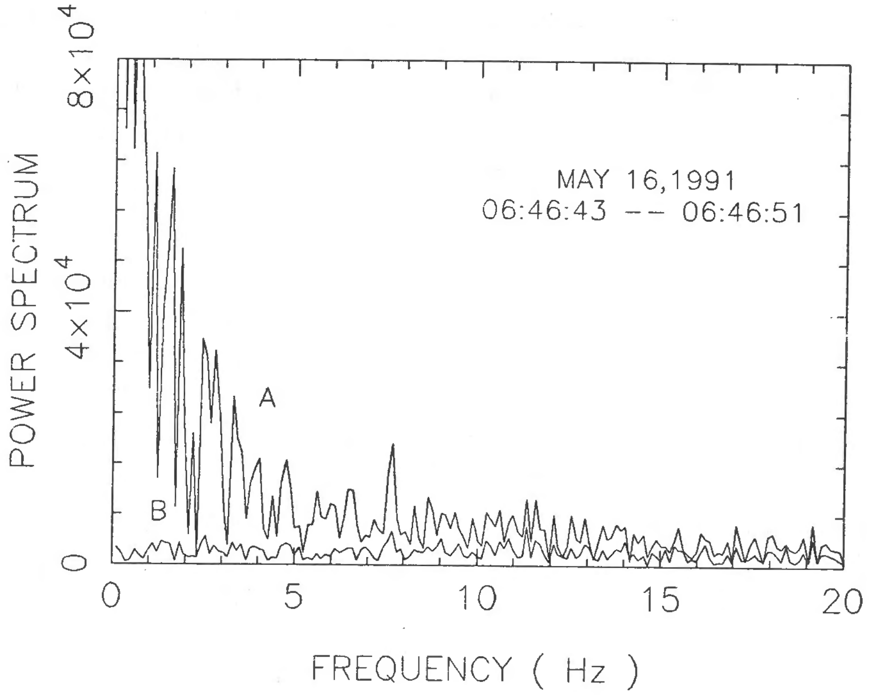

Fig. 5. Fourier spectrum curves.

III.Conclusion.

We had compared the smoothed averages of solar ms-resolution data with s-resolution data of the burst at 2.84GHz on May 16,1981 and found that the two kinds of data obtained from above equipment are not self-consistent, whether in calibration or trend of burst fluxex. But using above method , we have processed the data of May 16,1991 and found the ms-resolution record can be reduced to the s-resolution record. This fact makes clear that the data with various time constants from the receiver improved in 1990 are self-consistent.

In this paper, it is introduced that band-pass filter separates the components of rapid fluctuation with various time scales from ms-resolution data of solar bursts. Alough the components of rapid fluctuation with the time scale lower than 0.1s have not been found in data of May 16,1991; above method is very useful to examine and receive data from now on.

Reference

Liu Yuying, Chen Zhijun and Zhao Bing: CSGD February-March 1992.
Cheng Qian-sheng ‘ The mathematical principle of signal digital processing ’, Petroleum Publishing House (1979).
Zheng Le-ping and Liu Yu-ying: 1991, Acta Astronomical Sinica No.32, 56.
Zheng Le-ping and Liu Yu-ying: 1988, Acta Astronomical Sinica No.29, 175.
Zheng Le-ping and Liu Yu-ying: 1990, Solar Phys. 129,127.
Jin S-Z, Zhao R-y and Fu Q-j: 1989, Acta Astronomical Sinica No.30,70.
Ding Yue-rong and Zheng Da-wei ‘ The handling method of Astronomical measurement data’, 1990, Nanjing University Press.

Diagnostics of non-thermal processes in chromospheric flares: I. Hα and CaII K line profiles of an atmosphere bombarded by hecta keV electrons

C.Fang

Department of Astronomy, Nanjing university, Nanjing, 210008, China

J.C.Hénoux

Observatoire de Paris, DASOP-URA326 (CNRS), 92195 Meudon, France

W.Q.Gan

Purple Mountain Observatory, Academia Sinica, Nanjing, China

Abstract

The significance of non-thermal excitation and ionization of hydrogen and ionized calcium, by an electron beam, on the line profiles of Hα and CaII K lines has been investigated. Non-LTE Hα and CaII K line profiles have been calculated for the temperature distributions of semi-empirical flares models F_1 and F_2 (Machado et al. 1980). For reasonable values of the beam energy flux and power index, the hydrogen lines are greatly strengthened and broadened, and an obvious central reversal appears. The effects are weaker for the CaII K line. These effects can be used to diagnose electron beam bombardment during a solar flare, especially at its early phase. Any semi-empirical flare model that does not take into account non-thermal effects will overestimate the heating of the solar atmosphere.

Diagnostics of non-thermal processes in chromospheric flares: II. Hα and CaII K line profiles of an atmosphere bombarded by hecta keV protons

J.C.Hénoux

Observatoire de Paris, DASOP-URA326 (CNRS), 92195 Meudon, France

C.Fang

Department of Astronomy, Nanjing university, Nanjing, 210008, China

W.Q.Gan

Purple Mountain Observatory, Academia Sinica, Nanjing, China

Abstract

The effects on the Hα and CaII K line profiles of non-thermal excitation and ionization of hydrogen and ionized calcium by a hecta keV proton beam have been investigated. Non-LTE Hα and CaII K line profiles have been calculated for the temperature distributions of semi-empirical flares models F_1 and F_2 (Machado et al. 1980). For reasonable values of the beam energy flux and power index, the hydrogen lines are greatly strengthened. However, contrary to the case of an electron bombarded atmosphere, the lines are not broadened, and no central reversal appears. These effects, alone or in conjunction with linear polarization measurements or Lyα red wing observations, can be used to diagnose proton beam bombardment.

Stability of Lundquist Field and Prominence Exposing Helical-Like Patterns

Xu Ao-ao
Department of Astronomy,Nanjing University,Nanjing,China
Wu Gui-ping
Nanjing Railway Medical Colledge,Nanjing,China
Zhang He-qi
Purple Mountain Observatory,Chinese Academy of Sciences

Abstract

The stability of Lundquist field is analysed in the light of energy principle.The results show:(1)for disturbances of $m = 0$ mode,Lundquist-field is stable; (2) for disturbances of $m = 1$ mode, Lundquist-field will turn instable on certain condition. Whether the field will keep stable or not depends on parameters as the helical pinch angle,radius and length of the prominence. Comparison between theory and observations reveals that kink-instability in Lundquist field may be a critical physical reason for eruptive prominences exposing helical-like patterns.

1. Introduction

A helical prominence gives much information on its physical characteriztics , especially its electromagnetic properties.Many authors have studied the regularity and properties of its evolution and eruption either observationally or theoretically (Vrsnak et al. 1988; Vrsnak 1988; Srivastava 1991; Xu 1992; Wu et al. 1993) .A series of important results has been obtained. Xu(1992) and Wu et al.(1993) proposed particularly that Lundquist field may be a good configuration to discribe the inner magnetic distribution of the helical prominence by analyzing both some quiescent and eruptive prominences of such kind.In this paper,we begin with discussing the stability of Lundquist field , analyze it according to energy principle and give a stable criterion. Comparing theory with observational data of 28 helical prominences, we are not only confirmed in the reliability of using Lundquist field to describe a helical prominence , but also glad to find out the physical factor leading to its eruption .

2.Analysis of stability of Lundquist field

The linear symmertrical force-free Lundquist field in the cylindrical system takes the following form:

$$B_r = 0, B_\theta = B_1 J_1(\alpha r), B_z = B_1 J_0(\alpha r), \tag{1}$$

where B_1 is the magnetic field at the axis, α is the constant force-free factor, $J_0(\alpha r)$ and $J_1(\alpha r)$ are the zero and first order Bessel functions respectively.

According to the MHD theory of stability, the energy principle with which to judge the stability of a magnetic configuration is: when $\delta w > 0$,the magnetic configuration is stable; otherwise, unstable.In the following section ,the $m = 0$ and $m \neq 0$ modes are discussed respectively. When $m = 0$, δw is determined by Xu and Tang(1987):

$$\delta\, w = \frac{\pi}{2\mu_0} \int_0^{r_0} dr[r B_z^2 (\frac{d\xi_r}{dr})^2 + (\frac{B_z^2}{r} + 2\mu_0 \frac{dP}{dr})\xi_r^2] + \frac{\pi\, k^2}{2\mu_0} \int_0^{r_0} B_z^2 \xi_r^2 r dr \tag{2}$$

Given the force-free property of Lundquist field,$dp/dr = 0$,each term in the integral function in equation(2) only takes the positive value , i.e.,$\delta w > 0$ .Thus,for $m = 0$ perturbances ,Lundquist field is stable. For $m \neq 0$ mode,it's shown that kink instability of $m = 1$ mode occurs quite easily compared with $m > 1$ mode. Therefore, we only need to discuss the instability of $m = 1$ mode .For this mode ,δw takes the form:

$$\delta\, w = \frac{\pi}{2\mu_0} \int_0^{r_0} dr\{\frac{r(krB_z + B_\varphi)^2}{k^2r^2 + 1} (\frac{d\xi_r}{dr})^2 + [\frac{(krB_z - B_\varphi)^2}{r(k^2r^2 + 1)} - \frac{2B_\varphi}{r} \frac{d}{dr}(rB\varphi) \tag{3}$$

$$-\frac{d}{dr}(\frac{k^2r^2B_z^2 - B_\varphi^2}{k^2r^2+1})]\xi_r^2\} + \frac{\pi}{2\mu_0} \int_0^{r_0} dr \frac{(krB_z+B_\varphi)^2}{r} \xi_r^2$$

For Lundquist field , given the property of Bessel function, it can be proved that:

$$\delta\, w = \frac{\pi}{2\mu_0} \int_0^{r_0} dr F(r) \xi_r^2 \tag{4}$$

$$F(r) = k^2 r[\frac{2(k^2r^2B_z^2 - B_\varphi^2) + (krB_z + B_\varphi)^2(k^2r^2 + 1)}{(k^2r^2 + 1)^2} \tag{5}$$

It can be seen that longwave disturbances stimulate kink-instability easily. For plasma cylinder of a prominence with length L, the largest disturbed wavelength is $\lambda_{max} = L$.So,there is $k_{min} = 2\pi/\lambda_{max} = 2\pi/L$.For plasma cylinder of a prominence, usually there is $2\pi r/L < 1$. So $(kr)^2_{min} \ll 1$. For long-wave disturbances , $k^2r^2 + 1 \approx 1$. As the basic characteriztics of helical prominences may be described in figure 1,the pinch angle θ can be represented in term of:

$$\tan\theta = \frac{B_\varphi}{B_z} \tag{6}$$

Substituting equation(6) into $F(r)$,we get

$$F(r) = k^2 r B_z^2 (3k^2r^2 + 2krtg\theta - tg^2\theta) \tag{7}$$

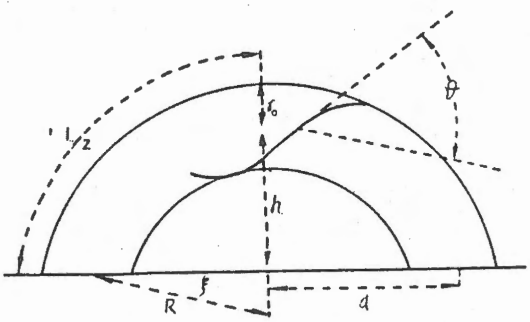

Fig.1.The Schematic of Helical Prominences

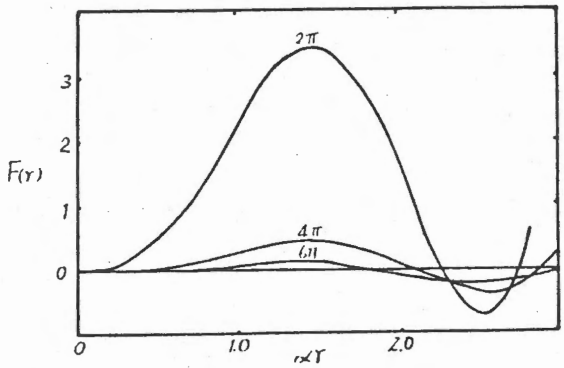

Fig.2.The Curve of F(r)

By looking into the property of $F(r)$, we can tell whether δw is positive or negative With αr as the varible. αL as a parameter. $F(r)$ curve is obtained (figure 2) , where αr_c expresses the value at the point where the curve intersects across the x- axis, i. e. $F(r_c) = 0$.The features of Bessel function imply more than one zero point, among which, the one with the smallest r_c (the first non-zero point intersecting across x-axis) is the most interesting to us. In the following discussion,r_c stands for the smallest value of r_c.When $r < r_c$,$F(r) > 0$; When $r > r_c$,positivity of $F(r)$ cannot be determined.Therefore,if the radius of a prominence $r_0 < r_c$,the integral function of equation (4) is always positive, i. e. $\delta w > 0$ and the prominence is stable. If $r_0 > r_c$, $F(r)$ can be either positive or negative and δw is possibly negative.In this case,the instability may occur and the prominence may take on an eruptive state. Other properties of $F(r)$ illustrated on figure 2 are also noteworthy: (1) r_c increases as αL decreases;(2)when αL is relatively small, the integral function contributes to the sum more positively than otherwise. So,for $\alpha L < 6\pi$, there must be $\delta w > 0$;while for $\alpha L > 6\pi$.there appears a different case,in which positivity or negtivity of δw will be determined by r_0.

3.Comparison with observational data

To make the comparison, we chart an $\alpha L - \alpha r_c$ curve from figure 2(figure 3) . Aaccording to the property of $F(r)$seen from figure 2,the $\alpha L - \alpha r_c$ plane may be devided into two large regions(see figure 3(a)) : in the shaddowed region Lundquist field is stable;and in the right-up region ,unstable . Vrsnak et al(1991) give basic observed data of 28 helical prominences (15 quiescent ones and 13 eruptive ones)and their typical parameters including z,r_0/d (confused to R in original table) and θ,where $z = h/d$.The physical meaning of h,d is seen in figure 1, from which ,it can be deduced that:

$$L = R(\pi \pm 2\zeta) = d(\frac{1+z^2}{2z})[\pi \pm 2\cos^{-1}\frac{2z}{1+z^2}] \tag{8}$$

thus,

$$\alpha L = \frac{\alpha r_0}{r_0/d}(\frac{1+z^2}{2z})[\pi \pm 2\cos^{-1}\frac{2z}{1+z^2}] \tag{9}$$

With the value of θ in table 2 (Vrsnak et al 1991) and $tg\theta = J_1(\alpha r)/J_0(\alpha r)$,$\alpha r_0$ may be calculated. Therefore,using equation(8)and the data in table 2, one can work out αL of the prominence.It should be pointed out that Vrsnak et al. classified 13 eruptive prominences into 3-types: the ones of the first are just beginning to erupt (ON) ; those of the second are undergoing fierce eruption(E) ; and the rest are on a stage of post acceleration of eruptive prominence(PE).Furthermore ,groups of observed data are available,including z, r_0/d and θ on different moments,and we have got up to 49 groups for all the 28 prominences. As an example, there are at hand 10 groups of data for the prominence on August 18, 1980. This facillitates our comparison of the theory with observations.

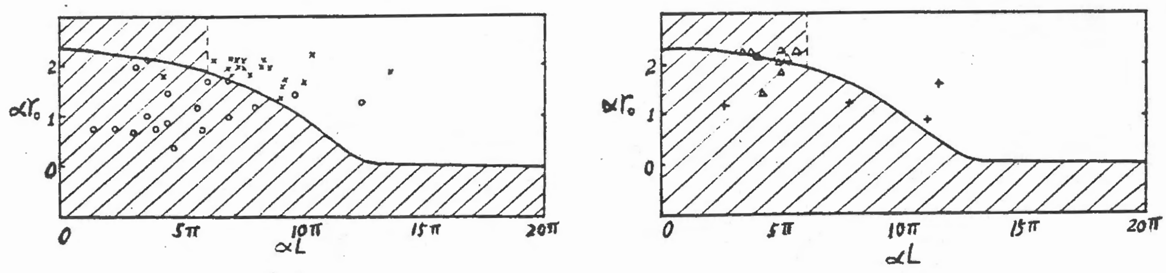

(a) (b)

Fig.3.The Comparison between Theory and Observations

According to different groups of αL and αr_0, the quiescent prominences can be located in $\alpha L - \alpha r$ plane.Figure 3(a)shows that,except for two points,the other 1 6 observed points fall into the stable region. One of the exceptional points stands very near the $\alpha L - \alpha r_c$ curve with another point (No. 15,on March 15,197 7, on the following moment) belonging to the same prominence located in the stable region. Thus, the prominence on March 15, 1977 may be considered as a quiescent one approching to a stable state in $\alpha L - \alpha r$ plane. In another word, the prominence on October 2, 1970 is the only exception. In the same way, 18 groups of data of eruptive prominences find their positions in unstable region in $\alpha L - \alpha r$ plane, seen from figure 3(a) .The results provide reliable evidence that kink-instability of Lundquist field induces prominence into eruptive phase.

For further comparison, we have plotted another two types of eruptive prominences (ON, PE) in $\alpha L - \alpha r$ plane(figure 3(b)).The result shows that their properties are not as apparent as those of the two types just discussed. We'd rather ascribe it to observational limitations.As for some prominences defined at the onset of eruptive phase, for lack of observable data of their relative progressing, it is difficult to tell to what extent the data concide with theory. For those on post acceleration phase, as a result of magnetic energy- releasing by kink-instsability, the inner Lundquist field relaxes from instability to stability. So, generally speaking, they should fall in stable region; while in the case of the prominences far away from the end of eruptive phase, Lundquist field stays on unstable state with the corresponding points located in unstable region in $\alpha L - \alpha r$ plane. To sum up , in spite of observational limitations, we are still sure that theory is not contradictory with observations.

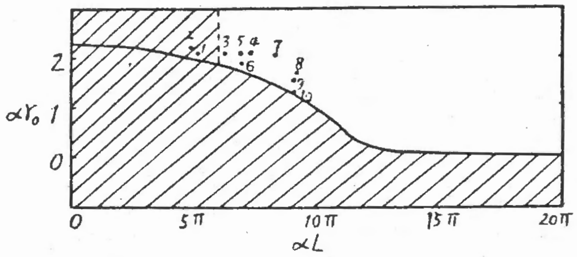

Fig.4. The Evolution of the Eruptive Prominence on August 18, 1980

Figure 4 shows that the parameters of Lundquist field in the eruptive prominence on August 18,1980 vary with time in $\alpha L - \alpha r$ plane.The whole process is seen clearly that the prominence began at stable state(point 1-2) , then went instable (eruptive points from 3 to 9) and returned to stable state in the end (point 10).This provides an eloquent argument that Lundquist field induced the prominence into erupting.

Through the comparison between theory and observations given by figure 3 and figure 4, it is fully proved that whether a helical prominence will keep quiescent or turn eruptive depends chiefly upon the existence of stability in Lundquist field.

4.Conclusion and Discussion

Through the analysis of instability of Lundquist Field and the comparison between theory and high qualitive observational data of helical prominences ,it is shown that:

(1) Inside the prominences, at least those exposing helical patterns, Lundquist field is the basic configuration;

(2) Lundquist field is stable for $m = 0$ mode.On some conditions,the long-wave disturbances of $m = 1$ mode may induce kink-instability to occur in helical prominences, which makes an important physical reason for eruptions;

(3) The pinch angle θ, radius r_0 and length L of the prominence are the basic parameters to determine whether the helical prominence will take on stable state or not.

References

Srivastava.N. et al.*Solar Phys.*,**133**(1991),339

Vrsnak.B.,Ruzdjak.V.,Brajsa,B.and Dzubur,A.,*Solar Phys.*,**116**(1988), 45

Vrsnak.B.,*Solar Phys.*,**127**(1990),129

Vrsnak,B.,Ruzdjak.V.and Rompolt,B.,*Solar Phys.*,**136**(1991),151

Wu Gui- ping.Yin Zhao and Xu Ao-ao.*Chinese Journal of Astronomy*,**34**(1993)

Xu Ao-ao and Tang Yu-hua." *Introduction of Cosmic Electrodynamics*",(1987) Chap.7,Higher College Publishing House

Xu Ao-ao.*Chinese Journal of Space Science*,**12**(1992),1

Development of the Fast Reconnection Mechanism in a Sheared Field

M. Ugai

Department of Computer Science, Faculty of Engineering
Ehime University, Matsuyama 790, Japan

Abstract

The development of the fast reconnection mechanism is studied in a sheared field geometry. Initially, there are antiparallel fields (of component B_{x0}) as well as a uniform sheared field component (B_{z0}). On the basis of the spontaneous fast reconnection model, the fast reconnection mechanism, initiated by a small disturbance, can fully be established. It is demonstrated that the thin (shock) transition layer standing in the quasisteady fast reconnection region is divided into the intermediate wave region, where magnetic field simply rotates without changing its magnitude, and the slow shock region, where a slow shock is coupled to an intermediate wave. In order to examine the detailed shock structure, one-dimensional MHD simulations with high numerical resolution study the temporal dynamics of MHD shocks that are placed in a noncoplanar situation. It is shown that for any case the noncoplanar shock structure can be sustained by physical dissipations involved. The resulting noncoplanar slow shock structure is, both qualitatively and quantitatively, in good agreement with the two-dimensional shock transition layer associated with the sheared fast reconnection mechanism. The reconnection (flux transfer) rate is estimated to scale as $E_0/[1+\tan^2(\Omega/2)]$, where $\Omega=2\tan^{-1}(B_{z0}/B_{x0})$ and E_0 is the reconnection rate for the coplanar case ($B_{z0}=0$).

1. Introduction

Magnetic reconnection may play an important role in a variety of space plasma phenomena, such as solar flares and geomagnetic substorms. In actual applications to solar flares where magnetic Reynolds number is extremely large, the so-called fast reconnection mechanism should be most effective. The fast reconnection mechanism may be characterized by standing slow shocks attached to a localized (small) diffusion region, since in the presence of slow shocks most part of stored magnetic energy can be effectively released by the large-scale motor effect. The analytical treatments argued that the fundamental structure of the fast reconnection mechanism was determined by external boundary conditions without need of any special form of internal finite electrical resistivity (Petschek, 1964; Forbes and Priest, 1987). On the contrary, we have proposed that the self-consistent interaction between localized microscopic plasma (anomalous) resistivities and macroscopic reconnection flows should be fundamental for this problem (Ugai and Tsuda, 1977; Ugai, 1984); in fact, it was recently demonstrated that the fast reconnection mechanism strongly depends on the resistivity model (Ugai, 1992). According to this idea, the fast reconnection mechanism should spontaneously build up and be set up without any direct influence of specified boundary conditions. This reconnection mechanism may hence be called "the spontaneous fast reconnection model".

Most of the previous studies on the fast reconnection mechanism have been directed to coplanar situations. In understanding the complicated plasma processes involved, it may be fundamental to clarify the basic structures of fast reconnection mechanism in realistic noncoplanar plasma situations. Hence, on the basis of the spontaneous fast reconnection model, we systematically study the fast reconnection structure in a sheared field geometry by 2.5 dimensional MHD simulations (for details, see Ugai, 1993). The associated three-dimensional skewed field line structure are examined in detail, and the noncoplanar shock structure associated with the sheared fast reconnection mechanism are examined. In particular, we are interested in how magnetic reconnection proceeds even without any magnetic neutral (zero) point. Also, note that in the sheared field geometry magnetic field should rotate across the shock transition layer, so that the Rankine-Hugoniot jump relations cannot be satisfied in such a noncoplanar situation. Hence, a question is how the noncoplanar shock-like transition layer can stand quasisteadily? In order to examine this question, we further perform one-dimensional dissipative MHD simulations with high numerical resolution. In what follows, computer simulations systematically study the above fundamental questions.

2. Simulation model and results

We first perform 2.5 dimensional simulations. The phenomenon to be studied is 2.5 dimensional in the sense that variables depend on x and y but not on z, whereas both the flow velocity **u** and the magnetic field **B** may have z components. As an initial configuration, a current sheet system with antiparallel field components (B_x) as well as a uniform sheared field component (B_{z0}) is assumed. As an initial disturbance, a small electrical resistivity is imposed in a local region near the origin in the initial time range $0<t<4$. Initiated by this disturbance, all the phenomena will develop from near the local region and extend outward on Alfven time scales. The reconnection process is strongly influenced by the resistivity model (Ugai, 1992), so that in the present study, an anomalous resistivity is assumed to increase with the relative electron-ion drift velocity when a threshold value is exceeded. The resistivity model is imposed for time $t>4$ after the initial disturbance is removed.

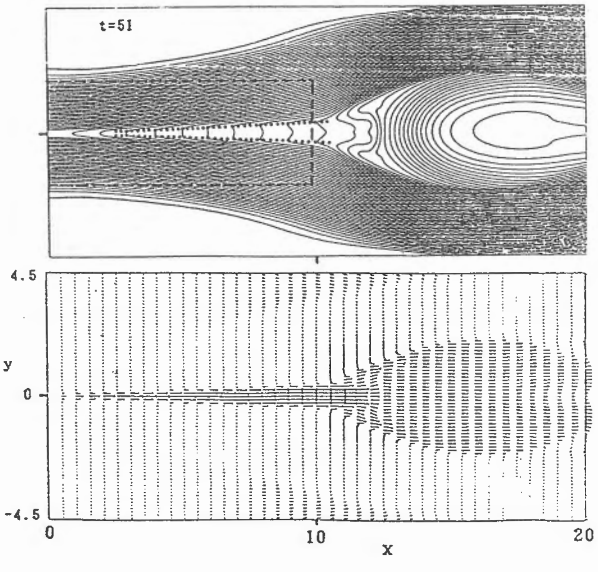

Fig. 1. Magnetic field and plasma flow configurations [projected onto the (x, y) plane], associated with the sheared fast reconnection mechanism for the case of $B_{z0}=0.25$, where a pair of quasisteady shock transition layers are shown by dotted lines.

We find that the fast reconnection mechanism can fully be established with the anomalous resistivity model. It is found that even in the noncoplanar situation a pair of thin shock-like transition layers could eventually be set up quasisteadily. Figure 1 typically illustrates the resulting magnetic field and plasma flow configurations (projected onto the (x, y)-plane) for the case of $B_{z0}=0.25$. We can readily see from this figure that the field lines in fact change topologically because of the reconnection process. As in the well-known coplanar situation, a pair of thin shock transition layers (denoted by dotted lines in Fig. 1) extend outward almost straightly from near the diffusion region and stand quasisteadily in the resulting fast reconnection configuration. Figure 2 also shows the changes in quantities across the transition layer shown in Fig. 1 and indicates that the transition layer can be divided into the intermediate wave region and the slow shock region; in the intermediate wave region, magnetic field simply rotates without changing its magnitude, whereas in the slow shock region a slow shock is combined with an intermediate wave. In Fig. 2, the intermediate wave region is located in $y_s<y<y_w$ and the slow shock region in $y_b<y<y_s$ (the propagation direction of the shock transition layer may be considered to be approximately the positive y direction in Fig. 1).

In order to examine the (noncoplanar) shock structure in more detail, we perform one-dimensional MHD simulations where all the variables depend only on x, but both the flow velocity **u** and the magnetic field **B** may have x, y, and z components. The simulation model is based on coplanar shock solutions which should be obtained from dissipative MHD equations. Here, every (coplanar) shock under consideration, which has only the x and y components of magnetic field, is treated in the shock frame and is designed so as to be located steadily in the middle of the computational region. At time t=0, the left, or upstream, state and the right, or downstream, state of the shock are given on the basis of the Rankine-Hugoniot jump relations in the so-called deHoffman-Tellar frame. Then, dissipative MHD equations are solved numerically with the free boundary conditions on the left and right boundaries, and we find that by the time t=40 the system relaxes to a steady shock profile that connects the initial left and right states according to the physical dissipations assumed. Note that by this time (t=40) the system has been coplanar ($B_z=u_z=0$ everywhere), and all the simulation runs will start from this situation.

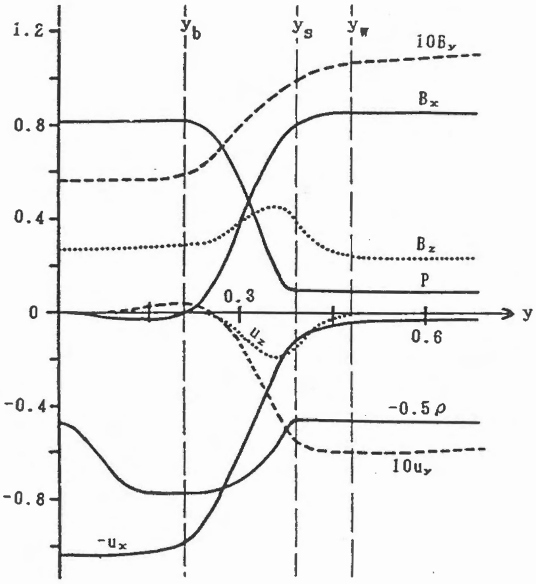

Fig. 2. Changes in quantities along the y direction at x=7.5 across the shock transition layer shown in Fig. 1, which is divided into two regions, $y_w>y>y_s$ and $y_s>y>y_b$.

In order to examine the shock behavior in a noncoplanar situation, we suddenly impose a uniform sheared field component $B_z=B_{z0}$ on the coplanar system at time t=40. Such a uniform sheared field gives rise to no effective force at any spatial point, but it effectively specifies definite noncoplanar boundary conditions ahead of and behind a shock. In a noncoplanar situation, the Rankine-Hugoniot relations can no longer be satisfied, and the shock profile should gradually change with time. Note that this simulation model is designed by considering the basic plasma situations in which the noncoplanar transition layers (Fig. 1) have been caused by the establishment of the fast reconnection mechanism in the sheared field geometry. Here, we examine the question with respect to the noncoplanar shock transition layers (Figs. 1 and 2) associated with the sheared fast reconnection mechanism. It is well known that in a coplanar fast reconnection structure, the thin transition layer should be identified with a switch-off shock (Ugai, 1992), so that we examine the case of switch-off shock in the present study.

In order to apply the present results to the noncoplanar shock transition layer (Fig. 2), we may choose the relevant case of η =0.002, which is found to be consistent with the physical (anomalous) resistivity involved in the transition layer shown in Fig. 2. Also, the plasma quantities ahead of the shock have been chosen so as to be consistent with Fig. 2 (except for the difference of the coordinate system). Figure 3 shows the resulting

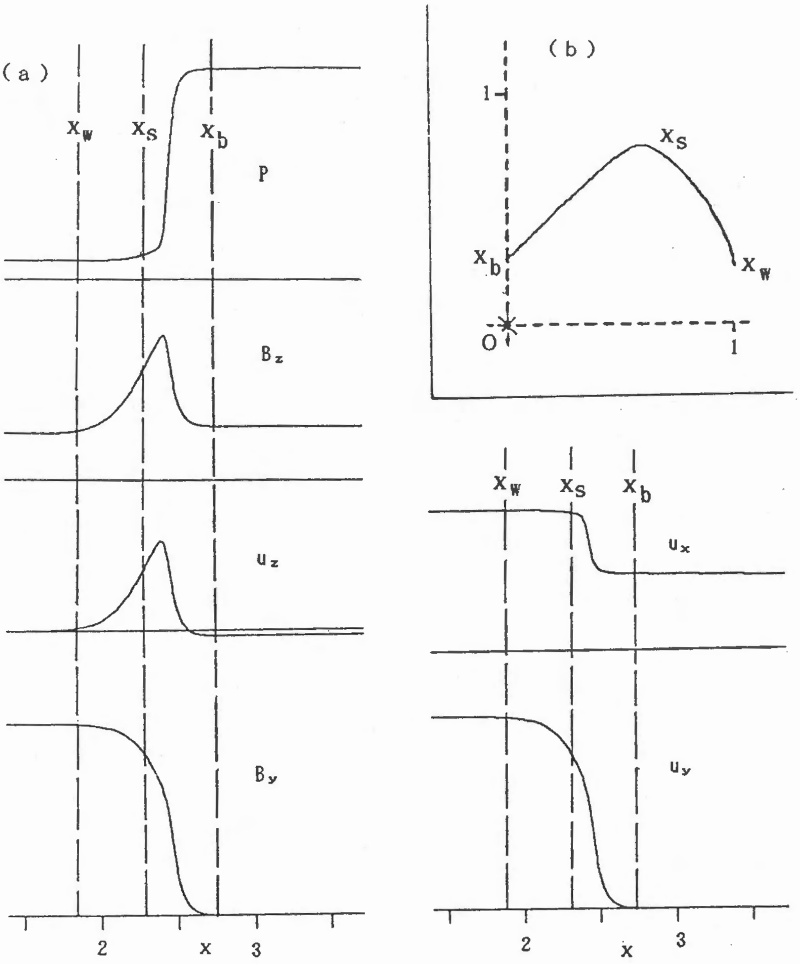

Fig. 3. (a) Profiles of quantities at time t=56 and (b) the corresponding magnetic hodograms, for the noncoplanar slow shock with B_{z0}=0.25 and η = 0.002.

noncoplanar shock structure at time t=56, which may be divided into the intermediate wave region $x_w<x<x_s$ and the noncoplanar slow shock region $x_s<x<x_b$ in the manner similar to Fig. 2 (note that in the present case the shock propagates in the negative x direction, whereas the shock transition layer in Fig. 1 propagates approximately in the positive y direction). Also, in Fig. 3(b) the corresponding magnetic hodogram is shown, in which the points corresponding to x_b, x_s, and x_w are indicated on the trajectory. Apparently, the noncoplanar shock layer (Fig. 3) is, both qualitatively and quantitatively, in good agreement with Fig. 2; in particular, in the noncoplanar slow shock region ($x_s<x<x_b$) a slow shock is combined with an intermediate wave, since magnetic field magnitude (plasma pressure) decreases (increases) [the length Ox_b is smaller than Ox_s in Fig. 7(b)], and at the same time the magnetic field notably rotates in the intermediate wave region ($x_w<x<x_s$) without changing its magnitude [$Ox_w=Ox_s$ in Fig. 7(b)]. The present numerical results may hence indicate that the 2.5 dimensional reconnection simulations by Ugai (1993) provide quite precise numerical results even in the thin shock layer.

3. Summary and Discussion

The present simulations have systematically studied the precise structure of the fast reconnection mechanism in a sheared field geometry (Ugai, 1993). In order to examine the resulting shock structure, the temporal dynamics of noncoplanar shock is further examined in the framework of one-dimensional dissipative MHD equations. This simulation model is based on coplanar shocks, on which a uniform sheared field component B_{z0} is imposed. Note that this model effectively specifies definite noncoplanar boundary conditions ahead of and behind a shock, since the magnetic field directions ahead of and behind a shock are readily specified. We then find that the noncoplanar shock structure can be sustained by physical dissipations involved, until the shock becomes coplanar as a result of magnetic field rotation in the wave plane.

The two-dimensional noncoplanar shock transition layer (Figs. 1 and 2), associated with the sheared fast reconnection mechanism, has a sufficiently long and thin structure that may be considered to be approximately one-dimensional. In fact, the present one-dimensional MHD simulations with much higher numerical resolution have obtained the noncoplanar shock structure (Fig. 3) that is, both quantitatively and qualitatively, in good agreement with Fig. 2. Since the one-dimensional noncoplanar shock structure can be sustained only in a finite time by physical dissipations involved, two-dimensional plasma processes should be important for the shock transition layer to stand quasisteadily in the (sheared) fast reconnection configuration (Fig. 1). For the fast reconnection flow, the ambient sheared magnetic field is continuously convected with the plasma inflow (Fig. 1) and is largely skewed when it enters the shock layer. In this respect, note that in the two-dimensional situation the resulting intermediate waves may propagate away from near the diffusion region along the shock layer. We may hence recognize that the noncoplanar shock transition layer (Fig. 1) could be sustained quasisteadily in a region not so far from the diffusion region, since the resulting intermediate waves may propagate away along the layer before the field rotation is not completed in the transition layer.

Acknowledgement

The author thanks T. Shimizu and M. Funama for preparing the numerical data. This work was partially supported by Grant-in-Aid from the Ministry of Education in Japan.

References

T. G. Forbes and E. R. Priest, Rev. Geophys. **25**, 1583 (1987).
H. E. Petschek, NASA Spec. Publ. 50, p. 425 (1964)
M. Ugai and T. Tsuda, J. Plasma Phys. **17**, 337 (1977)
M. Ugai, Plasma Phys. Controlled Fusion **26**, 1549 (1984).
M. Ugai, Phys. Fluids B **4**, 2953 (1992).
M. Ugai, Phys. Fluids B **5**, 3021 (1993).

CONSTRUCTIONAL DESIGN OF THE NINE CHANNEL LYOT FILTER

Li Ting, Chu Yingyi, Zhu liqing, Lu Haitian

Nanjing Astronomical Instrument Reasearch Centre, Academia Sinica

Key words: Nine channel Lyot filter, constructional design.

ABSTRACT

Nine channel Lyot filter (9-channel filter), as the key part of the Solar Multichannel Telescope (SMCT), is being finally adjusted in Huairou Solar Station of Beijing Observatory.

This filter was designed for observing the local region of the sun on nine different wavelengths in real-time. The filter, which comsists of about 1,500 pcs. of optical elements and weighs near 300kg, is the biggest and most complicated one in the world.

This paper describes the mechanical and electronic design of the 9-channel filter.

INTRODUCTION

The optical design of 9-channel filter was made by Ai Guoxiang and Hu Yuefeng of Beijing Observatory in 1986. In consideration of very long optical path, this filter has to be divided into two parts: The first (head) and second (body) part placed in convergent and colliamating beam respectively.

We made the mechanical and electronical design for the 9-channel filter with the following special features:

1. There are numerous optical elements to be used, so the filter is extraditional big and heavy, the oil-sealing and thermostatic control are rather difficult.
2. There are 52 pcs. of rotatable achromatic 1/2 waveplates used for tuning the passbands. It needs rather complicated driving mechanism and computer control.
3. Both 1st and 2nd parts of the filter should be remounted easily on their correct positions with accurate repeatability.

1. MECHANICS

Fig.1 shows the arrangement of the 9-channel filter inside the steel case of 60cm Gregorian tube of SMCT.

In the front of the filter head there is a small part composed of an infra-blocking filter, a 5-waveplates wheel driven by a step-motor and an achromatic KD*P cell, which is oil-sealed for high transmission and protection of the water-dissoluble KD*P material.

Nearly all optical elements of the head and body parts of the filter are enclosed in corresponding cuboidal oil-sealing chamber sorounded by four heating plates for thermostatic control. Outside the heating plates, step-motor boxes are placed for rotating the 1/2 waveplate through oil-sealing shaft and a slit wheel inside the box for giving a zero-point signal, which is given by a photoelectric sensor. In the body of the filter, 43 sets of step-motor boxes are surounded by another four heating plates, which take the role of primary thermostat.

There are five collimators in the front of the body part of the filter, just behind which there are nine interference filetrs for isolating the working wavelengths.

The working temperature (42°C) of the body part is monitored by a L-shape mercury-in-glass thermometer read by a small telescope in the end of 60cm tube.

By use of positioning wedge and backing support, the filter head and body can be remounted on their correct position respectively. The backing support also prevents the very heavy body part to strike on the followed optical elements (Fig.2).

2. THERMOSTATIC CONTROL

The thermostatic electronics are composed of: Heating coil and temperature measuring bridge around the heating plates; Control circuits and power supply in a separate controller.

The temperature is measured by a DC Wheastone Bridge, of which two fixed arms are made of G $-M_n$ wire with very small temperature coefficient, other two are of copper wire. Temperatue relays contacted with a heating plate are used for overheating warning and restricting the temperature to be less than 45°C. A 10-ring potentiometer on the filter cover is used for tuning temperature.

The control circuits in the controller case were designed for: Temperature autobalancing, quickly heating, overheating warning and protecting etc.

During one year trial operation, the temperature stability is about 0.01°C in the days not very cold.

3. COMPUTER CONTROL SYSTEM

A computer system (Fig.1) was developed for controlling eighty step-motors used for four tunable Lyot filters of SMCT.

The host computer is equipped with a programmable parallel data card (8255), of which the ports A, B, C are used for data, adress and communication respectively. For controlling the waveplates, we use 80 sets of slave computer subsystems, each one consists of a MCS-48 monolith computer and a step-motor driving unit (Fig.3).

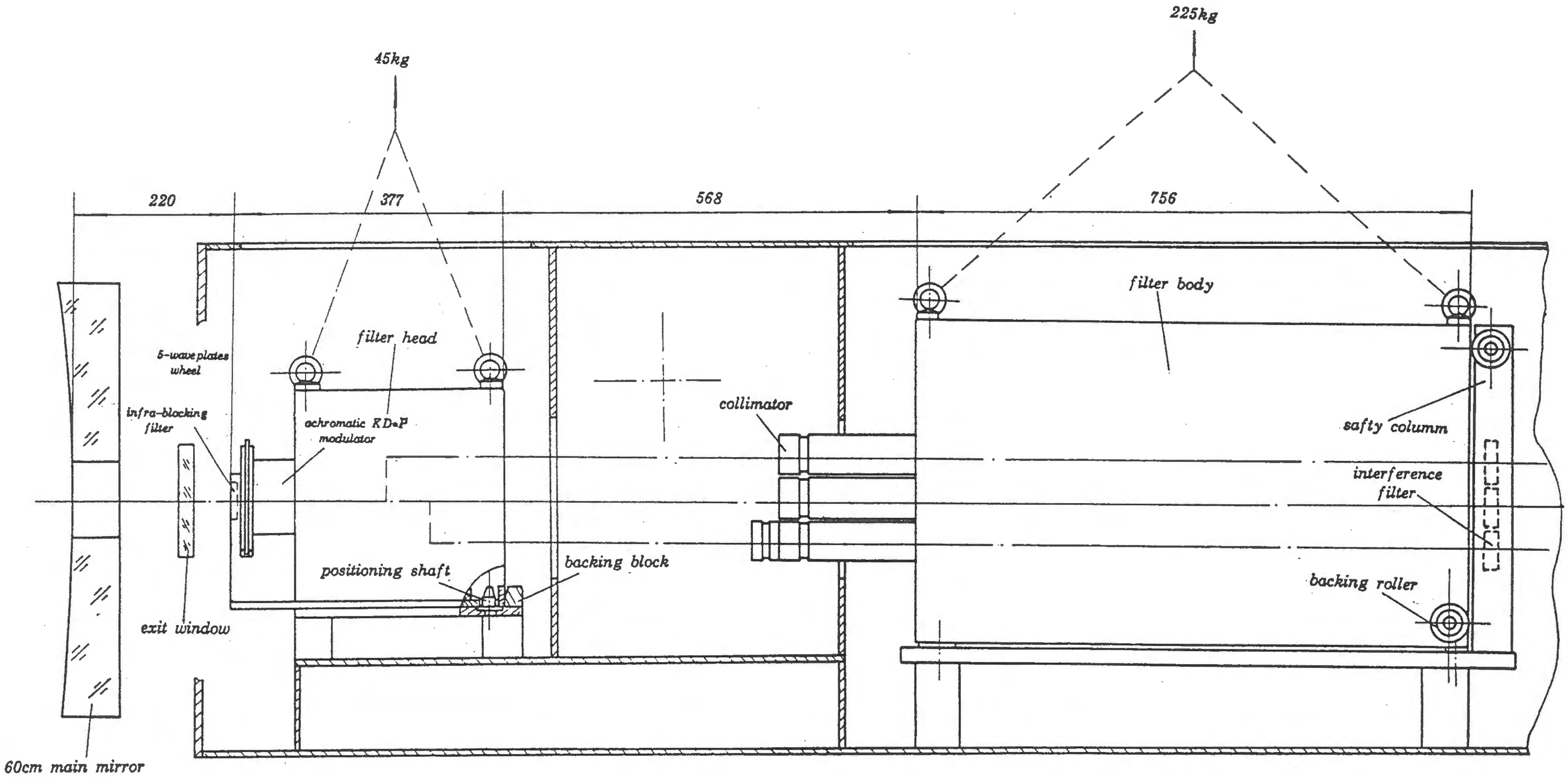

Fig.1. Arrangement of the nine-channel Lyot filter in 60cm Gregorian tube

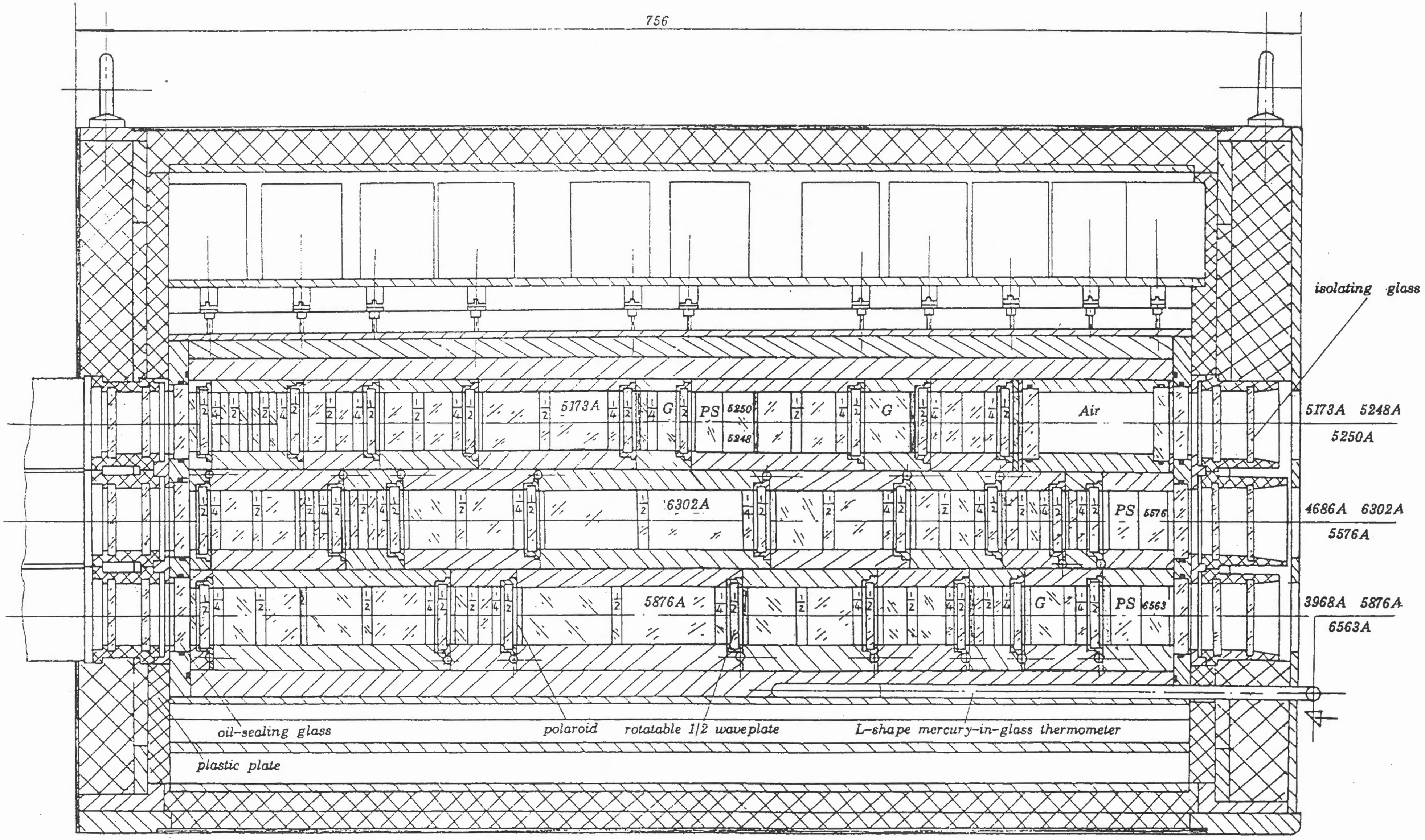

Fig.2. Vertical section of the filter body

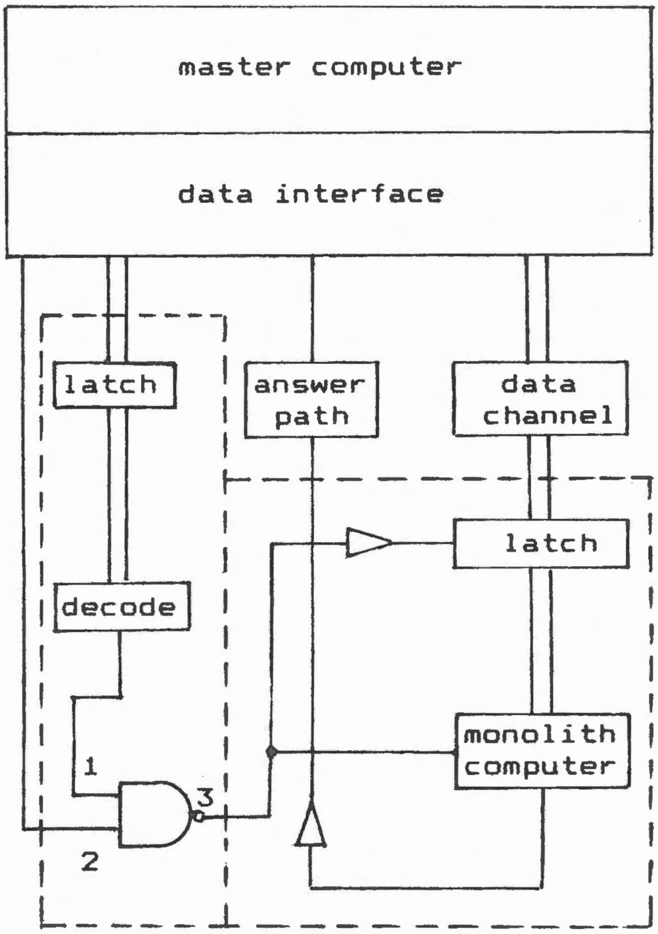

Fig.3. Block diagram of control system

Between the host and slave computers there is a set of interface circuit which consists of photoelectrical coupling isolation, channel number display, data path and detector network of the answering path. The data path so-called eighty-divider is composed of two-stage driving circuit. Answering path called eighty-way convertor concentrates the answering signals of eighty slave computers into a logical gate, then transmit them into the port C of the parallel data card, which informs the host computer to carry out a new operation.

The decoding network is used mainly to decode the preselective adress, which is sent by the host computer through the B port of 8255 card and selecting the corresponding slave computer. The special feature is that the decoding is done after latching, so the data are stable and reliable.

The host computer is a real-time control and command device to make parallel control for the rotating waveplates. It can not only select any one of eighty slave computers, but also send the data and commands to the selected slave computer to control the rotating waveplate (rotating direction, angular position and returning to zero-point). Another function of the host computer is to set up a big data library according to the needs of the users.

The first function of the slave computer is to communicate with the host computer and receive its commands. The second is to judge and decide the content of the commands which control the operation mode of the waveplates. The third is to run corresponding programs as step-motion, returning to zero-point etc.

Practically, the monolith slave computer is a driving system of the stepmotor (Fig.4). The zero-point of the 1/2 waveplate is decided by corresponding monolith slave computer and processed by software. An infra-photoelectric sensor with Schmidt circuit is used as a detective element with an accuracy of 0.01mm or 2 arc minutes, which is enough for tuning the passband.

The control programs of the host computer are divided into two parts: one is the observing program provided by astronomers. Another is the driving program for transmitting the commands and data from host to slave computer. The driving program is given with menu mode to be adopted by the observer. Besides, another checking program is provided for maintaining the control system.

The programs are written by assembly language. The developement of the monolith computer is done by use of a SICE emulator. Provided the microcomputer is jointed with a RS-232 standard interface, the emulator can share the resources of hadware and software, and perform the development for each monolith computer.

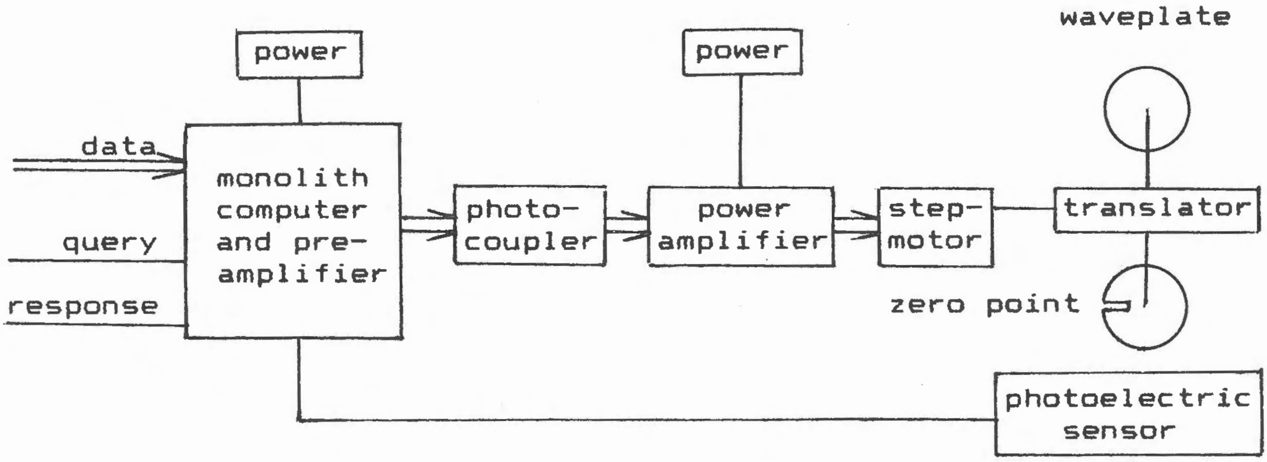

Fig.4. Block diagram of slave computer

ACKNOWLEDGEMENT

Ai Guoxiang of Beijing Observatory first suggested the idea and made the optical design for the 9-channel filter, he is also responsible to its optical assembling and adjustments. In this respect, his students Wang Jinshan and Deng Yuanyong also made excellent contributions.

In Nanjing Astronomical Instrument Factory, He Fengbao and Mao Weijung were responsible to the optical technology of a large amount of different kinds of crystal elements. A group of women opticians made the very hard works for figuring numerous crystal blocks. Li Kaishou made the coatings for the polarized prism splitters. The mechanical assembly and adjustment were made by Ni Houkung and Zhang Haiying. Zhong Wenzhi and Ding Yaofang have made very fine works in electronic assembling.

We must express our heartfelt thanks to above-mentioned colleagues for their hard works and effective collaboration.

High Resolution Image Recovery by Speckle Interference Method in Huairou's 60 cm Telescope

Yuanyong Deng, Guoxiang Ai and Bin Zhang
Beijing Astronomical Observatory, Beijing 100080

Abstract

On the basis of the speckle interference method and by a series of short exposure images (< 10 ms), high resolution granulation near the center of the solar disc has been recovered in Huairou's Multi–Channel Solar Telescope.

1. Introduction

How about is the fine structure of the Sun? This is a very important and far from solved problem in solar physics. High resolution observation data is the key to answer this question. But because of the turbulence of the atmosphere, the ground-based telescope can hardly obtain high resolution data better than 1 arcsec (especially for the fine magnetic field structure). So what we are interested in is how to remove the effect of the atmosphere in order to study the solar fine structure. There exist three ways to remove or avoid the effect of the atmosphere. The first is placing the telescope outside the atmosphere (space telescope); the second is adaptive optical technology. Although these two means are perfect and a few such systems have been achieved, many difficulties still exist under today's technical condition. The last way, an effective and relatively easy way for us, is the image restoration method.

In this paper, we will introduce the use of speckle interference method — one of the image restoration technology in Huairou's 60 cm Multi–Channel Solar Telescope. Some reconstruction images of the granulation near the center of the sun will be given.

2. Basic method of speckle interference image restoration.

Speckle interference method was introduced into astronomy by A. Labeyrie, a French astronomer, in 1970. From then on, it has been developed by many astronomers (Knox and Thompson 1974; Weigelt 1977; von der Luhe 1984; Keller and von der Luhe 1992; etc), and now it has become an important tool to study the fine structure of the Sun (von der Luhe 1984; Keller and von der Luhe 1992).

As for an image obtained by a ground-based telescope, the imaging equation is:

$$I_{(\vec{x})} = O_{(\vec{x})} * P_{(\vec{x})}$$

or in frequency domain it is:

$$\tilde{I}_{(\vec{q})} = \tilde{O}_{(\vec{q})}\tilde{P}_{(\vec{q})} \tag{1}$$

where, $\vec{x},\vec{q}$ are the 2–D space and frequency vector, I, O are the 2–D intensity distribution of the speckle sample and the object, "$\sim$" denotes the Fourier transform and "$*$" denotes convolution. $\tilde{P}$ is called the optical transfer function of the atmosphere and telescope system.

If I is recorded by long exposure as we usually do ("long exposure" means the exposure time is longer than the characteristic time scale of atmosphere turbulence), the resolution of the image will be determined by the atmosphere Fried Parameter r_0. Because the value of "r_0" is usually smaller than 10 cm in optical region for the solar observation, the resolution of the image can hardly be better than 1 arcsec. But if I is recorded by short exposure (<10 ms), high resolution information up to the diffraction limit resolution of the telescope can be retained. So it is the base of the speckle image recovery that a series of short exposure image replace the long exposure image. From these data the modulus and the phase of the object can be found separately by Korff's log-normal model of the atmosphere (Korff 1973).

(1) Modulus recovery by spectrum ratio

Start from equation (1)

$$|\tilde{O}_{(\vec{q})}|^2 = <|\tilde{I}_{i(\vec{q})}|^2> / <|\tilde{P}_{i(\vec{q})}|^2> \tag{2}$$

$$i = 1,2,\cdots,N$$

in this equation, "$|\quad|$" denotes the modulus of the function, "$<\quad>$" denotes the sequence average of the samples and "N" is the sample number. The "$<|\tilde{P}_{i(\vec{q})}|^2>$" is called the atmosphere modulation transfer function (MTF) and it can be determined only by the atmosphere Fried parameter r_0. The r_0 can be estimated by spectrum ratio method (von der Luhe 1984):

$$\varepsilon_{(\vec{q})} = |<\tilde{I}_{i(\vec{q})}>|^2 / <|\tilde{I}_{i(\vec{q})}|^2> \tag{3}$$

The log-normal model points out: the spectrum ratio drops to zero very rapidly when the frequency increases and approaches the r_0, and its value is zero when the frequency is larger than r_0 in the case of ideality. In fact we can only find a drop-off point (figure 2) in the curve of spectrum ratio because of noise. So the object modulus can be recovered as soon as the drop-off point of the spectrum ratio is found.

(2) Phase recovery by bispectrum

The bispectrum of a function is defined as:

$$\tilde{F}_{(\vec{q},\vec{p})} = \tilde{F}_{(\vec{q})}\tilde{F}_{(\vec{p})}\tilde{F}_{(-\vec{p}-\vec{q})} \tag{4}$$

Then we rewrite the imaging equation with bispectrum and average it:

$$< \tilde{I}_{i(\vec{p},\vec{q})} > = \tilde{O}_{(\vec{p},\vec{q})} < \tilde{P}_{i(\vec{p},\vec{q})} > \tag{5}$$

where, the last term of the right is called as Speckle–Masking transfer function and it can be proved to be a real function by the log-normal model. Then we will have a recursive equation:

$$\text{Phase of } \tilde{O}_{(\vec{p}+\vec{q})} = \text{phase of } \tilde{O}_{(\vec{q})} + \text{phase of } \tilde{O}_{(\vec{p})} - \text{phase of} < \tilde{I}_{i(\vec{p},\vec{q})} > \tag{6}$$

Because the object intensity distribution is real function in space domain, the phase of $\tilde{O}_{(\vec{0})}$ is zero, and so all of the phases can be found.

3. Some characteristic of the instrument

In section 2 we have mentioned that short exposure is the base of speckle image restoration. In this case the atmosphere can be "frozen" and high resolution information can be retained. So first of all, rapid exposure receiver must be needed. The CCD camera is used as the receiver and its exposure time can be changed from 0.1ms—20ms in our system.

On the other hand we have used atmosphere's log-normal model in our image recovery. In this case ergodic hypothesis must be satisfied. That is to say the number of the sample should be large enough and the time interval for sampling must be longer than the characteristic time scale of atmosphere's turbulence. The second condition can be satisfied easily because the CCD's sampling rate is 25 frames per second. For the first condition, large sample number means long sampling time. But this sampling time cannot be too long because we have assumed the object to be unchanged within this time. We choose 30 second sampling time and so 750 samples can be obtained (We do not think 30s is short enough but we have to do so by the limit of our instrument). We use TMT real-time hard disk as the storage. About 3000 MB data can be stored in it.

4. Results and discussion

In this section, some restoration examples and a brief discussion will be given. The observed object is granulation in quiet region and near the center of the Sun. The data were obtained in Huairou's 60 cm Multi–Channel Solar Telescope on June 4, 1993. The exposure time is 0.1 ms and the transmission band is 5250 ± 50 Å.

Figure 1b is a speckle sample. In this figure, you can find many fine structures even if a little distortion and blur exist. Figure 1a is the long exposure result and its resolution is obviously low. Figure 1c is also the long exposure result but before average, each image has been centered by correlation method in order to remove the image's shift caused by the atmosphere turbulence and the telescope instability. Figure 1d is the reconstruction image. We think its resolution is not worse than 0.5 arcsec (Our system can obtain about 0.25 arcsec recovery image in ideal case. But the CCD we are using causes some local fringes in the image. In order to remove them the resolution has to be lowered. We will use a better CCD in the future). The dark lanes between granules are sharper in 1d than in 1b, so we can say the resolution of the recovery image is higher than that of speckle sample. The r. m. s. of intensity fluctuation, which can be considered as the contrast of the image, has also proved this conclusion. Because the higher the resolution is, the larger the r. m. s. is. In 1b and 1d, the r. m. s. is about 10% and 14%.

Figure 3 consists of three segments and each segment is recovered separately. There is no new information, only for the effect of vision.

From these figures, we can say it is very successful to use the speckle interference method to recover high resolution image in our telescope. But it is only a good beginning. Our goal is to observed the fine magnetic structure of the Sun. We hope we can reach our end next summer.

Acknowledgments

The authors are grateful to Dr. Puzhang Qiu, Yaohui Qiou, Tongjiang Wang and Hongqi Zhang for their help and discussion in this work. They also thank NAOJ for supporting two of them to attend this workshop. Special thanks go to Professor Yangzheng Chen for his help in revising the English version. One of the authors, Yuanyong Deng, would like to thank Professor Hirayama for his encourage.

References

Keller, C. and O. von der luhe, 1992, A. A., 268, 374
Knox, K. T. and Thompson, B. J., 1974, Ap. J., 193, L45
Korff, D., 1973, J. Opt. Soc. Am., 63, 971.
Labeyrie, A., 1970, A. A., 6, 85
O. von der Luhe, 1984, J. Opt. Soc. Am. A., 1, 519
Weigelt, G., 1977, Opt. Comm., 21, 55

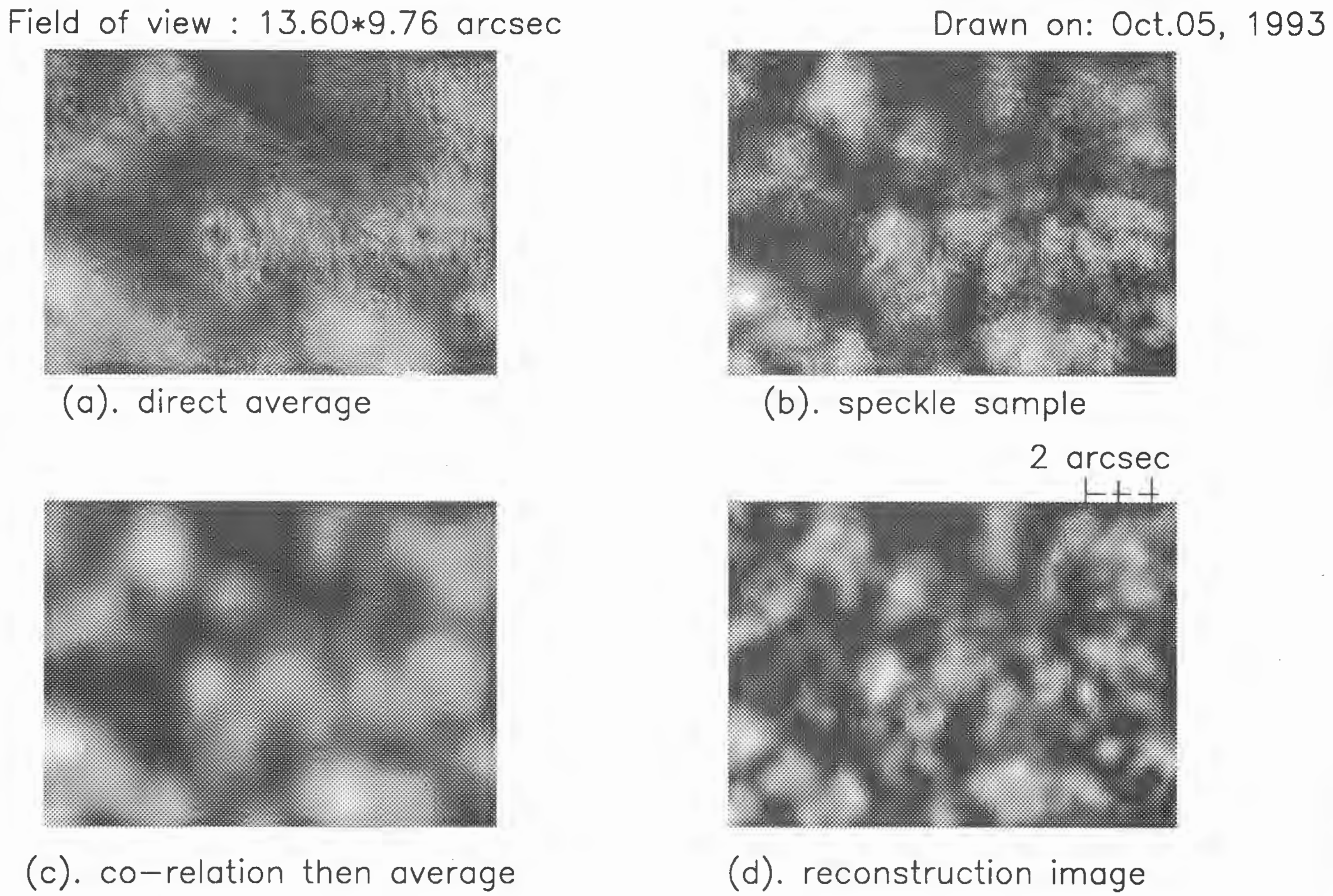

Field of view : 13.60*9.76 arcsec

Drawn on: Oct.05, 1993

(a). direct average

(b). speckle sample

(c). co-relation then average

(d). reconstruction image

Fig.1 RESULTS OF IMAGE RECOVERY

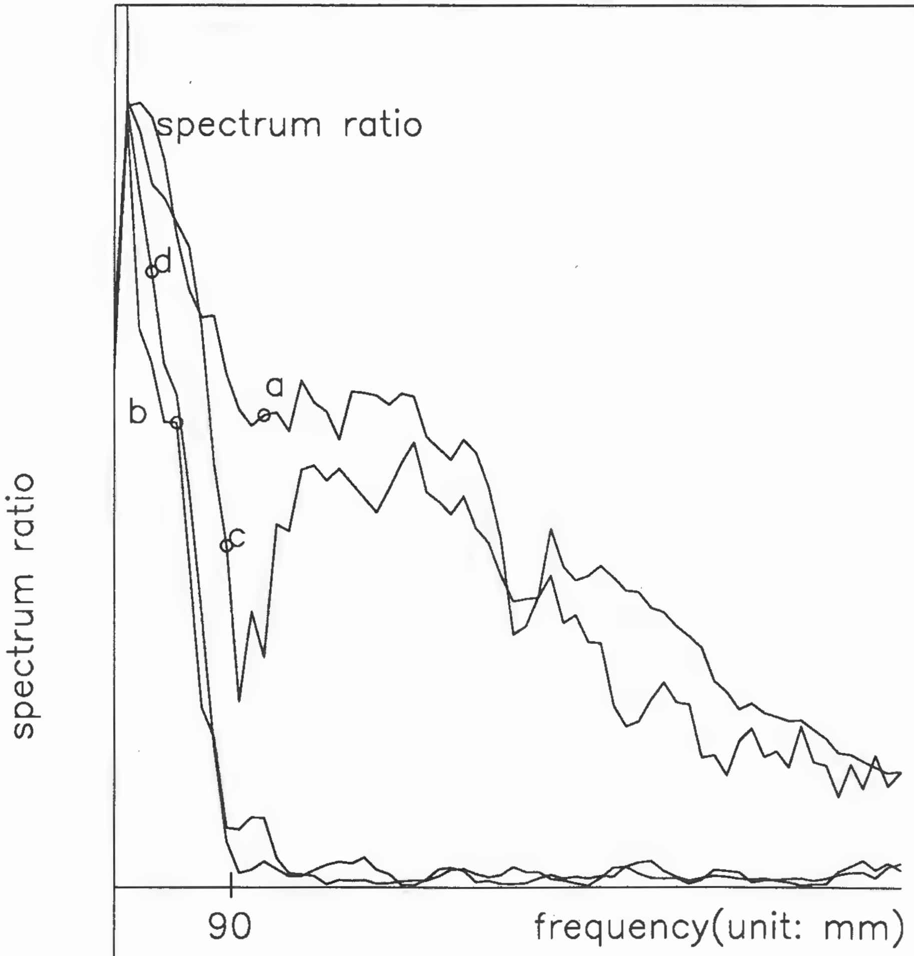

Fig.2 CURVE OF SPECTRUM RATIO

Field of view : 29.3*13.6 arcsec

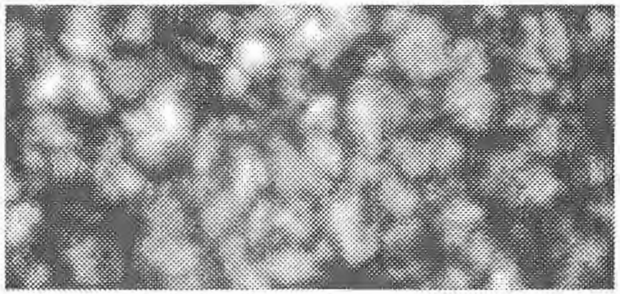

(a). speckle sample

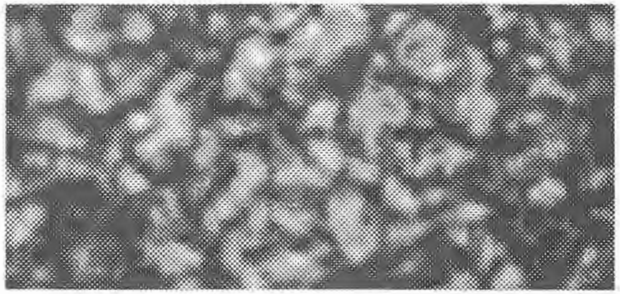

(b). reconstruction image
made by three segments

Fig.3 COMPARSION BETWEEN SPECKLE AND RECONSTRUCTION IMAGE

Some Schemes of Space Solar Telescope

Guoxiang Ai

Beijing Astronomical Observatory
Beijing 100080
China

1. Introduction

The Space Solar Telescope (SST) (Ai, 1993), similar to the Japanese Solar-B (Hirayama, 1993), has been proposal. In this paper, some schemes of the main optical telescope will be discussed. In my opinion the telescope should have the following functions:

(1) about 0.1" diffractive limiting spactial resolution in visible spectrum;
(2) additional polarization from the telescope should be as small as possible;
(3) stokes parameter profile of line with 2-Dimensional real time field of view;
(4) ability in ultra violet and near infrared.

According to the above functions, two Schemes of the main optical constructure, and some of the multichannel filters will be discussed.

2. Scheme I: Gregorian system add two total reflect prims

The Scheme is shown in Figure 1. The scheme has four characteristic points:
(1) two total reflect prisms, made out of BAK4 or TF2 are instead of the two reflect plates in OSL (Hartmann, 1991), the two prisms serve two functions: (A) they fold the beam to decrease the length of tube; (B) they act as an achromatic quarter wave plate. But in OSL, the additional polarization from two reflect plates is not definite and changes probably as time goes on. The retardation from the prism are shown in Table 1.

(2) The total transmitting birefringent filter (Ai and Hu, 1987) can be used, which has double the transmissivity than the traditional Lyot filter. When the bandwidth is 1/8 Å, the transmissivity is as high as 25%-30%, this is special advantage for decreasing the diameter of the telescope, increasing the spatial resolution and shorting the exposure time.

(3) The KD*P electrical-optical modulator is set in collimatic beam. The error of

retardation from field of view in the three type of KD^*P modulators are shown in Table 2. KD^*P modulator with narrow field of view is consisted of two conduct grasses sandwich a piece of KD^*P with $\pm\lambda/4$. The type I with wide field of view of KD^*P modulator is consisted of two group KD^*P modulators with $\pm\lambda/8$ in which opposite vantage are put and sandwich a $\lambda/2$ wave plate. The type II with wide field of view of KD^*P modulator are consisted of 4 group KD^*P, the first group and lost group are same, but with opposite voltage of $\pm\lambda/4$, the second and third one are same, but also with opposite voltage of $\pm\lambda/8$ and sandwich $\lambda/2$ wave plate. As an example, $d_1=d_4=2.08$, $d_2=d_3=1.50$mm, the results of field of view are shown in table 2.

If the relative error of ± 5% is permit, the largest field of view are separately 1.2°, 2.0° and 3.8° for Narrow, type I and type II of KD^*P modulators.

The type I is selected and is used in collimetric beam. When field of view is 2'×2', the angular magnifying power of the collimation lens is 45, the incident angle coming into the KD^*P is about 2°, so the type I of KD^*P can be used here.

(4) A tilt correlation tracker will be used to improving of the pointing accuracy of the telescope. A low spatial and temporal resolution Hartmann-shack type wavefront sensor will be used to sense and update the mirror alignment and wavefront error of optical ayatem.

3. Scheme II: Primary mirror add secondary lens.

The Scheme II is shown in Figure 2. The characteristic points are followings:
(1) The central obscuration decrease from 1/4 of diameter of primary mirror to smaller than 1/10, that will improve the Modulation Transfer Function of the system, then will permit larger the wavefront errors of the system.

(2) The heat rejection mirror in focus of the primary mirror can be set vertically to the optical axis, then the stop of field of view will have sharp limb, so the scattered light will be decreased.

(3) The polarizing analyser including KD^*P modulator and achromatic wave plates will be placed after the secondary lens, so the beam with small angle of field of view will pass the system.

(4) Similar to the Scheme I, the tilt correlation tracker and wavefront corrector can be set.

(5)The total transmitting filter can be used also for the system.

(6) The achromatism of the lens is not as good as the secondary mirror. It is necessary to design the lens in detail.

4. Filter

Three type of birefringent filters are proposed.

(1) A total transmitting universal filter with 1/7 Å in 5324 Å or 5250 Å. The transmissivity is about 0.25-0.30, which has double transmissivity than one of the traditional Lyot filter, it is special advantage that the diameter of the telescope decrease to 1/ 2, the focus and luminosity keep same. The size is 350^{mm} (length) $\times 120^{mm}$ (wide) × 80 (high).

(2) A two dimensional real time spectrograph with 8-channel, (Ai, 1991) and bandwidth is 1/8 Å in H_α is used to obtain the Stokes parameters of the spectral line, then vector magnetic field, velocity field and other physical field can observed simultaneously.

(3) A birefringent filter in λ 8600 Å of line P15 for an electrograph.

Now, a balloon telescope with 2/3 size, 67 cm diameter, is under developing for middle-stage experiment of the space of solar telescope.

Reference

Ai G., 1993, Proceedings of the First China-Japan Seminar on Solar Physics, 300.

Hirayama, T., 1993, The Next Japan Solar Satellite ESA Publication, in press.

Hartman, J. B., 1991, Status of the Orbiting Solar Laboratory (OSL) Mission.

Ai. G., Hu. Y., 1987, Multichannel Birefringent Filter (II), Science Sinica, Vol.XXX, No.10, 1069.

Ai. G., 1991, 2-D Real Time Polarimetric Spectrograph with 64-Channel, Solar Polarimetry, NSO/SP Summer Workshop Series No.11, 13.

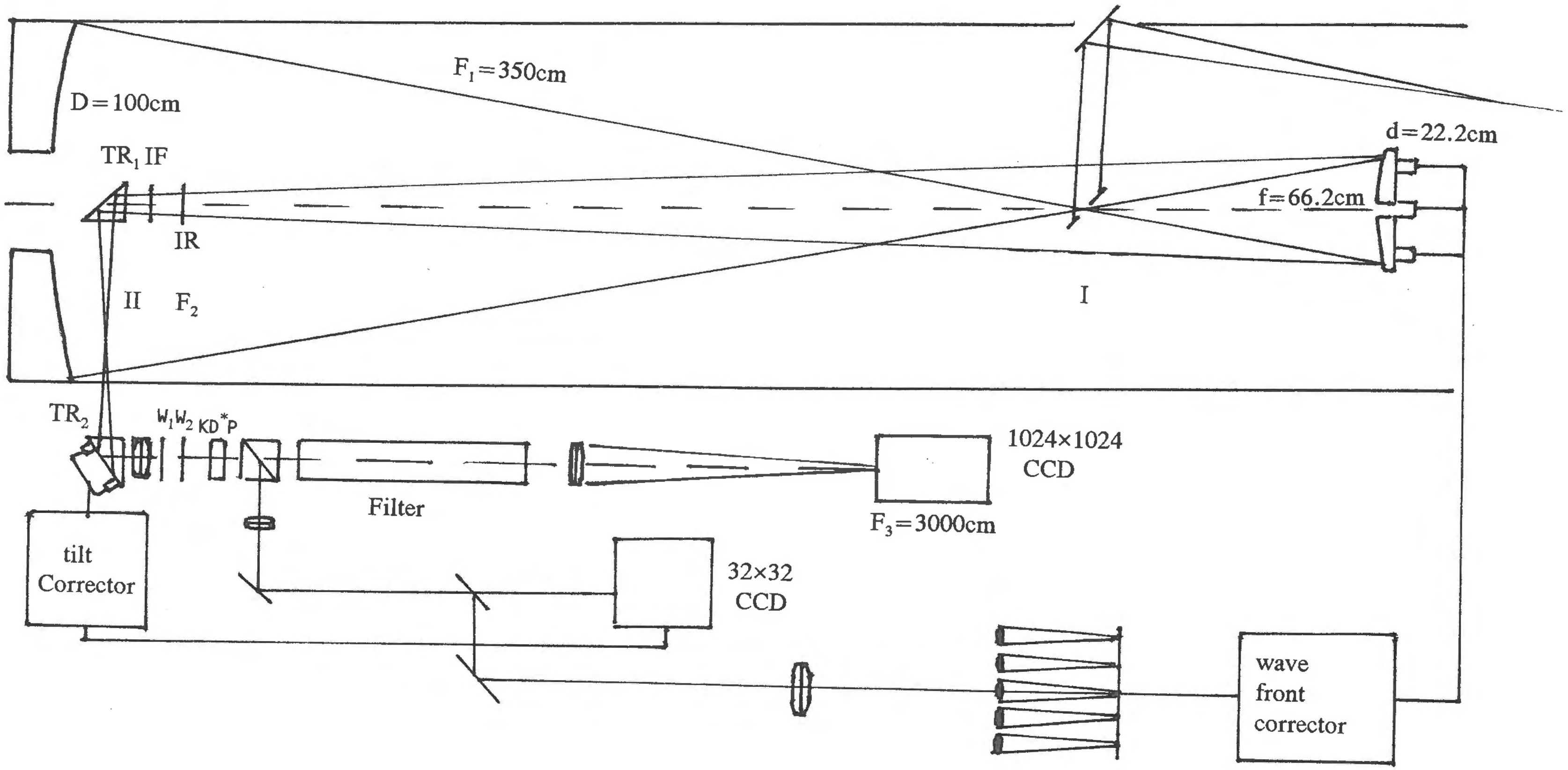

Fig.1 Scheme of Space Solar Telescope with Gergorian and two Totally Reflect Prizms

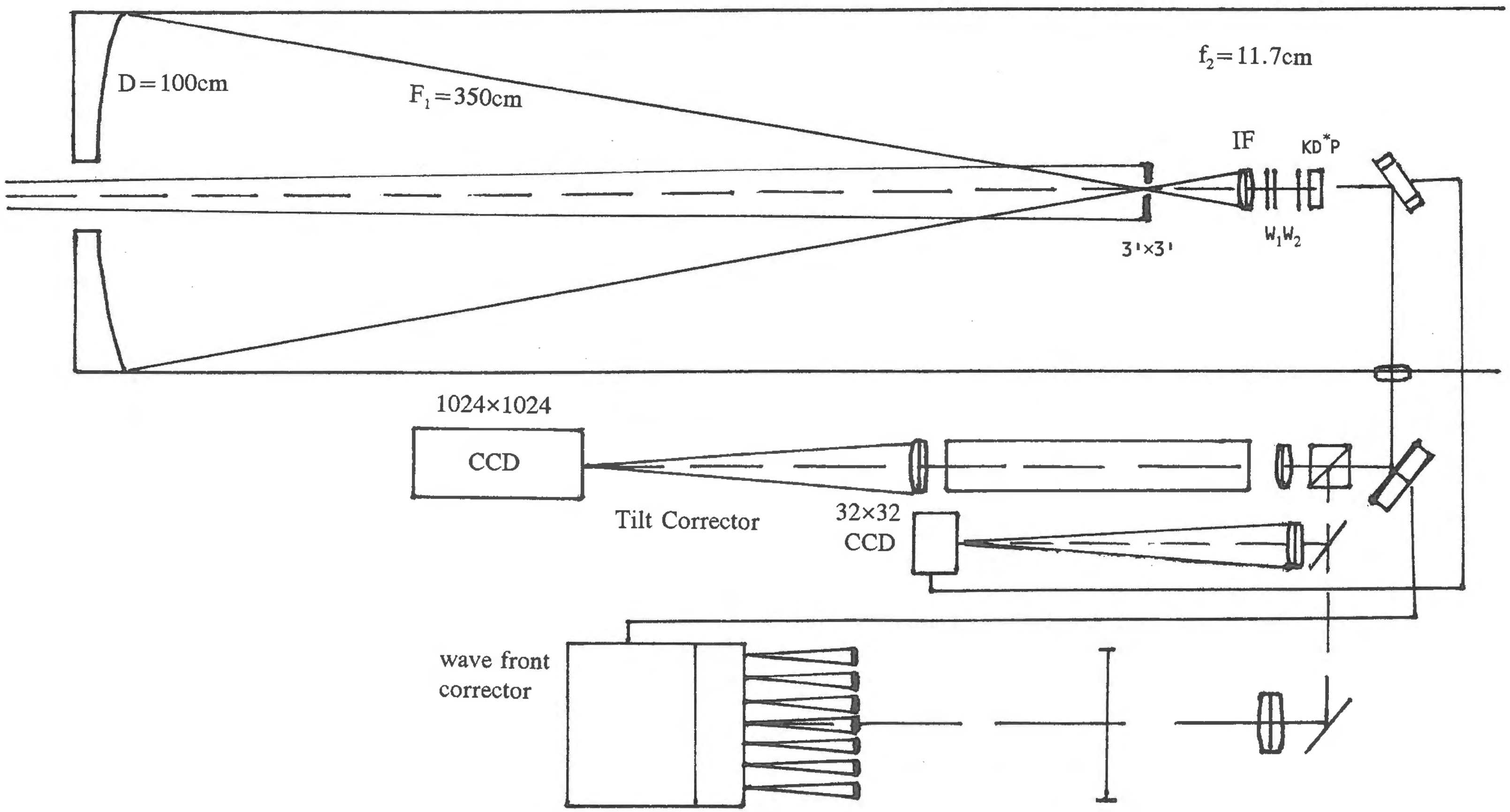

Fig.2 Scheme of Space Solar Telescope with a Secondary lens System

Table I. Phase difference of the total reflect prism

A· BAK—4

n	1.57364	1.56787	1.56321	1.55853	1.55456	1.55248	1.55240	1.54981	1.54674
	3650.1	4046.6	4358.4	4861.3	5460.7	5876.5	5892.9	6562.7	7665.0
45°	94.72	93.22	92.32	91.18	90.20	89.68	89.66	88.98	88.20
46°	48.70	48.05	47.66	47.17	46.75	46.53	46.52	46.23	45.89
44°	45.40	44.50	43.96	43.29	42.70	42.38	42.37	41.97	41.49
46°+44°	94.10	92.55	91.62	90.46	89.45	88.91	88.89	88.20	87.38
46.5°	49.18	48.57	48.20	47.75	47.36	47.15	47.14	46.88	46.56
43.5°	44.10	43.12	42.52	41.76	41.12	40.77	40.76	40.31	39.78
46.5°+43.5°	93.28	91.69	90.72	89.53	88.48	87.92	87.90	87.19	86.34

B· TF2

n	1.58304	1.57363	1.56825	1.56188	1.55661	1.55398	1.55380	1.55048	1.54667
	3650.1	4046.6	4358.4	4861.3	5460.7	5876.5	5892.9	6562.7	7665.0
45°	96.78	94.72	93.50	92.00	90.70	90.04	90.00	89.16	88.18
46°	49.59	48.70	48.17	47.52	46.97	46.68	46.67	46.31	45.89
44°	46.61	45.40	44.67	43.77	43.01	42.60	42.58	42.08	41.48
46°+44°	96.20	94.10	92.84	91.29	89.98	89.28	89.25	88.37	87.37
46.5°	50.01	49.18	48.68	48.08	47.56	47.29	47.28	46.95	46.56
43.5°	45.43	44.10	43.30	42.31	41.46	41.01	40.99	40.43	39.76
46.5°+43.5°	95.44	93.28	91.98	90.39	89.02	88.30	88.27	87.38	86.32

Table II. Errors of KD*P from field of view (λ =5324A, ± λ / 4)

Type	θ	0°	10°	20°	30°	40°	45°	50°	60°	70°	80°	90°
narrow field d=2mm	0.5°	0.23876	0.23948	0.24155	0.24468	0.24847	0.25046	0.25244	0.25612	0.25907	0.26098	0.26164
	0.6°	0.23372	0.23478	0.23781	0.24238	0.24787	0.25074	0.25358	0.25883	0.26303	0.26574	0.26667
I d=2mm	0.9°	0.25009	0.25148	0.25483	0.25837	0.26056	0.26085	0.26056	0.25837	0.25483	0.25148	0.25009
	1.0°	0.25007	0.25228	0.25744	0.26271	0.26587	0.26629	0.26587	0.26271	0.25744	0.25228	0.25007
II type with $d_1=$ 2.08mm add ±λ/4 $d_2≒$ 1.50mm add ±λ/8	0.1°	0.25027	0.25027	0.25027	0.25027	0.25027	0.25027	0.25027	0.25027	0.25027	0.25027	0.25027
	0.3°	0.25026	0.25026	0.25026	0.25026	0.25026	0.25026	0.25026	0.25026	0.25026	0.25026	0.25026
	0.5°	0.25025	0.25025	0.25024	0.25024	0.25023	0.25023	0.25023	0.25024	0.25024	0.25025	0.25025
	0.7°	0.25024	0.25023	0.25020	0.25018	0.25016	0.25016	0.25016	0.25018	0.25020	0.25023	0.25024
	0.9°	0.25024	0.25019	0.25010	0.25005	0.25004	0.25004	0.25004	0.25005	0.25010	0.25019	0.25024
	1.1°	0.25021	0.25006	0.24983	0.24979	0.24985	0.24987	0.24985	0.24979	0.24983	0.25006	0.25021
	1.3°	0.25020	0.24968	0.24816	0.24936	0.24976	0.24982	0.24976	0.24936	0.24816	0.24968	0.25020
	1.5°	0.25018	0.24847	0.24760	0.24880	0.25005	0.25024	0.25005	0.24880	0.24760	0.24847	0.25018
	1.7°	0.25016	0.24457	0.24458	0.24842	0.25127	0.25166	0.25127	0.24842	0.24458	0.24457	0.25016
	1.9°	0.24968	0.23367	0.24026	0.24899	0.25412	0.25479	0.25412	0.24899	0.24026	0.23367	0.24968
	2.1°	0.19743	0.21537	0.23662	0.25164	0.25933	0.260296	0.25933	0.25164	0.23662	0.21537	0.19743

Session 3: NOAA 7321

Coordinated Observations of Solar Active Regions (NOAA 7260, 7270 and 7321) at the Beijing Astronomical Observatory

Guoxiang Ai, Hongqi Zhang, Qijun Fu, Jialong Wang

Beijing Astronomical Observatory,
Beijing 100080
China

Abstract

Coordinated observations of solar active regions (NOAA 7260, 7270 and 7321) were made on August -- November, 1992 at the Huairou and Shahe Stations of the Beijing Astronomical Observatory. These observations include photospheric vector magnetic fields, chromospheric longitudinal magnetic fields, Doppler velocity fields, $H\alpha$, $H\beta$ filtergrams and solar radio patrol observations at 2840 Mhz (total flux) and double frequency channels 2545 -- 2645 Mhz (total flux and polarization).

1. Introduction

During August -- November, 1992 of the coordinated observations made in China and Japan, we continuously observed active regions (NOAA 7260, 7270, 7321) at the Huairou and Shahe Stations of the Beijing Astronomical Observatory.

2. Observational Data

2.1 Huairou Solar Station

The observations for NOAA 7260, 7270 and 7321 were made using the Solar Magnetic Field Telescope at the Huairou Solar Observing Station of the Beijing Astronomical Observatory. This Telescope belongs with the Multi-channel Telescope system. It consists of a 35 cm vacuum telescope, a 1/8 Å birefringent filter with 3 sets of KD^*P crystal modulator, a CCD camera and an Imaging Technology 151 system controlled by a AST - 386, which transmits the data to the Sun work station and VAX/11-750 for processing. Two working spectral lines used in this telescope are: FeIλ5324.19Å and H_β λ4861.34Å. The field of view of the telescope is about 4'×6'and the scale of each pixel on CCD is ~ 0.4"×0.7".The data on a frame of the solar image can be collected in 1/25 sec. The photospheric vector magnetograms, Dopplergrams, chromospheric longitudinal magnetograms and Dopplergrams of active regions NOAA 7260, 7270 and 7321 and corresponding filtergrams were obtained with this telescope system. In additional, H_α filtergrams, daily full disk calcium filtergrams, and full disk longitudinal magnetograms were also obtained at the Huairou Station.

2.2 Shahe Station

Solar radio observations were made at the Shahe Station of the Beijing Astronomical Observatory. Solar radio patrol observations at 2840 Mhz (total flux) with time resolution of 1 m sec, 10 m sec and 1 sec in the mode of continuous sampling, and at double frequency channels 2545 Mhz -- 2645 Mhz (total flux and polarization) with time resolution of 2 m sec and 1 sec in the mode of real-time spike statistics were obtained during the coordinated observations of active region NOAA 7260, 7270 and 7321. The diameters of paraboloid used are 2.5 m (2840 Mhz) and 2 m (2545 - 2646 Mhz). The sensitivity of the system at 2840 Mhz is 5 s.f.u. (with 10 m sec time constant). A number of microwave bursts occurred in the active regions NOAA 7260, 7270 and 7321 were registered at 2840 Mhz with time resolution of 10 m sec.

3. Brief Discussion

3.1 Active Region NOAA 7260

The magnetic class of active region NOAA 7260 was BGD on August 20 -- 23, 1992. This active region consisted of two large-scale magnetic structures A and B of negative polarity and surrounding magnetic structures of positive polarity in Figure 1. We can see that a magnetic island C of positive polarity formed inside of the large-scale magnetic structure B. Transverse components of the field were parallel to the magnetic neutral lines around the magnetic structures B and C. From a series of magnetograms, we can find that the magnetic structure C emerged in the middle of the magnetic structure B of opposite polarity, then the magnetic structure C disappeared gradually with its motion toward large-scale magnetic structures of same polarity.

3.2 Active Region NOAA 7270

The magnetic class of active region NOAA 7270 was a bipolar magnetic structures when this region rotated out from east limb of the sun (August 29). The distribution of the magnetic field is relative sample and porous. On September 3 and 4, the new magnetic flux emerged around the magnetic structure A of positive polarity. Some magnetic islands of negative polarity formed and the gradients of the longitudinal magnetic field increased in Figure 2. Some optical flares were observed in this active region. The flares occurred in the down flowing areas near the chromospheric velocity inversion line.

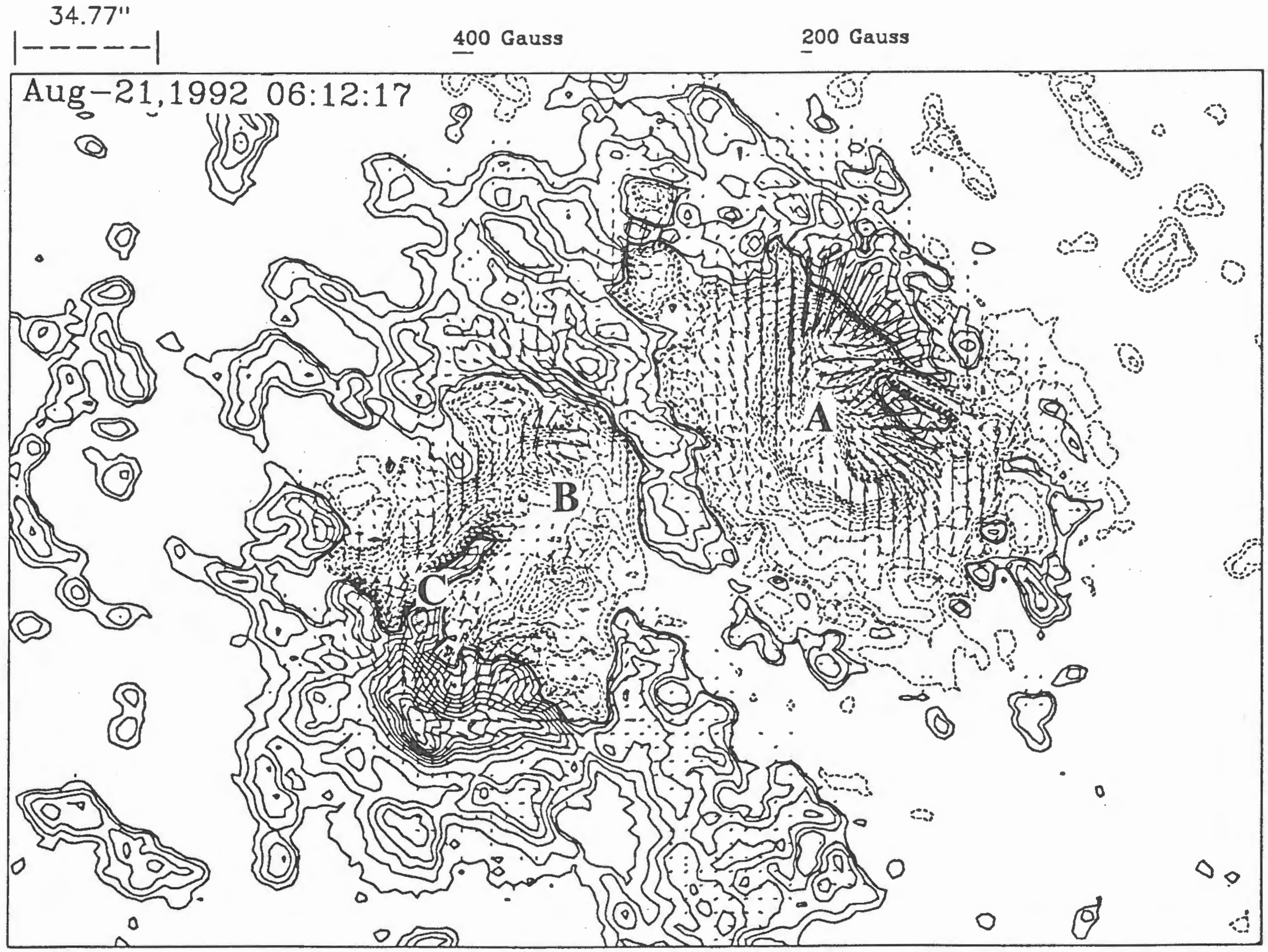

Fig. 1 A photospheric vector magnetograms in active region NOAA 7260. The shear of transverse field occurred near the magnetic neutral lines around the magnetic structure B.

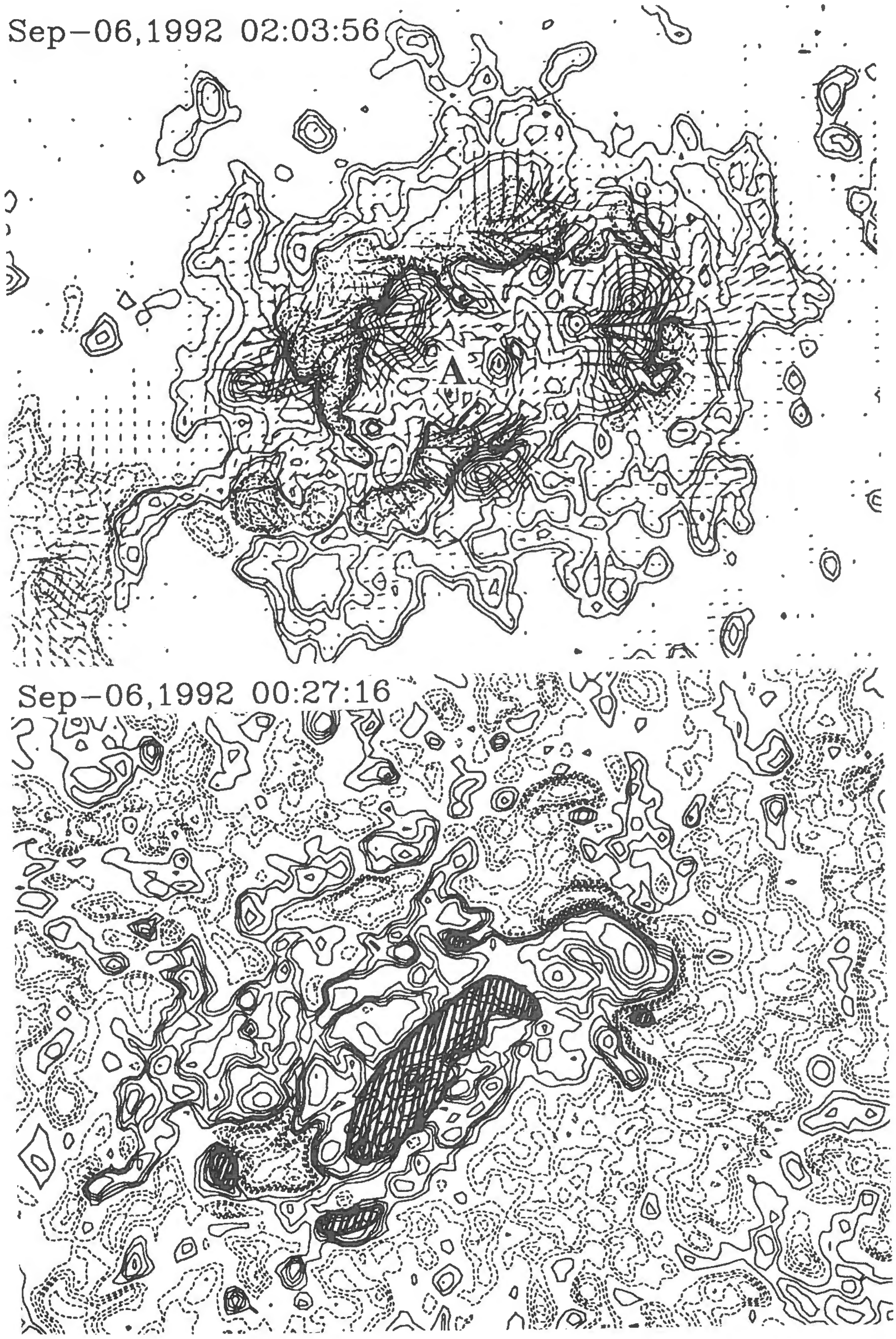

Fig. 2 A photospheric vector magnetogram top and a chromospheric Dopplergram bottom in active region NOAA 7270 on Sep.6, 1992. The solid (dashed) contours in the Dopplergram correspond down (up) ward flow and the shaded structures in the Dopplergram indicate the positions of flares at 0027UT.

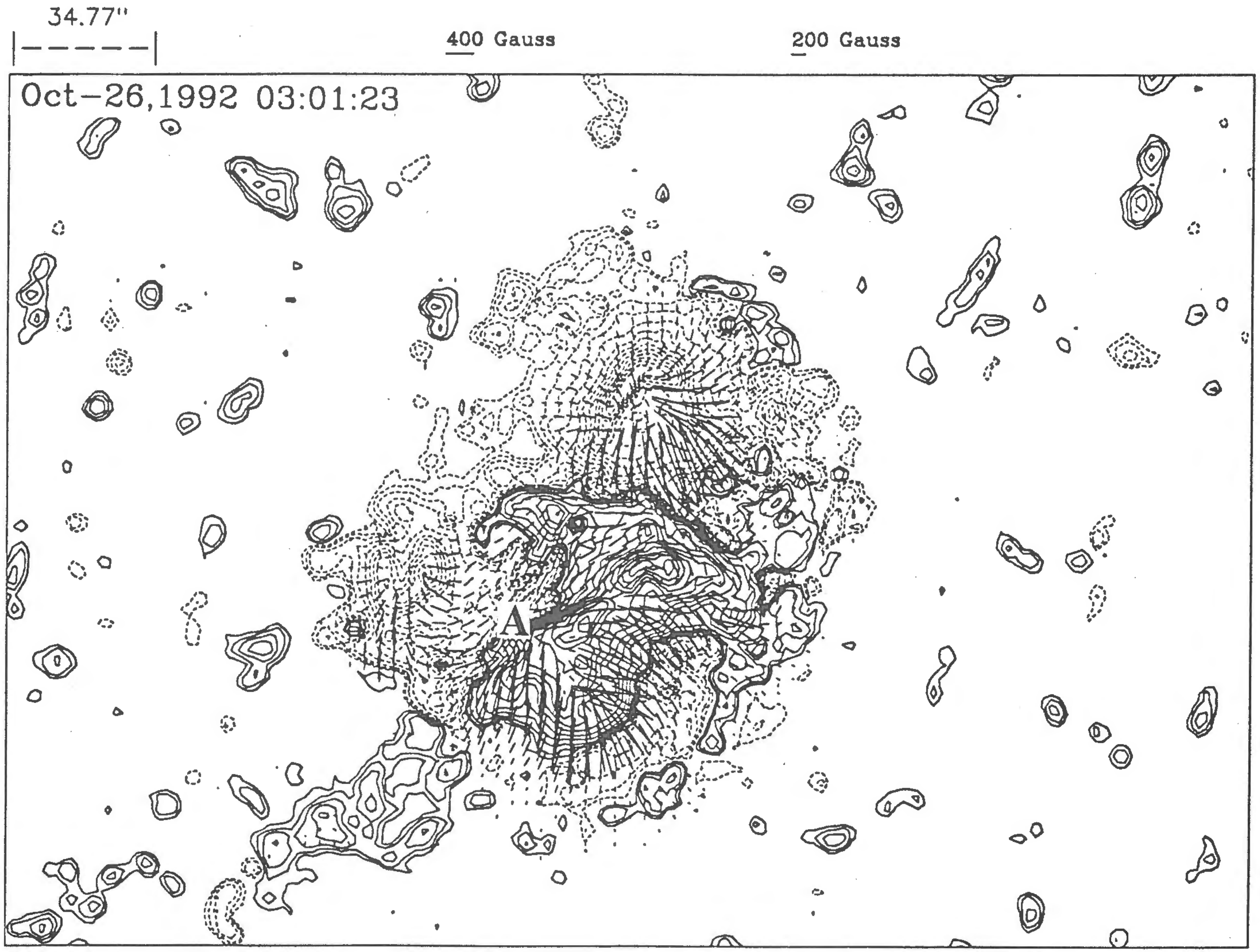

Fig. 3 A photospheric vector magnetogram in active region NOAA 7321. The transverse components of the field were parallel to the magnetic neutral line in the middle of the active region.

3.3 Active Region NOAA 7321

Active region NOAA 7321 was a emerging flux region. This region was born on October 24. The polarities of this region reversed from the Hale -- Nicholson law. We can find that the strong shear of transverse magnetic field formed near the magnetic neutral line A in Figure 3. The shear of the field accompanied the emergence of the magnetic flux. Some flares occurred near the magnetic islands, where the transverse magnetic field sheared. If compare with a series of photospheric vector magnetograms, we can infer that the shear of the transverse field probably was caused by the emergence of new flux of opposite polarities and the reconnection of the field at the lower solar atmosphere.

Observational Results of an Active Region (NOAA 7321) during October – November, 1992

Zhang Hongqi and Ai Guoxiang
Beijing Astronomical Observatory,
Chinese Academy of Sciences, Beijing 100080, China

Wang Tongjiang
Astronomical Department,
Nanjing University, Nanjing 200008, China

Abstract

NOAA 7321 was an emerging flux region (EFR) from October 24 to November 1, 1992. This EFR was born on October 24 – 25. The distribution of magnetic polarities in this region reversed from the Hale–Nicholson rules obviously. Due to the emergence of magnetic flux, magnetic structures in this region become complex. The shear of photospheric transverse magnetic field occurred in the emerging process of magnetic flux and it accompanied with flares.

Some flares were observed near the photospheric magnetic neutral line. After resolving the 180° ambiguity of the transverse field in the active region, the relationship between the flare bright points and longitudinal current density have been analyzed. Most of flare bright points did not occur at the peaks of the longitudinal current density in the emerging flux region.

1. Introduction

Photospheric vector magnetograms (FeI $\lambda5324.19$ Å), chromospheric longitudinal magnetograms (Hβ $\lambda4861.34$ Å) and corresponding Dopplergrams in the active region 7321 during October – November 1992 were observed at Huairou Solar Observing Station.

2. Formation of a New Active Region

2.1 Emergence of magnetic flux

The new magnetic flux emerged from subatmosphere to form a new active region (NOAA 7321) on October 24, 1992.

Inclination angles of the magnetic axis of main poles of this active region relative to the solar equator is about 60°. It is inverted to the Hale–Nicholson law.

2.2 Magnetic Shear near Magnetic Neutral Line

The magnetic field sheared gradually near the magnetic neutral line during the emergence of magnetic flux in the active region. The longitudinal magnetic features, as fibril-like form, were parallel to the transverse field.

The shear angles of the transverse field changed and were gradually parallel to the magnetic neutral line in Figure 1. Some of magnetic structures of opposite polarities disappeared near the magnetic neutral line as the growth of the new active region.

2.3 Velocity field of Emerging flux region

The chromospheric Dopplergrams showed that the evident upward flow of chromospheric mass occurred near the magnetic neutral line of new emerging magnetic flux and the downward flow at the foot points of the new emerging flux in the active region.

3. Direction of Vector Magnetic Field and Longitudinal Currents

3.1 Resolving the 180° Ambiguity of the Transverse Field

(a) Our first approximation was to adopt the choice of directions closest to that of the potential field fitted to the line of sight component of the observed magnetic field. This works well at most points but due to the shear of the magnetic field in the interesting regions the fits of the field probably fail, for example near the magnetic neutral line where the the transverse field were almost parallel to it.

(b) Spatial and temporal continuities of the transverse magnetic field are important parameters. We took into account the requirement of continuous change of the direction of the transverse magnetic field and their evolution in the active region.

3.2 Distribution of the Longitudinal Currents

According to a formula $J_z = \frac{\partial B_y}{\partial x} - \frac{\partial B_x}{\partial y}$, the distribution of the longitudinal current density can be obtained. The longitudinal currents of opposite directions can exist in one main pole of the magnetic field. Moreover, the relationship between the magnetic neutral line and inversion line of large-scale longitudinal current structures is not distinct in the active region 7321, but the longitudinal current of opposite directions with a tendency appeared in different sides of the main magnetic neutral line.

4. Flares

Some flares in this EFR were observed at Huairou Solar Observing Station.

27 Hβ flare bright points on October 25 and 26 in the emerging flux region were analyzed. These flare bright points occurred near the magnetic gulfs and islands of opposite polarities in the both sides of the magnetic neutral line in the active region shown in Figure 2.

Figure 2 also shows the distribution of the longitudinal electrical current density in the active region on October 25 and 26 1992, the active region was located near the solar disk center (S23, E8.5 on October 25). The statistical result of the relationship between the longitudinal current density and 27 Hβ flare bright points demonstrates that 6 bright points among them occurred at the peaks of the longitudinal current density, 17 bright points deviated from the peaks of the longitudinal current density, 4 bright points were located in the inversion lines of the longitudinal current density in the active region.

On October 27, we can find similar case. Some of Hβ flare bright points occurred at the peaks of longitudinal current density, while some not, which include some initial bright points of flares.

This means that the peaks of the longitudinal current density have not corresponding relationship with flare bright points in this emerging flux region.

5. Discussion

(a) The shear of the magnetic field near the magnetic neutral line increases with the emergence of new magnetic flux in the active region 7321. Even some flares occurred at the both sides of the magnetic neutral line.

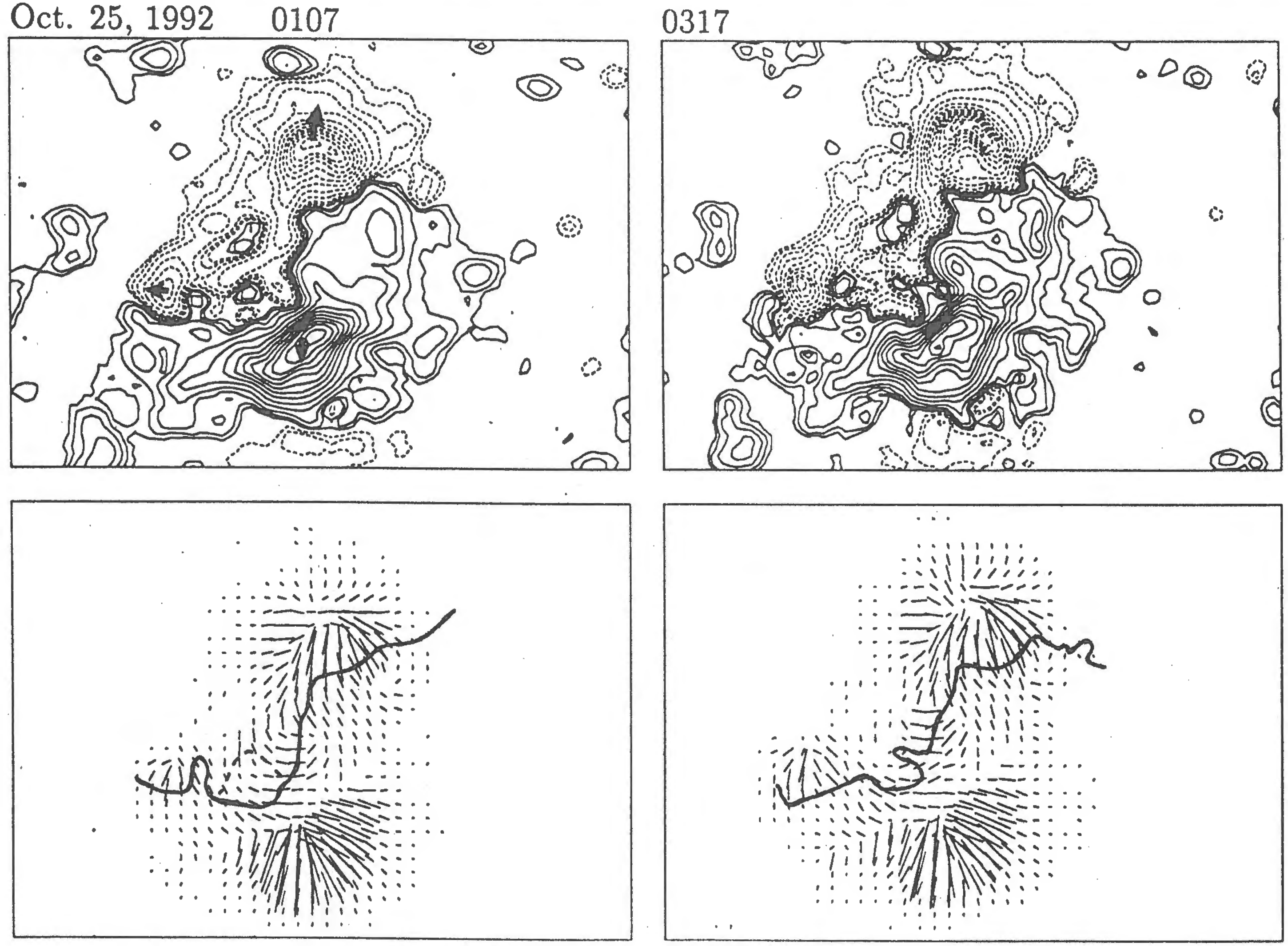

Fig. 1a. A series of photospheric longitudinal and transverse magnetograms in the active region 7321 on October 25, 1992. The thick solid lines in the transverse magnetograms mark the magnetic neutral lines. Arrows indicate the moving directions of the main poles of magnetic fields.

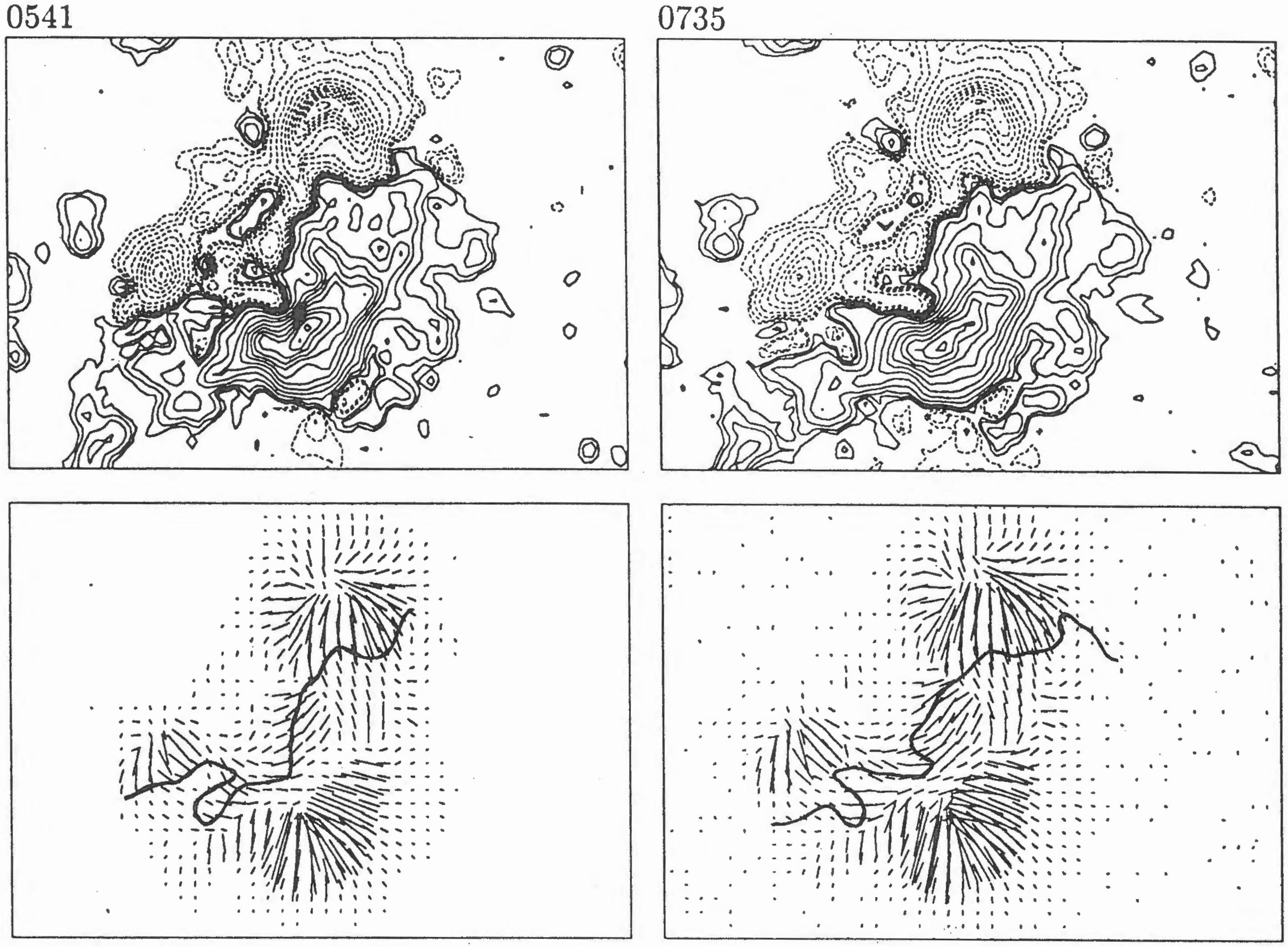

Fig. 1b.

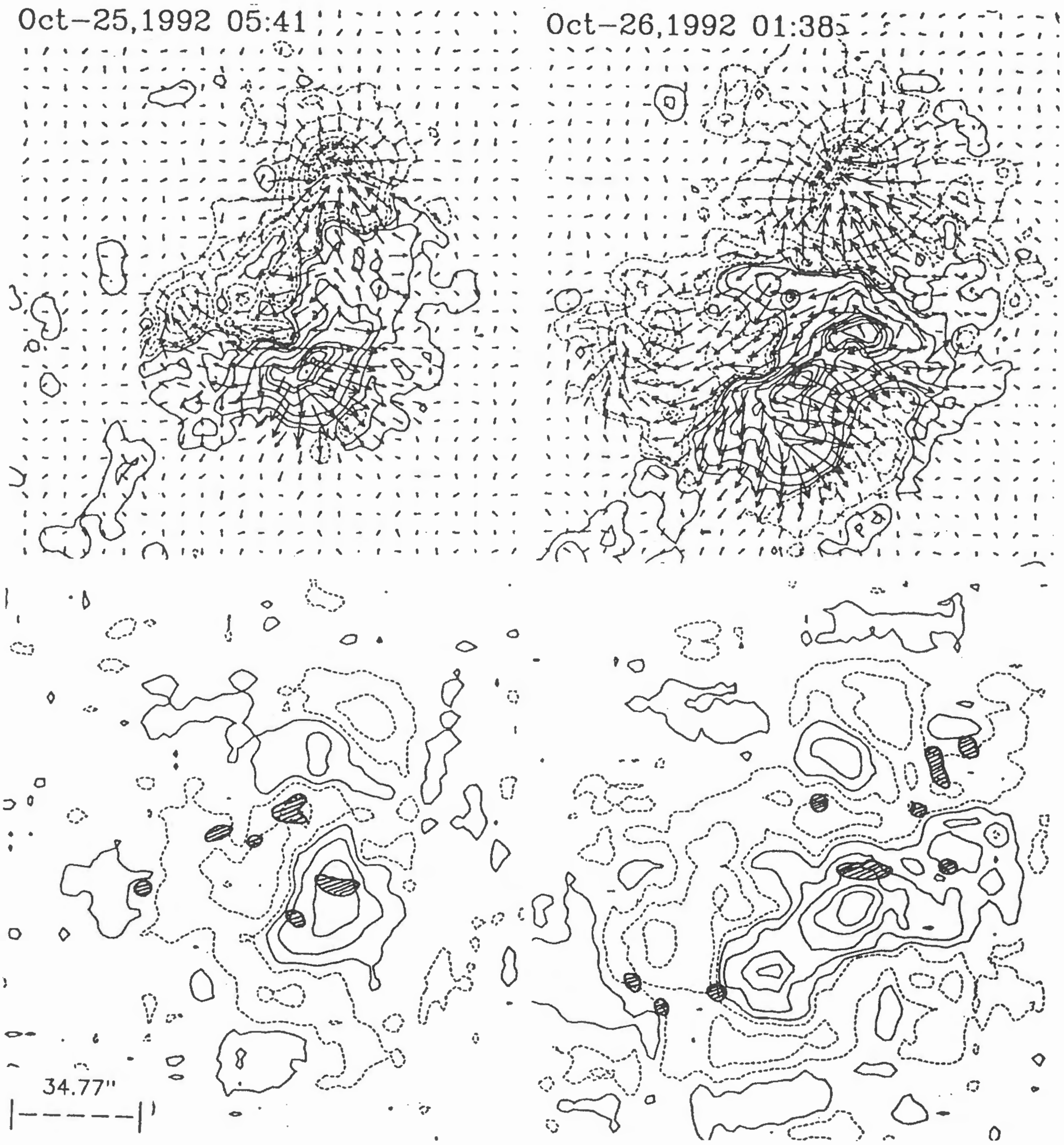

Fig. 2. Ambiguity-resolved vector magnetograms (top) on October 25 and 26 1992 and corresponding maps of longitudinal current density (bottom) in the active region 7321. The shadow areas in maps of longitudinal current density mark some flare bright points closed to the observational time of magnetograms and contours indicate the distribution of longitudinal current density of ±0.2, 0.4, 0.8, 1.0, 1.4, 1.6, 2.0×10^{-2} Am^{-2}. The thick solid lines mark the magnetic neutral lines.

(b) We can find that the longitudinal currents of opposite direction can exist in the one main poles of magnetic field. It is possible that in the emerging flux region the effect of the mass motion and gas pressure are not negligible. It deviates from force free approximation evidently.

(c) The flare ribbons avoid the stronger magnetic main poles, except the powerful flares, even where the magnetic twist or shear is strongly. Some flare ribbons do not occur at the peaks of the photospheric longitudinal current in the growing active region.

(d) The longitudinal current density only reflects the line-of-sight component of the current density inferred by the photospheric transverse field, but it is not contain all of the information of the photospheric vector current density. The analysis of the relationship between the longitudinal currents and flares need more carefully.

Acknowledgements

The authors would like to thanks to Drs. K. Ichimoto and Y. Suematsu for valuable discussion. This research was supported by the Chinese Academy of Sciences and National Science Foundation of China.

Observations of the Magnetic Field Structure in NOAA 7321 using the Solar Flare Telescope

Singo KAWAKAMI
Astronomy Section
Osaka Museum of Science
4-2-1 Nakanoshima, Kita-ku
Osaka 530, Japan

Abstract

The magnetic field structure of NOAA 7321 was observed using the Solar Flare Telescope of National Astronomical Observatory of Japan. We study the magnetic field structure and its relation to flare activities.

1.Introduction

NOAA 7321 was appeared on 24 October 1992, and went behind the west limb on 1 November. During its disk passage, sunspots were growing-up gradually (See Figure 1.) and flares occurred frequently.

In the following section, we investigate the Hα and magnetic field evolution of this active region on 27 October in detail.

2.Observations

Observations were made with the Solar Flare Telescope of National Astronomical Observatory (Ichimoto et al. 1993). On 27 October, about 170 pairs of vector magnetograms and Hα filtergrams were obtained with this telescope.

According to the *Solar Geophysical Data* (1993,No.584,Part II,p.16), two 1B-class flare occurred during observations at Mitaka. Hα images of these flares taken with the Solar Flare Telescope are shown in Figure 2.

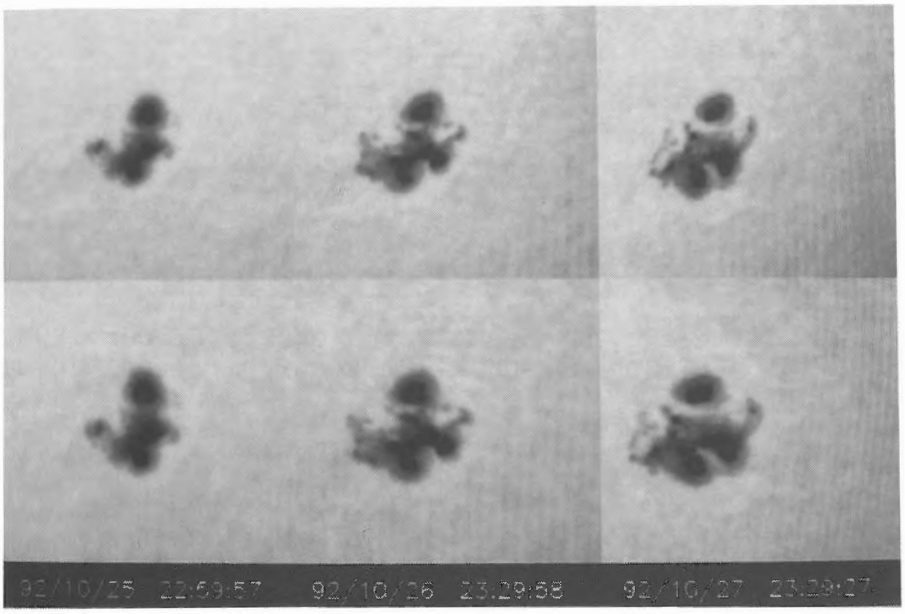

Fig.1 Sunspot evolution since 25 to 27 October.
Lower: observed images,
Upper: images corrected to the face-on view.

Observations of the Magnetic Field Structure in NOAA 7321 using the Solar Flare Telescope

Singo KAWAKAMI
Astronomy Section
Osaka Museum of Science
4-2-1 Nakanoshima, Kita-ku
Osaka 530, Japan

Abstract

The magnetic field structure of NOAA 7321 was observed using the Solar Flare Telescope of National Astronomical Observatory of Japan. We study the magnetic field structure and its relation to flare activities.

1.Introduction

NOAA 7321 was appeared on 24 October 1992, and went behind the west limb on 1 November. During its disk passage, sunspots were growing-up gradually (See Figure 1.) and flares occurred frequently.

In the following section, we investigate the Hα and magnetic field evolution of this active region on 27 October in detail.

2.Observations

Observations were made with the Solar Flare Telescope of National Astronomical Observatory (Ichimoto et al. 1993). On 27 October, about 170 pairs of vector magnetograms and Hα filtergrams were obtained with this telescope.

According to the *Solar Geophysical Data* (1993,No.584,Part II,p.16), two 1B-class flare occurred during observations at Mitaka. Hα images of these flares taken with the Solar Flare Telescope are shown in Figure 2.

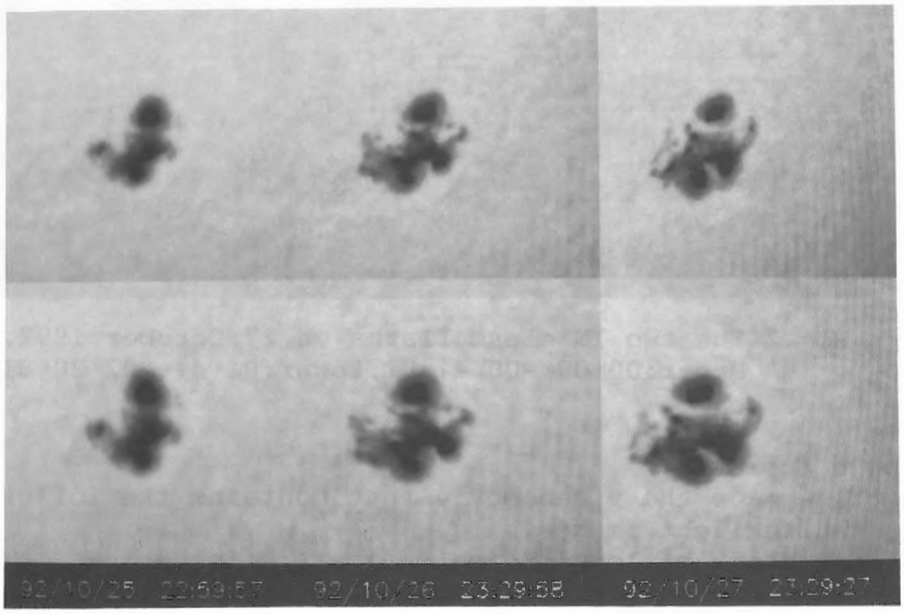

Fig.1 Sunspot evolution since 25 to 27 October.
Lower: observed images,
Upper: images corrected to the face-on view.

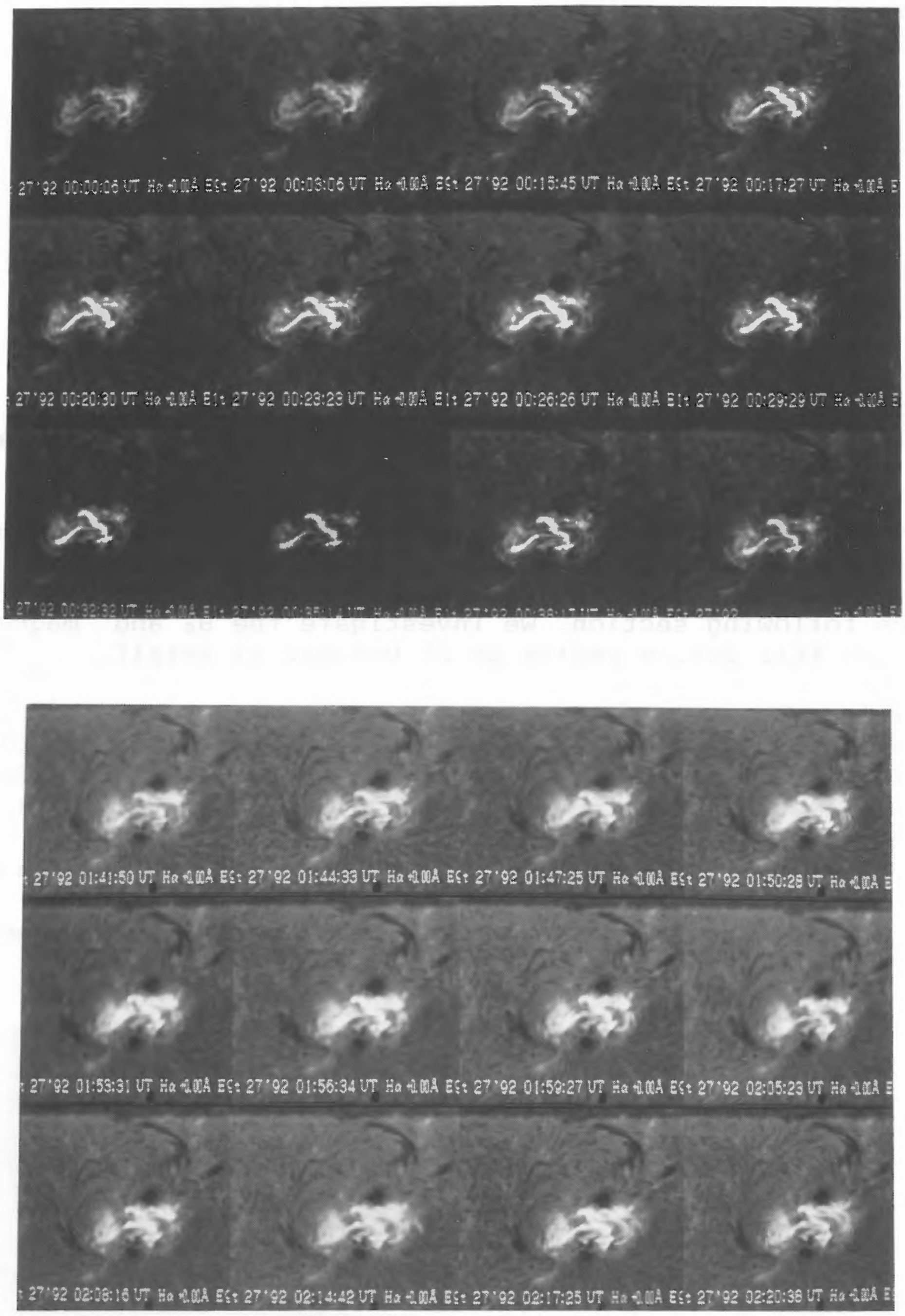

Fig.2 The two 1N class flares on 27 October,1992.
Upper:$00^h 00^m$-$00^h 41^m$ UT, Lower:$01^h 41^m$-$02^h 20^m$ UT

3.Analysis

3-1 Making a Movie

First, we made the video movie that contains the following:

white-light images,
strength of longitudinal magnetic field,
strength of transverse magnetic field, and
Hα images.

This type of movie is very useful to find the newly emerging flux region or the day-long changes of the active region.

3-2 The Evolution of NOAA 7321 on 27 October, 1992

Figure 3 and 4 shows the change of the sunspot and the magnetic structure during the day. We can find slight changes in white-light images and longitudinal magnetograms, except for the gradual growing at the west end part of the sunspot.

We also find the small changes of the direction of transverse magnetic field (maximum change about 20°).

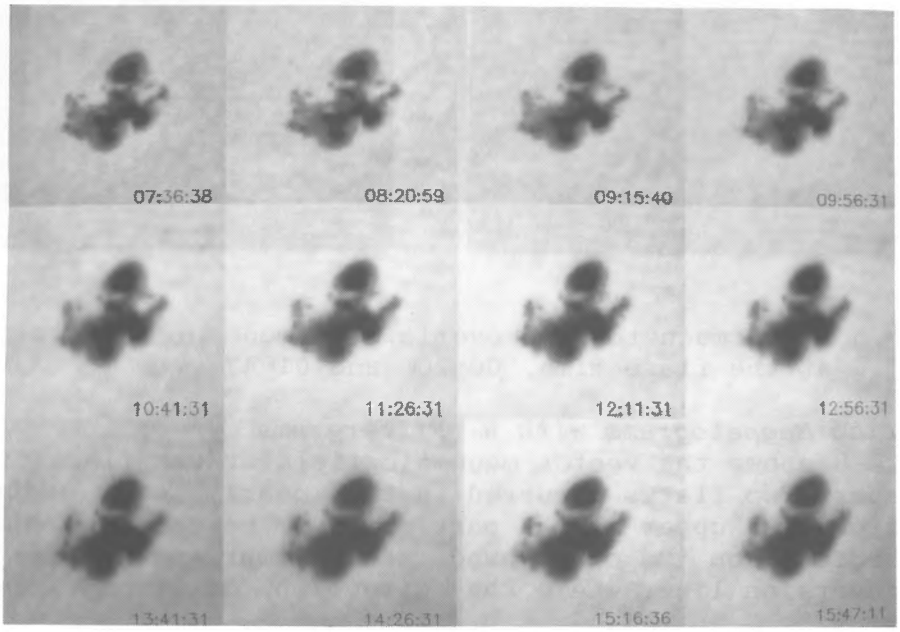

Fig.3 The evolution of sunspot on 27 October,1992.

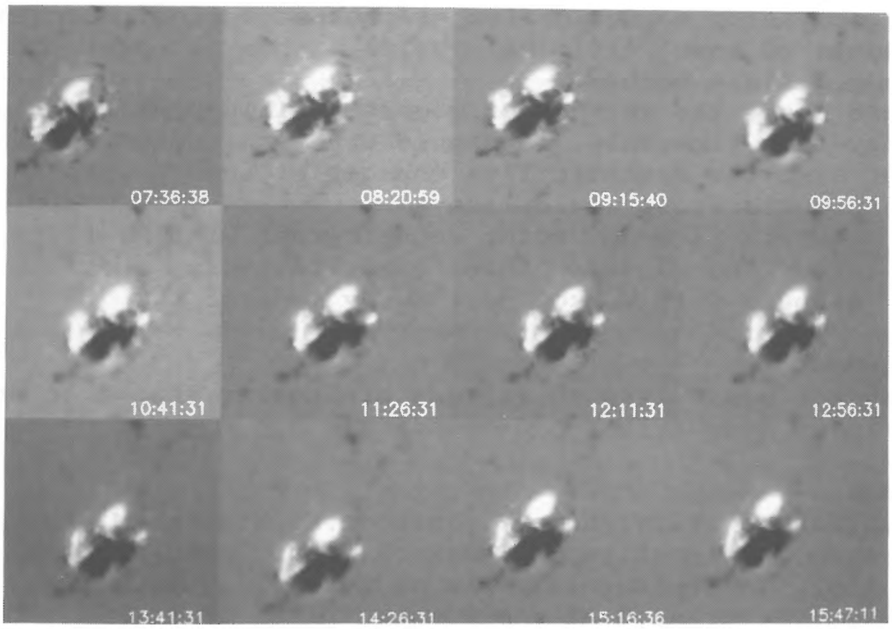

Fig.4 The evolution of longitudinal magnetic field on 27 October,1992.

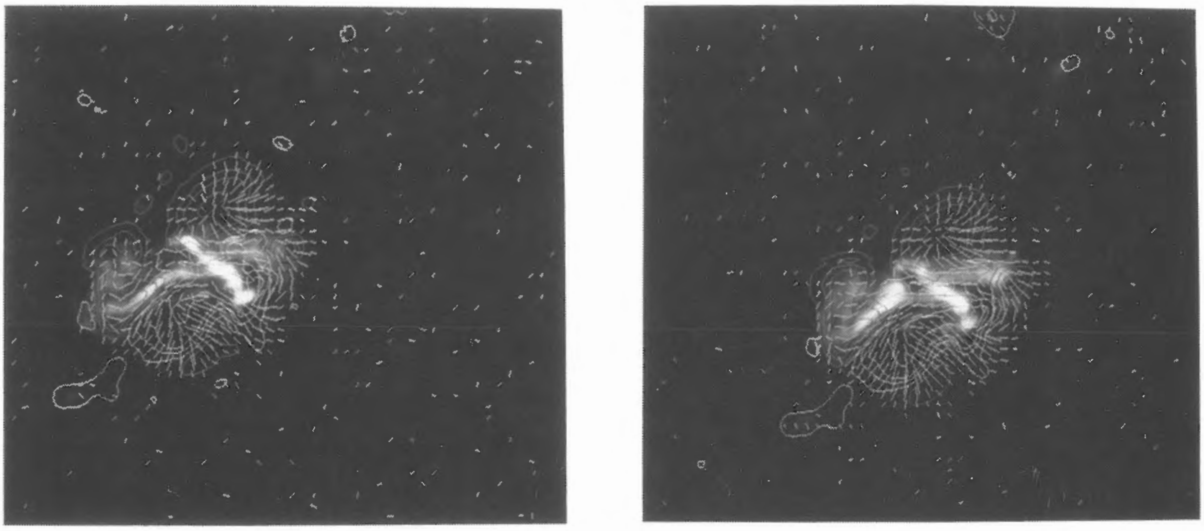

Fig.5 Vectormagnetograms overlaid Hα monochromatic images at the flare time, 00^h20^m and 01^h47^m.

3-3 Comparing Magnetograms with Hα Filtergrams

Figure 5 shows the vector magnetic field at the flare time overlaid the Hα images. Two flares occurred in the nearly same magnetic field configuration. The upper bright part seems to be connect the different polarity regions, on the other hand, the lower part lies along the magnetic inversion line, where the direction of transverse field is parallel to it.

4.Conclusion

We conclude that two flares occurred on this day are as called homologous flares. In this region, the magnetic shear is gradually built up by the increasing magnetic flux or sunspot motion. When the magnetic energy amounts to some ciritical value, then a part of energy is released and a flare occurs.

In this case, the changes of magnetic field configuration is very small in day-long timescale. We should study not only the morphological feature but also the magnetic flux changes at each points in detail.

In future stage, we would like to
compare face-on vector magnetograms with Hα filtergrams,
study the magnetic shear quantitatively, and
compare with Yohkoh soft X-ray images.

Acknowledgement

The author would like to express his hearty thanks to Dr.K.Ichimoto for his helpful suggestions and comments.

References

Ichimoto,K.,Sakurai,T.,Nishino,Y.,Shinoda,K.,Noguchi,M.,Kumagai,K. Imai,H.,Irie,M.,Miyashita,M.,Tanaka,N.,Sano,I.,Suematsu,Y. and Hiei,E.,1993, *in The Magnetic and Velocity Fields of Solar Active Regions*, ed. H.Zirin, G.Ai and H.Wang, p.166.

Optical and X-ray Observations of the X9 Flare on 2nd Nov. 1992

K. Ichimoto, T. Sakurai, Flare Telescope and Norikura Teams,
National Astronomical Observatory, Mitaka, Tokyo, 181, JAPAN
and Yohkoh SXT Team

Abstract:

The decay phase of the X9 limb flare on 2nd November 1992 was observed in X ray, Hα and optical continuum, simultaneously. Geometrical relation and temporal evolutions of the X-ray source and Hα loop system are investigated together with the mass balance between them. It is found that the observed characteristics are consistent with the standard model of two ribbon flares in which successive magnetic reconnection is thought to produce the post flare loop system. However a quantitative analysis suggests that the magnetic field which forms the flare loop may not be strong enough to confine the hot flare plasma rigidly as assumed in many theoretical works.

1. Introduction

Two ribbon flares and the associated post flare loop systems are generally interpreted by the successive reconnection of the open magnetic field above the magnetic neutral line (Hirayama, 1971, Kopp and Pneuman, 1976). The evidences of the ongoing magnetic reconnection process were also presented by the recent soft X-ray observations (Tsuneta, 1993). According to this model, new flaring loops are created successively by means of the progress of the reconnection to the higher corona. Each loop is initially filled by the 10^7K plasma due to the chromospheric evaporation driven by high energy electrons or heat conduction to form the soft X-ray source. Due to the following radiation and conduction, the loops are cooled and finally become visible in Hα. The 10^4K plasma is observed to fall down along both legs of the loops. A number of numerical simulations were carried out by focusing the dynamical evolution of the individual flaring loops. Basic point assumed in these models is that the magnetic field of the flare loop is strong enough for the flaring plasma to be rigidly confined throughout the flare process, i.e., the cross section of the loop is assumed to be constant with time and each loop keeps its identity. In this paper we call this scenario of flare as "standard model" regardless of the detailed mechanisms of the primary energy release and the energy storage.

The X9 flare on 2nd Nov. 1992 gives us a good opportunity for studying the validity of the standard model. The flare occurred in the active region NOAA 7321 that was located behind the west limb about 15deg. According to the GOES data, the flare started at 02:31UT and reached its maximum at 03:08UT.

The X-ray enhancement was observed to last for almost a day. Unfortunately, the Yohkoh was in the shadow of the earth at the initial phase, but the following decay phase was observed successfully by the Soft X-ray Telescope (SXT). At the same time, Hα observation was made by the Solar Flare Telescope at Mitaka and optical continuum images were obtained by the coronagraph at the Norikura Solar Observatory. In this paper, we study geometrical relations and temporal evolution of the flare sources obtained in the deferent wavelengths in order to check the consistency of the observational characteristics of the post flare system with the standard flare model.

2. Geometrical relation of the Hα and X ray sources

Figure 1 shows the Hα image and soft X-ray image taken with Al0.1 filter at around 05:07UT. To illustrate the geometrical relation the Hα image is overlaid with contours of the soft X-ray intensity. The Hα image shows a prominent loop system with a number of thin loops. The remarkable point is that the top of the Ha arcade is closely outlined by the lower boundary of the X-ray bright source. Hα loops are located just under the flaring hot plasma. This result supports the standard scenario of the successive cooling of the hot plasma to form the low temperature loops. It is also noted, however, that the X-ray source shows less distinct loop structures. It is hard to identify individual loops in X-ray images that correspond to the Hα loops. This is not

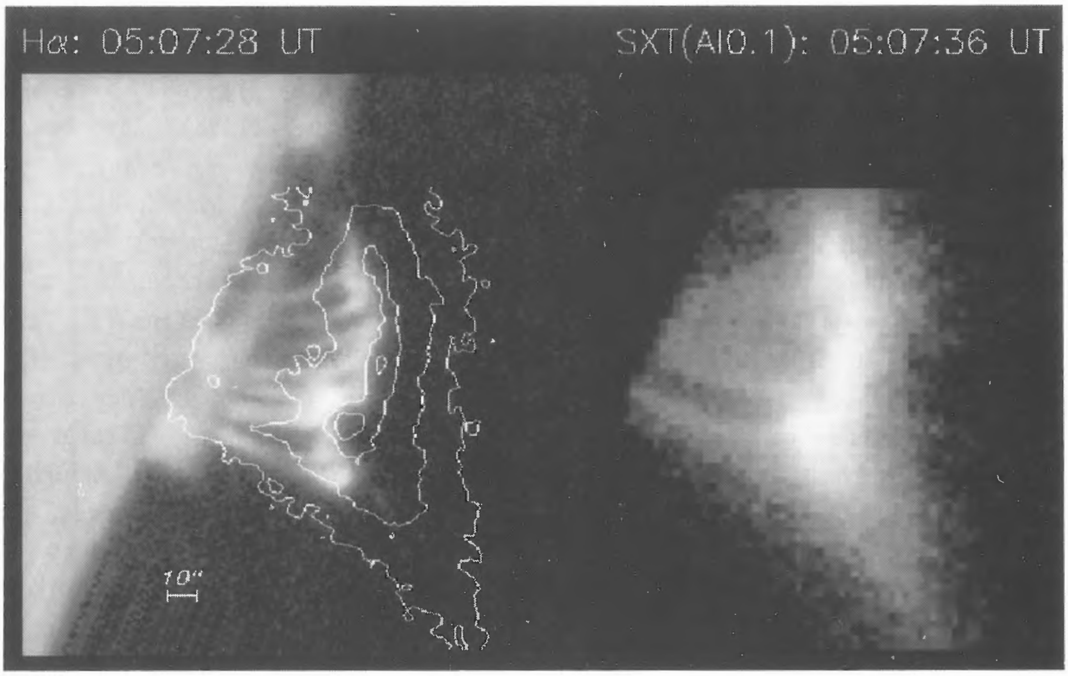

Figure 1. Hα (right) and Soft X-ray (left) images at 05:07:28UT and 05:07:36UT, respectively. Hα image is overlaid by the X-ray intensity contour to illustrate the geometrical relation of them.

due to the difference of the spatial resolution of two observations; SXT has enough resolution to resolve the structures of Hα loop size.

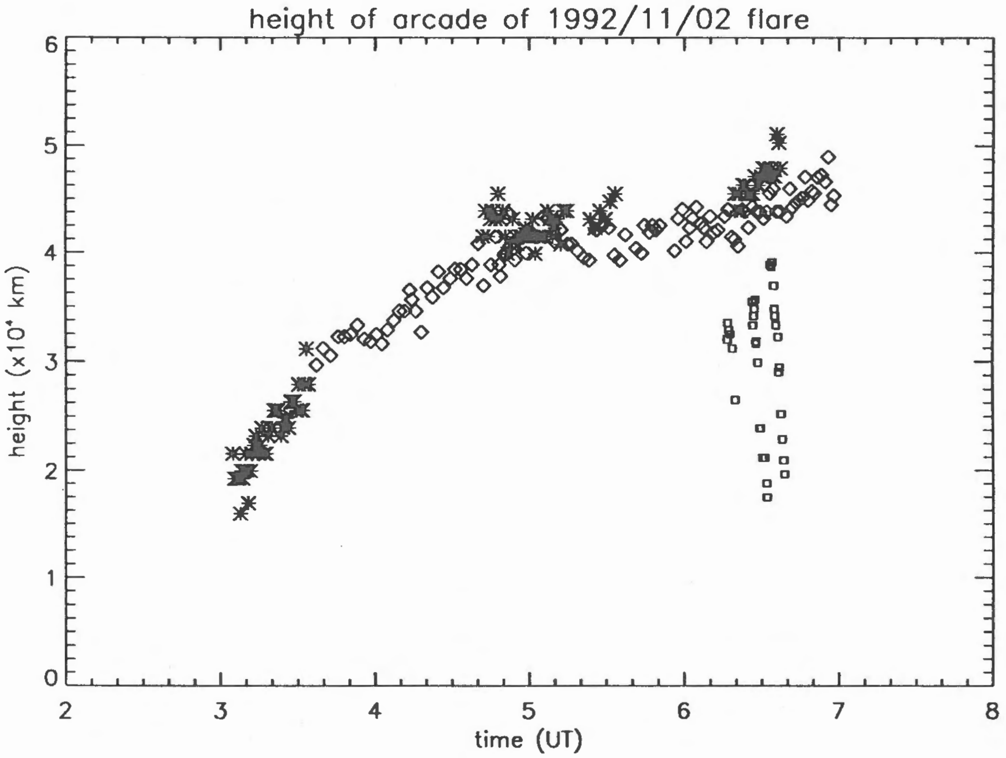

Figure 2. Time variation of the height of Hα and X-ray sources. Open diamonds show the average height of the Hα arcade and asterisks show the height of the X-ray source. The small squares show the location of the falling Hα blobs along the loop legs.

Figure 2 shows the time variation of the height of Hα and X-ray sources. Open diamonds show the average height of the Hα arcade and asterisks show the height of the X-ray source. Again we confirmed that the Hα arcade is located just below the X-ray source and the difference of height is about 3000km. Both sources show a gradual growth in height after an initial more rapid increase before ~4:30UT. The rate of the height change in the later phase is estimated to be about 0.7km/s. From this figure, we can derive a "cooling time" of the flaring plasma that is defined by the deference of times at which the X-ray source and the Hα arcade reach the same height. The rough estimation gives ~1 hour for the "cooling time".

The small squares below the main sources show the location of the falling Hα blobs along the loop legs. Although there are many Hα loops which show falling blobs, we plotted only a few samples. These plots give us the average velocity of the downward motion of ~60km/s.

3. Relation between the X-ray and continuum images

The combination of the X-ray intensity and the optical continuum produced by the Thomson scattering by free electron informs us the intrinsic electron density and geometrical thickness of the source, because the X-ray intensity gives $n_e^2 l$ and continuum intensity gives $n_e l$ (Ichimoto et.al. 1992). The coronagraph observation was made with the 10-cm coronagraph at the Norikura Solar Observatory in continuum at 6630A. Figure 3a and 3b show contours of $n_e l$ and $n_e^2 l$ derived from the continuum and X-ray intensities. The dashed line in figure 3b shows the edge of occulting disk of the coronagraph. From these figures we can estimate the total electron number $(n_e V)$ and the volume emission measure for the area that corresponds to the continuum image $(n_e^2 V)$. By combining these values, we can calculate the average electron density(n_e) and the volume(V). The obtained values are followings;

$n_e V \sim 3.6 \times 10^{39}$
$n_e^2 V \sim 9.5 \times 10^{49}$ cm^{-3}
$n_e \sim 2.6 \times 10^{11}$ cm^{-3}
$V \sim 1.4 \times 10^{29}$ cm^3.

We can also estimate the "apparent volume" of the source by taking the $A^{(3/2)}$, where A is the area of the source. If we adopt for A the area that is enclosed by the second soft X-ray contour and the edge of the occulting disk, the calculation gives 1.7×10^{29} cm^3 as the volume of the source. It is noticed that this value is nearly equal to that derived above from the continuum and the X-

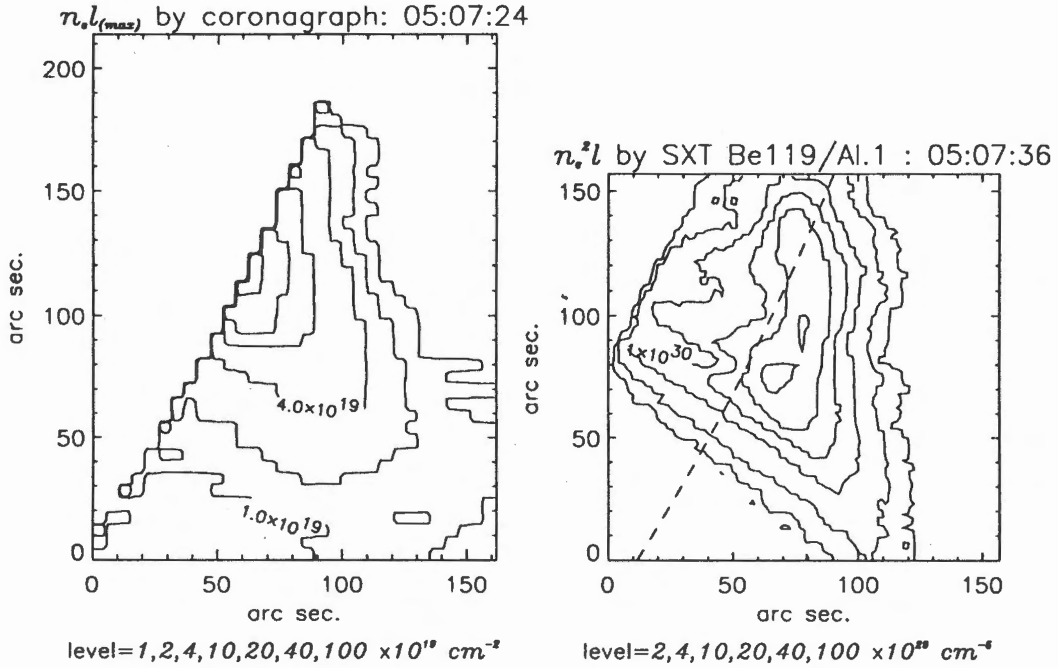

Figure 3. Distribution of $n_e l$ and $n_e^2 l$ obtained by the coronagraph and Yohkoh SXT.

ray intensities. This rsult means that the filling factor of the 10^7K plasma is almost 1 as inferred from the rather unstructured distribution of the X-ray source.

4. Discussions

In this section we discuss about the consistency of the standard flare model with the observation. It should be remarked first that the geometrical relation of the hot and cool plasma and their temporal evolution are fairly consistent with the standard scenario of the successive reconnection towards the higher corona. Now we consider about the mass balance between the hot plasma and the falling cool material. In section 3 we have derived the total electron number of the hot plasma to be $\sim 3.6 \times 10^{39}$. On the other hand, the falling rate of the cool plasma can be estimated by the following expression;

$$dn/dt \sim S*n*v*N*2$$

where S is the average cross section of the Hα loops, n is the particle density in the loop prominence, v is downward velocity of the falling material and N is the number of Hα loop at the moment. We adopted $S=(1.5 \times 10^8)^2$, v=60km/s, N=10 from the Hα images and $n=1 \times 10^{11.5}$ cm^{-3} as a typical value for the loop prominences (Hirayama, 1978). These values give the falling rate of 8.5×10^{35} particles/sec. If the origin of the cool plasma is the overlaying hot plasma as considered in the standard model, the total particle number of the hot plasma divided by the falling rate gives the time by which the flare loops are almost evacuated or, in other words, the time by which the hot plasma at the time is replaced by cool plasma. This value is calculated to be ~4200sec. It is noticed that this value is fairly consistent with the "cooling time" derived in section 2 from the geometrical evolution of the Hα and X-ray sources. The standard model of flare is, therefore, consistent with the observation in the point of view of the mass balance between hot and cool plasma.

Finally we consider about the magnetic and gas pressures in the flare loop. As already be mentioned, it is difficult to identify the individual loops in X ray images, i.e., it is difficult to trace the history of individual flare loops as expected from the standard modeling. Actually the quantitative analysis in section 3 shows that the filling factor of the hot plasma is nearly equal 1, whereas the filling factor of the Hα loop system seems to be much less than 1. What dose this result implies? One possible explanation may be that the magnetic loops expand during their hot phase due to the high pressure of the hot plasma. The gas pressure of the 10^7K plasma can be derived from the electron density obtained in the previous section and it is about 55dyne/cm^2. On the other hand the photospheric magnetic field obtained on 28th Oct. and the potential field extrapolation to the corona infer the magnetic field strength of about 30G at the height of 5x10^5km. This value corresponds to the magnetic pressure of about 36dyne/cm^2. Therefore the situation mentioned above may be the case because the gass pressure exceeds, or at least comparable with, the magnetic pressure. The magnetic field which forms the flare loops may not be strong enough to confine the hot flare plasma rigidly as assumed in many theoretical works. It is not clear, however, whether this results can be generalized to other smaller flares or not. Further analysis and coordinated observations with X-ray and optical telescopes are desired.

Acknowledgments

The authors are appreciated to Mrs. J.Denpo and T.Fukushima for making the Hα data reduction.

References

Hirayama,T., 1971, Solar Phys. 17, 50.
Hirayama,T., 1978, Proceeding of the IAU Colloquium No.44, 4.
Ichimoto,K., Hirayama,T., Yamaguchi,A., Kumagai,K., Tsuneta,S., Hara,H., Acton, L., and Bruner,M.E., 1992, Publ.Astron.Soc.Japan, 44, L117.
Kopp,R.A. and Pneuman,G.W., 1976, Solar Phys. 50, 85.
Tsuneta,S., 1993, Astronomical Society of the Pacific Conference Series, Vol.46, 239.

Hard X-ray images at the flare on 1992 October 27

Tatsuo TAKAKURA

Department of Astronomy, University of Tokyo, Tokyo 113, Japan

and the HXT group

Abstract

Hard X-ray images in the impulsive phase of the flare of 0145UT, 27 October 1992 are presented. The images show double source structure. One footpoint shows nonthermal spectrum, while the other shows thick target X-rays from super hot thermal electrons with 80 million degrees. This observation is consistent with the anomalous heat conduction model for the the loop flare.

Comment

Time profiles in four energy bands of the X-ray burst are shown in Figure 1. X-ray images in the three energy bands are shown in Figure 2, in which photon energy and the time of snap shot are indicated in each panel. The panel number of each X-ray map is identical with the numeral shown in the top panel of Figure 1 indicating the time range of snapshot of the X-ray map. The two peaks in the contour maps lie on the regions with opposite magnetic polarities. Consequently, the double source is probably foot points of a single coronal loop. The X-ray spectrum can be obtained from the brightnesses (counts/s/pixel) in the three energy bands. It is interesting that the average brightnesses on 3×3 pixels in each energy band in the lower source (B) at the Time (2) and (3) give a thick target spectrum from the electrons flowing into the chromosphere with quasi- thermal distribution, $T_e \simeq 8 \times 10^7$ K at the Time (3), otherwise power law spectral index for the X-ray photons is 3.6 between L and

M1 bands and 5.3 between M1 and M2 bands. The thermal electron number density is $2 \times 10^{7} \mathrm{cm}^{-3}$ at the Time (3). On the other hand, the spectrum for the upper source (A) is nonthermal and seems to be a mixture of power law and thermal spectra. It becomes approximately power law at the Time (3) with the X-ray photon spectral index of 3.3, i.e., the index for electron energy is 4.8, and the electron number density above 15 Kev is $2.6 \times 10^{7} \mathrm{cm}^{-3}$. This observation is consistent with the 'anomalous heat conduction model' presented by the simulation (Takakura, 1992) for the loop flares. These images are not compared with the radio contour maps yet, but the source (A) is probably much brighter than (B) in the radio maps.

References

Takakura, T. 1992, *Solar Phys.*, **142**, 327.

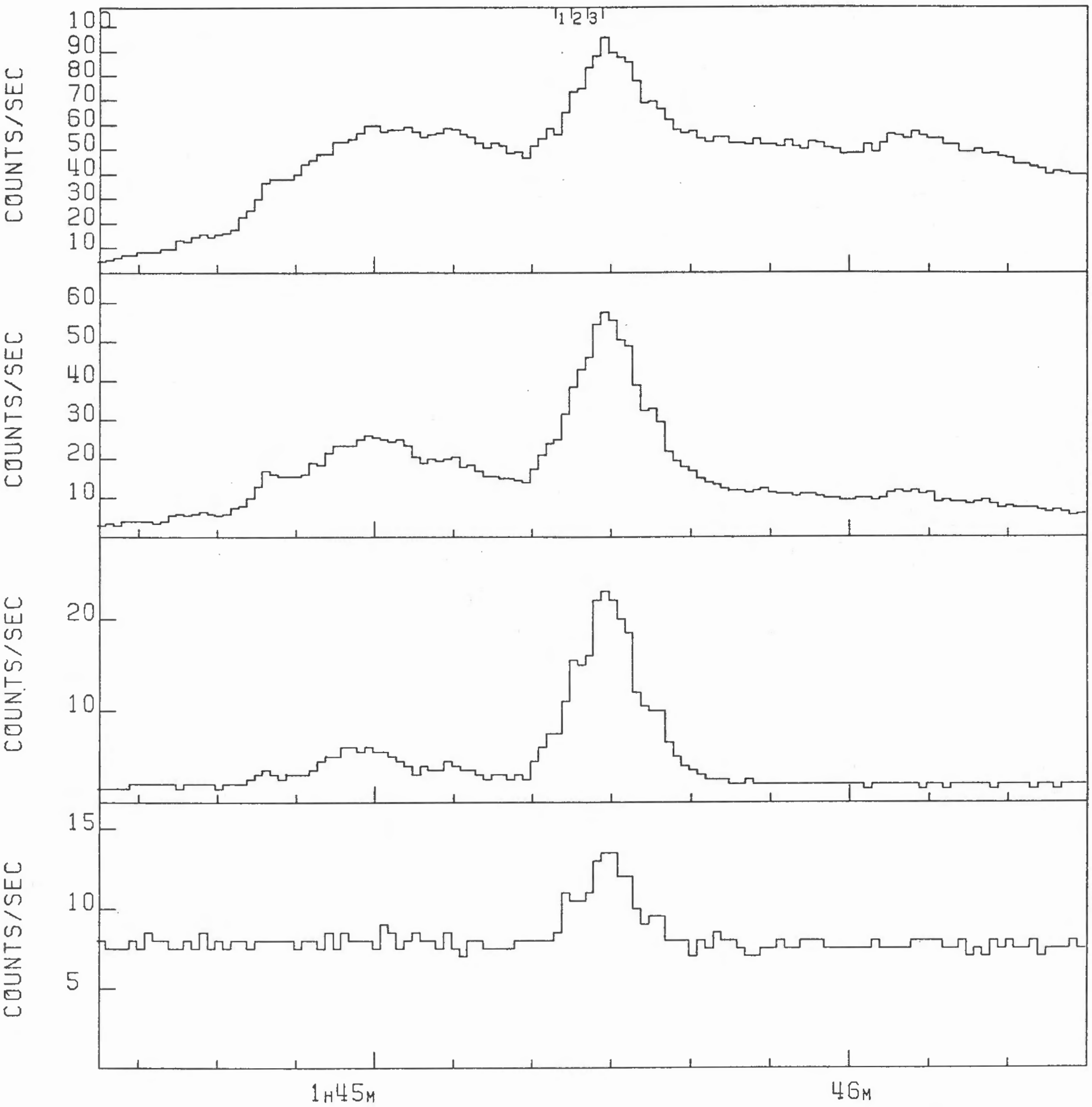

Fig.1. Time profiles of the X-ray burst on 1992 October 27 in four energy bands L, M1, M2, and H from top to bottom: L; 13.9-22.7 keV, M1; 22.7-32.7 keV, M2; 32.7-52.7 keV, H; 52.7-92.8 keV. Since the effective mean collecting area per each collimator is about 1 cm^2, the vertical scale is approximately X-ray flux ($\mathrm{c\,s^{-1}cm^{-2}}$). The numerals marked on the curve in the top panel show the times of snapshots of X-ray maps shown in Figure 2.

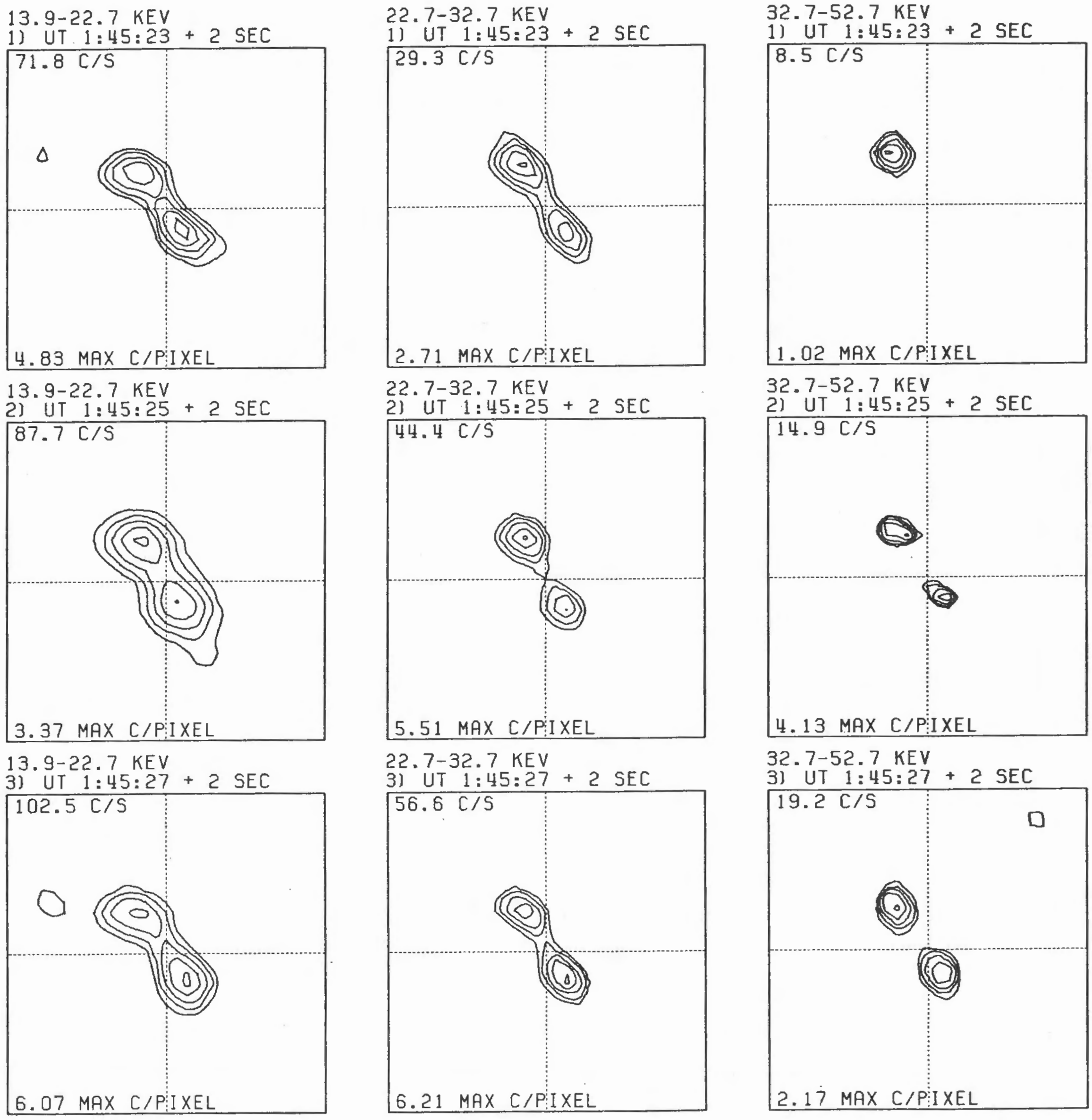

Fig.2. X-ray contour maps of the burst. The photon energy, the starting time and integration time of the map are shown in each panel. The panel number is identical with the numeral shown in Figure 1 indicating the time of the snapshot. The minimum contour level is 0.1 times the peak brightness in each map and the contour steps are logarithmic with $\sqrt{3}$ steps. The map size is 76.6 arcsec square. The map center is 4.663 arcmin west and 8.031 arcmin south from the solar center. The solar north is upward (y-axis) in the maps. In each panel, X-ray count/sec and count/pixel in the brightest pixel are shown.

Evolution of Radio Features in a Flare Productive Active Region NOAA7321

Masanori NISHIO[1], Tatuo TAKAKURA[2], Shinzo ENOME[1], Hiroshi NAKAJIMA[1],
Kiyoto SHIBASAKI[1], Toshiaki TAKANO[1], Yoichiro HANAOKA[1], Yong-Seok CHOI[1,2], and Hideki KOSHIISHI[1,2]

[1]*Nobeyama Radio Observatory, National Astronomical Observatory, Minamisaku, Nagano 384-13, Japan*
[2]*Department of Astronomy, School of Science, The University of Tokyo, Bunkyo-ku, Tokyo 113, Japan*

Abstract

By the Nobeyama Radioheliograph, evolution of radio features in flare productive active region NOAA7321 was observed. Delay of emergence of radio feature was detected comparing with soft X-ray feature observed by Yohkoh, which implied that coronal region above NOAA7321 had weak magnetic field strength and high temperature at initial phase of evolution. From observations by the radioheliograph and radio polarimeters, burst spectra with high turnover frequency and steep lower cutoff was obtained,it is suggested that the radio bursts in NOAA7321 were caused by continuous appearance of strong magnetic field regions to lower corona.

1. Introduction

The Nobeyama Radioheliograph started routine observation at late June 1992. This instruments is an interferometer dedicated to solar observations, with which two dimensional images of the whole sun are observed with spatial resolution of about 10″ and temporal resolution of 50 ms (Nakajima et al. 1994). Observation frequency is 17GHz, where energetic electrons with few hundred KeV have a important role in radio burst. In 1992, we had observed three flare productive active regions NOAA7260, 7270 and 7321 by the radioheliograph. These flare productive active regions had complex features and occupied large area wider than few arc-min. Therefore, wide field of view of the radioheliograph is quite essential to study these flare productive active regions.

In this paper, we will describe radio images of NOAA7321 observed by the Nobeyama radioheliograph and discuss evolution of radio emitting sources in NOAA7321.

2. Observation

The active region NOAA7321 emerged at S24E11 on Oct. 24, 1992 and quickly evolved on succeeding few days. This region reached to west limb on Nov.1 and was behind the west limb on Nov. 2. In the radio images taken by the Nobeyama Radioheliograph, no radio feature was detected associated with NOAA7321 on Oct. 24, where observation time was from 2300UT on Oct. 23 to 0640UT on Oct. 24. On the other hand, in Yohkoh soft X-ray images taken at 0423UT on Oct. 24, a small source with weak brightness enhancement was seen associated with NOAA7321. On Oct. 25, a bipolar radio feature was observed at the location of NOAA7321, which two sources were placed in northwest to southeast direction. Northwest source of this bipolar feature polarized to left circular polarization (≈ 40%) and southeast source showed right circular polarization (≈ 20%). This feature was similar with those observed by white light, where two sunsopts were seen on northwest and southeast sides.The radio feature associated with NOAA7321 became more complex in following few days. On Oct. 28, five bright radio sources were observed in NOAA7321. Evolutions of radio features of NOAA7321 is shown in figure 1. The partial images in this figure are cut out in equal latitude. Therefore, displacement of brightest portions on north-south direction is real. On Oct. 31, a post flare radio loop were observed in NOAA7321.

By the Solar Geophysical Data (SGD), flares were detected after Oct. 25 in NOAA7321 and many flares were reported until Nov. 2. By the radioheliograph, radio counterparts of 30 GOES soft X-ray flares were observed in NOAA7321, in which one X-class flare (X9.0 flare on Nov. 2) and three M-class flares (M1.0 and M1.1 flares on

Oct. 27, and M1.3 on Oct. 31) were included. Summary of these radio events is shown in table 1. In many bursts observed in NOAA7321, polarization enhancements of about 10% were detected before or during impulsive phase. Onset of the X9.0 flare was 0231UT on Nov. 2. As mentioned above, NOAA7321 was behind the west limb on Nov. 2. By the radioheliograph, extremely bright sources were detected at west limb just in front of the location of NOAA7321.

The flares listed in table 1 were also observed by radio polarimeters at Nobeyama and Toyokawa. Observation frequencies of these polarimeters are 1, 2, 3.75, 9.4, 17, 35 and 80 GHz. With these radio polarimeters, we can obtain spectral profiles of radio bursts. The estimated spectra of the bursts in NOAA7321 had turnover frequencies of higher than or equal to 17 GHz in many case. In addition, steep lower cutoff profiles were obtained in some case. Figure 2 shows time profiles of the M1.1 flare on Oct. 27 obtained by 2, 3.75 and 9.4-GHz radio polarimeters at Toyokawa. We can see impulsive burst activities at 9.4 GHz. On the other hand, no clear variation was detected at 3.75 and 2 GHz associated with impulsive activities at 9.4 GHz. On Oct. 25 0653UT,

Oct. 28 0118UT, 0122UT and 0445UT, and Oct. 31 0658UT, negative bursts were observed by 2, 3.75 and 9.4-GHz polarimeters. These were not detected by the radioheliograph, and no information was obtained about positions. However, the negative burst on Oct. 25 was observed during a Hα flare activities in NOAA7321. Other negative bursts were observed before or after the radio burst activities in NOAA7321.

3. Discussion and Summary

From soft X-ray and radio observations of NOAA7321, it was found that emergence of radio feature was delayed by one day comparing with those of soft X-ray feature. As well known, both soft X-ray and radio emission originate in coronal region. Intensity of soft X-ray emission closely depends on plasma temperature and density of emitting region. On the other hand, radio emission with strong circular polarization is closely related with magnetic field structure in emission region. Assuming that slowly varying radio emission in NOAA7321 was caused by thermal gyro-resonance mechanism and third harmonics of gyro frequency was dominant, magnetic field strength of radio emitting region comes out to be about 2000 Gauss. The delay of emergence of radio feature suggests that coronal region above NOAA7321 had weak magnetic field strength and high temperature at initial phase of evolution.

The radio bursts in NOAA7321 had high turnover frequency comparing with usual radio bursts. The turnover frequency ν_{max} of nonthermal radio emission is given by

$$\nu_{max} = AN^{1/3}B^{2/3},$$

where N is the column density of the source, B is the magnetic field strength and A is constant (cf. Tandberg-Hanssen and Emsli, 1988). From high turnover frequencies and steep lower cutoff spectral profiles of the bursts, and polarization enhancements before or during the bursts, it is implied that the radio bursts occurred in lower lying loops with strong magnetic filed strength and lower frequency radio emission from burst region was cut off by overlying gyro-resonance layer or plasma cutoff layer.

We have no clear observational result to identify the position of observed negative bursts with NOAA7321. However, the times of these events coincided with those of flares or radio bursts in NOAA7321, and it is possible to consider that the observed negative bursts occurred in NOAA7321. The negative bursts are usually related with surge activities or quick changes of electron density, electron temperature and magnetic field configuration (Shibasaki et al., 1979). The surges and the changes of magnetic field configuration are sometimes associated with flux emergence. Therefore, the observed negative bursts suggests that flux emergence in NOAA7321 continued for long time.

From these discussion, it is suggested that the radio bursts in NOAA7321 were caused by continuous appearance of strong magnetic field regions to lower coronal region.

References

Nakajima, H., Enome, S., Shibasaki, K., Nishio, M., Takano, T., Hanaoka, Y., Torii, C., Sekiguchi, H., Bushimata, T., Kawashima, S., Shinohara, N., Irimajiri, Y., Koshiishi, H., Kosugi, T., Shiomi, Y., Sawa, M., and Kai, K. 1994, *Proc. IEEE,* in press.

Tandberg-Hanssen, E., and Emsli, A. G. 1988, *The Physics of Solar Flares,* Cambridge University Press, Cambridge, p.193.

Shibasaki, K., Ishiguro, M., Enome, S., Takayanagi, T., and Torii, C., 1979, *Proc. Res. Inst. Atmospherics, Nagoya Univ.,* **26**, 53.

Table 1. Reported GOES flares on NOAA7321 and associated radio bursts observed by the Nobeyama radioheliograph

	X-ray				Hα	Radioheliograph			17GHz
DATE	BEGIN	MAX	END	CLASS	CLASS	BEGIN	MAX	END	FLUX[3]
OCT.25	0051	0057	0103	C1.5	-	Not detect[4]			-
	0519	0524	0533	C1.2	-	(0519)	–	–	-
OCT.26	0230	0235	0244	C2.0	-	(0227)	–	–	-
	0315	0319	0327	C1.3	-	0330	0330	0330	-
	0505	0509	0515	C1.3	-	0507	0508	0512	-
	0557	0600	0604	C1.3	-	0546	0546	0548	-
						0613	0613	0617	-
	2255	2302	2305	C1.9	SF	$\leq$ 2258	2302	2308	-
OCT.27	0011	0020	0025	M1.0	1N	0013	0016	0035	50
	0143	0150	0159	M1.1	-	0145	0146	0206	100
	0207	0210	0212	C4.5	-	(0207)	–	–	-
	0355	0358	0401	C2.3	-	0336	0356	0404	20
	0430	0433	0436	C1.4	-	0430	0430	0437	22
	0616	0620	0632	C5.2	-	0533	0615	$\geq$ 0640	-
OCT.28	0418	0422	0426	C2.3	SF	0420	0420	0421	185
OCT.29	0631	0634	0638	C2.1	1N	0632	0632	0633	70
	2359	0004	0010	C4.9	SF	0001	0001	0018	20
OCT.30	0053	0057	0101	C1.3	-	(0054)	–	–	-
	0217	0222	0248	C1.5	SF	0217	0217	0218	26
	0252	0300	0307	C2.5	-	0305	0305	0306	-
	0340	0346	0359	C1.1	-	(0345)	–	–	-
	0400	0418	0426	C1.5	1F	0431?	0431?	0431?	27
	0551	0554	0556	C1.9	SF	0530	0552	0604	-
OCT.31	0011	0027	0043	M1.3	SF	0018	0026	0046	23
	0347	0352	0403	C5.9	-	0348	0349	0407	24
	0429	0433	0435	C4.1	SN	0431	0431	0431	34
	0448	0455	0503	C5.2	-	0449	0449	0450	50
	0536	0543	0550	C6.3	-	0523	0523	0526	38
						0538	0538	0542	-
NOV.01	0050	0110	0125	C1.6	-	0108	0109	0110	-
	0131	0134	0137	C1.3	-	0141	0141	0141	-
NOV.02	0040	0057	0109	C1.4	-	(0045)	–	–	-
	0231	0308	0328	X9.0	-	0232	0249	$\geq$ 0640	30000

1. Times in ( ) is estimated by manual operation from radio images because no burst was detected by a burst detection procedure installed in the Nobeyama radioheliograph.
2. BEGIN, MAX, END are times in UT.
3. 17GHz FLUX is radio flux measured by 17-GHz radio polarimeter at Nobeyama and its unit is sfu.
4. GRF was observed in NOAA7323 at this time.

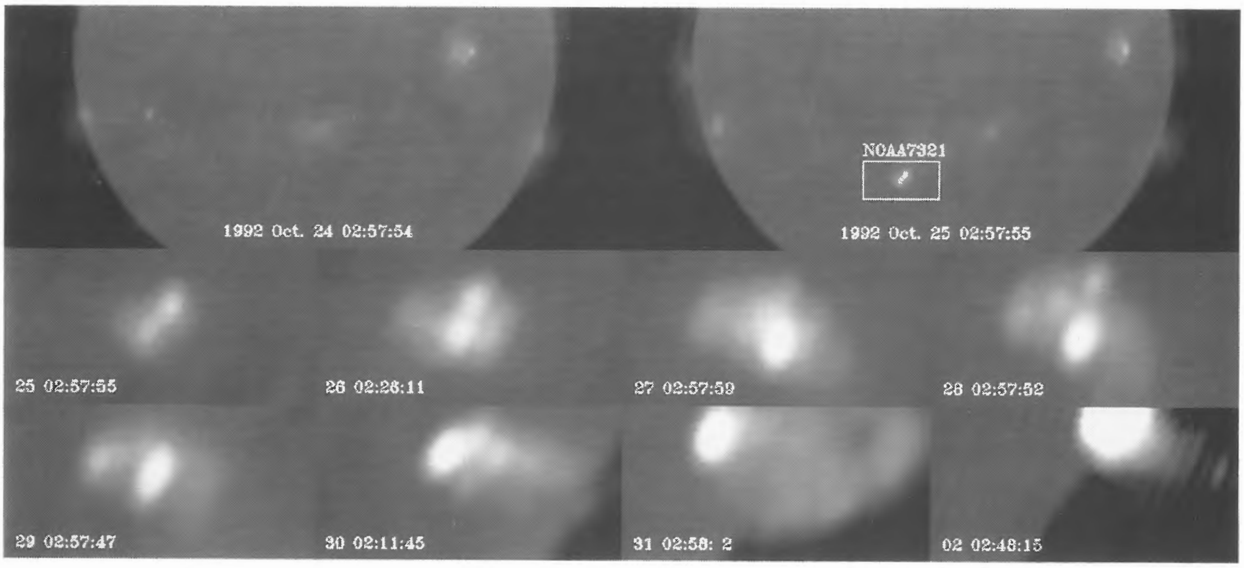

Fig. 1. Evolution of radio features in NOAA7321 observed by the Nobeyama Radioheliograph. Partial images shown in lower column are cut out in equal latitude. Therefore, displacement of brightest portions in these images is real.

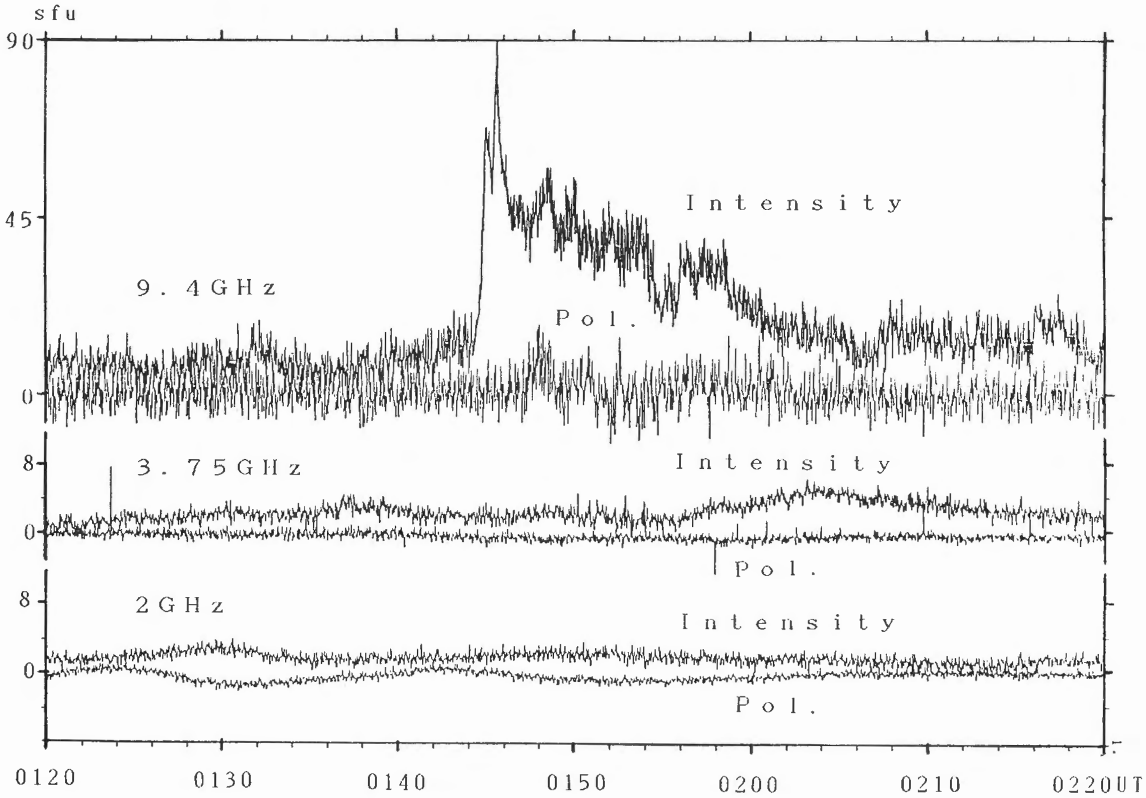

Fig. 2. Total radio flux density variations associated with M1.1 GOES flares on Oct. 27 observed by the Toyokawa 2, 3.75, and 9.4-GHz radio polarimeters.

Hα and Soft X-ray Activities in NOAA 7321 Region during 26-28 October, 1992

Yoshinori Suematsu and Nobuyuki Tanaka

National Astronomical Observatory, Mitaka, Tokyo 181, Japan

Abstract

We report some characteristics of the active phenomena which took place in the active region NOAA 7321 between 26 and 28 October, 1992, using Hα data from Mitaka flare patrol system and soft X-ray data from SXT/Yohkoh in addition to GOES X-ray data. It is shown that most Hα events well coincide with corresponding soft X-ray events, and that radiation energy in Hα is comparable to or greater than that in soft X-ray.

1. Introduction

The active region NOAA 7321, which appeared in the end of October, 1992, showed moderate activity (cf. other papers in this proceedings), and were observed with the soft X-ray telescope (hereafter referred to as SXT) on board Yohkoh satellite (Ogawara et al. 1991 and this proceedings) and a new flare patrol telescope at Mitaka (Tanaka et al. 1993).

We investigated this active region with aim of making clear the relationship between the soft X-ray and Hα activities. This type of investigation had been made before by Teske (1971) for minor activities on the limb and by Thomas and Teske (1971) for flares. Although their X-ray instrument had no angular resolution (OSO-III satellite), they found good time-association and good correlation in radiation flux between the soft X-rays and Hα activities. Since the SXT has good angular and time resolution (Tsuneta et al. 1991), we may have opportunity to make the relationship confirmative and further to find out the mechanisms of activities.

The SXT has been confirmed to be sensitive enough to detect small-scale coronal activities of the thermal energy less than 10^{28} ergs (e.g. Shimizu 1992, 1994; Shimizu et al. 1992, 1994) and it was turned out that some of them are spatially associated with Hα brightenings (e.g. Suematsu et al. 1994).

2. Hα and Soft X-rays Data

In real-time operation, the new Hα flare patrol system at Mitaka, which consists of 4-cm doublet, a Lyot filter of passband 0.5 Å, CCD camera, and a personal computer, provides us a time plot (four sec interval) of the ratio of Hα maximum intensity on the solar disk to the average intensity of its surrounding quiet region, the coordinate of the maximum intensity point, and also digitized Hα solar disk images at one min intervals (Tanaka et al. 1993). The intensity resolution is of 8 bits and one pixel size corresponds to about 5 arc sec. The Hα time plot turned out to be very powerful in detecting solar active phenomena.

For further analysis, we use the stored images of one min time resolution. The Hα disk images were corrected for center-to-limb variation, when the intensity ratio is calculated. The Hα intensity was normalized with an average intensity over a wide region around the disk center, excluding dark filaments and bright regions; therefore, the intensity of quiet region at disk center is unity by definition.

Regarding Hα radiation energy, excess Hα flux was calculated by summing the intensity larger than a threshold intensity, and subtracting the threshold intensity. The Hα excess flux was compared with soft X-ray flux from GOES.

Finally, the Hα images were coregistered with SXT/Yohkoh images (Figures 1a-b), using positions of sunspots, in order to compare the location of Hα brightenings and their spatial scales with those in SXT. In this analysis, we mainly used SXT partial frame images (64×64 pixels) of 5.2 or 2.6 arcmin square field of view, taken through thin Al filter effectively sensitive in the wavelength range of 5 to 15 Å.

3. Results

Figure 1 shows the evolution of active region NOAA 7321 in soft X-rays by SXT and Hα from 26 to 28 October, 1992. In early time of Oct. 26, the active region corona consisted of several separate loops lying mostly in the north-south direction. Some of the loops get brightened later on and the overall coronal structure changes; some of the loops disappeared out and the others changed the directions of axes. It should be noted that Hα bright regions correspond to footpoint regions of the coronal loops.

When the coronal loop brightened, the corresponding footpoint region in Hα get brightened too (e.g. 02:29:01 UT)

On Oct. 27, the active region corona looked quite different from Feb. 26, although Hα bright structure looked similar on both days. The coronal loops got highly sheared and weaved. It is likely that the loop in the west (righthand side of the figure) was expanding to the west. One can find out many brightening events this day (see Figure 2), including two GOES M1-class flares. The restructuring and activities of the active region continued on Oct. 28.

Figure 2 gives time plot of excess Hα flux from NOAA 7321 region and soft X-ray flux in 1 to 8 Å band from GOES satellite on 27 October. Note that the latter flux comes from the entire sun.

The Hα flux coinside very well with soft X-ray flux not only on the time variation but also on its amplitude. In the large flares, Hα flux tend to be lower than the soft X-ray flux. This could be due to the narrow passband (0.5 Å) of the Hα filter; some of flare emission can escape away from the passband.

In close look at the time-plot, we perceive that some brightening in Hα are almost missing in the soft X-rays. For instance, the Hα event at 04:15 UT in Figure 2 is very weak in the soft X-rays. In this event, we found that the bright structure in Hα, which looked like a crescent, was quite similar to that in SXT images. This implies that energy release responsible for this event took place in the low corona or possibly in the upper chromosphere.

For the coronal events equal to or smaller than GOES C-class, in general, the excess Hα flux defined here tend to be much larger than the soft X-ray flux in 1–8 Å band, when the apparent structures are quite similar each other, suggesting low-corona events. On the other hand, the Hα flux is comparable to the soft X-ray flux in the case of high-corona events, in which Hα brightenings appear at a few footpoints of brightened coronal loops. We will need much more data to make the results confirmative and quantitative.

We like to note that detailed analysis of Hα data will be very helpful to detect and study soft X-ray activities in the corona.

We would like to thank the entire SXT/Yohkoh teams for providing us the data and data analysis softwares. We are also grateful to the staff of Solar Physics Division, National Astronomical Observatory, for the routine observation of Hα flare patrol.

References

Ogawara, Y. et al. 1991, *Solar Phys.* **136**, 1.
Shimizu, T. 1992, Master Thesis, Department of Astronomy, The University of Tokyo
Shimizu, T. 1994, this proceedings.
Shimizu, T. et al. 1992, *Publ. Astron. Soc. Japan* **44**, L147.
Shimizu, T. et al. 1994, *Astrophys. J.*, in press.
Suematsu, Y. Shimizu, T. and Tanaka, Y. 1994, in "The New Solar Physics from YOHKOH", eds. by Y. Uchida et al., University Academy Press Japan, in press.
Tanaka, N., Suematsu, Y., and Yamaguchi, K. 1993, *Rep. Nat. Astron. Obs. Japan*, **1**, .
Teske, R.G. 1971, *Solar Phys.*, **21**, 146.
Thomas, R.J. and Teske, R.G. 1971, *Solar Phys.*, **16**, 431.
Tsuneta, S. et al., 1991, *Solar Phys.* **136**, 37.

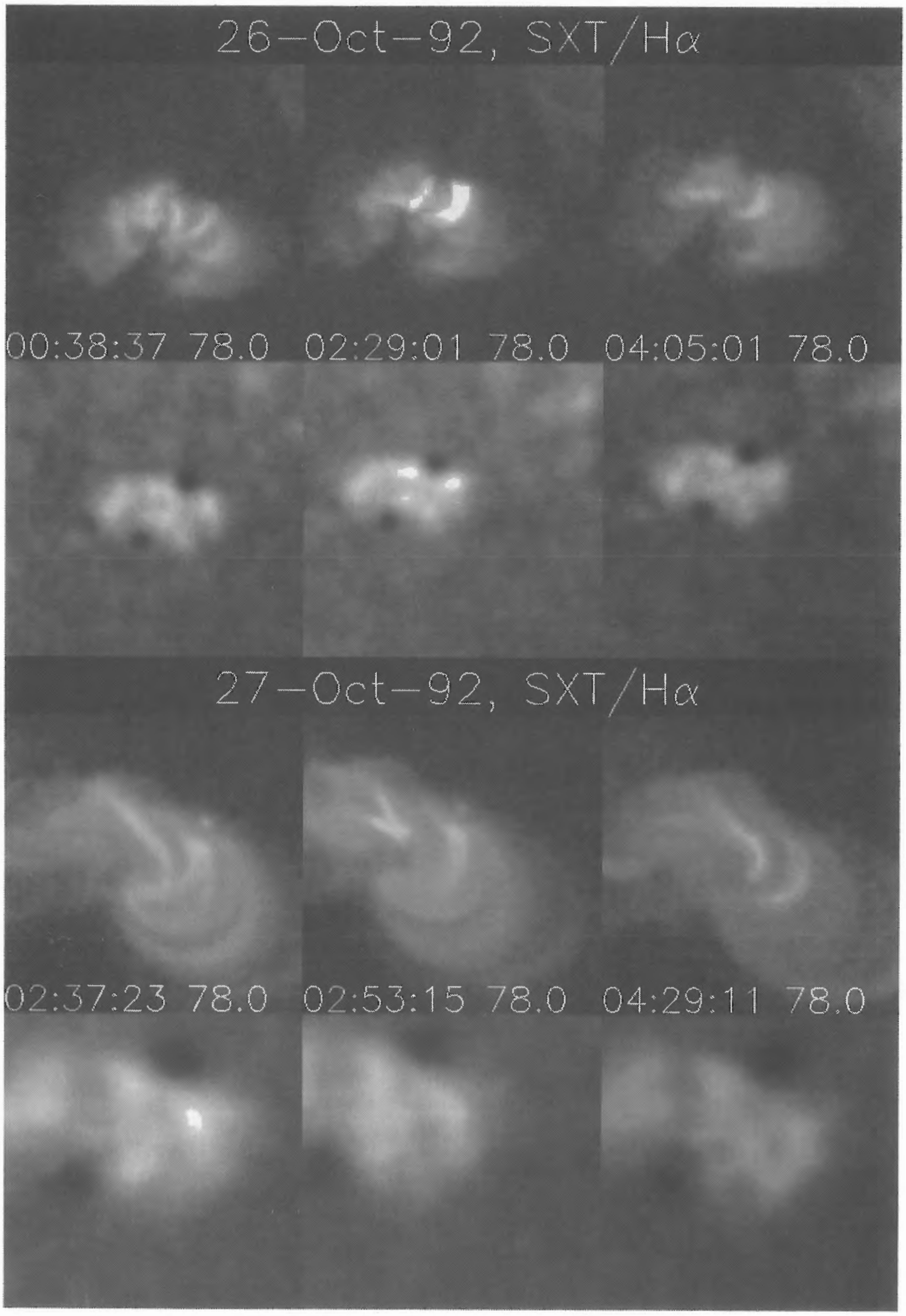

Figure 1a. Evolution of the active region NOAA 7321 in soft X-rays through thin Al filter of SXT (upper row) and in Hα (lower row) on 26-27 October 1992. The observed time in UT and exposure time in msec for soft X-rays are given in each soft X-ray sub-images. The field of view is 5.2 arcmin square for Oct. 26 and 2.6 arcmin for Oct. 27, respectively.

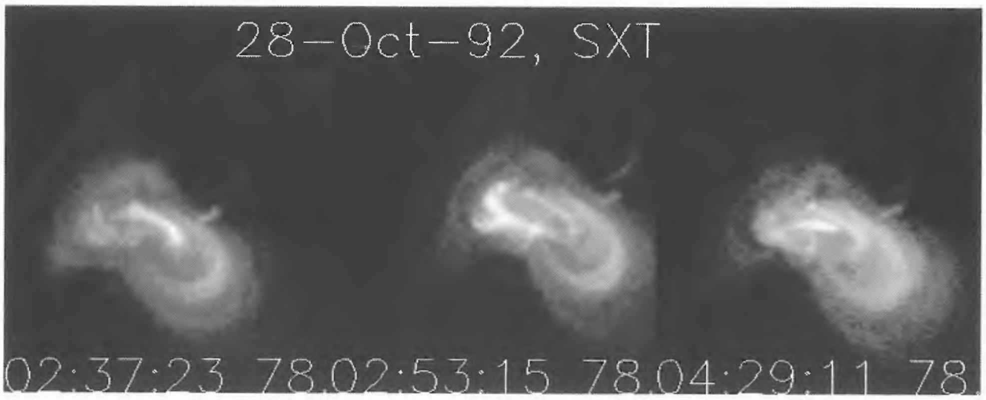

Figure 1b. Evolution of the active region NOAA 7321 in soft X-rays through thin Al filter of SXT on 28 October 1992. The observed time in UT and exposure time in msec are given in each sub-images. The field of view is 5.2 arcmin square.

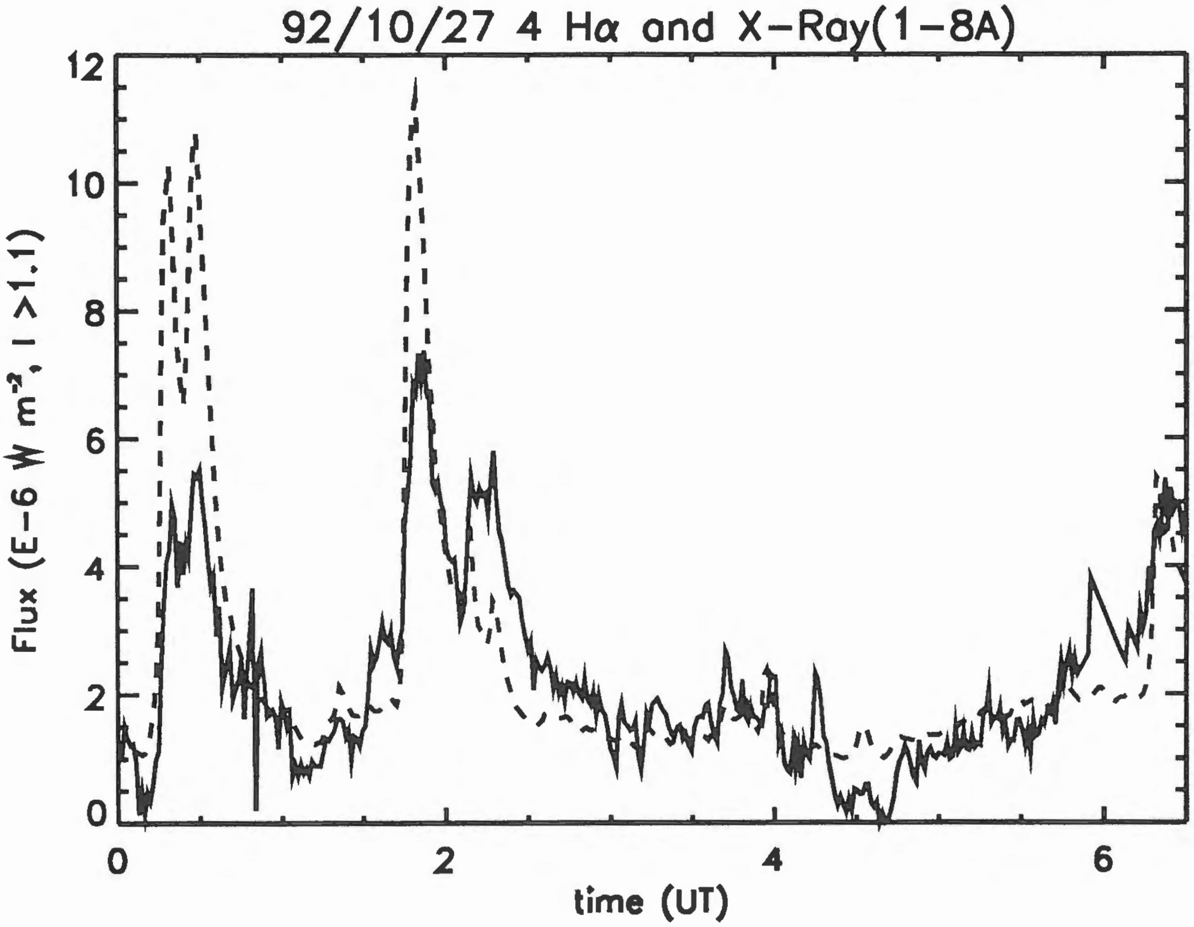

Figure 2. Time plot of excess Hα flux through 0.5 Å passband (solid line) from the active region NOAA 7321 and soft X-ray flux in 1–8 Å channel of GOES (dashed line) from the entire sun on 27 October 1992.

Session 4: NOAA 7260

An Overview of AR 7260

Jianqi You

Purple Mountain Observatory, Nanjing, China, 210008

Abstract

A brief description of the observations of AR 7260 and its evolution are given. It is found that most of the flares occurred around Aug.20, while great magnetic shear built up due to new emerging flux and sunspot motion.

1. Introduction

AR 7260 appeared at the east limb on Aug.11, 1992 and rotated to west limb on Aug.24. The maximum area of this sunspot group was 1440x10^{-6} Hemi (Aug. 20) and its longitudinal extent up to 15° for 6 days, so it is a quite large sunspot group. From SGD we learned that 134 optical flares and 63 XR events had been recorded. However, more than 92% of them are subflares, and not a >1N flare or >M4 XR event has been observed. In this paper, by combination of the information from Huairou and Purple Mountian Observatory, a brief description of the data observed is introduced. Besides, some dicussions about the flare occurrence are presented as well.

2. Observations and Data

First we tentatively define E_o and E_x to measure the daily solar activity as follows:

$$E_o = N_s + 10N_1$$
$$E_x = N_c + 10N_m$$

where N_s, N_1 are the numbers of subflares and the numbers of class 1 flares per day respectively, and N_c,N_m the numbers of SXR events of class C and M per day. As known the energy released in a class 1 flare is about 10 times that of a subflare. So E_o and E_x might be roughly proportional to the daily energy released by outburst. From figure 1 it is noticed that the E_o and E_x changed in similar way and both reached maximum on Aug.20. The observations we made are listed in table 1. The photographic observations of Hα and white light became available since Aug.17 and the magnetogram even later.

3. Evolution and Activity

As the Huairou magnetogram was not available until Aug.20, we have to refer to Kitt Peak magnetograms published in SGD. Before Aug.17 both the p spot and the main part of following small spots appeared to be S polarity and both embedded in a quite large area of N polarity, resulting in a SNSN sandwith magnetic configuration. We looked up SGD and found this might relate to the evolution history of AR 7260 (table 2). There existed another active region 7232 last rotation, located near the same disk position, only 6° westward. AR 7232 faded away when it passed the meridian and no visibile spot could be detected for three days. It reappeared on July 25 as a normal bipolar group with a p spot of S polarity. It seems that AR 7260 developed

Table 1 A summary of observations of AR 7260.*

Date August	Time (UT) H_α	White	Magnetic fields	Time (UT) Start–Max–End	Importance optical	XR
17	0059–0341	0236–0334				
		0635–0705				
18	0131–0158	0612–0656				
	0240					
19		0257–0320				
		0628–0738				
20	0645–0837	0149–0327	0152	0616–0642–0702	SF	C2.0
		0615–0700		0710–0714–0814	SF	
21	0254–0317	0227–0259	0054	0251–0251–0259	SF	
			0612	0304–0323–0409	SF	C3.5
22		0120–0124	0458			
23	0748–0836		0636	0713–0715–0817	SN	C4.0
			0918			
24	0058–0153					
	0306–0317		0234	0307	SF	
	0654–0703		0412			

* Magnetic fields observations were made by BAO and H_α , white light by PMO. Listed in the last two columns are the corresponding SGD data.

Table 2 Evolution history of AR 7260

Carrination rotation number	Active region	Absolute heliographic longitude	Mean heliographic latitude
1858	7232	261	N16.1
1859	7260	255	N16.3
1860	7276	261	N15.5

on the remains of AR 7232 and formed a complex of activity.

An arch filament system (AFS) was detected in the east part of the group in $H\alpha$ on Aug.18(0158 UT). The appearance of AFS implies an emerging flux region (EFR) was growing. The magnetic flux kept emerging in this region by Aug. 20. Successive emergence of new dipoles caused stress and reconnection of magnetic fields and a series of flares occurred. The subflare (figure 3) occurred in the region where an AFS took place about 30 minutes ago.

Usually when an EFR comes up behind an older region, the p spot will plow through the f polarity. In AR 7260, we did find a small elongated (shear) spot of S polarity pushed westward at a speed of 0.05 km/s (Aug.19 to Aug.20), than accelerated to 0.3 km/s (Aug.20 to Aug.21). At the same time, a narrow region with polarity N stretched inside the back of S region. In company with the spot motion, a dark filament formed between the central N and moving S region, and both the filament and the magnectic inversion line moved westward at 0.12

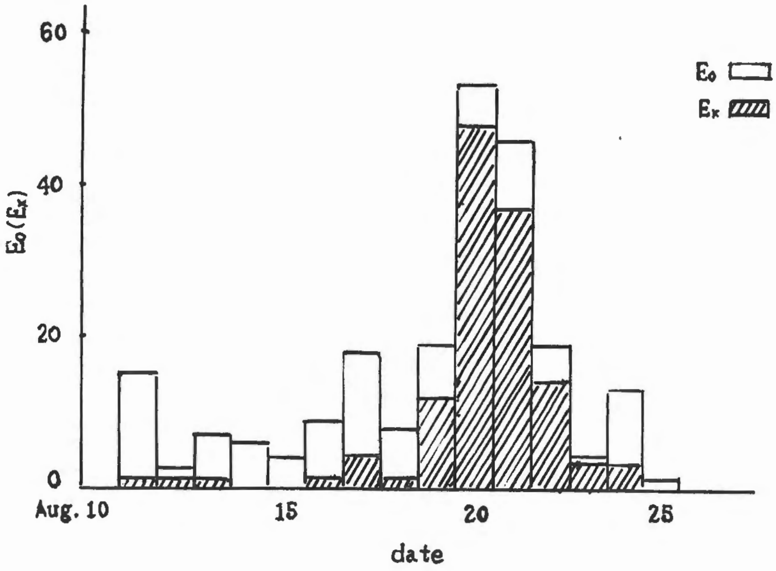

Fig.1 Active history of AR7260

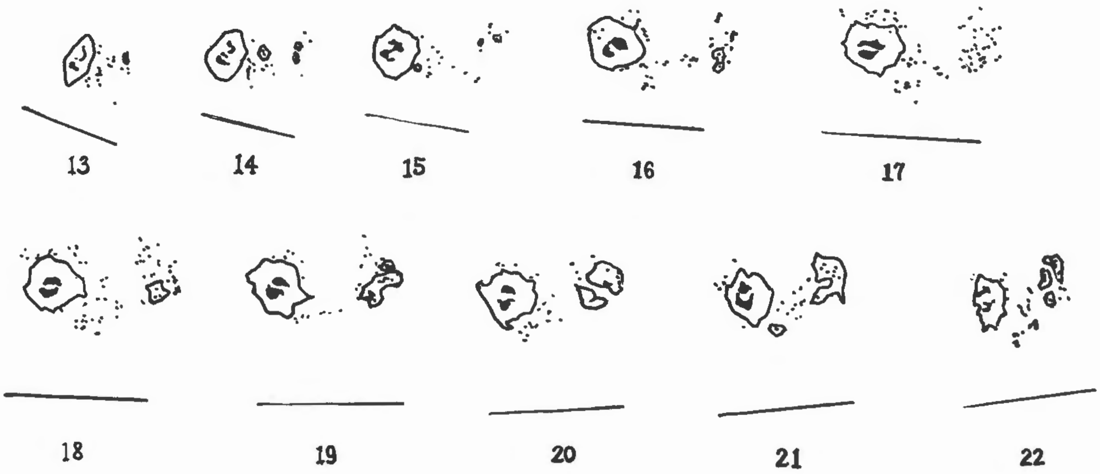

Fig.2 Daily sunspot drawing of AR7260. The lines under active region are paralled to the latitude circle

km/s, while the extent of the group almost kept constant. The motion of the spot caused the magnetic field highly sheared and the central N region was squeezed. The shear of flux line could also be confirmed by the vector magnetogram of Huairou (figure 4). A series of flares, say, the subflare of Aug. 21, resulted from the motion and magnetic shear occurred near the inversion line.

The spot stopped moving on Aug.21 and its shape turned to be round, a stable structure. The magnetograms show that the following S region merged

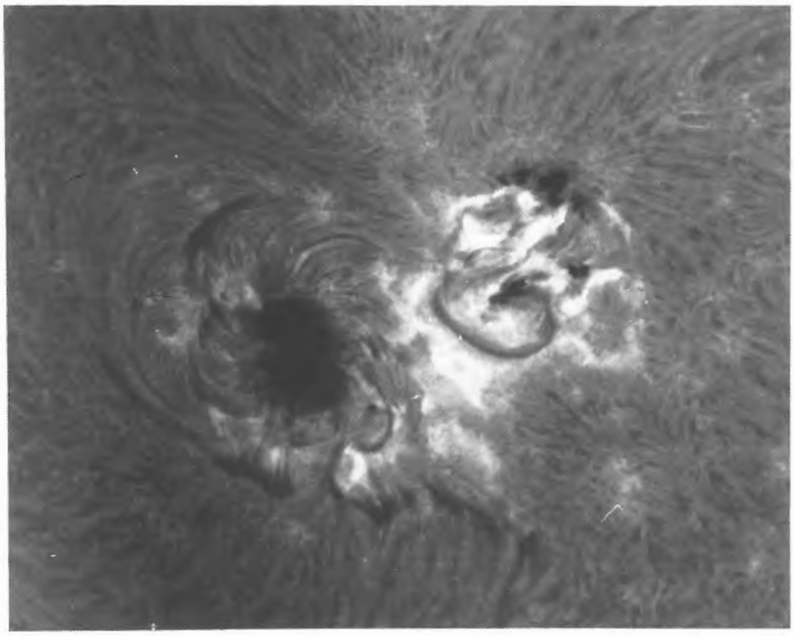

Fig.3
A subflare at Aug. 20, 1992 0717 UT. South is at the top and west is on the left.

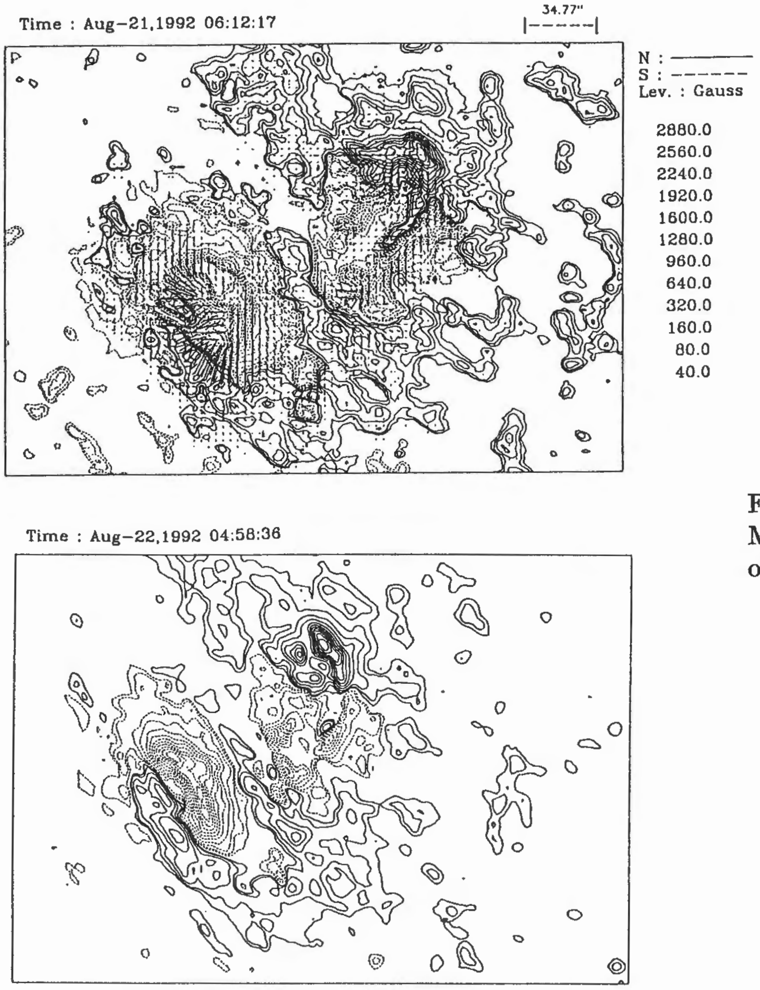

Fig.4
Magnetogram of Huairou

with the proceeding S region, first on the south part, resulting in the middle N region surrounded by S region like a peninsula on Aug.21, then almost merged in one on Aug.22, only some small regions of N remained. At the same time, the fragmentary regions of N in front of the large S spot merged in a large region of N. Two new filaments occured along the west and the north inversion lines. Some small flares and surges occurred in the north part and to the west of the large p spot. AR 7260 even recurred in next rotation (1860) as AR 7376. There must be magnetic flux successively emerging from beneath to keep the area active.

It is noticed that the relative position of three umbrae of the large p spot, as well as the magnetic axis of the group seem to rotate counter-clockwise. Having corrected the project effect, we find the rotate angles are,as listed in table 3, larger than the measure uncertainty (about ±5°). The rotation mainly took place between Aug.19 and Aug.23, the most active period. However, something not easy to explain is that the rotation made the f, not the p spot, closer to the equator, which is not consistent with the Joy law (Zirin, 1988).

Also detected in AR 7260 is the mass motion. The mass flows of 20–80 km/s were observed in a large spiral fibril–FTA for sevral times on Aug.18 and Aug.20. The fibril–FTA connected the west gap of two umbrae of p spot to a small N polarity far away (near the middle of the group). Both upward and downward flows were recorded, but usually blue shifts obtained near p spot. It seems that there existed a rather steady channel for mass and energy transport.

Table 3 Rotation of umbrae of p and the whole group

Date August, 1992	13	14	15	16	17	18	19	20	21	22	23
Rotation angle of the sunspot group*						0		4	10		14
Rotation angle of the umbrae of p*	65	65	65	58	63	67	65	78	92	95	

* The angle is measured from the latitude circle and increases when it rotated counter-clockwise.

Hence we conclude that AR 7260 was a long live active region. It survived due to successive emerging flux. But as the magnetic fields involved were not very complex and intense and the new p spot motion did not push westward so fast as usual (1 km/s). Many small flares occurred, but the energy level was not very high.

Acknowledgements

I wish to express my thanks to Dr. H. Q. Zhang of Beijing Astronomical Observatory, Misses B.Wu and Q. D. Wu of Purple Mountain Observatory for collecting and forwarding the magnetograms, Hα and white light photos.

Reference

Zirin, H. 1988, *Astrophsics of the Sun (Cambridge Univ. Press, Cambridge)*, p.307.

A purely Polarized Radio Source Associated with NOAA 7260

Kiyoto SHIBASAKI, Shinzo ENOME, Hiroshi NAKAJIMA, Masanori NISHIO, Toshiaki TAKANO,
Yoichiro HANAOKA, Chikayoshi TORII, Hideaki SEKIGUCHI, Susumu KAWASHIMA,
Takeshi BUSHIMATA, Noriyuki SHINOHARA, Hideki KOSHIISHI, and Yasuhiko SHIOMI
Nobeyama Radio Observatory, National Astronomical Observatory, Minamimaki, Minamisaku, Nagano 384-13

Abstract

A purely polarized bright radio source was found at 17 GHz by the Nobeyama Radioheliograph. This source was associated with a large sunspot of NOAA 7260. The source structure of this S-component was resolved due to high spatial resolution of the radioheliograph. A soft X-ray image of this active region taken by Yohkoh Satellite shows no counterpart for the radio source. Emission mechanism of the radio source is identified as gyroresonance. Magnetic field of the sunspot was measured by the Haleakala Vector Magnetograph at Mees Solar Observatory. The field strength at the half power level of the radio source was 2000 gauss at the photospheric level. This correspond to the third harmonic layer. A bright soft X-ray loop, whose footpoint is at the penumbra of the large sunspot, can also be seen in the radio map. This loop is strongly curved, to form a part of spiral, which reflects strong electric current. Vector magnetogram shows strong rotation of the transverse field in the sunspot, which also corresponds to strong electric current. Due to this current and also to the density and the temperature enhancement near the X-ray loop, the radio peak is shifted toward the loop and has no dip.

The sense of the circular polarization of the radio source was left handed which corresponds to the extraordinary mode. In the course of the solar disk transit of the active region, the sense changed to right handed. This polarization reversal occurred near W60. No reversal was found in the eastern hemisphere. The reversal of the circular polarization can be interpreted as the result of the mode coupling when the radio wave crosses the quasi transverse magnetic field in the active region.

Reference

Shibasaki, K., Enome, S., Nakajima, H., Nishio, M. Takano, T., Hanaoka, Y., Torii, C., Sekiguchi, H., Kawashima, S., Bushimata, T., Shinohara, N., Koshiishi, H., Shiomi, Y. and Irimajiri, Y. 1994, *Publ. Astrn. Soc. Japan*, **46**.

A Flare of 1992 Aug. 17 23:58 UT

Masaaki Takahashi (Tokai Univ.), Jun-ichi Sakai (Toyama Univ.),
Tetsuya Watanabe, Taro Sakao, Takeo Kosugi, Takashi Sakurai,
Shinzo Enome (NAOJ), Saku Tsuneta (IAUT), Nariaki Nitta (LPARL),
Hugh S. Hudson (Univ. of Hawaii), Shizuyo Hashimoto (Tokai Univ.)

Abstract

A flare of GOES X-ray class C4.3 was observed in NOAA 7260 on 1992 Aug. 17 at 23:58 UT. All the instruments on board Yohkoh made high time and spatial resolution observations. The soft X-ray time profile in the 3 – 15 keV energy range obtained by Soft X-ray Spectrometer (SXS) shows double peaks around Aug. 18, 00:00 and 00:05 UT. Images of Soft X-ray Telescope (SXT) show that four discrete points brighten in a straight line from northeast to southwest around Aug. 17 23:58 UT, which are also bright in Hard X-ray Telescope (HXT) images. We name these four points in SXT images as Points 1, 2, 3 and 4 from the northeast of the sun. Four points observed by SXT can be considered as the foot points of magnetic flux tubes. Moreover HXT contour images show that another hard X-ray source exists between Point 3 and Point 4. The logarithmic-scale SXT images indicate the existence of two loops connecting Point 1 with Point 4, and Point 2 with Point 3. Overlaid SXT images on the vector magnetogram obtained by the Solar Flare Telescope (National Astronomical Observatory of Japan) reveal that a magnetic neutral line runs between the second and third points. With the electron temperature and emission measure obtained by the SXT filter ratio method, the RTV scaling law (Rosner, Tucker, and Vaiana 1978) implies the connections of Point 1 with Point 4 and of Point 2 with Point 3 in the flare decay phase. The time profiles of electron temperature derived from the Bragg Crystal Spectrometer (BCS) also have double peaks. Simultaneous brightenings of two loops which connect Points 1 and 4, and Points 2 and 3, and a reasonable agreement with the simulation results suggest a possibility of collision of the two parallel current loop.

1 Introduction

Yohkoh satellite (Ogawara et al. 1991) observed a flare of 1992 Aug. 17 23:58 UT from its rise phase to decay phase. It was an impulsive C4.3 flare in GOES 1 – 8 Å intensity scale and showed a double peak feature in soft X-ray energy ranges. Yohkoh had four instruments on board, which were Hard X-ray Telescope (HXT) (Kosugi et al. 1992), Soft X-ray Telescope (SXT) (Tsuneta et al. 1992), Wide Band Spectrometer (WBS) (Yoshimori et al. 1992) and Bragg Crystal Spectrometer (BCS) (Culhane et al. 1992). X-ray images were obtained with high spatial resolutions (2.5 arcsec for SXT and 5 arcsec for HXT) and high time resolutions (2.0 sec for SXT and 0.5 sec for HXT).

This flare was also observed by the magnetograph of Solar Flare Telescope at NAOJ, Mitaka (Ichimoto et al. 1991). Yohkoh images were overlaid on magnetograms of Solar Flare Telescope with an 2 to 5 arcsec accuracy, as the both imaging X-ray telescopes have the coaligned optical aspect instruments.

The 1980 Jun 7 flare had a feature of quasi-periodicity in X-ray and gamma-ray light curves (Chupp 1983; Forrest and Chupp 1983; Nakajima et al. 1983; Kiplinger et al. 1983). The 1982 November 26 flare also showed quasi-periodic oscillations in the light curve of the 17 GHz interferometer at Nobeyama Solar Radio Observatory, Japan and of the Hard X-ray Burst Spectrometer (HXRBS) on Solar Maximum Mission (SMM). These flares are interpreted as those excited by quasi-periodical collisions of two current loops, which then coalesce after several collisions (Sakai and Ohsawa 1987). The magnetic reconnection during the two parallel current loop coalescence can be classified into six categories from a viewpoint of the MHD theory (Sakai and Koide 1992), which are identified in vectormagnetograms with a moderate spatial resolution of 2.5 – 5 arcsec.

In this paper, we investigate the possibility of the interaction of two parallel loops, which may have caused this flare.

2 Overview of the flare of Aug. 17 23:58 UT

The 1992 Aug. 17 23:58 UT flare has two peaks in the time profile of Soft X-ray Spectrometer (SXS) at Aug. 18 00:00 UT and at 00:05 UT, and the time interval between their two peaks is about 5 minutes. SXT observations show four bright points at the flare onset of Aug. 17 23:58 UT (Fig. 1). We name these four points as Points 1, 2, 3, 4 from the northeast of the sun. A loop appears, which connects Point 2 and Point 3 around Aug. 18 00:00 UT. At Aug. 18 00:05 UT, a loop originating from Point 1 increases its brightness to the direction of the southeast and gradually becomes spatially extended (Fig. 1). Four bright points in the HXT image, which is processed by the maximum entropy method (MEM), correspond to Points 1, 2, 3 and 4 in the SXT image of Aug. 17 23:58:46 UT, while another hard X-ray source exists between Point 3 and Point 4 (Fig. 2). Overlaying the four points in the SXT image on the magnetogram of Solar Flare Telescope reveals that a magnetic neutral line runs between Point 2 and Point 3, and that Point 1 and Point 2 have N-polarity, and Point 3 and Point 4 have S-polarity (Fig. 3). The time profiles of electron temperature derived from soft X-ray emission lines in BCS also show two peaks at about Aug. 18 00:00 UT and 00:05 UT.

By overlaying a SXT image taken before the flare onset, it is obvious that Point 2 and Point 3 are continuously bright features well before the flare starts. During the flare, a loop-like structure appears, connecting Points 2 and 3. Because these two points show opposite polarities, this structure can be considered as a real coronal magnetic loop. Another faint loop-like structure emanated from Point 4 can be recognized in the logarithmic-scale SXT images. Points 1 and 4 also show opposite polarities in the magnetogram.

3 RTV model

Temperatures and emission measures of these four points are derived by the SXT filter ratio method (Hara et al. 1992). SXT images with the filters of Be (119 μm) and Al (12 μm) are used. Figure 4 shows a scatter diagram of emission measure vs electron temperature for different observed instants. Temperatures and emission measures are obtained from the 9 (3 x 3) pixel areas centered at the four points in the SXT image. Point 1 and Point 4, and Point 2 and Point 3 in the decay phase of the flare occupy similar locations in Figure 4. The emission measures of Points 1 or 4 and Points 2 or 3 are noted as EM_{14} and EM_{23}, respectively. It is interesting to note that the slopes of EM_{23} and EM_{14} against temperature in Fig. 4 are very close to 4. A simple coronal loop model of Rosner, Tucker and Vaiana (1978), hereafter RTV, is adopted in this paper. If a constant heat input per unit volume along the loop is assumed, the following equation is derived,

$$T = 1.4 \times 10^3 (pl)^{\frac{1}{3}} \tag{1}$$

where T , p and l are the maximum temperature at the loop top, the constant loop pressure in the loop and the semi-loop length, respectively. If it is supposed that the width of a loop is nearly constant along the loop, and the unique relationship for the coronal temperature distribution in the loop to the maximum temperature at the loop top is assumed, the following relation can be derived,

$$T^4 \propto EM \cdot L \tag{2}$$

where T , EM and L are the temperature and the emission measure of the above 9 pixel areas of the coronal loop and the distance of the loop foot points, respectively. If a circular shape of the loop is assumed, the distance of the loop foot points can be substituted in Equation (2). Therefore, the RTV model explains the observed slope of EM vs T during the flare decay phase, despite of its assumption of the steady state (constant heating rate with time). From Equation (2), the relation,

$$\frac{EM_{23}}{EM_{14}} = \frac{L_{14}}{L_{23}} \tag{3}$$

is obtained, where L_{14} and L_{23} are the foot point distances of the loops 1 – 4 and 2 – 3. Applying the least square method to the data in the decay phase, the ratio of EM_{23} / EM_{14} at the same temperature is 2.75. The distance ratio, L_{14} (4.96×10^9 cm) / L_{23} (1.76×10^9 cm) derived from the SXT image on Aug. 17 23:58:46 UT (Fig. 1) is 2.82. Therefore, the emission measure ratio is almost identical to the loop length ratio. Thus, this correspondence indicates the coronal loop connections of Point 1 to Point 4 and Point 2 to Point 3.

The magnetic energy can be derived from the magnetogram of Solar Flare Telescope. Photospheric magnetic field strength at the four foot points is nearly $B = 10^2$ Gauss. It is supposed in the SXT images that the magnetic field strength in the corona is not so different from that in the photosphere, as the width of the loops is nearly constant in the corona. The radius of the loop is obtained as $r = 3.37 \times 10^8$ cm, which is common for the both loops. In case of the circular shaped loop, the volumes of the loops 2 – 3 and 1 – 4 are $V_{23}\,(loop\ 2-3) = 9.86 \times 10^{26}\mathrm{cm}^3$ and $V_{14}\,(loop\ 1-4) = 2.78 \times 10^{27}\mathrm{cm}^3$, respectively, and the total volume of the two loops is estimated to be $V = 3.77 \times 10^{27}\mathrm{cm}^3$. Therefore, the total magnetic energy of two loops is $\left(\frac{B^2}{8\pi}\right) V \sim 10^{30}$ ergs. Using the electron temperature (log T_e =6.95) and emission measure (log EM =49.05) at Aug. 18 00:05 UT, which are derived from the SXT filter ratio method, the total thermal energy is estimated to be $3k\sqrt{\frac{EM}{V}} \times T_e \sim 10^{29}$ ergs. As a result, the magnetic field strength in the loops is found to be capable of providing the whole energy for heating the soft X-ray thermal plasma of the flare.

4 Discussion

Based on these observations, a bold hypothetical scenario of this flare is the following : At Aug. 17 23:58 UT, the first collision of two loops occurred. The non-thermal electrons were accelerated and hit the chromosphere. Four foot points of the two loops brightened in both SXT and HXT images. HXT observed a hard X-ray source (22.7 keV – 32.7 keV) as well between Point 3 and Point 4. Twist of magnetic field lines around Point 1, the foot point of the loop 1 – 4 in SXT images, became loose as the flare went on. Around Aug. 18 00:05 UT, the second collision of the two loops took place, and the EM of Point 1 increased rapidly, while no rapid increase of the intensity of the loop connecting Point 2 to Point 3 was observed, because the chromospheric evaporation in the loop 2 – 3 was suppressed by high electron density due to the evaporated material already filled in the loop. On the other hand, the magnetic configuration at Point 1 was changed so that the accelerated electron easily hit the chromosphere. At Aug. 18 00:05 UT, electron densities of the loops, n_{23} (loop 2 – 3) and n_{14} (loop 1 – 4), were estimated to $n_{23} = \sqrt{\frac{EM23}{V23}} = 3.01 \times 10^{10}\mathrm{cm}^{-3}$ and $n_{14} = \sqrt{\frac{EM14}{V14}} = 9.51 \times 10^{9}\mathrm{cm}^{-3}$, where log EM_{23} =47.95 (average of Point 2 and Point 3), log EM_{14} =47.40 (average of Point 1 and Point 4).

Theoretical simulations based on the collision of two parallel loops (I-type) (Chargeishvili et al. 1992; Zhao et al. 1993) support this view of the flare. The time interval between the collisions of two current loops is $3\tau_a$, where τ_a is Alfven wave transit time. The length of the interaction region of the two loops is estimated to 1.5×10^9 cm in the SXT image. If the ratio of the magnetic field along each loop to the azimuthal field is assumed to be 10, with electron density of $10^{10}\mathrm{cm}^{-3}$ derived from SXT and with the field along the loop is 100 Gauss from the magnetograph observation, then the Alfven transit time is estimated to be 68 s and the collision time interval is 3.4 min, which gives a consistent time scale for the observed collision recurrence.

It is noted that the highest electron temperature (log T_e =7.15) is obtained in the area between Point 3 and Point 4 in SXT images (Fig. 4). An additional hard X-ray source (22.7 keV – 32.7 keV) seen in the HXT image is located in the same region at Aug. 17 23:55:44. Zhao et al. (1993) shows that particles can be accelerated to about 30 keV within a second in the magnetic reconnection region and the thermal plasma of 10^8 K can be produced in two-parallel-loop collisions with reasonable ranges of parameters. These facts imply that the region between Point 3 and Point 4 may be the interaction region of the two loop collision.

References

Chargeishvili, B., Zhao, J. and Sakai, J-I. 1993, *Solar Phys.* **145,** 297.

Chupp E. L. 1983, *Solar Phys.,* **86,** 383.

Culhane, J. L., Hiei, E., Doscheck, G. A., Cruise, A. M., Ogawara, Y., Uchida, Y., Bentley, R. D., Brown, C. M., Lang, J., Watanabe, T., Bowles, J. A., Deslattes, R. D., Feldman, U., Fludra, A., Guttridge, P., Hemins, A., Lapington, J., Magraw, J., Mariska, J. T., Payne, J., Philips, K. J., Sheather, P., Slater, K., Tanaka, K., Towndrow, E., Trow, M. W., and Yamaguchi, A. 1991, *Solar Phys.,* **136,** 89.

Forrest, D. J., Chupp, E. L., 1983, *Nature,* **305,** 291.

Hara H., Tsuneta S., Lemen J. R., Acton L. W., and McTiernan, J. M. 1992, *Publ. Astron. Soc. Japan,* **44,** L135.

Ichimoto, K., Sakurai, T., Yamaguchi, A., Kumagai, K., Nishino, Y., Suematsu., Y., Hiei, E., and Hirayama, T. 1991, *in Flare Physics in Solar Activity Maximum 22, Lecture Notes in Physics 387,* ed. Y. Uchida, R. C. Canfield, T. Watanabe, and E. Hiei (Springer Verlag, Berlin), p.320.

Kiplinger, A. L., Dennis, B. R., Frost, K. J., and Orwig, L. E. 1983, *Astrophys. J.,* **273,** 783.

Kosugi, T., Makishima, K., Murakami, T., Sakao, T., Dotani, T., Inda, M., Kai, K., Masuda, S., Nakajima, Y., Ogawara, Y., Sawa, M., and Shibasaki, K. 1991, *Solar Phys.,* **136,** 17.

Nakajima, H., Tajima, T., Brunel, F., and Sakai, J. 1984 *in Proc. Course and Workshop on Plasma Astrophysics,* ESA SP-207, P.193.

Ogawara, Y., Takano, T., Kosugi, T., Tsuneta, S., Watanabe, T., Kondo, I., and Uchida, Y. 1991, *Solar Phys.,* **136,** 1.

Rosner, R., Tucker, W. H. and Vaiana. G. S. 1978, *Astrophys. J.* **220,** 643.

Sakai, J-I., and Ohsawa, Y. 1987, *Space Sci. Rev.* **46,** 113.

Sakai, J-I., and Koide, S. 1992, PAFS-5, *Research Report on Plasma Astrophysics and Fusion Science,* Toyama Univ.

Tsuneta, S., Acton, L., Cartura, R., Freeland, S., Jurcevich, B., Morrison, M., Ogawara, Y., Hirayama, T., and Owens, J. 1991, *Solar Phys.,* **136,** 37.

Yoshimori, M., Okudaira, K., Hirashima, Y., Igarashi, T., Akasaka, M., Takai, Y., Morimoto, K., Watanabe, T., Ohki, K., Nishimura, J., Yamagami, T., Ogawara, Y., and Kondo, I. 1991, *Solar Phys.,* **136,** 69.

Zhao, J., Chargeishvili, B., and Sakai, J-I. 1993, *Solar Phys,* **147,** 131.

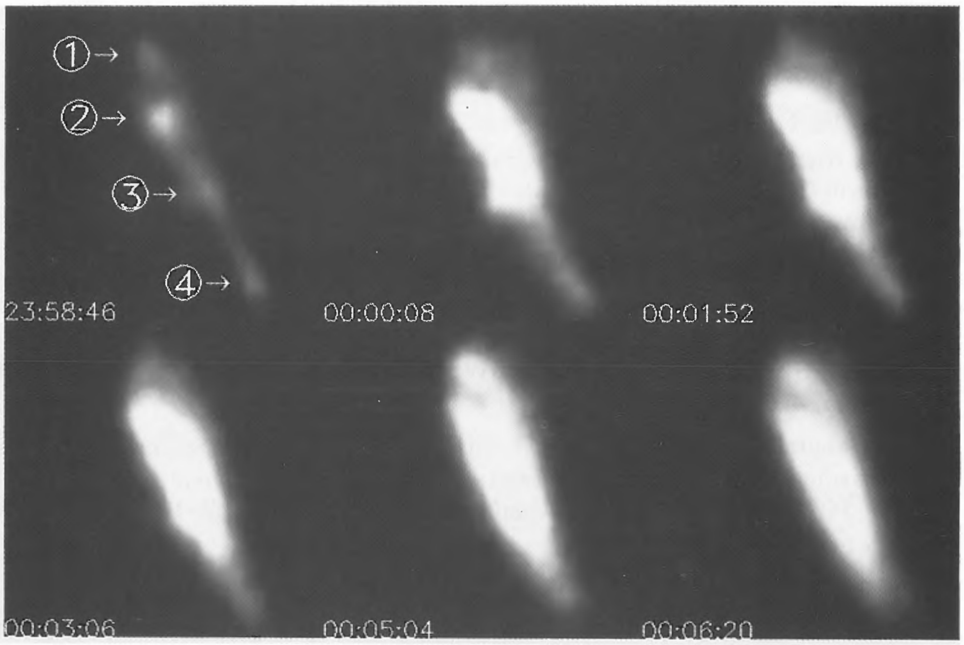

Figure 1: Time sequence of SXT images with the filter of Be 119 μm during a flare of 1992 Aug. 17 23:58 UT.

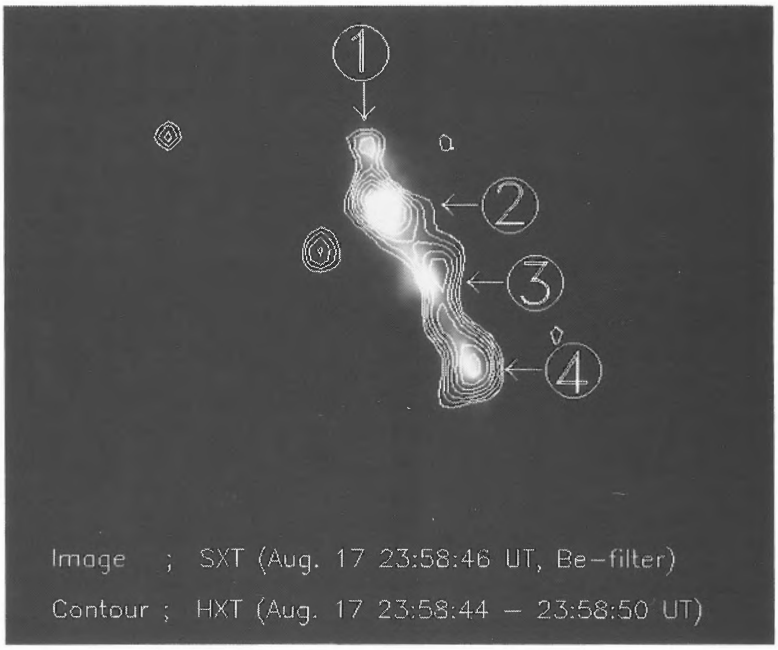

Figure 2: HXT Low channel (13.9 keV – 22.7 keV) image contour overlaid on SXT image. The HXT image is integrated and synthesized during Aug. 17 23:58:44 UT to 23:58:50 UT. The SXT image is obtained on Aug. 17 23:58:46 UT, with the filter of Be 119 μm.

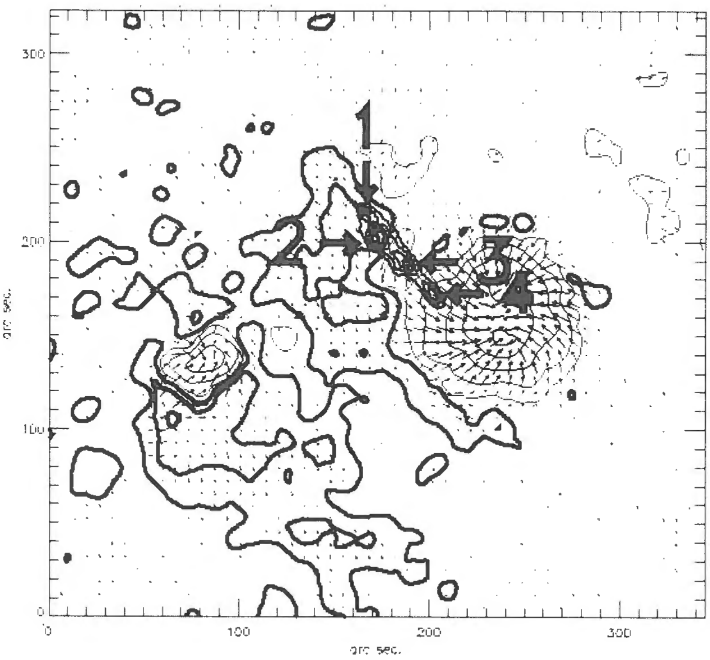

Fig. 3. A magnetogram at the post flare phase, at Aug. 18 01:50:15 – 01:51:21 UT, obtained by the Solar Flare Telescope at Mitaka. The SXT image of Aug. 17 23:58:46 UT is superposed as contours on the magnetogram. Contours in the magnetogram show the magnetic field strengths of ±50, 200, 500, 1000, 1500 Gauss.

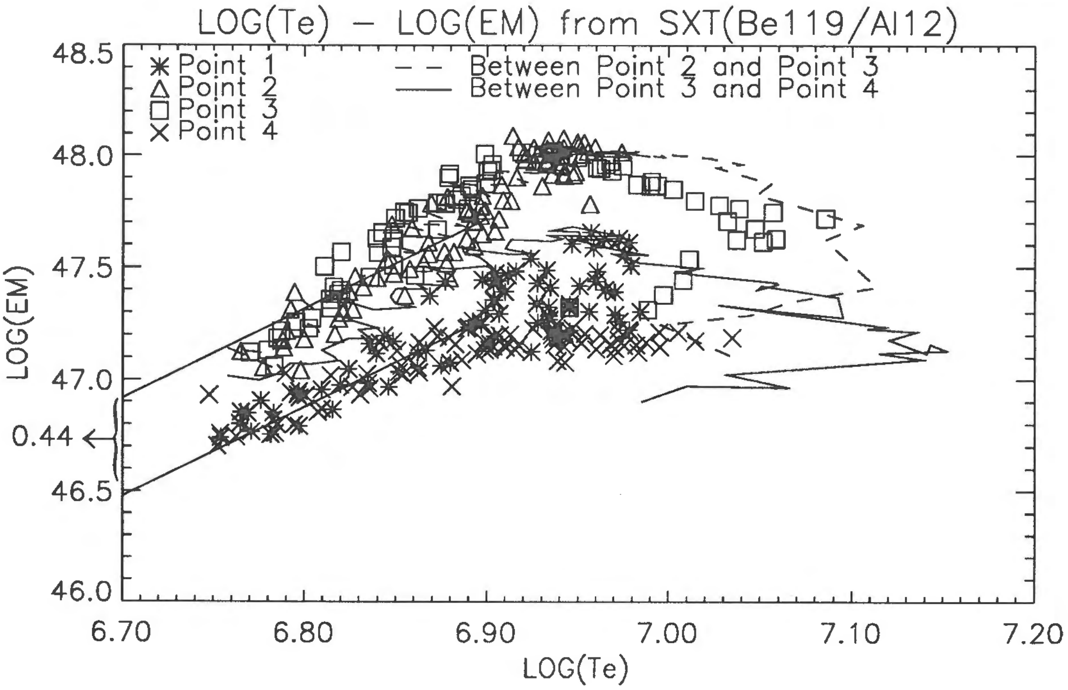

Fig. 4. The scatter diagram of emission measure vs electron temperature derived from the SXT filter ratio method with the filters of Be 119 μm and thick Al 12 μm. The emission measure ratio of the loop 2 – 3 to the loop 1 – 4 at the same temperature is log(2.75)=0.44.

Hard X-ray images at the flare on 1992 August 17

Tatsuo TAKAKURA

Department of Astronomy, University of Tokyo, Tokyo 113, Japan

and the HXT group

Abstract

Hard X-ray images of the flare of 2359UT, 17 August 1992 are presented. The images show more than three sources. The southern source shows nonthermal spectrum, while the other shows thick target X-rays from super hot thermal electrons with 85 million degrees.

Comment

Time profiles in four energy bands of the X-ray burst are shown in Figure 1. X-ray images are shown in Figure 2, in which photon energy and the time of snap shot are indicated in each panel. The panel number of each X-ray map is identical with the numeral shown in the top panel of Figure 1 indicating the time range of snapshot of the X-ray map. Precise comparison of these with the SXT and Radio maps is not yet made, but the two peaks at the Time (4) probably coincide with the sources (2) and (4) presented in the preceding papers by Takahashi and Enome. The X-ray maps, however, suggest that the sources (2) and (4) are foot points of a common coronal loop, so that the week central X-ray source, probably the source (3) in the Takahashi's paper, is the top of this loop. The X-ray spectra at the Time (4) are obtained from the three energy bands in the same way as mentioned in my previous comment on the burst of October 27. The source (2) shows thick target X-ray spectrum from the electrons flowing into the chromosphere with quasi- thermal distribution, $T_e \simeq 8.5 \times 10^7$ K and the number density is $3 \times 10^6 \mathrm{cm}^{-3}$. On the other hand, the spectrum for the source (4) shows power law with the X-ray photon spectral index of 3.1, i.e., the index for electron energy is 4.6, and the electron number density above 15 Kev is $6 \times 10^6 \text{cm}^{-3}$. The above result is consistent with the radio observation that the brightest source is located near the source (4) at about the Time (4).

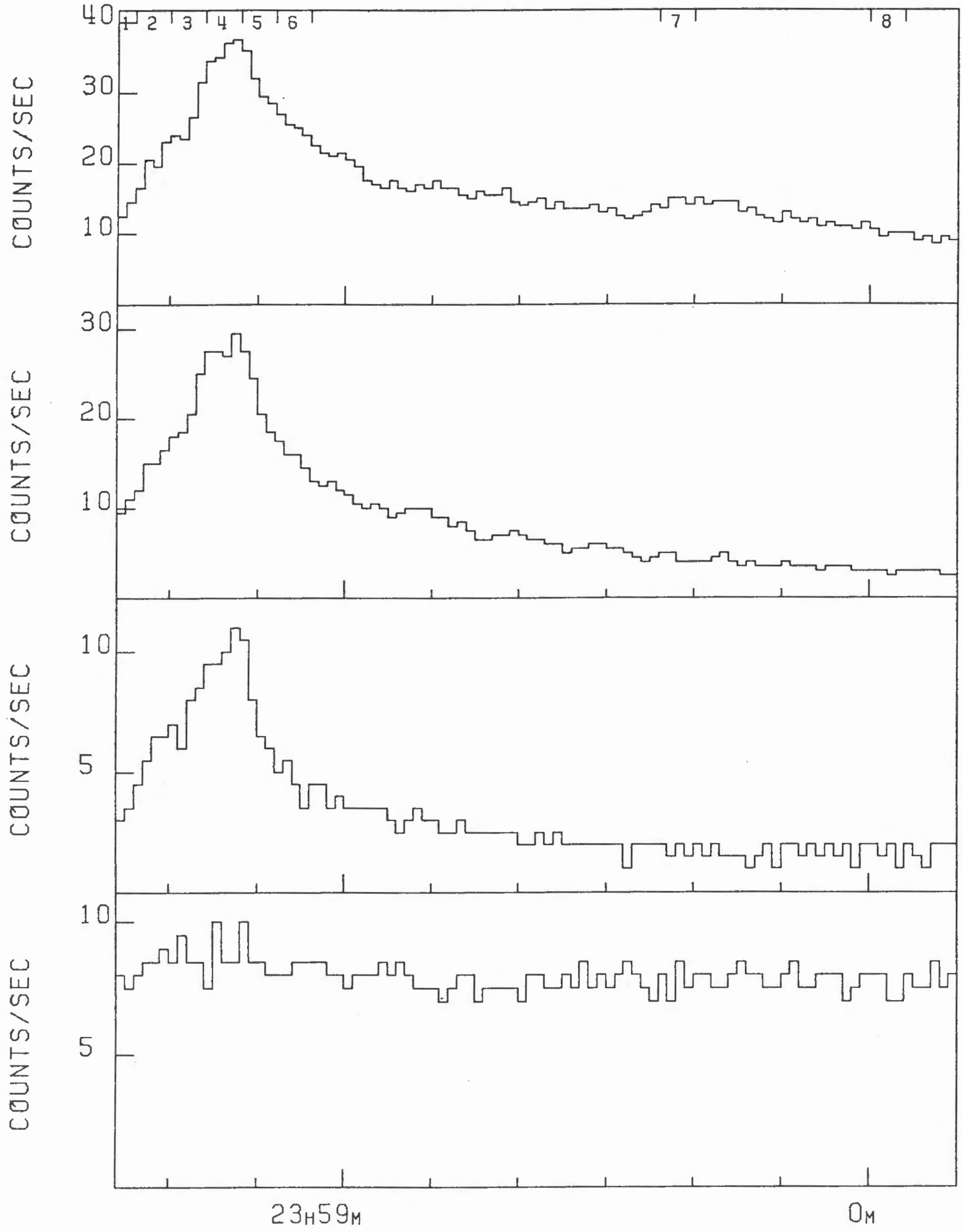

Fig.1. Time profiles of the X-ray burst on 1992 August 17 in four energy bands L, M1, M2, and H from top to bottom: L; 13.9-22.7 keV, M1; 22.7-32.7 keV, M2; 32.7-52.7 keV, H; 52.7-92.8 keV. Since the effective mean collecting area per each collimator is about 1 cm^2, the vertical scale is approximately X-ray flux (c s^{-1}cm^{-2}). The numerals marked on the curve in the top panel show the times of snapshots of X-ray maps shown in Figure 2.

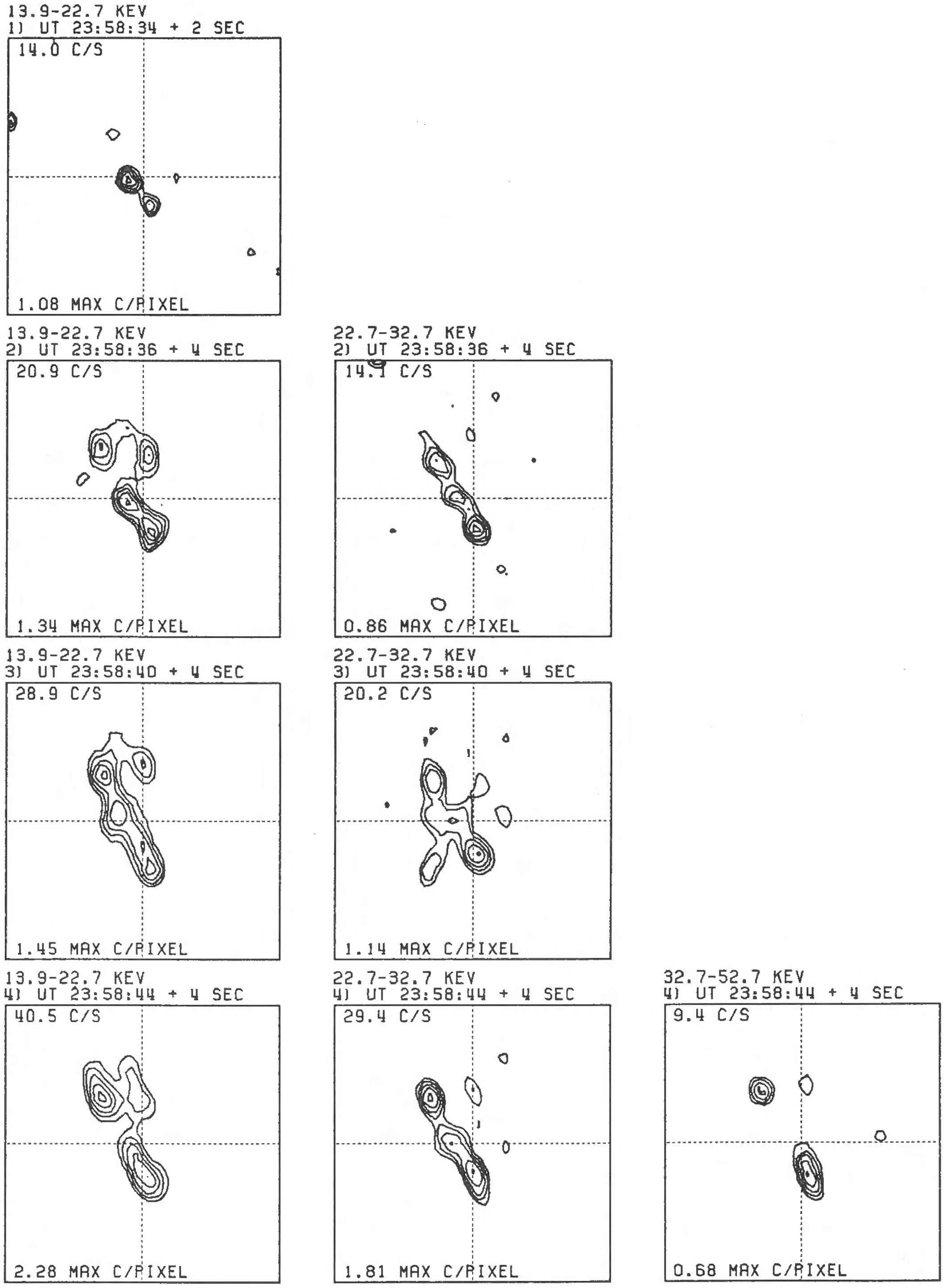

Fig.2a. X-ray contour maps of the burst. The photon energy, the starting time and integration time of the map are shown in each panel. The panel number is identical with the numeral shown in Figure 1 indicating the time of the snapshot. The minimum contour level is 0.1 times the peak brightness in each map and the contour steps are logarithmic with $\sqrt{3}$ steps. The map size is 126 arcsec square. The map center is 0.13 arcmin west and 3.05 arcmin north from the solar center. The solar north is upward (y-axis) in the maps. In each panel, X-ray count/sec and count/pixel in the brightest pixel are shown.

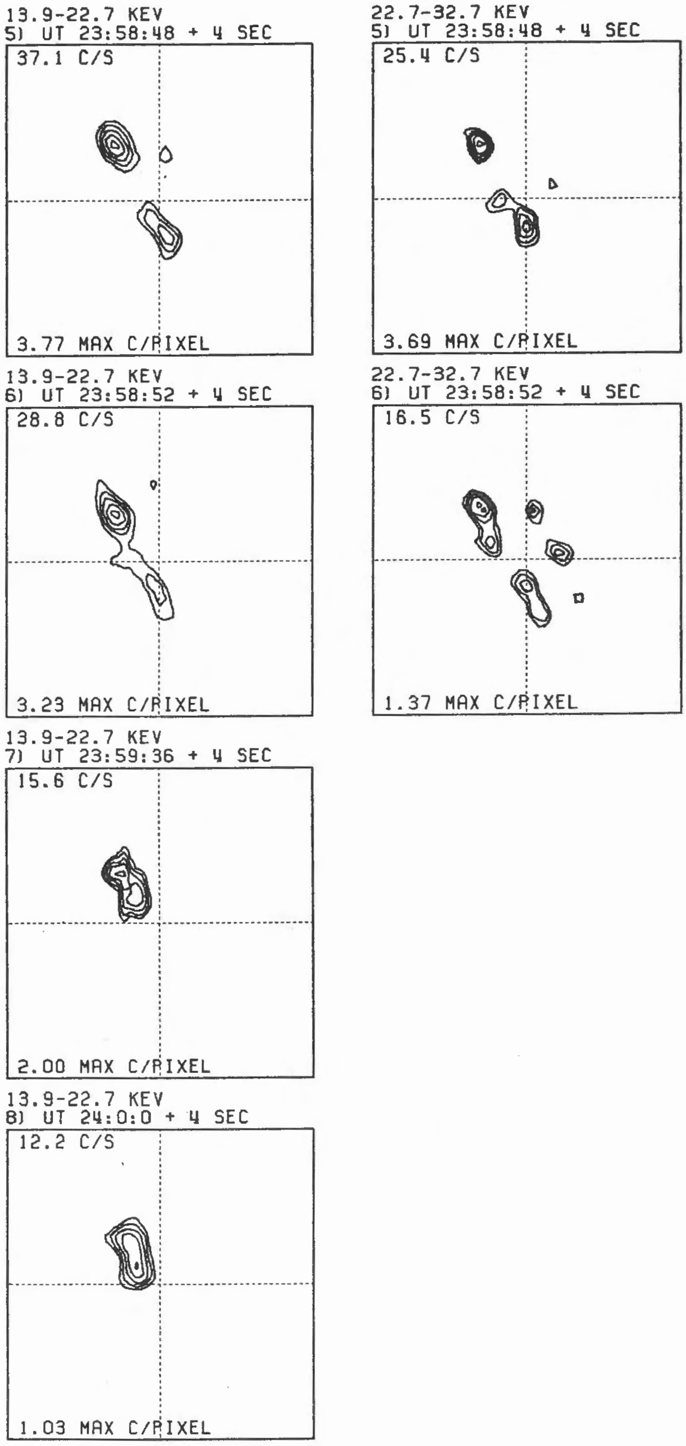

Fig.2b. Same as Figure 2a, but later time.

The Numerical Analysis on Characteristics of Plasma Temperature Variation about the Aug.17,25:58UT, 1992 Flare

Jie Zhao and Jun-ichi Sakai
Department of Electronics and Information, Faculty of Engineering
Toyama University, Toyama, 930 JAPAN
and
Bidzina Chargeishvili
Abastumani Astrophysical Observatory of Georgian Academy of Sciences
Tbilisi 380000, Georgian Republic

Abstract

The characteristics of plasma temperature variation during the collision of two current loops are described. It is revealed that the plasma temperature has an oscillatory feature with damping amplitude and growing quasi-period in the case of an I-type collision. In the case of a Y-type collision, if the initial current becomes strong enough, there also occurs pulsation of the temperature. The temperature profile of an X-type collision is characterized by the single pulse only. Based on the observatory phenomena, the Aug.17, 25:58UT, 1992 flare wave induced by the two loop interaction whose configuration was the I-type loop-loop interation. The numerical results agree with the observed one quite well.

1. Introduction

The solar flare phenomenon is a manifestation of the explosive release process of magnetic energy stored in the lower corona, including plasma heating and particle acceleration. Since the Smm and Hinotori satellites were launched, it has become clear that flares have a close correlation with current loop collisions. From Yohkoh's soft X-ray images, it is apparent that the interaction of coronal loops may be an important physical process for energy release in the solar corona (Shimizu 1992). Theories and simulations (see Sakai and Ohsawa 1987) have shown that, during the coalescence of two current loops through the magnetic reconnection process, magnetic energy stored in the current loops converts to plasma heating and production of high-energy particles. Such physical processes depend on the magnetic field geometry and the configuration of the interacting current loops (Sakai and de Jager 1991). Investigating the nonlinear coalescence instability of current loops, Tajima et al. (1987) paid attention to the double subpeak structure in quasi-periodic oscillations found in the time profiles of two solar flares on June 7, 1980 and Nov. 26, 1982. Chargeishvili et al. (1993) have classified loop-loop interactions into three types according to the ratio between the plasma pressure gradients in the Z and R directions, and pointed out the oscillatory character of physical quantities in the case of an I-type collision.

In this paper, we study the characteristics of plasma temperature near the interacting region in three types (X,Y,I) of loop-loop collisions by using a MHD approach developed by Chargeshivili[1]. Comparing the numerical results with Yohkoh data, we deduce that the flare of Aug.17, 23:58 UT, 1992 may correspond to the case of an I-type loop-loop interaction.

2. Characteristics of plasma temperature

Using MHD equations with gravity and resistivity effects, we get self-consistent expressions and a set of equations governing the behavior of all physical quantities (see Chargeishvili et al. 1993). From the numerical simulations, we found that the plasma β, the type of loop collision, and the initial current strength have significant effects on the characteristics of plasma temperature. Prescriptions of the physical parameters are given as follows. The case of an I-type loop-loop collisions is defined by $L_r/L_z<<1$, the case of a Y-type is defined by $L_r/L_z=1$, the case of an X-type is the opposite case of I-type, where $L_r=|(1/p)(\partial p/\partial r)|^{-1}$, $L_z=|(1/p)(\partial p/\partial z)|^{-1}$ and p is plasma pressure. The initial current strength is proportional to reverse of B_1, where $B_1=B_{r0}/B_{\varphi 0}$, B_{r0} and $B_{\varphi 0}$ are components of initial magnetic field in radial and azimuthal directions, respectively. Time is normalized by $\tau_A=(4\pi\rho_0)^{1/2}L_r/B_{\varphi 0}$. As for the time profile of plasma temperature, the case of an X-type has only one peak. In the case of a Y-type, there occurs pulsation. The case of an I-type shows oscillating character with damping amplitude and growing quasi-period.

First we consider the effect of the type of the collision on the time profile of plasma temperature. Figure 1, Figure 2 and Figure 3 show the different characters of the temperature profile for the different types of collisions. One can see that a pulsation phenomenon in the case of an I-type collision is more apparent than in the case of a Y-type. Next, considering the initial current strength, we found out that a stronger initial current leads to more evident oscillations in the temperature time profile (see Figure 1 and Figure 2). For a weak current case ($B_1=0.1$) that may correspond to a weak flare, the temperature is enhanced by a few times, while for a strong current case ($B_1=10^4$) which may correspond to a strong flare, the temperature can increase up to a hundred times. In the strongest current case, the Figure 2(d) shows that the time profile of plasma temperature of the Y-type collision has five peaks and that the third peak is much higher than the first one. However there is still a single pulse in the case of an X-type collision, even though the amplitude of the peak becomes higher (shown by Figure3(d)). As for the plasma β, an increase of it causes an increase of the first peak width and quasi-period and a decrease of the peak amplitude. Out of the range of the known values of β, the oscillation phenomenon disappears. In the weak current case, it happens near $\beta=0.02$.

3. Flare of Aug.17, 23:58 UT, 1992

The Aug.17, 23:58 UT, 1992 flare observed by Yohkoh showed double peaks in the soft X-ray flux. During the first peak, four brightening footpoints were located along a line, and they were divided into two pairs by the magnetic neutral line. No high energy particles were detected, only plasma heating occurred and small fraction of electron with energy about 20 KeV was observed before the first peak of soft X-ray flux (Takahashi et al. 1992). Comparing the numerical results with the time profile of the soft X-ray flux, we deduce that only the case of an I-type collision could provide such an event. The interval between the first and second peaks obtained from the simulation coincides well with the observed one, if the flare scale, plasma density and B_1 are about 10^9 cm, 10^{11} and 0.1, respectively. The enhanced maximum temperature in the first peak is about three times higher than the one in the second peak. By using a particle acceleration model (Zhao et al. 1993), we get results that particles can be accelerated to about 30 KeV within 1 second, which precedes the first temperature maximum. There is no particle acceleration near the second peak because electric field is not strong enough.

4. Conclusion

We describe characteristics of plasma temperature variation during loop-loop collisions for different initial conditions, such as plasma β, the type of the collision and initial current strength. Enhancement of plasma temperature is caused by adiabatic heating. Strong initial current strength leads to a strong flare and effective plasma heating. We suggest that comparing these characteristics with observed time profiles of physical quantities, one can conjecture the initial conditions of loop-loop interactions such as Alfven transient time, loop-loop configuration, current strength and so on.

Acknowledgements

The authors (J. Zhao and B. Chargeishvili) are grateful to Japanese Government (Monbusho) for Scholarship. One of the authors (J. Sakai) was in part supported by a Grant-in-Aid for Scientific Research from the Ministry of Education (03640247).

References

Chargeishvili, B., Zhao, J. and Sakai, J-I.: Solar Phys. **145**, 297, 1993

Sakai, J-I., and Ohsawa, Y.: Solar Phys. **58**,127, 1987.

Sakai, J-I., and de Jager, C.: Solar Phys. **134**, 329, 1991.

Shimizu, T., Tsuneta, S., Acton, L.W., Lemen, J.R., and Uchida, Y.: Publ. Astron. Soc. Japan **44**, L147, 1992.

Takahashi, M., Sakai, J-I., Sakao, T., Kosugi, T., Tsuneta, S., Watanabe, T., and Hudson, H.: Proceeding of Japan Fall Annual Astronomical Conference, B71, 1992

Tajima, T., Sakai, J-I., Nakajima, H., Kosugi, T., Brunel, F., and Kundu, M.R.: Astrophysics.J. **321**, 1031, 1987.

Zhao, J., Chargeishvili, B., and Sakai, J-I.: Solar Phys. **146**, 331, 1993

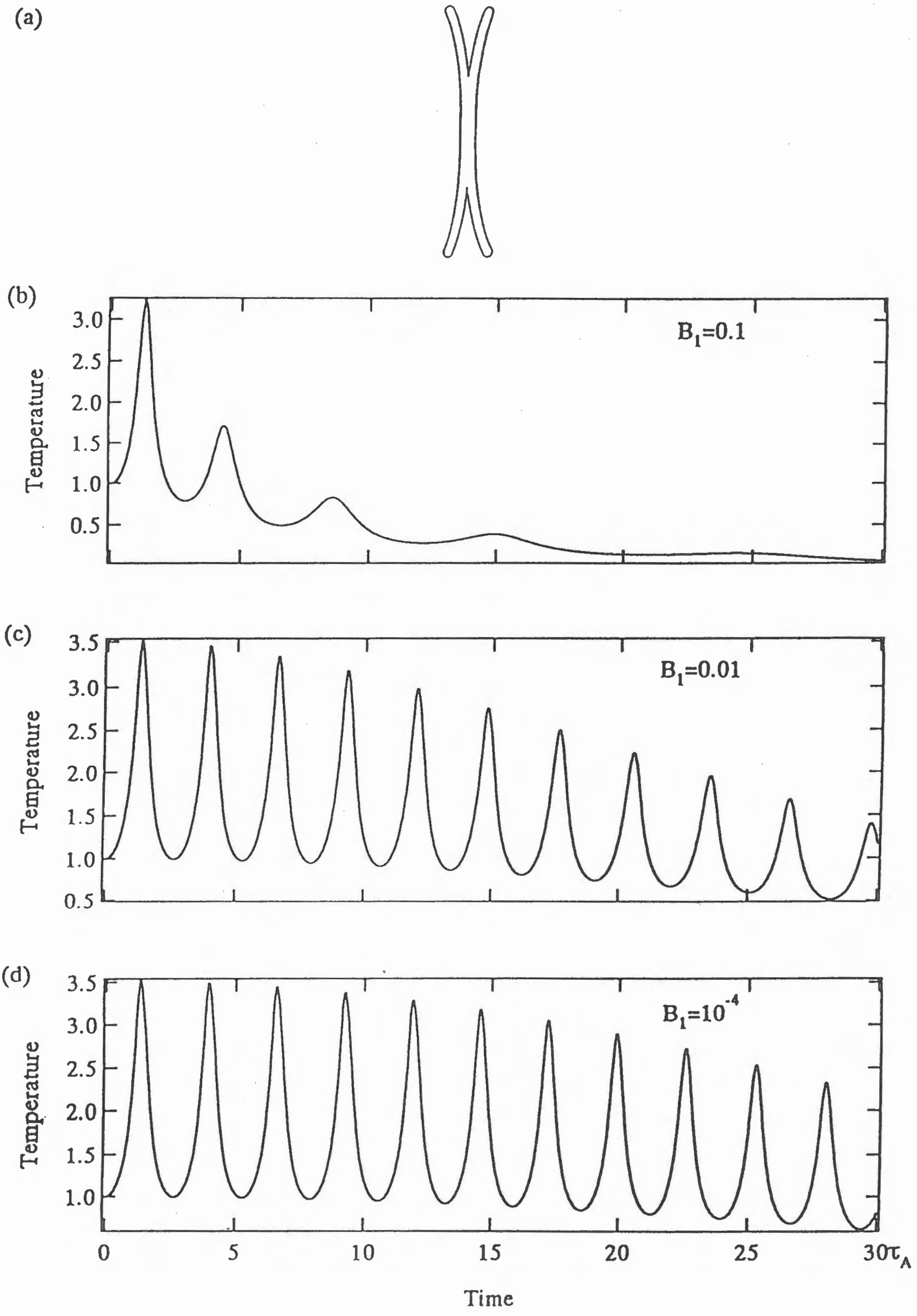

Figure1. The I-type of loop-loop collision and corresponding time profiles of plasma temperature for the different initial current strength

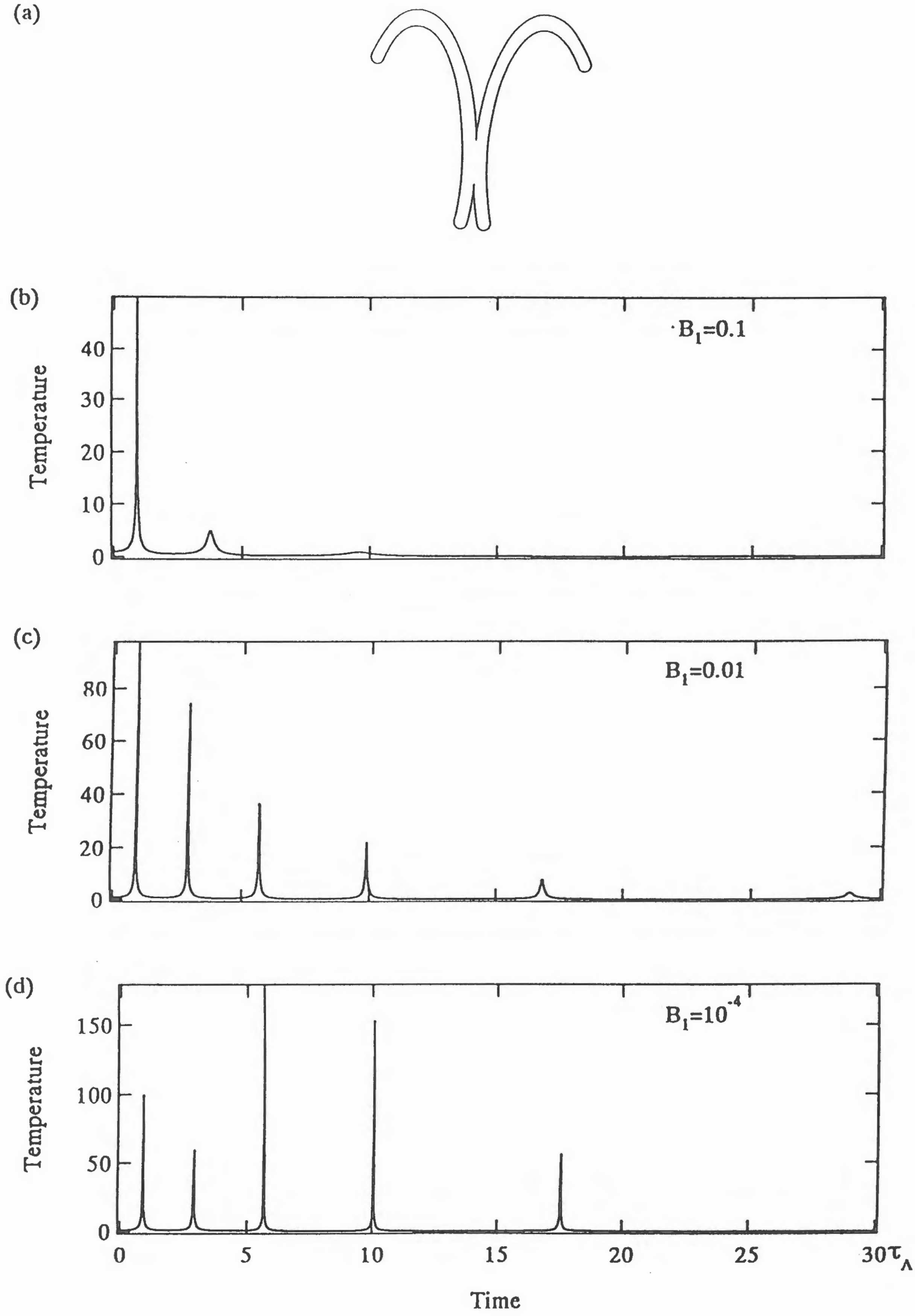

Figure2. The Y-type of loop-loop collision and corresponding time profiles of plasma temperature for the different initial current strength

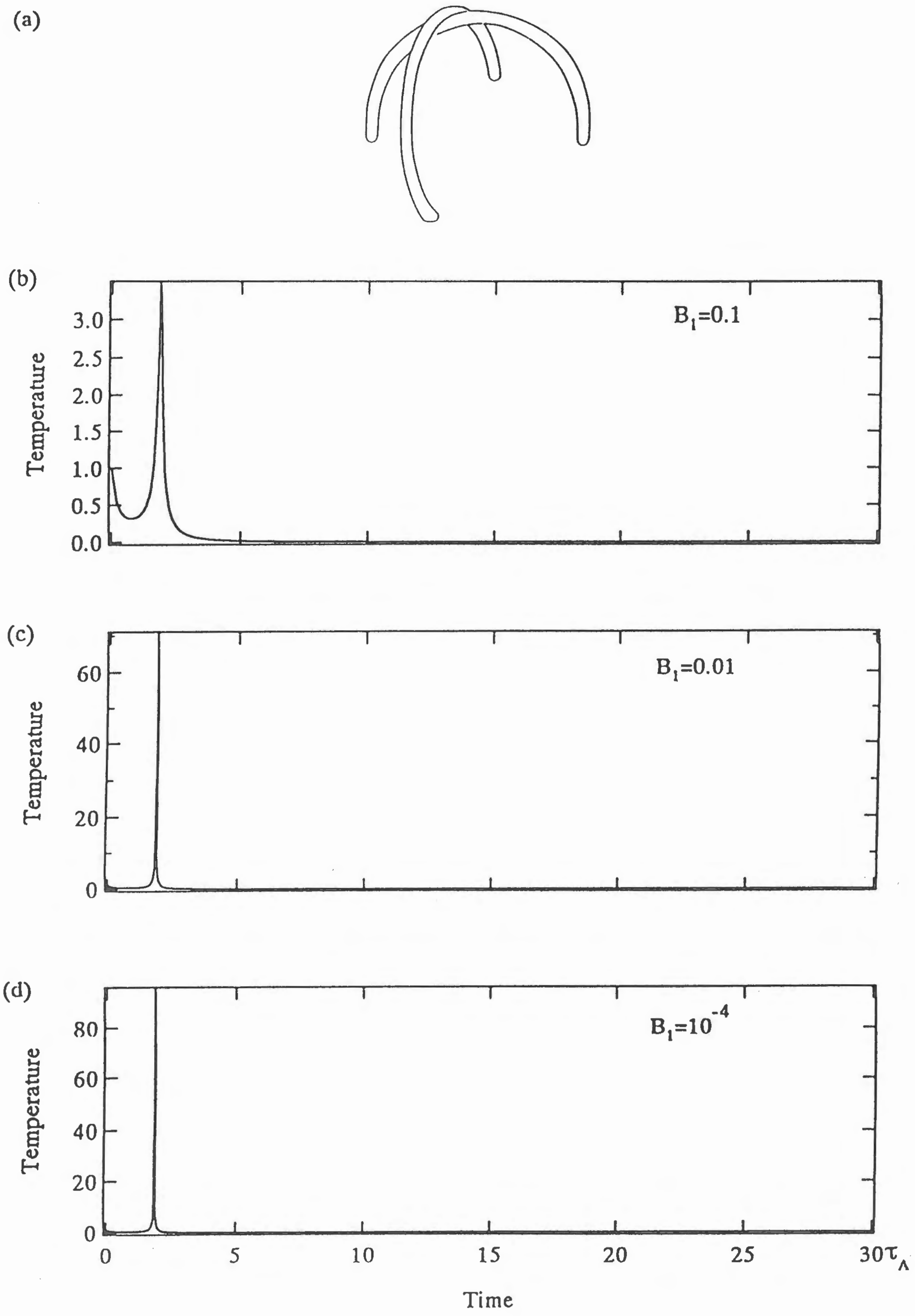

Figure3. The X-type of loop-loop collision and corresponding time profiles of plasma temperature for the different initial current strength

Active-Region Transient Brightenings in NOAA 7260

Toshifumi SHIMIZU
Institute of Astronomy, The University of Tokyo, Mitaka, Tokyo 181

Abstract

In this paper, we discuss transient brightenings appeared in an active region NOAA 7260 from the point of view of their morphology and spatial distribution. In this region, more than half of transient brightenings show simple brightening structures with a single loop, although one third of them are simultaneous brightenings of multiple loops. This result is different from the result of transient brightenings appeared in NOAA 6891. This difference may be due to the dominance of small-size brightenings in NOAA 7260. Transient brightenings are observed to be localized in two areas in NOAA 7260. One of them is a growing emerging magnetic flux region embedded in the following plage area, suggesting that some transient brightenings are associated with the emergence of the magnetic flux. Other transient brightenings appear around the outer boundary of the penumbra of a preceding well-developed spot.

1. Introduction

Soft X-ray Telescope (SXT) aboard the *Yohkoh* satellite (Ogawara et al. 1991) has found that active regions show many tiny flare-like brightenings (Shimizu et al. 1992). Intense brightenings are believed to be soft X-ray counterparts of hard X-ray "microflares" observed by hard X-ray balloon-borne observations with high sensitivity (Lin et al. 1984). The SXT observes fainter brightenings which are not detectable with other instruments, such as the *GOES* soft X-ray full-sun monitors. Transient brightenings appear on average every a few minutes in active regions of high activity. In relatively quiet active regions, the frequency of their occurrence falls down to once every 1 hour.

Transient brightenings appear in forms of single or multiple loops, although some brightenings are point-like. Shimizu et al. (1994a) statistically investigate the morphology of transient brightenings appeared in the active region NOAA 6891, which is the most energetic active region since the *Yohkoh* launch (*Solar Geophysical Data*), and find that simultaneous brightenings of multiple loops are more often seen than brightenings of single and point-like structures. In this paper, we investigate transient brightenings appeared in another active region NOAA 7260 from the point of view of their morphology and physical states, and then make a comparison between the morphological results in NOAA 7260 and NOAA 6891. We also discuss the spatial distribution of transient brightenings in NOAA 7260.

2. Observation and Data Analysis

The SXT is a grazing incidence X-ray telescope covering the 3 to 60 Å wavelength equipped with a 1024×1024 charge coupled device (CCD) detector. Two filter wheels and a mechanical shutter are mounted in front of the CCD detector to choose energy band and exposure time. The CCD camera, shutter, and filter wheels are controlled by on-board microprocessors. The detailed description of the instrument is given by Tsuneta et al. (1991).

The data used in this analysis are obtained from 15 to 20 August, 1992. During this period, partial CCD images with two different X-ray filters (Al 1265Å filter, Al 12μ filter) are available every 32 sec. The target region of the partial images is NOAA 7260, which is located at the disk center on 18 August, 1992, with the 5×5 arcmin field of view. The pixel size of the images is 2.46 arcsec. The exposure durations are controlled by an on-board automatic exposure control logic. We selected the sequence of images which had a time coverage of more than 25 min. The total time coverage of all the selected data is about 10 hours.

We examined the data by visually inspecting images and picked up those events that were observed throughout their lifetime and events observed from beginning up to maximum phase. 291 transient brightenings are selected in total. By applying the spline fitting function to light curves of a transient brightening, the peak X-ray fluxes, the background X-ray fluxes, and the lifetimes are obtained for each filter. Here the peak flux is meant to be the maximum enhancement in excess of the background flux.

The background flux is assumed to be the minimum flux just prior to the rising phase. The lifetime is defined as the duration above half maximum intensity. The length and width of a brightening feature are determined from the image showing the brightening in peak phase. The heliocentric address of a transient brightening is also calculated. These physical parameters are obtained after the CCD corrections (dark subtraction, decompression from 8 bit to 12 bit and so on) and the removal of the satellite jitter motions. Morphological properties are determined by visually inspecting the images and are then classified following the categories of Shimizu et al. (1994a).

3. Morphology

Transient brightenings are classified into three categories: (1) simultaneous brightenings of multiple loops, (2) brightenings of single loop, and (3) point-like brightenings. The classification of transient brightenings appeared in NOAA 7260 is presented in Table 1. As a reference, Table 1 has the classification of transient brightenings in NOAA 6891, which comes from Shimizu et al. (1994a).

Table 1. Morphological Classification of Transient Brightenings.

NOAA 7260

classification	number	percentage
Total analyzed event	291	
POINT-like event	32	11.0%
SINGLE-loop event	184	63.2%
MULTIPLE-loop event	75	25.8%

NOAA 6891

classification	number	percentage
Total analyzed event	142	
POINT-like event	26	18.3%
SINGLE-loop event	59	41.5%
MULTIPLE-loop event	57	40.2%

(From Shimizu et al. 1994a)

In NOAA 7260, more than half of transient brightenings show quite simple brightening structures with a single loop. A quarter of transient brightenings is simultaneous brightenings of multiple loops. On the other hand, in NOAA 6891, the percentage of multiple-loop brightenings is comparable to that of single-loop brightenings. The percentage of multiple-loop brightenings in NOAA 7260 is smaller than that in NOAA 6891. Reversely, the percentage of single-loop brightenings in NOAA 7260 is larger than that in NOAA 6891. This means that there is apparent difference in the morphology of transient brightenings between the active regions, although we cannot find any significant difference in the percentage of point-like brightenings between them.

It is concluded in Shimizu et al. (1994a) that some of single-loop and point-like brightenings could have multiple-loop structures on sub-loop scales and that most of transient brightenings may consist of multiple loops. This conclusion comes from the fact that the size of the loops in single-loop and point-like brightenings is smaller than that of the loops in multiple-loop brightenings. To discuss the difference in the morphology of transient brightenings between the active regions, we should know the distribution of the size of the loops in NOAA 7260 (Figure 1). Comparing Figure 1 with that in NOAA 6891 (Figure 2 of Shimizu et al. 1994a), we find that single-loop and point-like brightenings have similar distributions in both regions. The size distribution of multiple-loop brightenings in NOAA 7260 is, however, quite different from that in NOAA 6891. NOAA 7260 is lacking in the long-size part of multiple-loop brightenings. This means that transient brightenings with small size are dominant in NOAA 7260, so that many transient brightenings can be regarded as single-loop brightenings which may have multiple-loop structures on sub-loop scales. In addition, the driving forces of transient brightenings might be different in both active regions.

Even in NOAA 7260, the initial brightenings at the footpoints of the loops are observed in many multiple-loop brightenings as well as in single-loop brightenings. Enhanced emission at the sites where

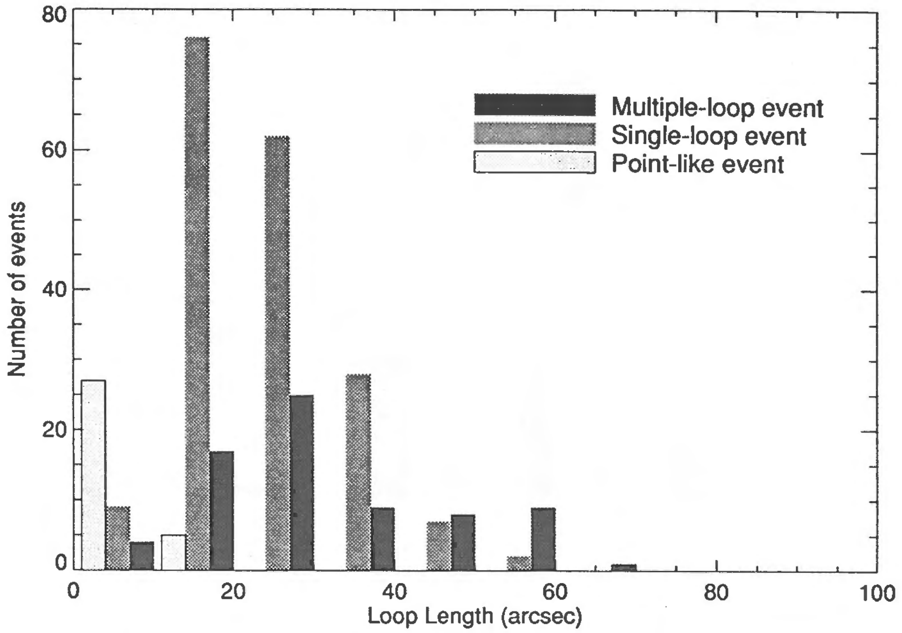

Fig. 1. The Distribution of the loop length of Transient Brightenings.

the loops are in contact is, however, rarely observed in NOAA 7260, although in NOAA 6891 we frequently observe enhanced emission at the contact points. The significant difference in the regions is that the diffuse background structures are relatively brighter in NOAA 6891 than in NOAA 7260. This implies that at the beginning of transient brightenings, the coronal plasma may have higher density or temperature in NOAA 6891 than in NOAA 7260, so that enhanced emission at the contact points is frequently observed in NOAA 6891. We also observe several X-ray jets (Shibata et al. 1991) associated with transient brightenings. Many X-ray jets appear around the following spots which have newly emerged during the observation.

4. Soft X-ray Peak Flux

Here the distribution of soft X-ray peak flux of transient brightenings is discussed with their morphology, to know how bright brightenings appear in NOAA 7260. Figure 2 is the histogram of soft X-ray peak flux (through Al 1265 Å filter) of transient brightenings appeared in the region. The horizontal axis is the total intensity of brightening features at the maximum phase, which is described in the unit of DN (data number) per sec. Note that there is a good correlation between soft X-ray peak flux and *GOES* high channel (0.5 ~ 4 Å) flux for transient brightenings (Shimizu et al. 1994b): 10^5 and 10^6 DN s^{-1} roughly correspond to 10^{-9} (<B1 class) and 10^{-8} (~B3 class) W m^{-2} in the *GOES* high channel, respectively. We know that most of transient brightenings appear with the peak flux of 10^4 to 10^6 DN s^{-1}. There is no significant difference in distribution of the peak flux among three kind of morphological structures, except that multiple-loop brightenings are slightly brighter than single-loop or pointlike.

5. Spatial Distribution of Transient Brightenings

Finally we discuss the global distribution of the occurrence location of transient brightenings appeared in NOAA 7260. Figure 3 shows the locations of transient brightenings appeared in the period of 15 to 20 August, 1992. The asterisks show the locations of multiple-loop brightenings, the diamonds of single-loop, and the squares of point-like. They are marked on the center position of brightening structures. The projective locations of transient brightenings at 0 UT on 18 August are calculated with the assumption of the differential rotation of the active region. The shadows show umbrae and the dashed lines express

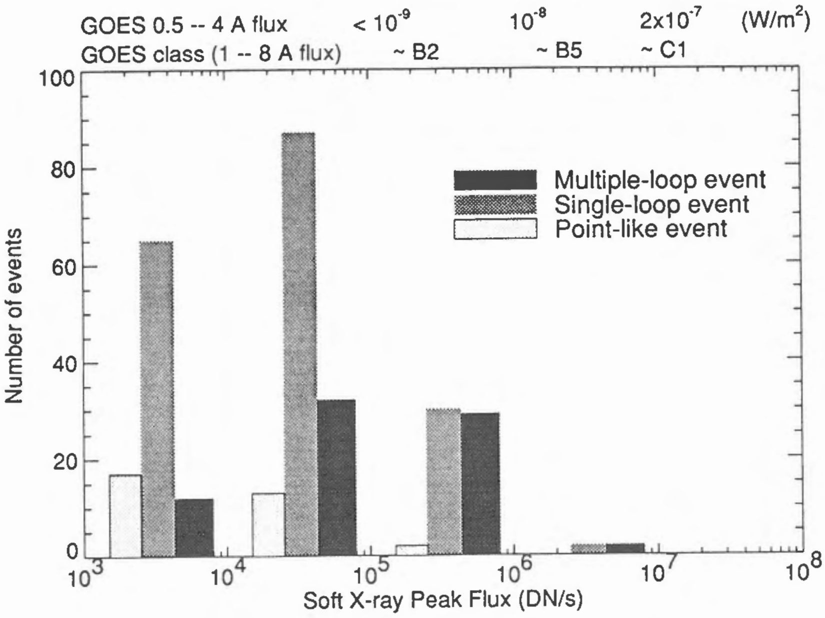

Fig. 2. Soft X-ray Peak Flux of Transient Brightenings.

the outer boundaries of penumbrae observed around 0 UT on 18 August.

We find that transient brightenings are localized in two areas: One is the outer boundary of the penumbra of a preceding spot and the other is a following area. The preceding spot is well-developed and the following area is an emerging flux region embedded in the following plage area during the observation (Jianqi 1993; Nitta et al. 1993). Transient brightenings in the following area are possibly associated with the growing emerging magnetic flux, because transient brightenings rarely appear before the appearance of the emerging flux region. A more interesting feature is frequent brightenings around the outer boundary of the well-developed sunspot. Near well-developed sunspots like this spot, many small magnetic bipolar features, or satellite spots are observed to movie outward from the outer boundaries of their penumbrae into network boundaries (Harvey and Harvey 1973). The moving magnetic loops due to the horizontal motions may approach each other and so have a magnetic reconnection in a current sheet between them. Moreover, some transient brightenings are observed to be located at a magnetic shear region near the eastern boundary of the preceding spot (Sakurai et al. 1993). To clarify the relationship between transient brightenings and the driving forces, we need to make a detailed comparison of transient brightenings with high spatial resolution Hα, continuum, and magnetic data and know their detailed correlation with the photospheric motions, magnetic shear, and other information from optical data.

We are grateful to all the members of the *Yohkoh* team for the instrumental developments and daily operations. We would like to thank Drs. H. Kurokawa, K. Shibata, and N. Nitta for helpful comments. The author acknowledges the support by Fellowships of the Japan Society for the Promotion of Science for Japanese Junior Scientists.

References

Harvey, K., and Harvey, J. 1973, *Solar Phys.*, **28**, 61.

Jianqi, Y. 1993, *in proceedings of the 2nd Japan-China Seminar on Solar physics* (this proceeding).

Lin, R. P., Schwarts, R. A., Kane, S. R., Pelling, R. M., and Hurley, K. C. 1984, *Astrophys. J.*, **283**, 421.

Nitta, N., Driel-Gesztelyi, L. V., Leka, K. D., Mickey, D. L., Metcalf, T. R., Wuelser, J. P., Ichimoto, K., Sakurai, T., and Shibata, K. 1993, *in Symposium on New Look at the Sun with Emphasis on Advanced Observations of Coronal Dynamics and Flares.*

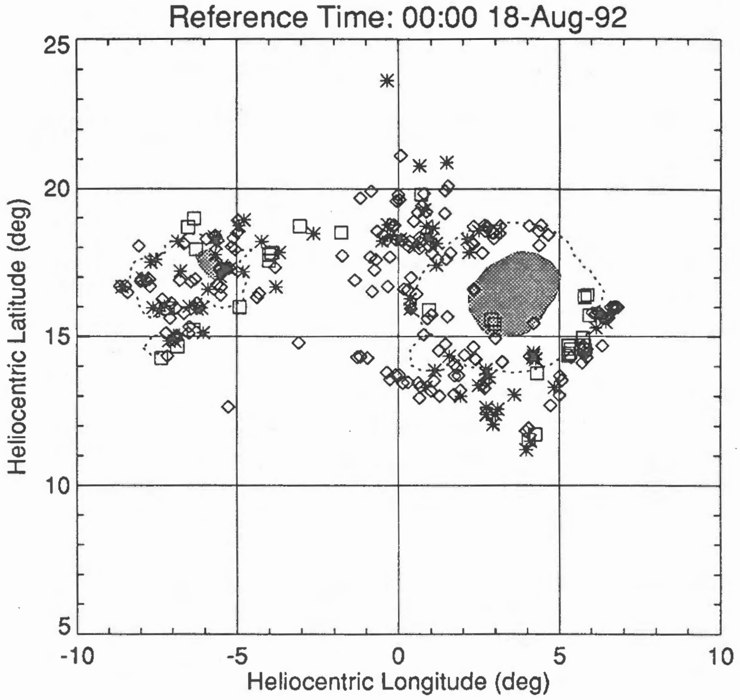

Fig. 3. Spatial Distribution of Transient Brightenings in NOAA 7260.

Ogawara, Y., Takano, T., Kato, T., Kosugi, T., Tsuneta, S., Watanabe, T., Kondo, I. and Uchida, Y. 1991, *Solar Phys.,* **136,** 1.

Sakurai, T., Takata, M., Shibata, K., and Ichimoto, K. 1993, *in proceedings of the 2nd Japan-China Seminar on Solar physics* (this proceeding).

Shibata, K., Ishido, Y., Acton, L. W., Strong, K. T., Hirayama, T., Uchida, Y., McAllister, A. H., Matsumoto, R., Tsuneta, S., Shimizu, T., Hara, H., Sakurai, T.,Ichimoto, K., Nishino, Y. and Ogawara, Y. 1991, *Publ. Astron. Soc. Japan,* **44**, L173.

Shimizu, T., Tsuneta, S., Acton, L. W., Lemen, J. R., and Uchida, Y. 1992, *Publ. Astron. Soc. Japan,* **44**, L147.

Shimizu, T., Tsuneta, S., Acton, L. W., Lemen, J. R., Ogawara, Y., and Uchida, Y. 1994a, *Astrophys. J.,* in press (to appear in Feb. 20 issue).

Shimizu, T. et al. 1994b, in preparation.

Tsuneta, S., Acton, L., Bruner, M., Lemen, J., Brown, W., Caravalho, R., Catura, R., Freeland, S., Jurcevich, B., Morrison, M. 1991, *Solar Phys.,* **136,** 37.

X-Ray Activity in Coronal Loops and Its Photospheric/Chromospheric Counterparts

Takashi Sakurai, Kazunari Shibata, and Kiyoshi Ichimoto
National Astronomical Observatory, Mitaka, Tokyo 181
and
Masao Takata
Department of Astronomy, The University of Tokyo, Bunkyo-ku, Tokyo 113

Abstract

Brightenings seen in X-ray coronal loops are compared with Hα and magnetograph observations obtained at Mitaka. An indication of magnetic field changes of about 50 gauss is found at a footpoint of a loop in association with its X-ray brightenings.

1. Introduction

Now it is generally believed that flares take place when the magnetic field has accumulated excess energy. A most likely form of magnetic field which stores excess energy is the so-called sheared magnetic field. Magnetic field observations often showed that after a flare the shear relaxes (Sakurai et al., 1992). The aim of this study is to investigate whether such magnetic field changes are found in smaller scale events, for example loop brightenings seen in X-ray coronal loops in active regions (Shimizu et al., 1992).

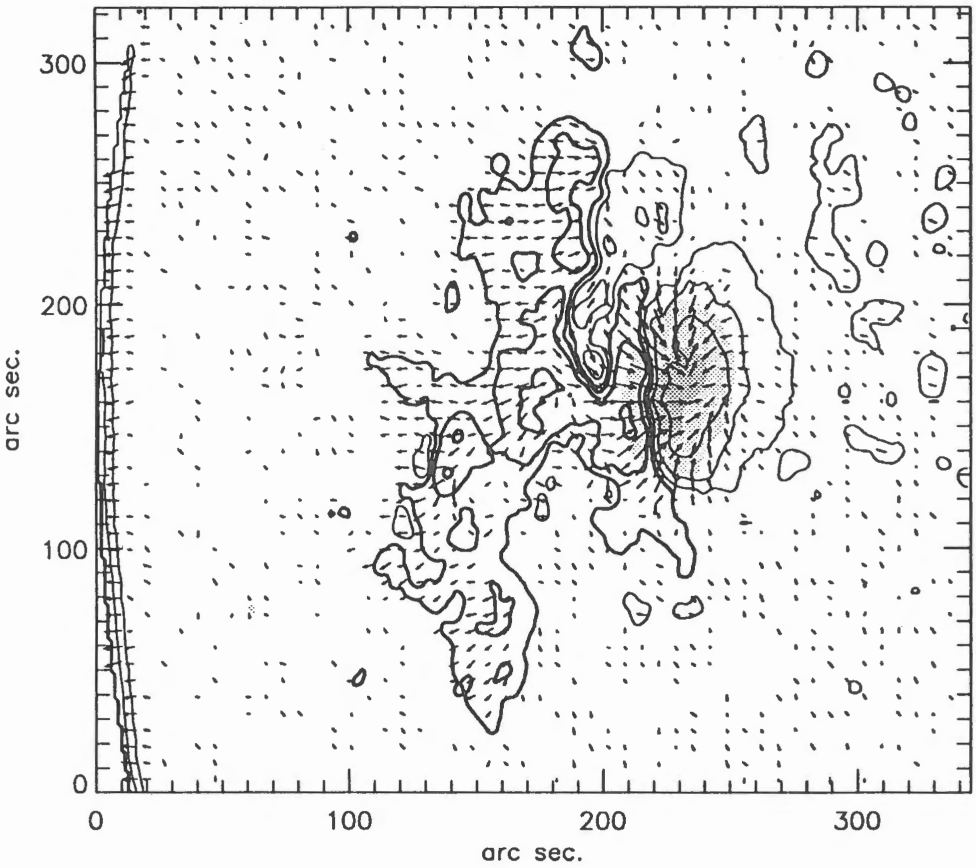

Fig. 1 A magnetogram of NOAA 7260 on 1992 August 14 observed with the Solar Flare Telescope

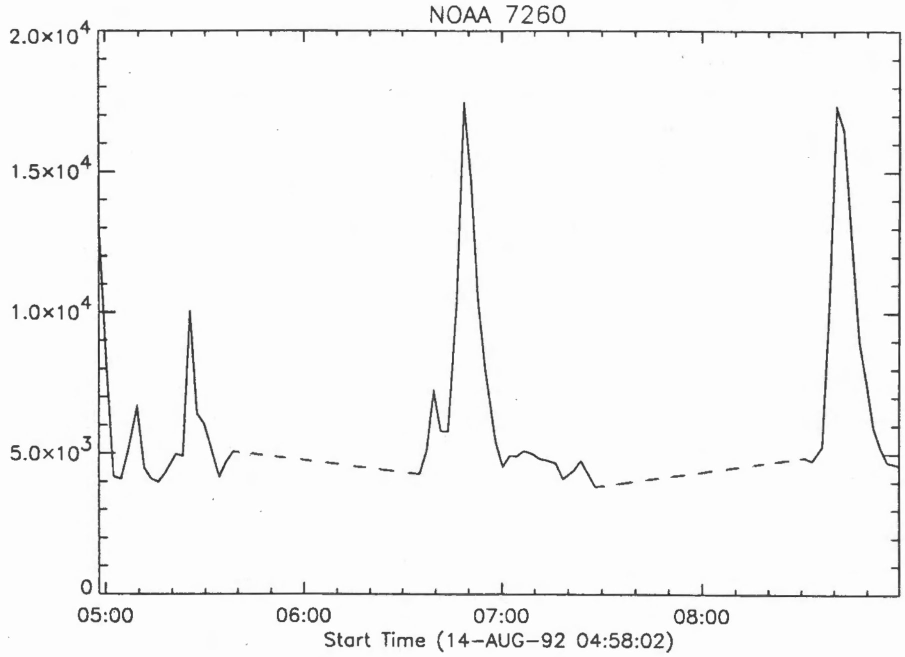

(a) X-ray Light Curve

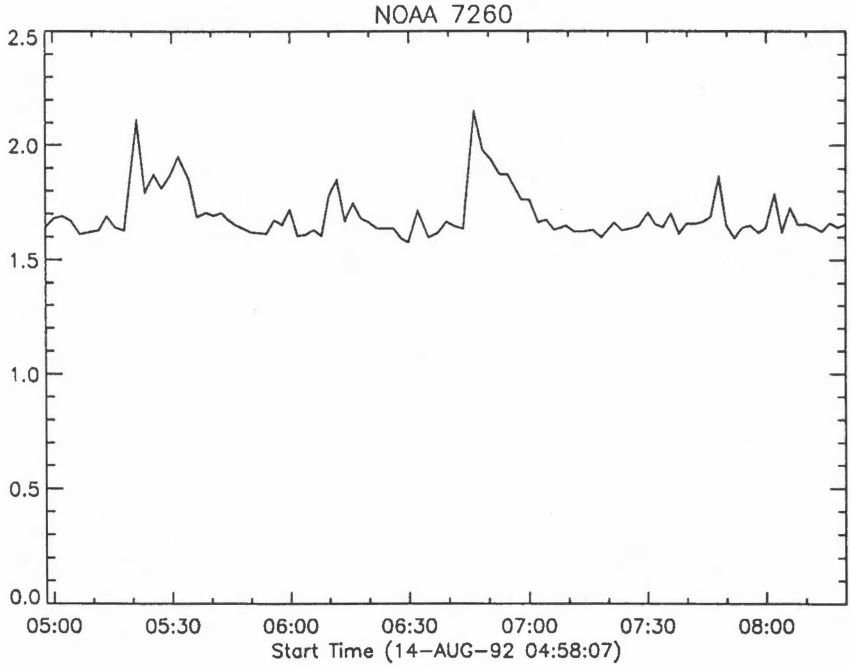

(b) Hα Light Curve

Fig. 2 (a) X-ray and (b) Hα light curves of NOAA region 7260 on August 14, 1992.

2. Observations

We picked up the region NOAA 7260 of August 14, 1992. The Solar Flare Telescope at Mitaka (Ichimoto et al., 1991) had continuous magnetogram coverage for three hours from 04:56 UT to 08:19 UT, with 3 minute cadence (figure 1). Within this interval, the soft X-ray telescope of Yohkoh (SXT) had its partial frame observing region pointed at the same region. The images were taken through Al 0.1 μm and Al 1.2 μm filters, with a format of 128 × 128 pixels. The resolution was 2.5 arcseconds per pixel. Through each filter, images were taken every 2 minutes, with night gaps of about 50 minutes. We only use the data taken through Al 0.1 μm filter covering the interval between 4:58 UT and 8:59 UT. For the overlay of X-ray and magnetograms, we used optical images taken with the aspect sensor of SXT.

Figure 2a is the X-ray light curve of this region during the observing period mentioned above. The brightness of the brightest pixel in the field of view is plotted in this figure. In the same manner, figure 2b shows the Hα light curve of this region obtained from the video disk recording of Hα images with the Solar Flare Telescope. Several brightening events were found, which took place in the loops emanating from the east-side (limb-side) penumbra of a large sunspot.

Figure 3 shows an example of X-ray brightenings which took place at 0646 UT. By makeing a difference between the brightening and the pre-brightening images, the brightening in a small loop becomes clearly visible.

Figure 4 shows the Hα image taken near the time of the X-ray brightening of figure 3, and two points located at the footpoints of the X-ray loop showed brightenings.

The overlay of X-ray images and magnetogrms shows that the loops ran across the magnetic neutral line with a very acute angle, indicating sheared magneric field. Because the region is close to the limb, the spot showed the so-called shadow (inverse) polarity on the limb-side of the spot. Although both footpoints of the loops were apparently rooted in the same magnetic polarity, the correction of the view angle effect shows that actually the loops connected the opposite polarities.

3. Magnetic Field Changes

By viewing magnetograms as a movie, it is noticed that the magnetic field changes in a restricted area which coincides with the south-western footpoint of the X-ray loop that showed brightenings (figure 5). The time variation of the magnetic field in this region is shown in figure 6 together with data from other (control) points. The magnetic field change associated with loop brightenings was detected with the magnitude of about 50 gauss in the longitudinal field. Since the region is 50 degrees east of the central meridian, the change can be explained if the loop which had run nearly parallel to the solar surface became slightly elevated with respect to the surface. The change is rather gradual and it is not certain whether the magnetic field change is the cause or the result of the loop brightenings.

References

Sakurai, T., Shibata, K., Ichimoto, K., Tsuneta, S., and Acton, L.W. 1992, *Publ. Astron. Soc. Japan*, **44**, L123.

Shimizu, T., Tsuneta, S., Acton, L.W., Lemen, J.R., and Uchida, Y. 1992, *Publ. Astron. Soc. Japan*, **44**, L147

Ichimoto, K., Sakurai, T., Nishino, Y., Shinoda, K., Noguchi, M., Kumagai, K., Imai, H., Irie, M., Miyashita, M., Tanaka, N., Sano, I., Suematsu, Y., and Hiei, E. 1993, *IAU Colloquium*, **141**, 166.

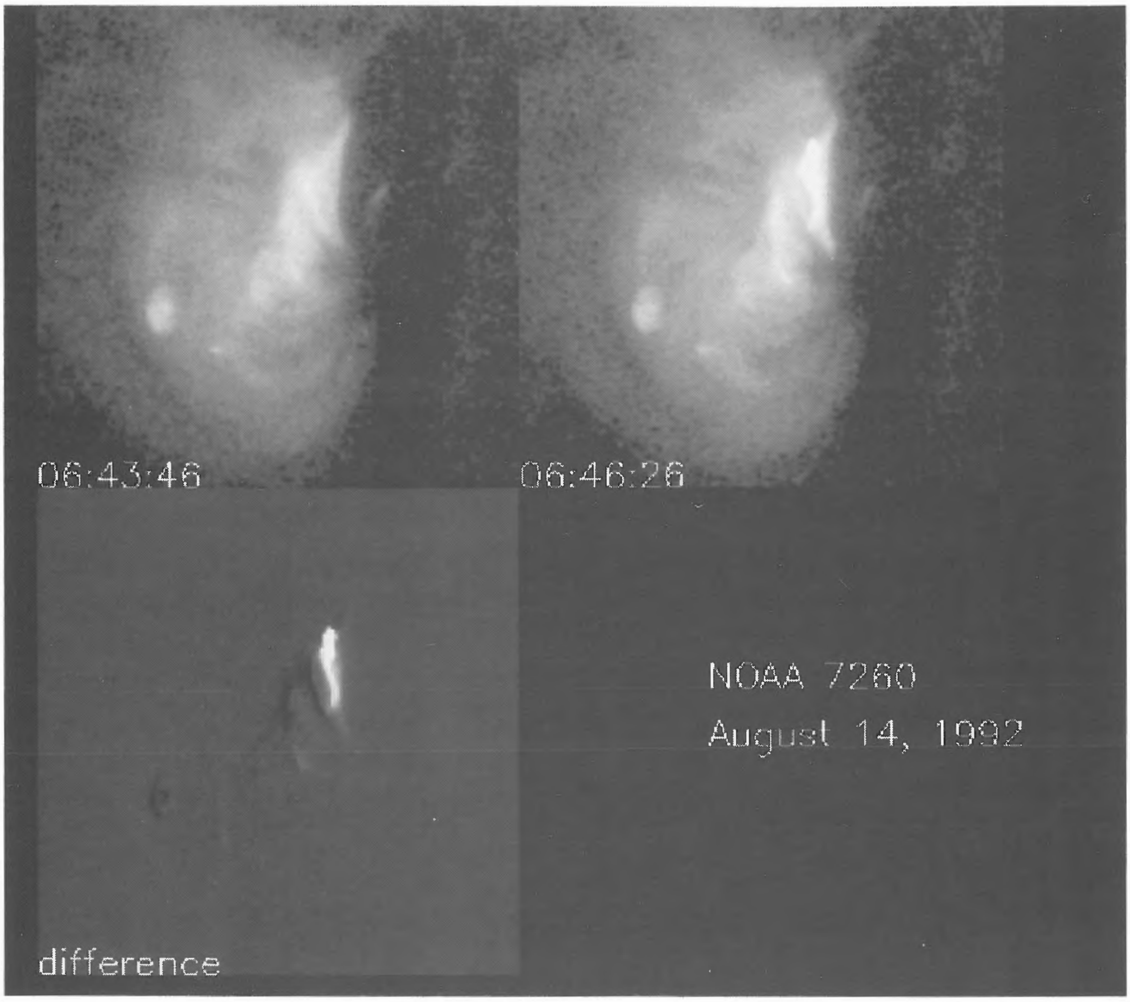

Fig. 3 Yohkoh soft X-ray images of the loop brightening at 0646 UT. The difference image (lower left) is made from the two frames taken at 0646 UT (at the brightening) and at 0643 UT (before the brightening).

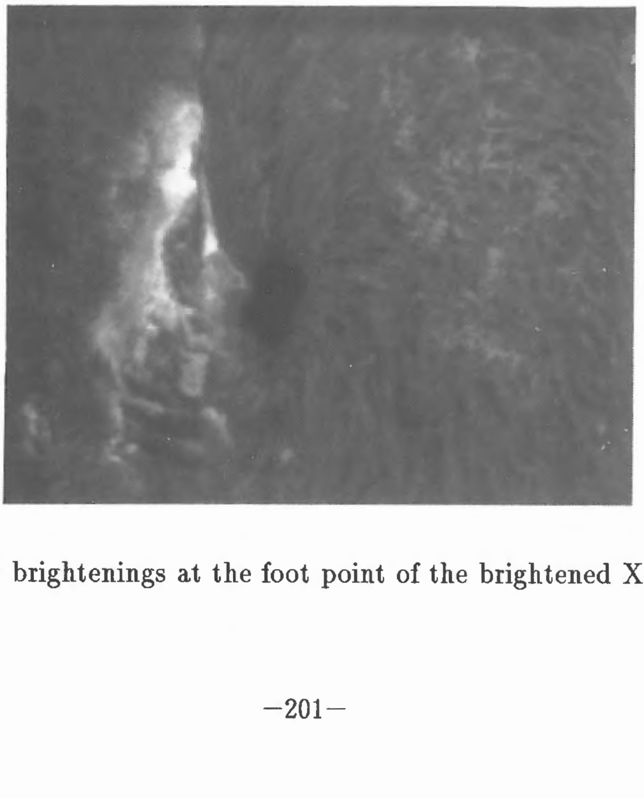

Fig. 4 Hα brightenings at the foot point of the brightened X-ray loop.

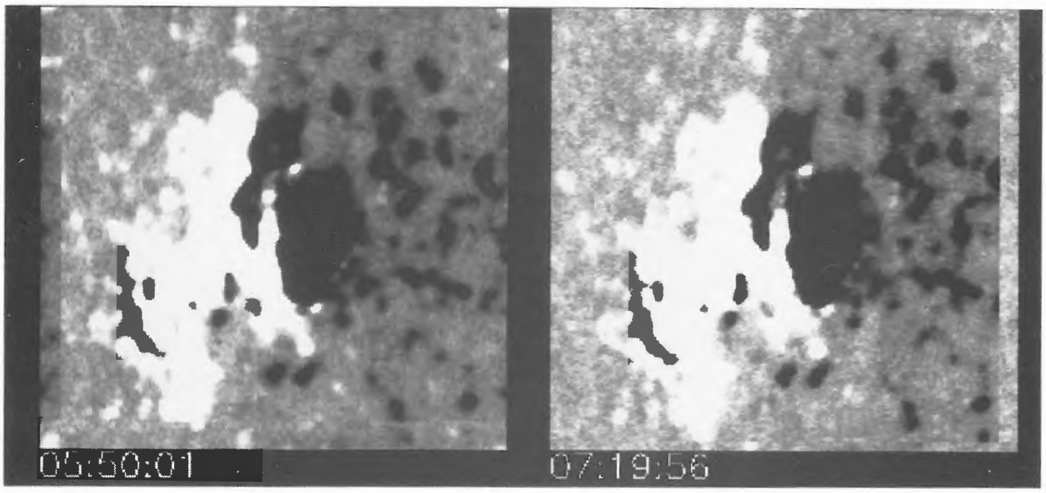

Fig. 5 Longitudinal magnetograms in gray scale representation, taken 80 minutes apart. The disappearance of a patch of positive (white) polarity is clearly seen.

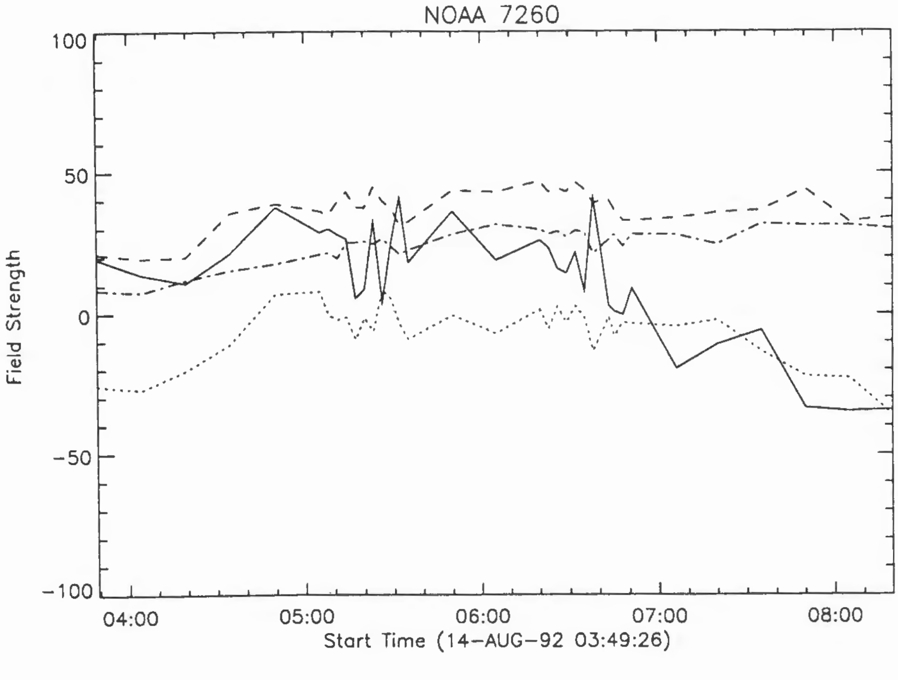

Fig. 6 Changes of magnetic fields in time. The solid line corresponds to the patch of disappearing positive polarity in fig. 5. The other points (indicated by dotted, dashed, and dot-dashed lines) do not show such systematic variations.

Session 5: NOAA 7270

NOAA 7270： A Brief Report of Observations

Mingchan WU

Yunnan Observatory,P.O.Box 110, Kunming 650011, China

Abstract

The NOAA 7270 was one of two main active regions on solar disk in first ten days of September,1992.The AR 7270(S10 L035)appeared on east limb on August 29, 1992. It had a simple magnetic structure of the sunspot until September 4. And the region began its rapid development on September 5. The flare activity of the region reached its maximum on September 6.when it produced two X-class X-ray flares.In this paper , it is briefly reported the observational data of NOAA 7270,including the obsevations with 26cm Solar Telescope at Yunnan Observatory.

1.Introduction

The three active regions, NOAA 7260, 7270 and 7321,investigeted in this Workshop, all occurred in desending phase of Cycle 22, when the general level of the solar activity was going down. But when the three active regions appeared, the solar activity in August-November,1992 increased temporally.In fact,the YOHKOH X-ray Image Video show that the solar X-ray bursts and active phenomena in corona were very frenqunt and rich during the period mentioned above.

2.Outline of NOAA 7270

The AR7270 appeared on east limb of the solar disk on 1992 August 29. During the first seven days, the configuration of the sunspot group and the magnetic field was simple. The sunspot was C or D in McIntosh classification and the magnetic class was B as shown in Figure.1, At the same days, the flare activity of the region was low. Only some small flares occurred.They were subflares in optical and C-class in X-ray.

The AR7270 began develope rapidly on September 5. As shown in Figures 1, 2 and 3, the sunspot group became complex EKI, the magnetic configuration became BDG and the sunspot area increased to about 500×10^{-6} hemi.At same time,the flares in the region occurred frenquntly. The flare activity of the region reached its maximum on September 6, when it produced 9 M-class X-ray flares and two X-class X-ray flares. They were X1.7/2B flare at 1852UT and X 1.3/1N flare at 2059UT, which were the strongest flares occurred in AR7270. Unfortunately, the two flares occurred in midnight of Japan and China.

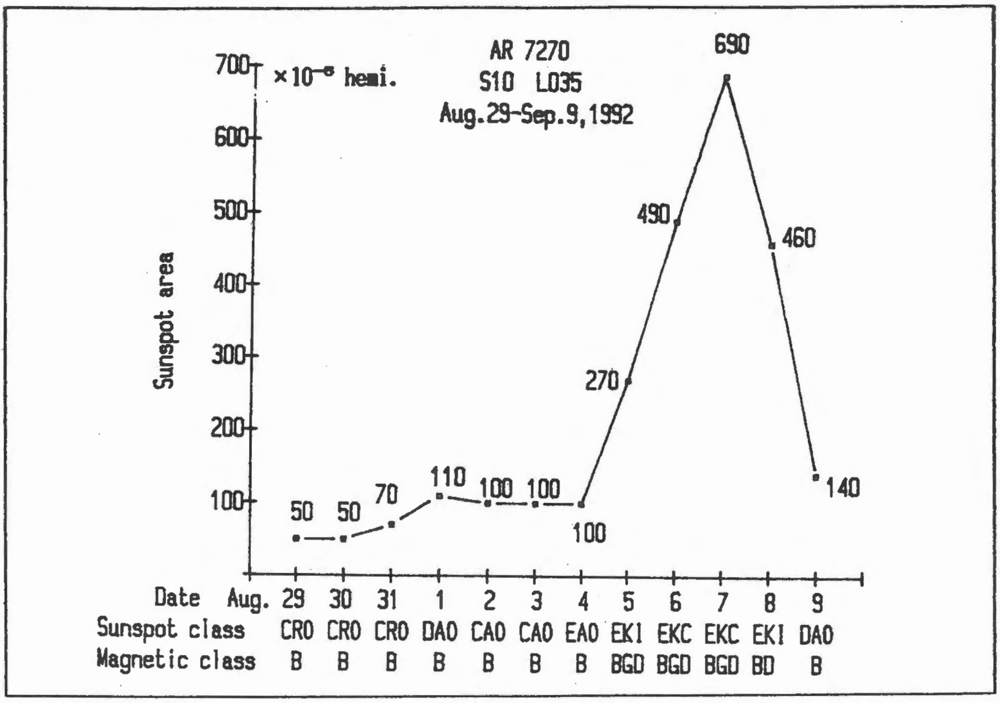

Figure 1.The sunspot and the magnetic class of the NOAA 7270.

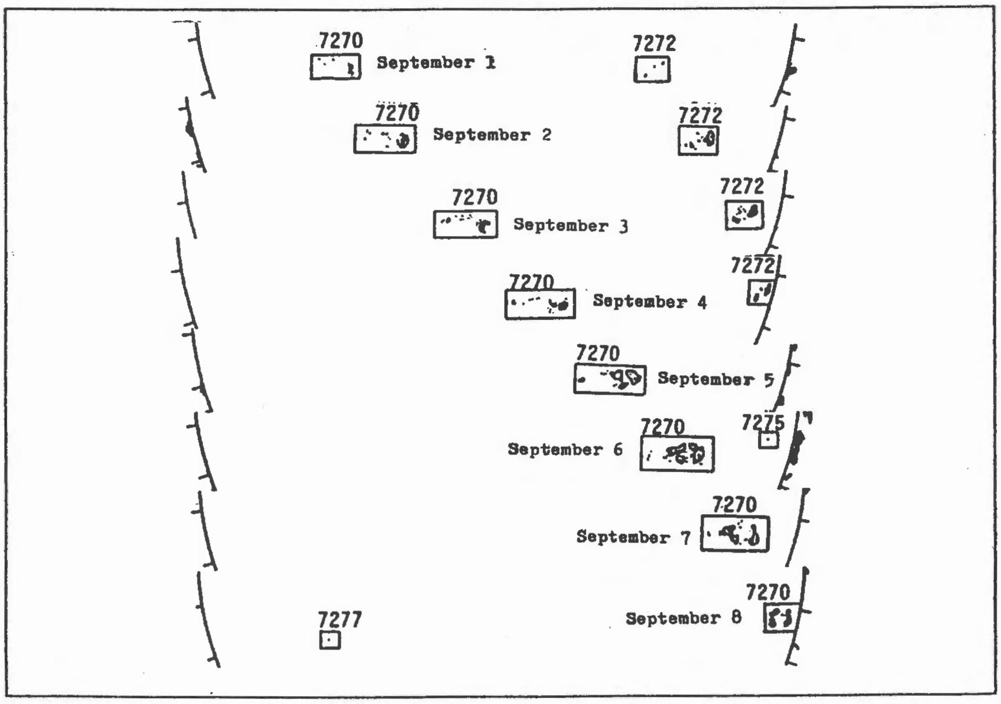

Figure 2.The evolution of the sunspot of the NOAA7270.

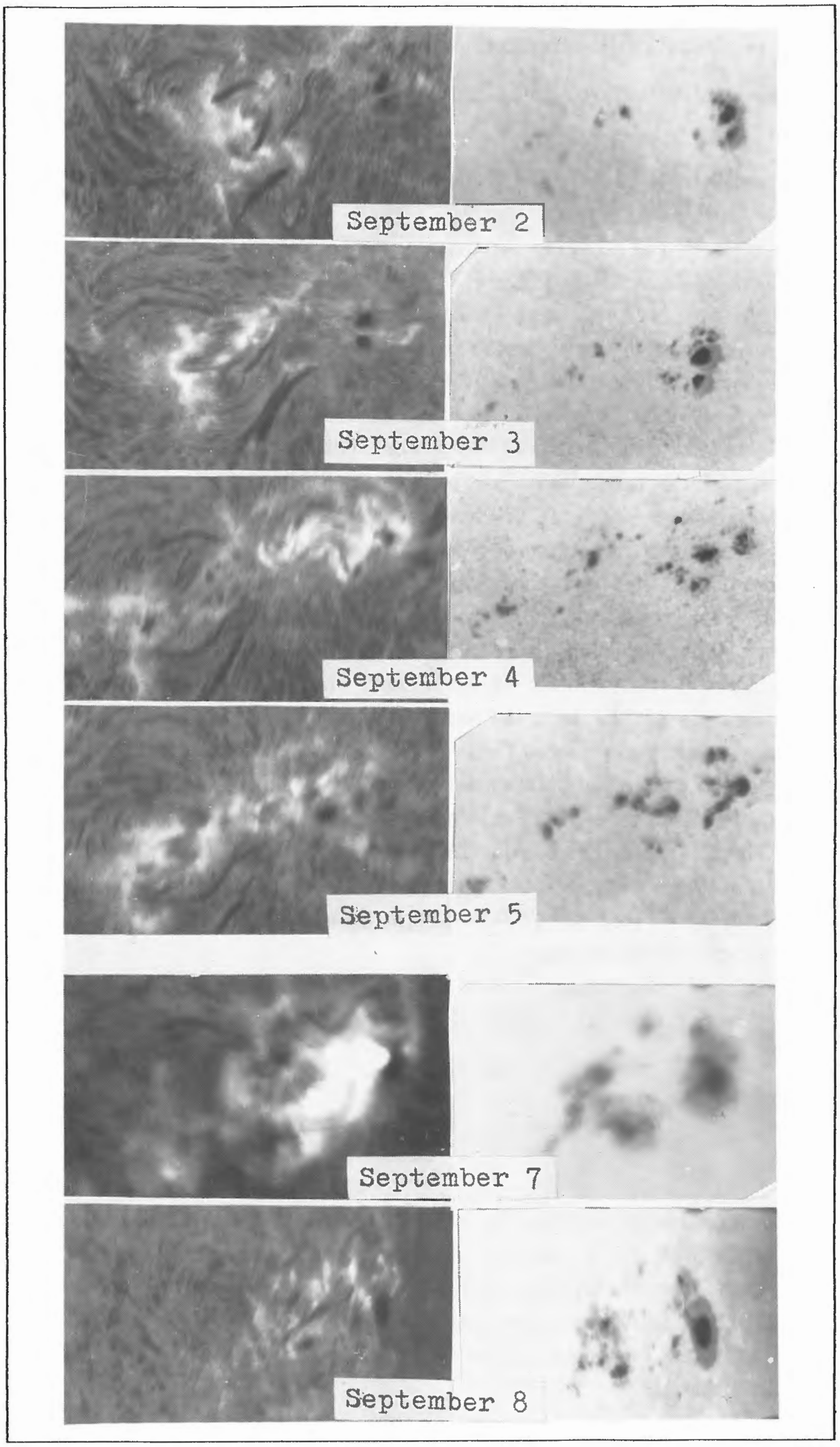

Figure 3.The daily images in Hα and in white light of the NOAA 7270 on September 1-9,1992.
Scale: 4 arcsec/mm

On September 7 and 8, the region stopped its development and the flare activty decreased gradually. On September 9,the region was near the west limb.

3.Observed Results of The NOAA 7270

The lists of the sunspots and the flares of the NOAA 7270 have been published in SGD(1992a, 1992b, 1993) and SESC PRF(1992). A diagrams of GOES X-ray with Hα and X-ray flares have been published in SGD(1993) also.The majorety of contribution of the X-ray intensity with flares in the daily diagrams(September 1 to 9) belong to the AR 7270. A Solar Activity Indices at 17GHz with GOES X-ray profiles during the period when the NOAA 7260, 7270 and 7321 passed through the solar disk have been published by Y. Hanaoka of Nobeyama Radio Observatory (1993) . The list and the diagrams of YOHKOH Hard X-ray Bursts have been published by T.Kosugi ed al.(1993).

The observation of the AR7270 have been carried out by the 26cm Solar Telescpe at Yunnan Observatory. But the observed data were not so good, because the weather and the seeing of Kunming were poor during the first ten days of 1992 September. The daily Hα -filtergrams and the white light sunspots are shown in Figure 3 . On September 7, two Hα flares were observed by 26cm Solar Telescope. The first one was the C4.5/SN flare at 0158UT. It was a small flare associated with a mass ejection which shape was similar as a fan shown in Figure 4. In the Fig.4,we can see that the dark mass downforward ejected from the flare site near the g-sunspot at 0202UT. And only few dark mass moved upforward (it was shown in simultaneous Hα -blueshift images which not published in this paper for limit of the pages).The second one was the M3. 6/2B flare at 0353UT. The flare occurred in location between two major sunspots of the region shown in Figure 5. An another flare,the M7.1/2B at 0634UT was observed by 18cm Flare Patrol Telescope at Yunnan Observatory . This flare also occurred near the major g-sunspot.

The magnetic observation of NOAA 7270 was obtained in Beijing Observatory and was reported by G.X.Ai et al.(1993)in this Workshop.

4.Summary

Generally, the NOAA 7270 is an active region with middle activity in decreasing phase of Cycle 22.Its active life is short,only four days when the new magnetic flux emerged, the sunspots in the region moved, impacted and combined each other. At same time,the flare activity was frenqut.Once the region evolved to its maximum which was indicated by the two X-class X-ray flares on September 6. it stopped development and fade-out gradually.

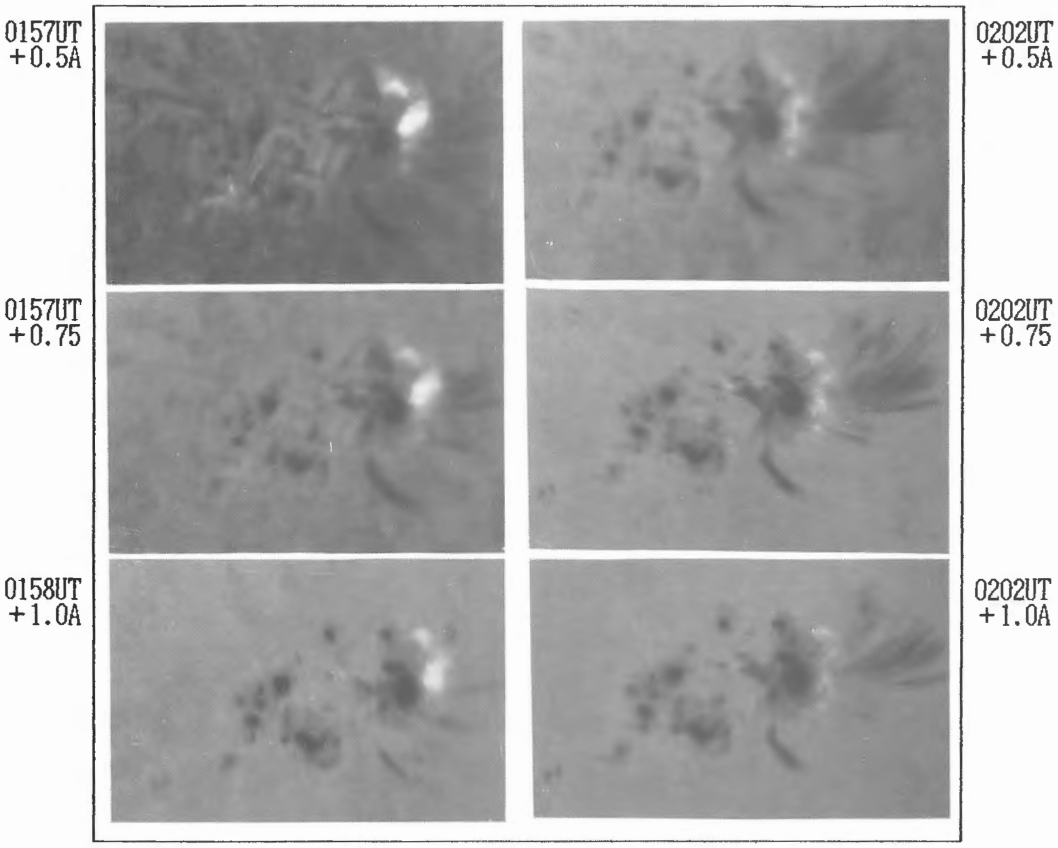

Figure 4. The C4.5/SN flare and associated mass ejection on September 7, 1992.
Scale: 4 arcsec/mm

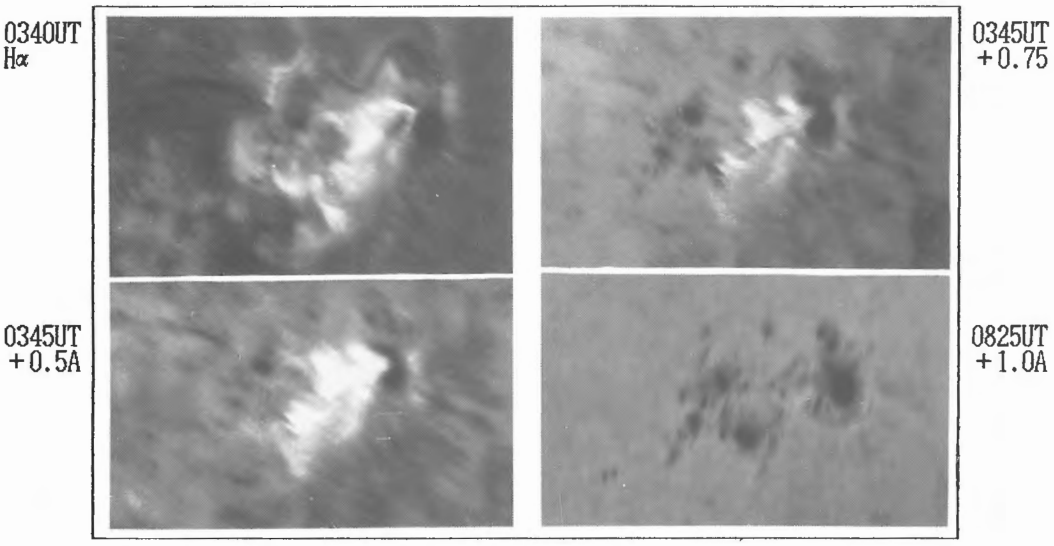

Figure 5. The M7.1/2B flare on September 7, 1992.
Scale: 4 arcsec/mm

References

Ai,G.X.et al.,1993, In this Workshop.
Hanaoka,Y.,1993,Solar Activity at 17GHz,Nobeyama Radio Observatory,In this Workshop.
Kosugi,T.,et al.,1993, THE YOHKOH HXT DATABOOK(I).
SESC PFR,1992,No.889, September 15,p.7.
SGD,1992a, No.578 Part 1, October, p.27-28.
SGD,1992b, No.579 part 1, November,p.83-84.
SGD,1993, No.583 Part 2, March,p.47-48.

EMERGING FLUX REGIONS AND SURGE ACTIVITIES IN NOAA 7270

H. Kurokawa, R. Kitai, Y. Funakoshi, and Y. Nakai
Kwasan and Hida Observatories, Kyoto University, Kamitakara, Gifu 506-13
K. Ichimoto, and K. Shibata
National Astronomical Observatory, Mitaka, Tokyo 181
H. Zhang
Beijing Astronomical Observatory, Beijing 100080, China

ABSTRACT

The evolutional characteristics of a rapidly growing active region NOAA 7270 was studied with high resolution Hα filtergrams. At least six emerging flux regions are found to grow during a short period from 5 through 6 September, 1992. Most of flares and surges during this period were caused by these emerging flux regions and or the interactions between them. A special attention is given to the conspicuous surge activities observed at the leading edge of the preceding sunspot, where some parasitic magnetic flux of opposite polarity is found. We conclude that the surges were produced by the reconnection between the new emerging flux and the surrounding older magnetic fields.

I. Introduction

The causal relations between flares and emerging flux regions have been pointed out by many optical observations, which are summarized in Kurokawa (1991). Kurokawa (1991) reached to a conclusion that the emergence of twisted magnetic flux rope is the most important factor for a major falre activity, and suggest that more detailed studies of the evolutional changes of the flare productive emerging flux regions are necessary, combined with high resolution Hα images, magnetograms and X-ray images.

NOAA 7270 is one of such regions as to be studied in details, because it rapidly developed and produced many flares and surges from 5 through 7 September, 1992. Firstly, therefore, we study when and where emerging flux regions came up in the region and how they interacted with each other to build up the energy of the flares and surges.

Secondly we present the observational results of a conspicuous surge activity observed at the leading edge of the preceding sunspot in NOAA 7270 and discuss the causal relation between the surges and the emerging flux region.

II. Emerging Flux Regions in NOAA 7270

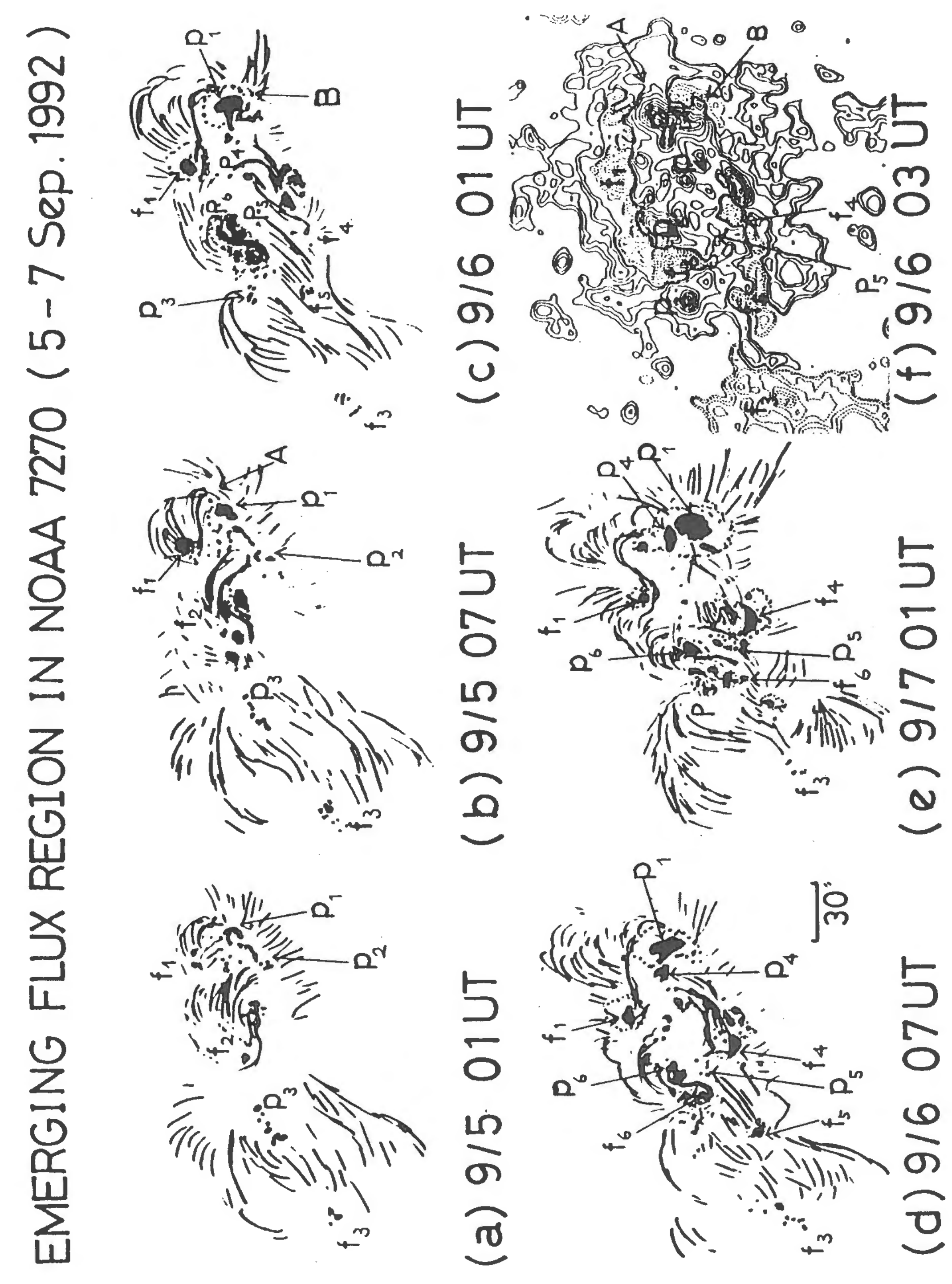

Fig. 1. The six emerging flux regions p_1 - f_1,.....,p_6 - f_6 identified in NOAA 7270. Thin lines are Hα dark fibrils and filaments representing directions of the chromospheric transverse magnetic field. The dark spots, dots and dotted circles shows sunspot umbrae, pores and penumbrae, respectively.

High resolution Hα images of NOAA 7270 are obtained from 5 through 7 September, 1992 with the Dmeless Solar Telescope (DST) at Hida Observatory, Kyoto University. Some of Hα images showing the evolutional changes of the region are presented in Figure 1 of Kitai et al.(1994) in this proceedings. Examining them in details, we studied when and where emerging flux regions came up and how they interacted with each other to build up the flare energy.

Figure 1 shows the evolutional changes of Hα dark fibril structures which present the direction of chromospheric transverse magnetic field. The sunspot umbra, pore and penumbra are shown by dark spots, dots and dotted circles, respectively. We found six newly-emerging bipolar pairs or emerging flux regions and marked p_1 - f_1, ..., p_6 - f_6 in Figure 1. the p (positive) and f (following) polarities are determined by comparing sunspot images with the longitudinal magnetic field maps observed by the Mitaka flare telescope of National Astronomical Observatory and the Huairou magnetograph of Beijing Astronomical Observatory.

From 01 UT through 07 UT of 5 September, three emerging flux regions p_1 - f_1, p_2 - f_2, p_3 - f_3 are found to be developing. Notice the rapid growth of the p_1 - f_1 pair and the development of sheared dark fibrils between them. Another remarkable is a drastic change in the direction of Hα fibrils at the central part of NOAA 7270 between 07 UT of 5 September and 01 UT of 6 September. Note the new emergence of p_4 - f_4, p_5 - f_5 pairs whose axes are nearly perpendicular to that of the p_2 - f_2 pair in Figure 1 (b) and (c). The emerging flux pair p_6 - f_6 also showed a dratic change in its magnetic field structure. Notice a conspicuous growth and a big change in the direction of the neutral-line fibril between the p_6 - f_6 pair, or the development of the magnetic shear in Figure 1 (b) and (c).

These three active emerging flux regions were major sources of the flare activities observed in NOAA 7270 from 5 through 7 September.

III. Surge Activity at the Edge of an Emerging Flux Region

Conspicuous Hα surge activities were continuously observed at the leading edge of the preceding sunspot p_1 from 5 through 7 September. Examining the video images obtained with Flare Monitoring Telescope (FMT), which was recently installed at Hida Observatory, we determined the start, maximum and end times of each surge. The result is summarized in Table 1. We found the following characteristics of the surge activities: (1) Surges repeatedly spouted out from two locations A and B indicated in Figure 1 (b), (c) and (f) where Figure 1 (f) is a longitudinal magnetic field map observed by Huairou Station of Beijing Astronomical Observatory. The surge activities are especially strong at the location A on 5 September, and at the location B on 6 September. (2) The mean life time of the surges is about 15minutes. (3) The surges were repeatedly produced at the same location every about 25 minutes. Some examples of the surges observed with DST in Hα line wing, are shown in Figure 2.

Table 1. List of Surges Observed with Flare Monitoring Telescope at Hida Observatory.

DATE	TIM (UT)			PHENOMENA	REGION AND NOTE
	START	MAX	END	($H\alpha$ CENTER)	
9/4	23:19	23:24	23:30	SURGE	leading edge of preceding spot: (A)
	23:38	23:43	23:46	SURGE	(A)
	23:45	23:50	23:57	FLARE	central part of the region
9/5	00:01	00:05	00:10	SURGE	(A)
	00:12	00:15	00:35	FLARE, SURGE	east edge of the region
	00:41	00:45	00:55	SURGE	(A)
	01:05	01:08	01:22	SURGE	leading edge of preceding spot: (B)
	01:09	01:13	01:21	SURGE	(A)
	01:30	01:35	01:45	SURGE	(B)
	01:41	01:46	02:00	SURGE	(A)
	01:55	02:00	02:05	SURGE	(B)
	02:01	02:03	02:15	SURGE	(A)
	02:46	02:48	02:59	SURGE	(B)
	03:15	03:20	03:28	SURGE	(B)
	03:26	03:35	04:05	SURGE	(A)
	04:10	04:15	04:30	SURGE	(A)
	04:37	04:41	04:50	SF, SURGE	(A)
	05:02	05:07	05:38	SF, SURGE	(A)
	05:40	05:46	05:56	SF, SURGE	(A)
	06:07	06:11	06:20	SF, SURGE	(A)
	06:20	06:34	06:50	SF	(A)
	07:10	07:14	07:33	SF	along the preceding edge
	07:50		07:58	SURGE	(A)
9/6	00:28	00:38	00:50	SF, SURGE	(B) and (A)
	00:55	01:05	01:15	SURGE	(B)
	01:16	01:22	01:32	SURGE	(B)
	01:40	01:46	01:51	SURGE	(B)
	01:58	02:01	02:20	FLARE,SURGE	central part of the region
	02:15		02:30	SURGE	(B)
	02:22	02:28	02:45	FLARE	along the leading edge of p spot
	02:49	02:52	02:58	BP, SURGE	(B)
	02:58		03:15	BP, SURGE	(B), brightening at 03:01 and 03:08
	03:50	03:54	04:05	BP, SURGE	(B)
	04:09	04:11	04:25	SUBFLARE(SF)	north-east part of the region
	04:28	04:32	04:42	SURGE	(A)
	04:38	04:44	04:50	SURGE	(B)
	04:51		05:10	SURGE	(B)
	05:13	05:18	05:30	FLARE	(A) and north of (A)
	05:27		05:35	SURGE	(B)
	05:40	05:42	05:52	SF	(A)
	05:45	05:52	06:02	SURGE	(A)
	06:13		06:20	SURGE	(B)
	06:34		06:40	SURGE	(A)
	06:45	06:48	06:55	SURGE	(A)
	06:54	07:01	07:25	FLARE	central part of the region
	06:55		07:15	SURGE	(A)
	22:55		23:30	SURGE	(B)

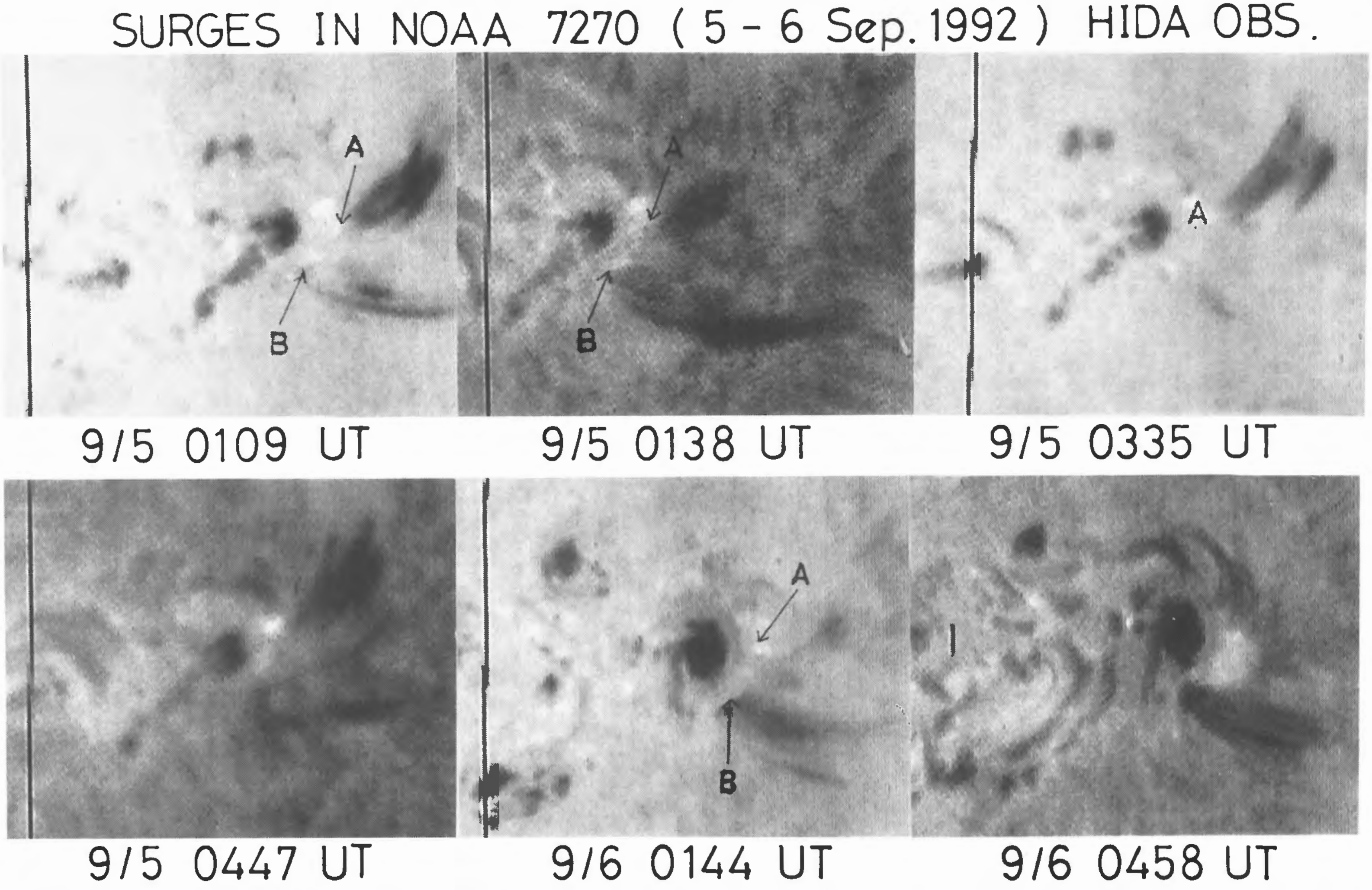

Fig. 2. Cntinous Surges Activities observed at the leading edge A and B of the preceding sunspot of NOAA 7270.

IV. Discussion and Conclusion

Kurokawa (1988) found Hα surges are often observed at the earliest stage of emerging flux regions (EFR), and Kurokawa and Kawai (1993) called them EFR-surges. They found that EFR-surges spout out from the site where emerging flux collides with pre-existing magnetic field of oppsite polarity, and concluded that the EFR-surges are produced by the magnetic field reconnection between the EFR and the surrounding region.

The p_1 - f_1 pair of NOAA 7270 is rapidly growing emerging flux region as studied in the section 2. The surrounding region of the p_1 spot has the same magnetic polarity as the p_1, and the surge activity described in the previous section may contradict the conclusion of Kurokawa and Kawai (1993). We can notice, however, some parasitic magnetic fields of following polarity around the location B in the Huairou magnetogram (Figure 1 (f)). In addition, the surge activities are nearly continuously observed simultaneously with the successive emergence or constant growth of the p_1 - f_1 pair. With these two evidences we cnclude that the conspicuous surge activities observed at the leading edge of NOAA 7270 are produced by the same reconnection process as proposed by Kurokawa and Kawai(1993). We suggest that the absence of any parasitic magnetic field of the following polarity at the location A in Figure 1 (f) is due to an insufficient resolution of the magnetogram.

References

Kitai, R., Kurokawa, H., Funakoshi, Y., Nakai, Y., Ichimoto, K., Shibata, K., and Yaji, K. 1994, in this proceedings.

Kurokawa, H. 1988, Vistas in Astronomy, **31**, 67.

Kurokawa, H. 1991, Lecture Notes in Physics, **387**, 39.

Kurokawa, H. and Kawai, G. 1993 ASP Conference Series, **46**, 507.

Flares on September 6, 1992

R. Kitai, H. Kurokawa, Y. Funakoshi, Y. Nakai
Kwasan and Hida Obs., Kyoto University, Kamitakara, Gifu 506-13
K. Shibata, K Yaji
National Astronomical Observatory, Mitaka, Tokyo 181
N. Nitta
Lockheed Palo Alto Research Laboratory, Palo Alto, CA 94303, U.S.A.
and
YOHKOH team and NAOJ Flare Telescope Team

Abstract

We present some preliminary results of our observational study of typical eruptive flares in NOAA7270 on September 6, 1992. (1)Magnetic shear and flux emergence are strongly related to flare production. (2)Observed flares showed a common temporal relation between cool plasma dynamics seen in Hα and coronal energy releases seen in YOHKOH data.

1. Introduction

NOAA7270 produced many M or C class flares on Sep 5-7, 1992. The region grew its area rapidly during this period, and formed δ type magnetic configurations at 4 parts of the region on Sep 6. All the flares were observed to be related to these δ type magnetic configurations. Here we report the results of Hα optical observation of the eruptive flares on Sep 6, at the DST of Hida. We will also discuss the results of cross-comparative analyses of YOHKOH observations of the flares, especially on the spatial and temporal relations of Hα mass explosion, SXT brightenings and HXT bursts.

2. Evolutional Characteristics of NOAA7270

As can be seen in figure 1, NOAA7270 evolved rapidly from Sep 5 through Sep 7. On Sep 5, there appeared an EFR at the northern part of the preceeding spot (EFR A). The axis of the EFR was directed nearly along the N-S direction. On Sep 6, the axis of the region rotated in counter-clockwise direction. And the distance between opposite polarities grew rapidly. As a result of these motions of rotation and separation, a highly sheared magnetic structure was formed on Sep 6. M-class flares ocurred at this site of the region repeatedly.

The emergence of another EFR (EFR B) was essential to the evolution and the activity of NOAA7270. The EFR B appeared at the central part of NOAA7270, pushing the pre-existing magnetic structures aside on Sep 5-6. The specific character of the EFR was its way of emergence. The magnetic structure was highly sheared since the beginning of the emergence. Hα features in the region were nealy parallel to the magnetic neutral line. This site was also active for producing M-class flares on Sep 6.

3. Flares

On Sep 6, following four M-class flares were observed (figure 2):

(1) M1.0/1N flare (0156-0225 UT) : Threads or low-lying filament were observed on a magnetic neutral line. Part of the filament was highly excited and a bright loop in Hα was observed to expand with a velocity of 200 km/sec at the explosive phase. Following the initial expansion, an arcade system of Hα plasma, possibly situated underneath the covering neutral filament, started to expand. One or two minutes after the first Hα explosion, a hard X-ray burst started. In SXT images, two bright kernels, situated in opposite magnetic polarity regions, were observed.

(2) M1.1/SF flare (0232-0251 UT) : Surrounding the leading spot, there was a system of superpenumbral filaments in highly sheared form. Parts of the filaments which emanated radially outwards from the leading spot, were gathered to a following spot, forming a twisted bundle of loops in Hα. After about half an hour of internal motions in the twisted bundle, the flare started. The flare itself was of a slow type. Soft X-ray flux increased and then decreased gradually. No hard X-ray bursts were detected in this flare.

(3) M2.4/2N flare (B0515-0614 UT) : The flare occurred at the same part as the flare (2) with a similar Hα morphology, but was different from (2) in some respects. The flare firstly brightened at both sides of the neutral filament in Hα. In SXT images of YOHKOH, there appeared a bright loop, pararell to the magentic neutral line, connecting two-ribbons of Hα bright patches. A filament eruption occurred at the explosive phase. Then there appeared another pair of Hα bright ribbons adjascent to the initial ribbons. A faint loop or a cusped loop in soft-X rays was observed, related to the second two-ribbons. A hard-X ray burst was also observed 1-2 min after the explosive phase.

(4) M1.3/1F flare (B0657-0818 UT) : The flare occurred at the same part as the flare (1) and showed a very similar behavior as the flare (1), though there were some differences in the explosive filament morphology.

4. Discussion

As was stated above, the characteristics of initial time evolutions of M1.0/1N flare (0156-0225 UT), M2.4/2N flare (B0515-0614 UT) and M1.3/1F flare (B0657-0818 UT) were very similar to each other (figure 3). After the pre-heating stages of 5 to 10 min, there came explosive phases associated with Hα filament eruptions ($v \simeq 200$ km/s). Then about 1 to 2 min later, hard X-ray bursts started. We think that the observed temporal evolution is typical of erupting flares. Nearly simultaneous occurrence of Hα bursts of brightening, of filament explosions, and of soft-X ray bursts is a very interesting fact. It may indicates that sites of initial energy release of flares are not in high corona, but in lower layers, i.e., in the chromosphere or in the lowest layer of corona. From a quick look of Hα and SXT images in pre-heating and explosive stages of the observed flares, the initial energy releases of the flares occurred at very compact regions in the neighbourhood of neutral lines. This may also support the idea of energy releases in lower layers at initial phases of eruptive flares. Results of our detailed analyses will be published in another paper.

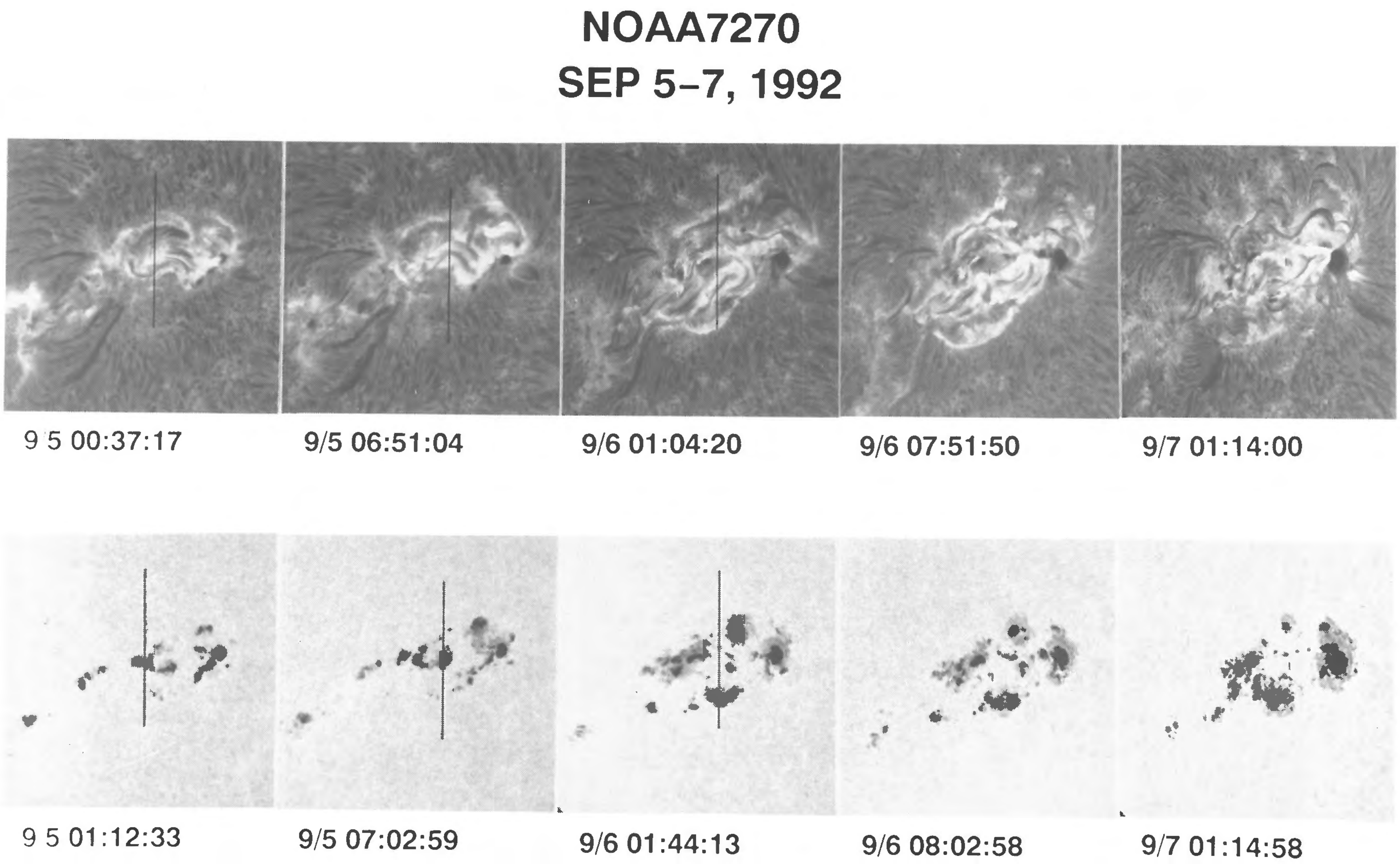

Fig. 1. Temporal evolution of NOAA7270. Upper row : Hα images. Lower row : Continuum images. North is to the top. East is to the left.

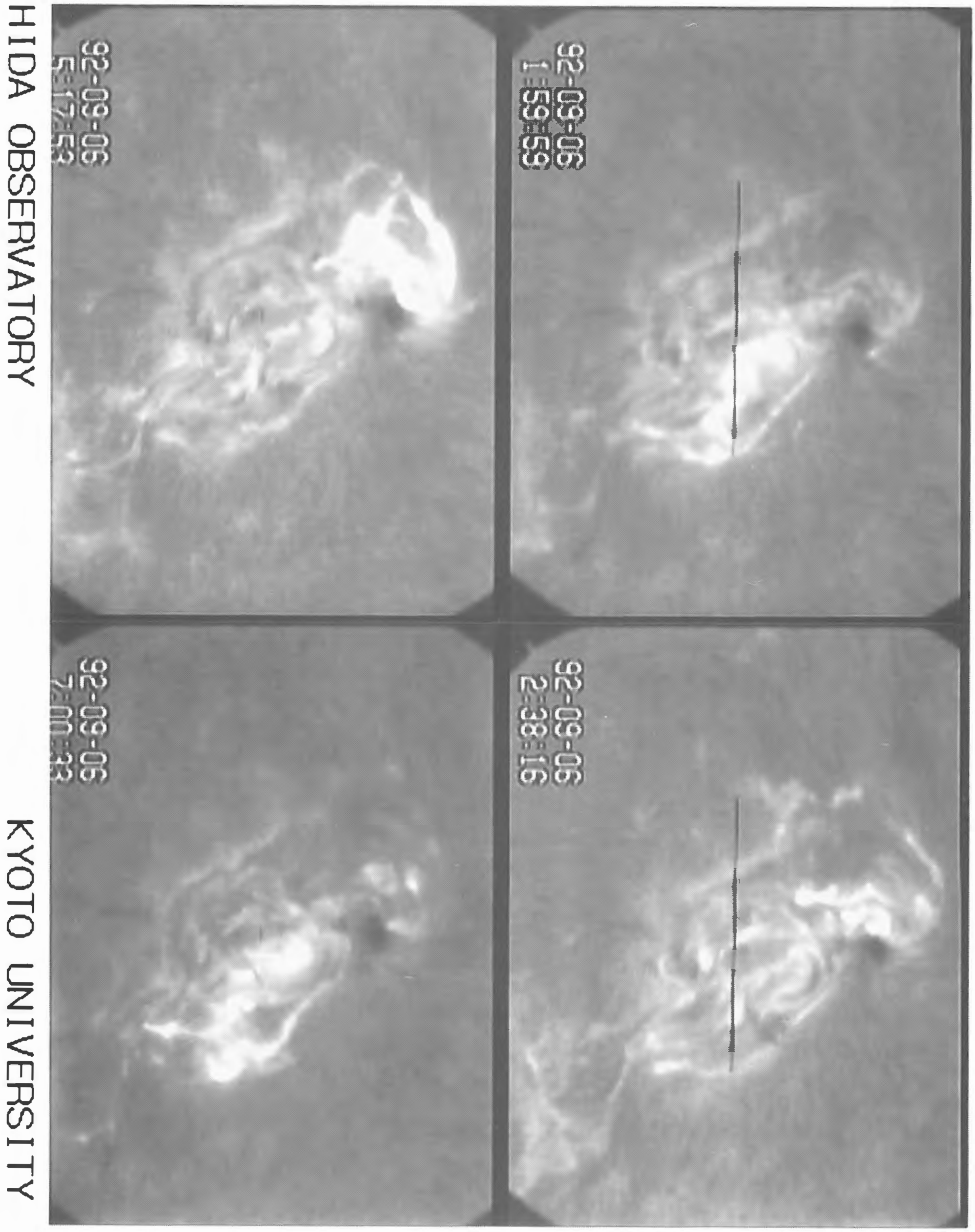

Fig. 2. **Hα line center images of the four flares observed in NOAA7270 on September 6, 1992.**

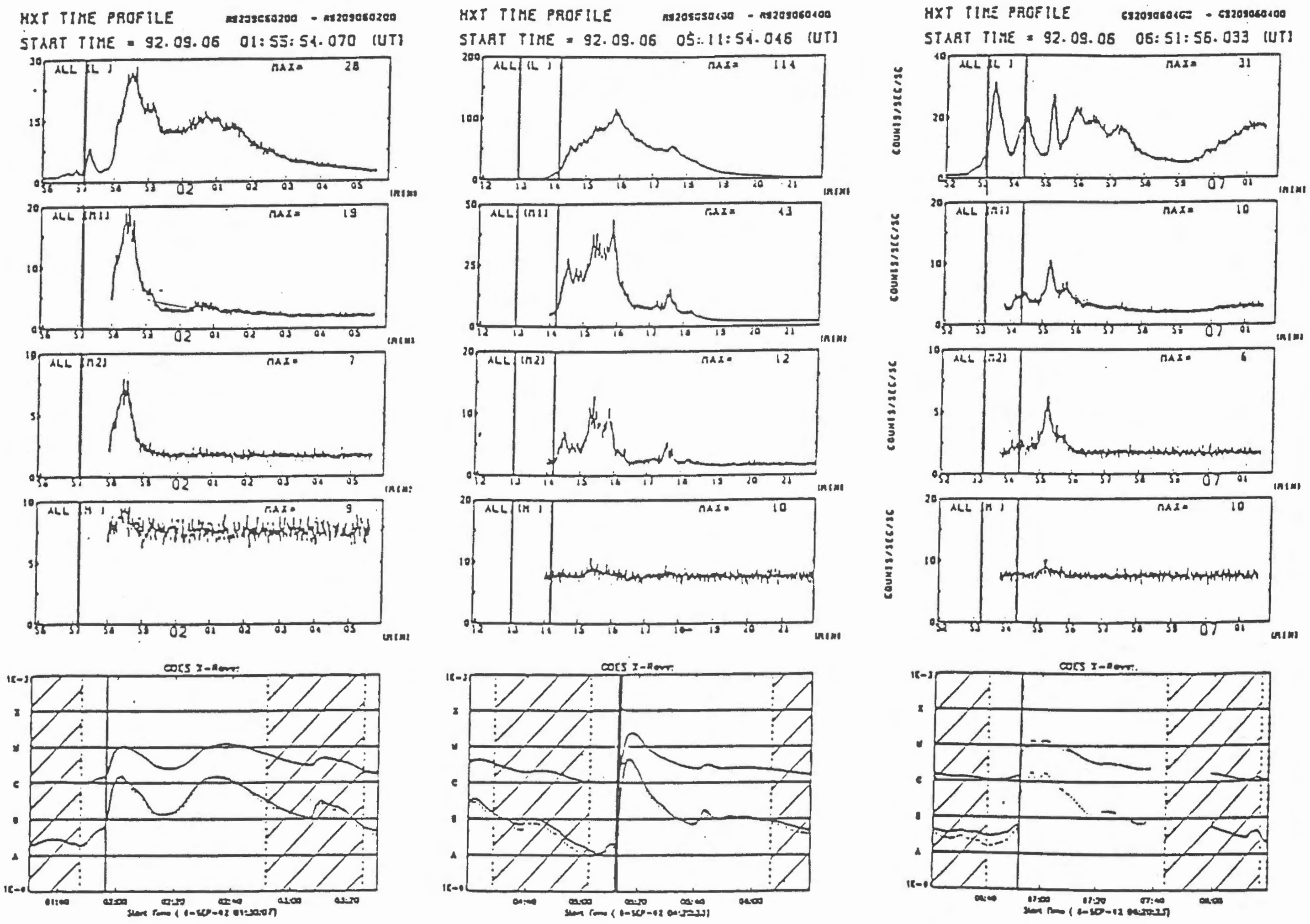

Fig. 3. Temporal evolution of the M-class flares observed. Top panels show time profiles in four channels of HXT of YOHKOH. Lower panels are GOES plots. Vertical bars in each panel indicate the start-times of Hα explosions.

FLARES ON SEPT. 6, 1992 IN NOAA 7270: SXT OBSERVATIONS AND COMPARISON WITH H ALPHA AND HXT OBSERVATIONS

K. Shibata[1], N. Nitta[2], R. Kitai[3], H. Kurokawa[3], K. Yaji[1], T. Sakurai[1],
and H. Zhang[4]

[1] National Astronomical Observatory, Mitaka, Tokyo 181, Japan
[2] Lockheed Palo Alto Research Laboratory, Palo Alto, CA 94304, U.S.A
[3] Kwasan and Hida Observatories, Kyoto Univ., Kamitakara,
Gifu 506-13, Japan
[4] Beijing Astronomical Observatory, Chinese Academy of Sciences,
Beijing 100080, China

Abstract

The soft X-ray images of four M-class flares in the active region NOAA 7270 on Sep. 6, 1992, taken with *Yohkoh* soft X-ray telescope (SXT) show that these flares consist mainly of *single bright loop*, suggesting that these flares might be classified as *simple loop flares.* Hα images taken at Hida observatory (Kitai 1993), however, show entirely different features; i.e., at least three of these four flares (1:58 UT, 5:13 UT, 6:51 UT) show vigorous filament (or spray) eruptions, suggesting these flares should be classified as *eruptive (or ejective) flares* or *two ribbon flares.* Detailed comparison between SXT images and Hα images leads us to conclude that *it is very dangerous to determine the type of flares only from SXT images*, and casts a doubt for the existence of *simple loop flares.* The comparison with *Yohkoh*/HXT data is also briefly mentioned.

1. Introduction

The active region NOAA 7270 produced many flares during Sep. 5 - 7, 1992. Among them, 4 M-class flares have been observed by *Yohkoh* and by ground based observatories in Japan. The purpose of this short note is to report on preliminary results of morphological studies of these four flares. We will describe morphological evolution of four M-class flares in SXT (soft X-ray telescope) images and compare them with Hα images taken at Hida Observatory (Kitai 1993) and *Yohkoh*/HXT (hard X-ray telescope) images (Yaji 1993). The white light images and magnetograms taken at Mitaka (Sakurai 1993) and Huairou (Zhang 1993) are also used to make clear the relation between the neutral line and flaring loops.

2. SXT Observations

2.1. *M1 flare at 1:58 UT*

This flare occurred near the southern spot of NOAA 7270. The HXT (low channel) intensity increased much during 1:57 and 1:59, showing an impulsive nature of this flare. A bright single loop appeared in SXT images at around 1:58 over a neutral line. One transient soft X-ray bright point was seen on the southern outer edge of active region between 1:55 and 2:01. The direction of the loop was initially oblique to the neutral line (at 1:58), but gradually became perpendicular to the neutral line at 2:24 (i.e., the loop evolved to non-sheared geometry).

2.2. *M1.1 flare at 2:23 UT*

This flare occurred near the west-north spot. The light curve of the HXT (L) has shown that this flare is similar to the LDE (=Long Duration Event) flare, though the time scale of the flare is not long (less than 16 min based on HXT light curve). A bright simple loop appeared in SXT images at 2:23 over a neutral line near the west-north spot. The SXT loop evolves to non-sheared geometry well after the flare at 3:30. A faint, cusp-like structure was seen above the compact bright loop at 2:23. A bright point appeared just on the southern footpoint of the single bright loop between 2:23 and 2:25

2.3. *M2.4 flare at 5:13 UT*

This flare occurred again near the west-north spot. The light curve of the HXT (L) has shown that this flare is impulsive. In SXT images, double bright points appeared at 5:14 UT, and then the loop connecting these two points brightened as a single loop at 5:16 UT (see Fig. 1). The angle between the loop and the neutral line changed with time though the direction is opposite to the previous two flares; in this case, the loop became more oblique to the neutral line (at 5:34). It is also interesting to note that a large scale loop with a faint, cusp-like structure was seen above the compact bright loop in SXT images in late stage. The size of the large scale loop increased with time, and the loop top is brightest.

2.4. *M1.3 flare at 6:51 UT*

This flare occurred near the southern spot. The HXT (L) light curve shows very impulsive nature during 6:53 and 7:02. The time evolution of morphology of this flare in SXT images is as follows; one bright point appeared at 6:58, and another bright point appeared at 7:00 (see Fig. 2). A faint elongated feature was seen to move westward at $\sim$ 70 km/s in SXT image at 7:00. At 7:03, a single bright loop connecting above two points appeared, and the length and thickness of the loop increased until 7:21.

3. Comparison with Hα Observations

As we have seen above, the SXT images showed one single bright loop (sometimes with a less-bright point nearby). There was no eruption-like feature in SXT images except for a very faint moving feature found in M1.3 flare at 6:51 UT. These are quite typical structures of the flare observed by SXT (e.g., Acton *et al.* 1992), and one might conclude that flares occurred in quasi-static *simple loops*. However, Hα images and movies (Kitai 1993) show that these flares are very different from such quasi-static *simple loop flares*:

In the case of the *M1 flare (1:58 UT)*, an Hα filament on neutral lines erupted at 1:57 UT.

A quick look at the *M1.1 flare (2:23 UT)* does not show any eruption feature in Hα image, but a close inspection of the Hα video movie has revealed that a very faint dark feature erupted from the upper part of the filament at 2:20-2:30.

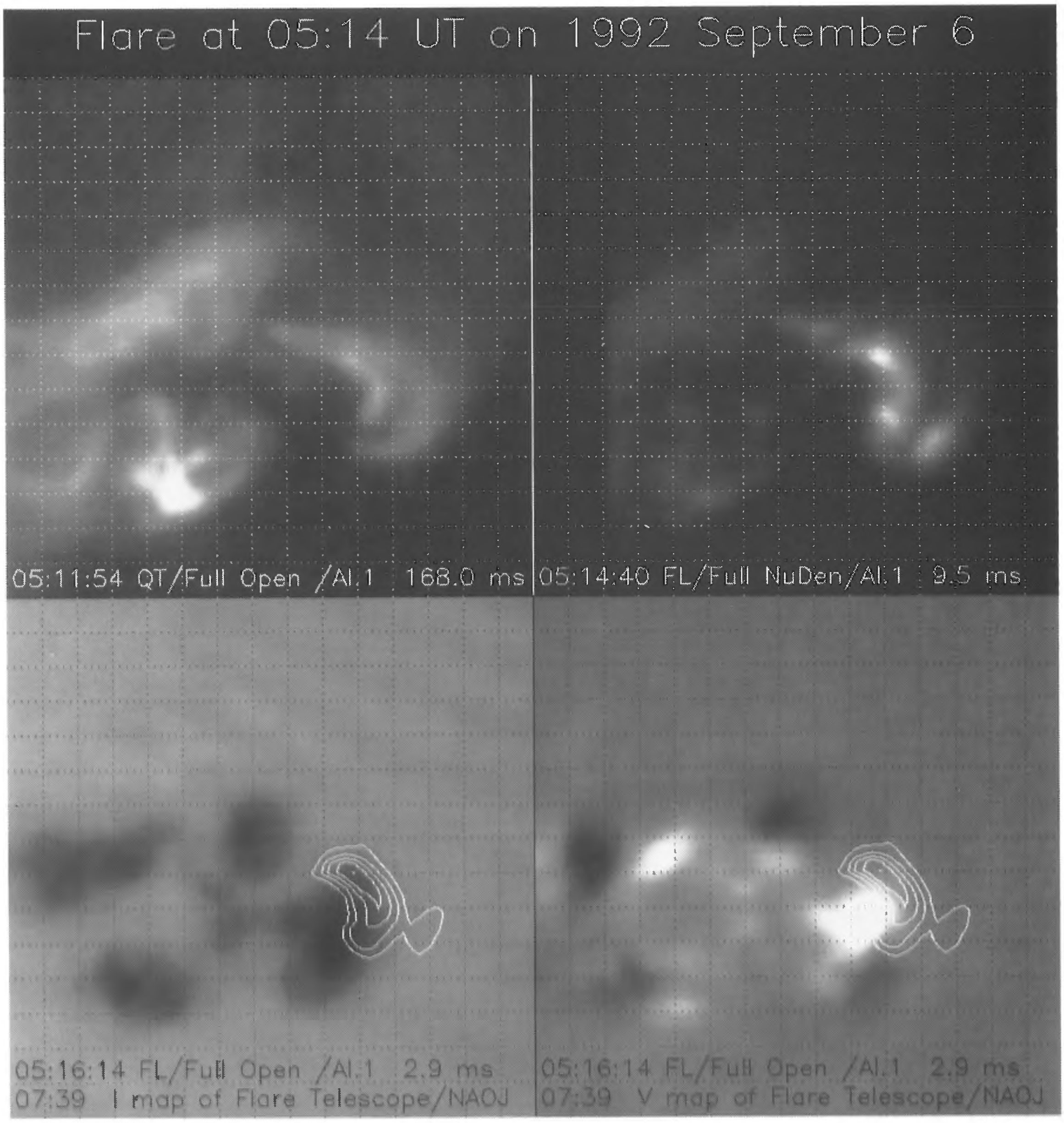

Fig. 1 SXT images of the M2.4 flare at 5:13 UT. Upper left: 5:11 UT (preflare). Upper right: 5:14 UT (impulsive phase); note that double points at the foot of the loop are bright. Lower left: single SXT loop (contour) at 5:16 UT overlaid on white light image at 7:39 UT taken with the Flare Telescope at Mitaka. Lower right: single SXT loop (contour) at 5:16 UT overlaid on magnetogram at 7:39 UT taken with the Flare Telescope at Mitaka.

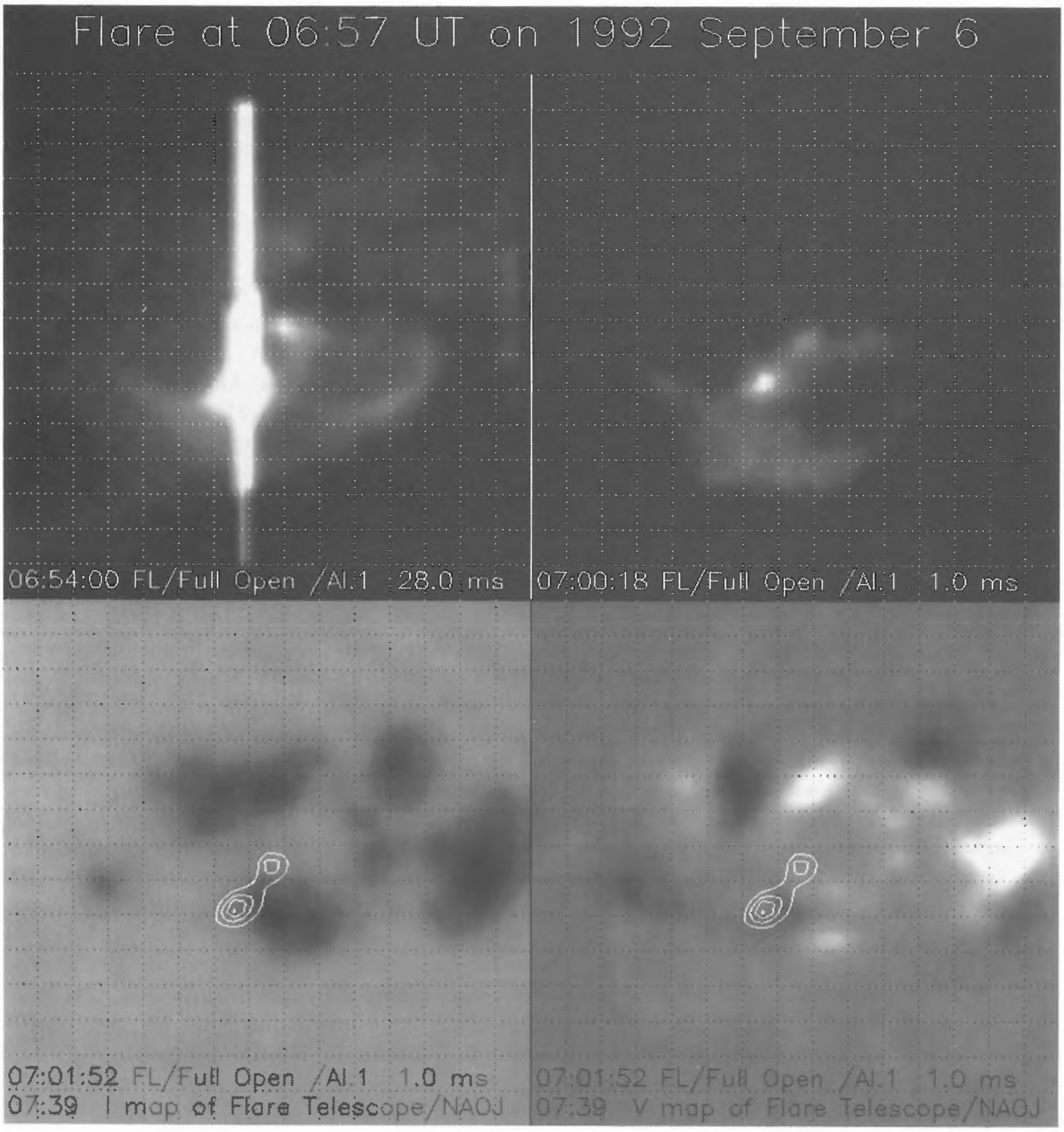

Fig. 2 SXT images of the M1.3 flare at 6:51 UT. Upper left: 6:54 UT (impulsive phase). Upper right: 7:00 UT (impulsive phase); note that double points are bright. Lower left: double points (contour) at 7:01 UT overlaid on white light image at 7:39 UT taken with the Flare Telescope at Mitaka. Lower right: double points (contour) at 7:01 UT overlaid on magnetogram at 7:39 UT taken with the Flare Telescope at Mitaka.

The *M2.4 flare (5:13 UT)* started with the eruption of an Hα filament at 5:13. The velocity of the erupting filament is estimated to be $\sim$ 200 km/s (Kitai 1993). In Hα, the flare was seen as four ribbon flare; each pair of two ribbons corresponds to each pair of footpoints of compact and larger loops seen in SXT.

The *M1.3 flare (6:51 UT)* was associated with a vigorous ejection of Hα dark feature (maybe, filament eruption or spray) at 6:53 UT.

Consequently, three of these four flares were associated with vigorous Hα mass ejection (filament eruption or spray). Even the gradual-type flare at 2:23 was associated with a very faint eruption of dark filament.

4. Summary and Conclusion

Table 1 summarizes the morphological characteristics of four M-class flares on Sep. 6, 1992, observed by SXT, HXT (Yaji 1993), and Hα (Kitai 1993). (See Hanaoka 1993, for a summary of radio observations of these flares.)

One apparent, important conclusion of this study is as follows: Although SXT images show that all these four flares consist of single bright loop (often with a less-bright point nearby), Hα images taken by Kitai (1993) clearly showed the vigorous eruption of filament or spray at least for three of four flares. These observations lead us to conclude that *it is very dangerous to determine the type of flares only from SXT images.* This result further casts a doubt for the existence of *simple loop flares.* That is, although SXT images of these four flares show such simple loop-like feature, these four flares are classified as *eruptive (and ejective) flares* or classical *two ribbon flares* if we see corresponding Hα images. Common evolutionary changes, such as apparent relaxation of sheared loop configuration, would be explained by the succesive reconnection between sheared open field lines produced by the filament eruption. Note that similar apparent relaxation of sheared loop configuration has also been found in the flares on Nov. 15, 1991 (Sakao *et al.*, 1992) and on Feb. 6, 1992 (Sakurai *et al.* 1992).

Kurokawa (1993) and Kitai (1993) pointed out that the regions where these four flares occurred correspond to the region of emerging magnetic flux. It is very likely that the filament eruption is triggered by emerging flux. Even a direct interaction between emerging flux and overlying field might play a role in generating flares, because bright loops always appeared near the emerging flux in all four flares. It is suggested that these flares might be classifed as a mixed type of CSHKP (= Carmichael-Sturrock-Hirayama-Kopp-Pneuman) model and emerging flux model (Heyvaerts *et al.* 1977, Shibata *et al.* 1992, Yokoyama and Shibata 1992).

This report is mainly based on the discussion during the small workshop on "flares on Sep. 6, 1992" which was held in April of 1993 at ISAS. We would like to thank all participants of the workshop, especially to Drs. T. Kato and Y. Hanaoka, for fruitful discussion.

References

Acton, L. *et al.* 1992, *Publ. Astron. Soc. Japan*, **44**, L71.
Hanaoka, Y. 1993, in these proceedings.
Heyvaerts, J., Priest, E. R., and Rust, D. M. 1977, *Ap. J.*, **216**, 123.
Kitai, R. 1993, in these proceedings.
Kurokawa, H. 1993, in these proceedings.
Sakao, T. *et al.* 1992, *Publ. Astron. Soc. Japan*, **44**, L83.
Sakurai, T. *et al.* 1992, *Publ. Astron. Soc. Japan*, **44**, L123.
Sakurai, T. 1993, in these proceedings.
Shibata, K., Nozawa, S., and Matsumoto, R. 1992, *Publ. Astron. Soc. Japan*, **44**, 265.

Yaji, K. 1993, in these proceedings.

Yokoyama, T. and Shibata, K. 1993, *in Proc. of the Fourth International Conference on Plasma Physics and Controlled Nuclear Fusion, held in Toki, Japan, 17-20 November 1992 (ESA SP-351)*, pp. 203–206.

Zhang, H. 1993, in these proceedings.

Table I Summary of Observations

time (UT)	GOES	SXT image	HXT image	Hα	SXT-faint	HXT light-curve
1:58	M1	single loop (+ another point)	double points (+ another point)	filament eruption	–	impulsive
2:23	M1.1	single loop	loop	very faint filament eruption	cusp-like structure ?	gradual soft
5:13	M2.4	double points ↓ single loop	double points	filament eruption	cusp-like structure	impulsive
6:51	M1.3	double points ↓ single loop	point-like ↓ loop	Hα ejecta (spray ?)	–	impulsive

Flares in the Region NOAA7270 Observed with the Nobeyama Radioheliograph

Yoichiro HANAOKA
Nobeyama Radio Observatory, National Astronomical Observatory,
Minamimaki, Minamisaku, Nagano 384-13, Japan

Abstract

The Nobeyama Radioheliograph observed the flare-productive active region NOAA7270 appeared in September 1992 and caught many flares. The advantages of the Radioheliograph observations enables us to study some interesting features. Some of them, successive flarings and the radio and hard X-ray spectra are briefly reviewed here.

1. Introduction

The active region NOAA7270 appeared in September 1992 is one of the most flare-productive active region for the Nobeyama Radioheliograph, which started the regular observation in June 1992. The radio flares in this region are generally rather gradual, besides the radio flares in the region NOAA7260 and 7321, which were discussed in the meeting are generally impulsive. Since the characteristics of the radio flares strongly depend on magnetic field configurations, the difference in the flare characteristics suggests the difference in the magnetic field configurations related to the flare occurrence.

On September 5-6, several magnetic bipoles rapidly emerged at once and the magnetic features in the region became very complicated one. Magnetograms obtained with the Flare Telescope at Mitaka on these days are shown in Figure 1. Many flares occurred due to the rapid development of the region. The Nobeyama Radioheliograph observed nine M-class flares and numerous C-class flares in the region NOAA7270 in September 5-9.

Since the general features of this region in soft X-rays, hard X-rays, and Hα are described in other papers appeared in these proceedings, we present interesting features in the radio images of the flares in this paper to encourage future collaborations. In Section 2, successive flarings are described. In Section 3, relations between time profiles of flares in radio frequencies and those in hard X-rays are described.

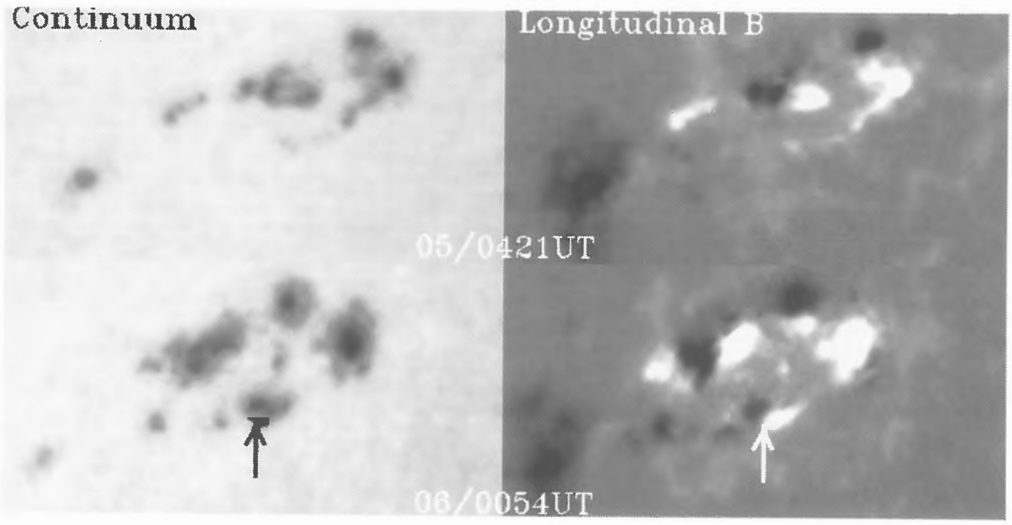

Fig. 1 Continuum images and magnetograms of longitudinal fields of NOAA7270 on September 5 and 6 obtained with the Flare Telescope at Mitaka. White stands for positive polarities, and black stands for negative polarities in the magnetograms.

2. Successive Flarings

On September 6, the flare activity was especially high. Sometimes several flares, which were related to each other, occurred successively in short times. In Figures 2 and 3, two examples of the successive flarings are shown.

In the flares during 00-01^{h}UT shown in Figure 2, the sources 1, 2, and 3 were brightened successively. The source 3 consists of two bright points; they are double footpoints of a flare loop.

In the flares during 02-03^{h}UT in Figure 3, the source 1 was impulsively brightened and reached the maximum first. Before the brightening of the source 1, the source 2 started the gradual brightening and it reached a maximum at 0208UT. After the source 2 reached the maximum, the sources 3 and 4 were brightened gradually. The source 3 reached the maximum at 0226UT. The source 4 shows two footpoints first, and then the loop which connect the footpoints was appeared and it decayed gradually.

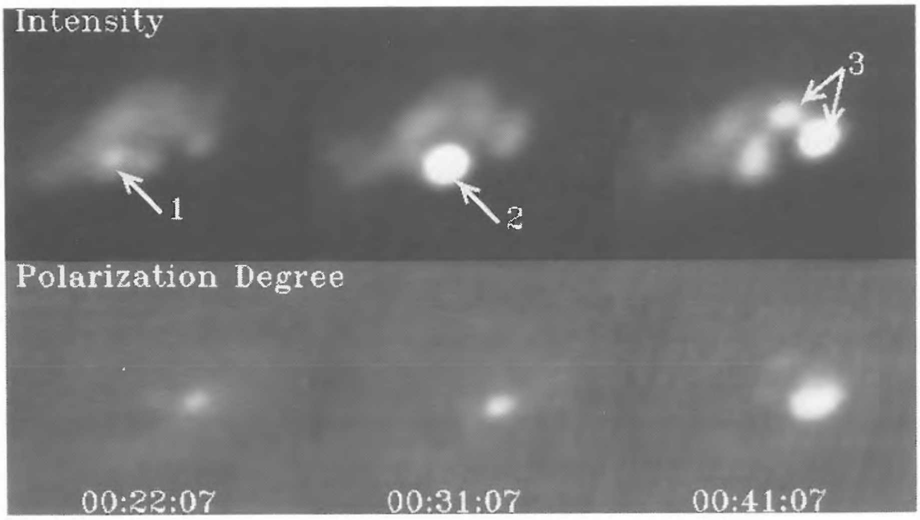

Fig. 2 Successive flarings during 00-01^{h}UT on 1992 September 6 observed with the Nobeyama Radioheliograph.

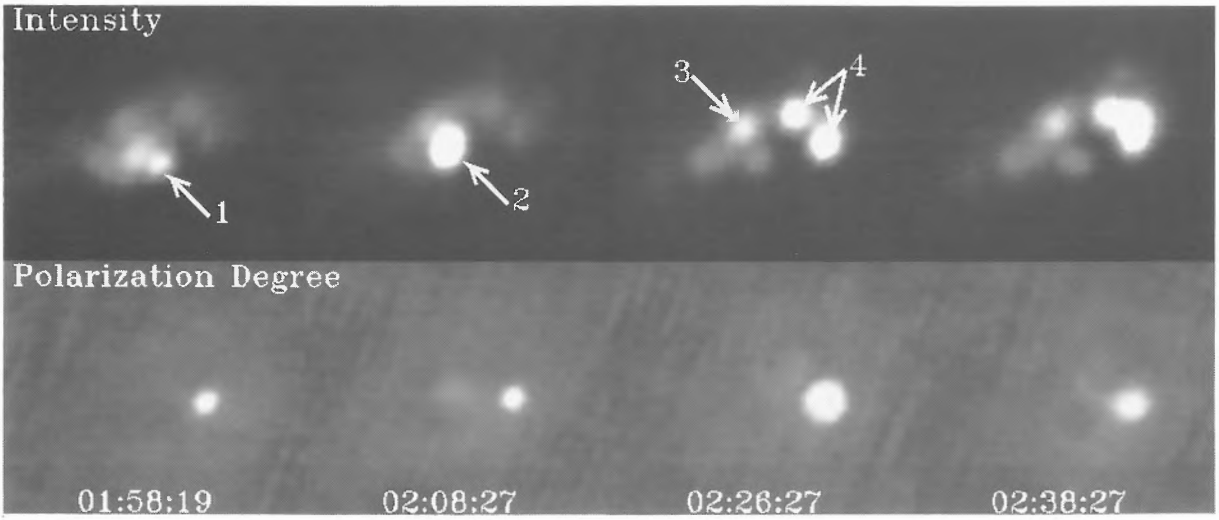

Fig. 3 Successive flarings during 02-03^{h}UT.

The positions of the sources of these successive flarings are shown is Figure 4. In both flares the first brightened points are around the same region. Consulting the magnetograms in Figure 1, we can find that the newest emerging flux, which is directed by arrows in Figure 1, corresponds the first brightened points.

This active region consists of several magnetic bipoles and it shows very complicated structure. Magnetic free energy should be stored in various places. In particular the magnetic fields at the newest bipole are probably most stressed. Therefore the first manifestation of the flares tends to occur at the newest bipole, and due to the abrupt magnetic field change by the first flare, the other flares occurred successively. This is the scenario of the successive flarings.

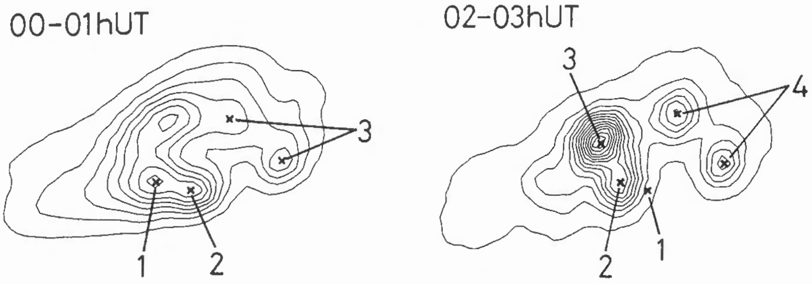

Fig. 4 Flare sites of the successive flarings on the contours of the radio maps.

Radio images generally show footpoint brightenings at the early phase of flares. In particular the Radioheliograph can catch smaller flares because of its high sensitivity. Therefore the observations of such successive flarings with the Radioheliograph show how the flare triggerings propagate from a bipole to another bipole.

3. Relation between hard X-rays and 17GHz

In general hard X-ray time profiles of flares are similar to those at 17 GHz. For example, time profiles of an M2.4 flare at 0519UT (GOES) on September 6 at 17GHz and in hard X-rays observed with the *Yohkoh* HXT shown in Figure 5 are very similar to each other. Even small fluctuations are seen in both time profiles. Therefore such fluctuations shows actual fluctuations in electron accelerations.

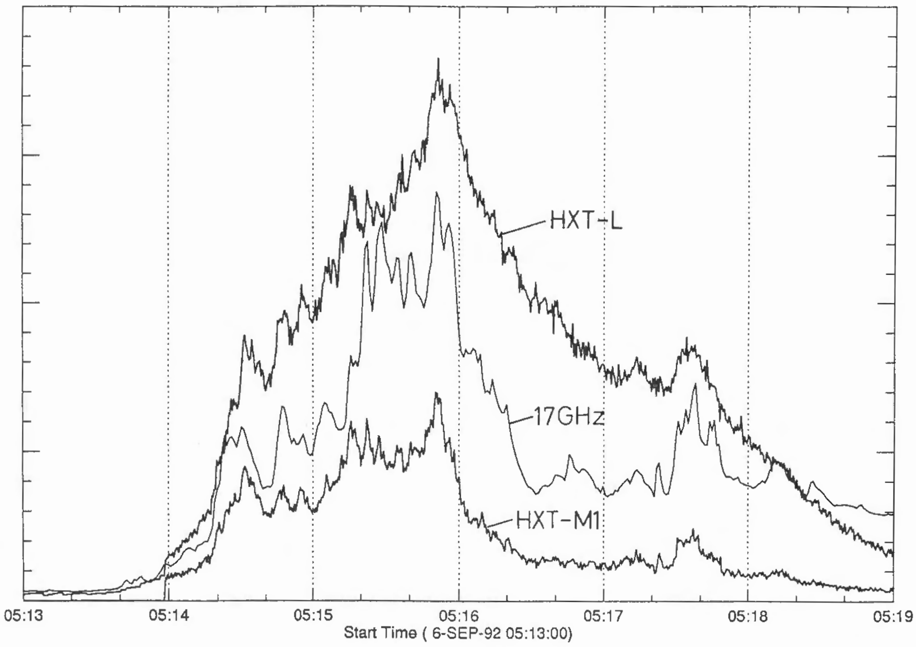

Fig. 5 The time profiles in the M1-channel of the HXT and at 17GHz(correlation) of the flare at 0519UT (GOES) on September 6, 1992. The correlation at 17GHz is averages of Fourier components in higher spatial-frequency region. It is a good index of flare activities. The scale in ordinate is arbitrary.

However, the flares during 02-03^{h}UT shown in Figure 3 are not the case. Time profiles of this period in various frequencies are shown in Figure 6. The brightening of the source 1 in Figure 3 at 0158UT, which was not so intense at 17 GHz, was the strongest one among the brightenings during 02-03^{h}UT in hard X-rays. However, the peak at 0158UT is clearly seen at lower frequencies. Other brightenings during 02-03^{h}UT, which were strong at 17GHz, show only weak hard X-ray radiation. The facts that the turn-over frequency of the 0158UT peak is low and that no polarization was observed at this peak suggest low magnetic-field strength at the source. The peak at 0208UT and the gradual brightening from 0220UT have higher turn-over frequencies than the 0158UT peak. Such differences in the relation between radio and hard X-rays imply the differences in the magnetic fields of the sites of flares. Therefore we can obtain information on magnetic field of the flare sites from the radio observations.

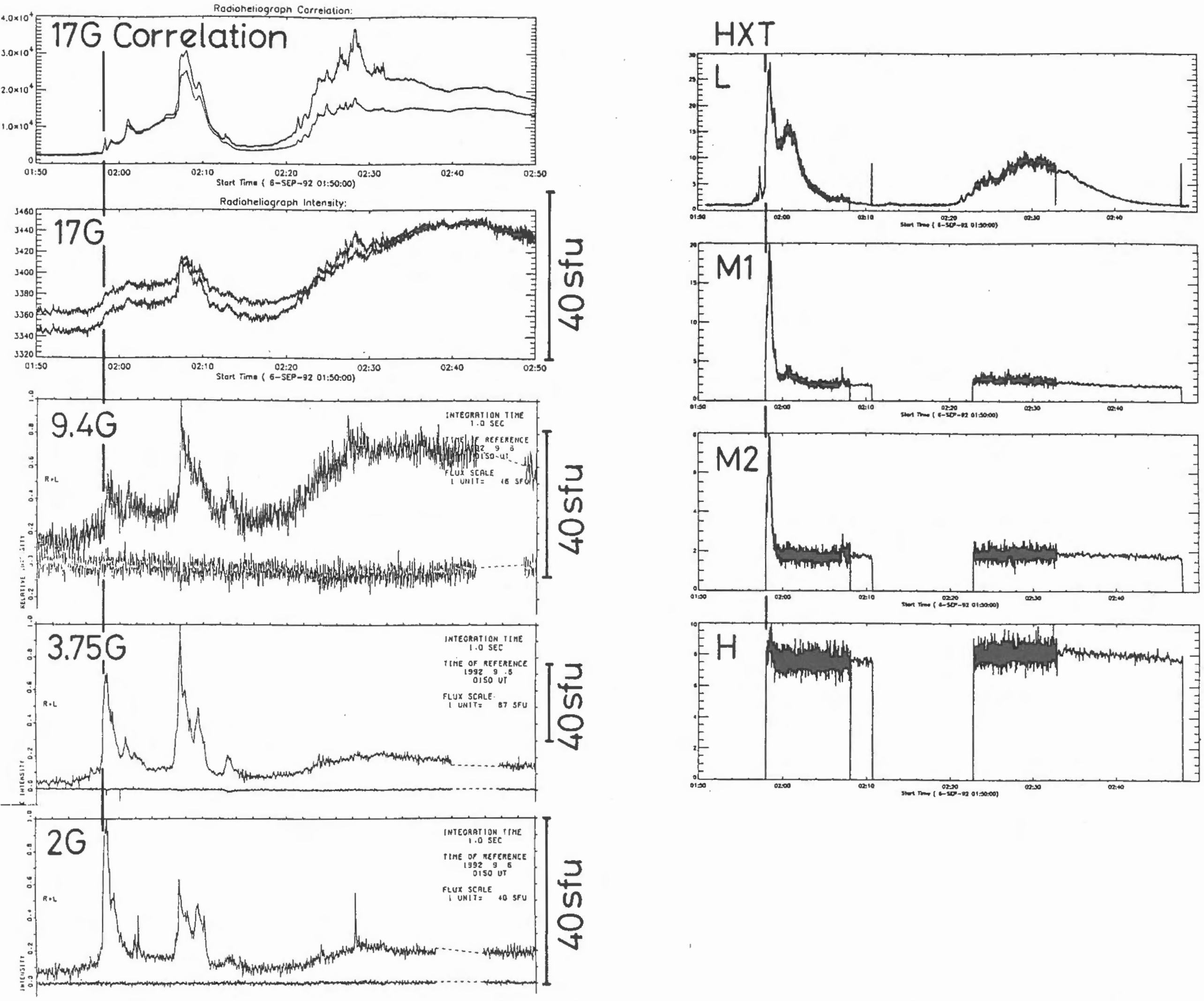

Fig. 6 Time profiles at 17 GHz (the Nobeyama Radioheliograph), 9.4 GHz, 3.75 GHz, and 2 GHz (Toyokawa data) in radio frequencies and those in the L, M1, M2, and H channels of the HXT during 0150UT-0250UT. The vertical lines show 01:58:00UT.

The Mitaka Flare Telescope Group kindly provided the author with the magnetograms. We are very grateful to the members of the Nobeyama Radioheliograph Group. The author are also very grateful to Prof. Ogawara of the ISAS and all of the Yohkoh Team members for operating the spacecraft.

Meterwave Solar Radio Emission from NOAA7260

Shinichi WATARI
Communications Research Laboratory, 4-2-1 Nukuikita, Koganei,
Tokyo 184

Takeshi ISOBE
Hiraiso Solar Terrestrial Research Center, 3601 Isozaki, Nakaminato,
Ibaraki 311-12
and
Yohkoh SXT Team

Abstract

Meterwave bursts are emitted associated with disturbances in the solar corona. *Yohkoh* observes almost the same height range of the solar corona, by the Soft X-ray Telescope (SXT) with high resolution, as meterwave radio does. Several strong meterwave bursts have been observed in Hiraiso (N36.27E140.63) simultaneously with *Yohkoh*. An intense solar radio burst on 1992 August 20 and a soft X-ray arcade, associated with this event, above NOAA7260 were analyzed and it is found that activated large loops have an important role for strong and long-lasting meterwave radiation.

1. Introduction

Solar radio emission has been observed by a digital swept-frequency radiospectrograph and fixed frequency radiometers at Hiraiso Solar Terrestrial Research Center (N36.37 E140.63), Communications Research Laboratory. Meterwave bursts are emitted associated with coronal disturbances. The SXT on board *Yohkoh* can detect solar coronal phenomena with high resolution. We examined solar images taken by the SXT and found several enhancements in them associated with strong meterwave radio bursts. Here we report strong meterwave radiation observed on 1992 August 20 and a large soft X-ray arcade, associated with it, above NOAA7260.

2. Observations

A strong meterwave burst of continuum radiation occurred at around 0300UT on 1992 August 20. This burst continued for several hours and exhibited strong right-hand polarization. Solar radio flux and polarization at 100, 200, and 9500 MHz in Hiraiso are shown in Figure 1. Radio bursts

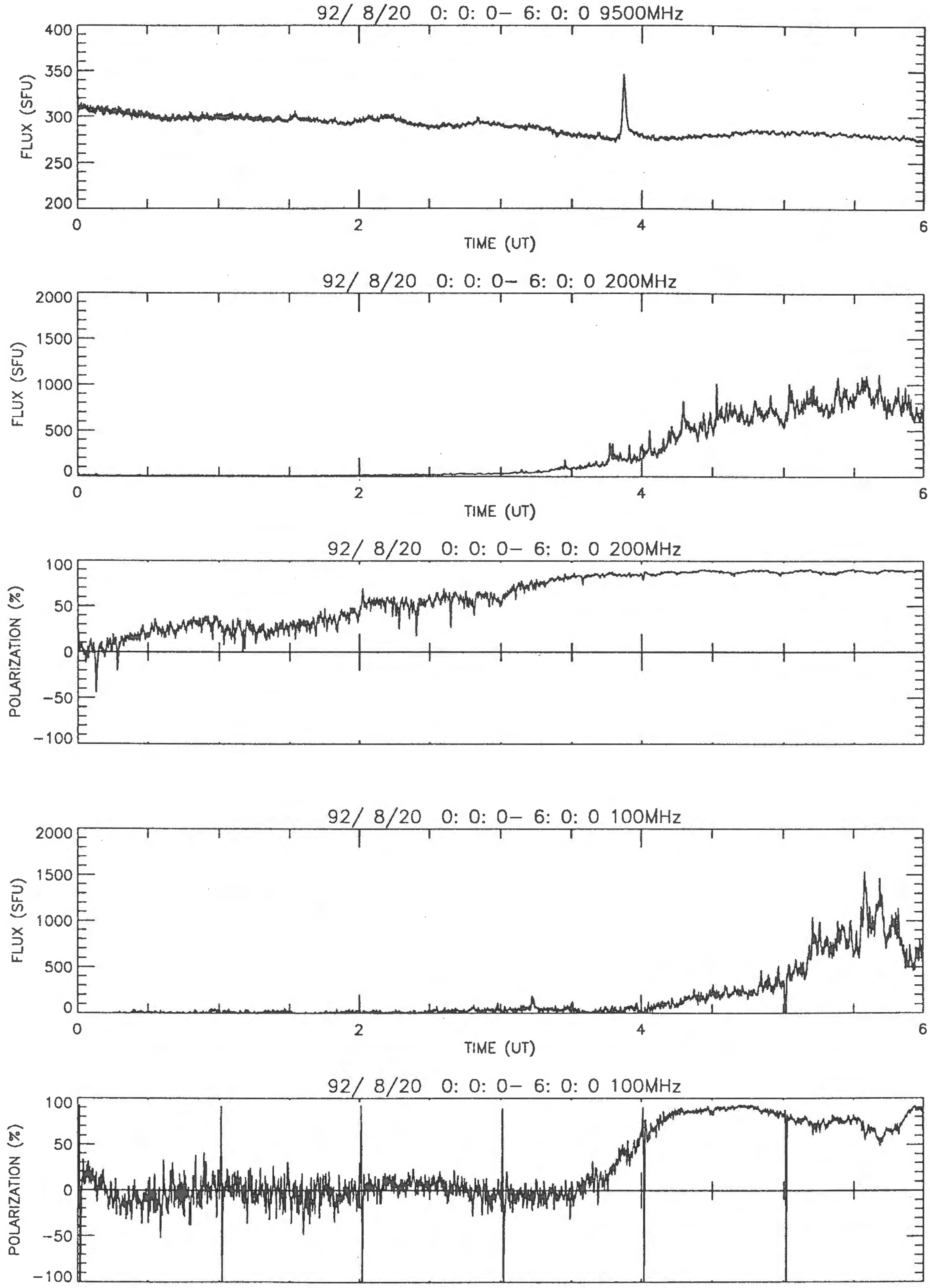

Fig. 1. Time plots of solar radio flux and polarization at 100, 200, and 9500 MHz observed in Hiraiso Solar Terrestrial Research Center.

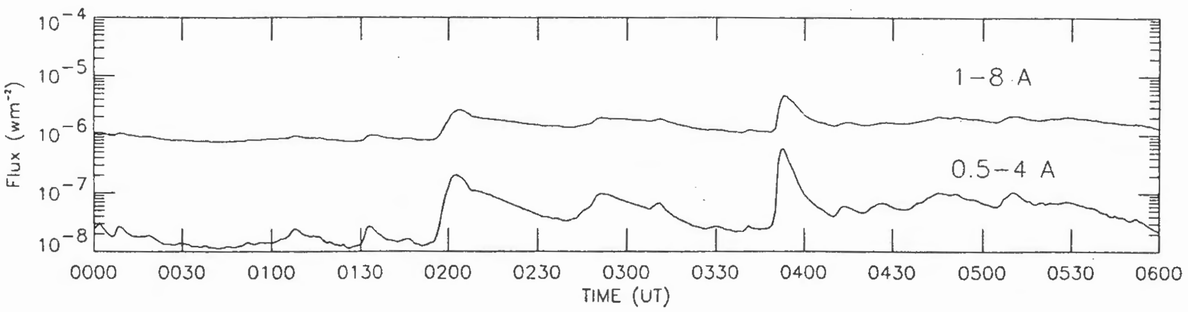

Fig. 2. Time plots of *GOES* X-ray flux on 1992 August 20.

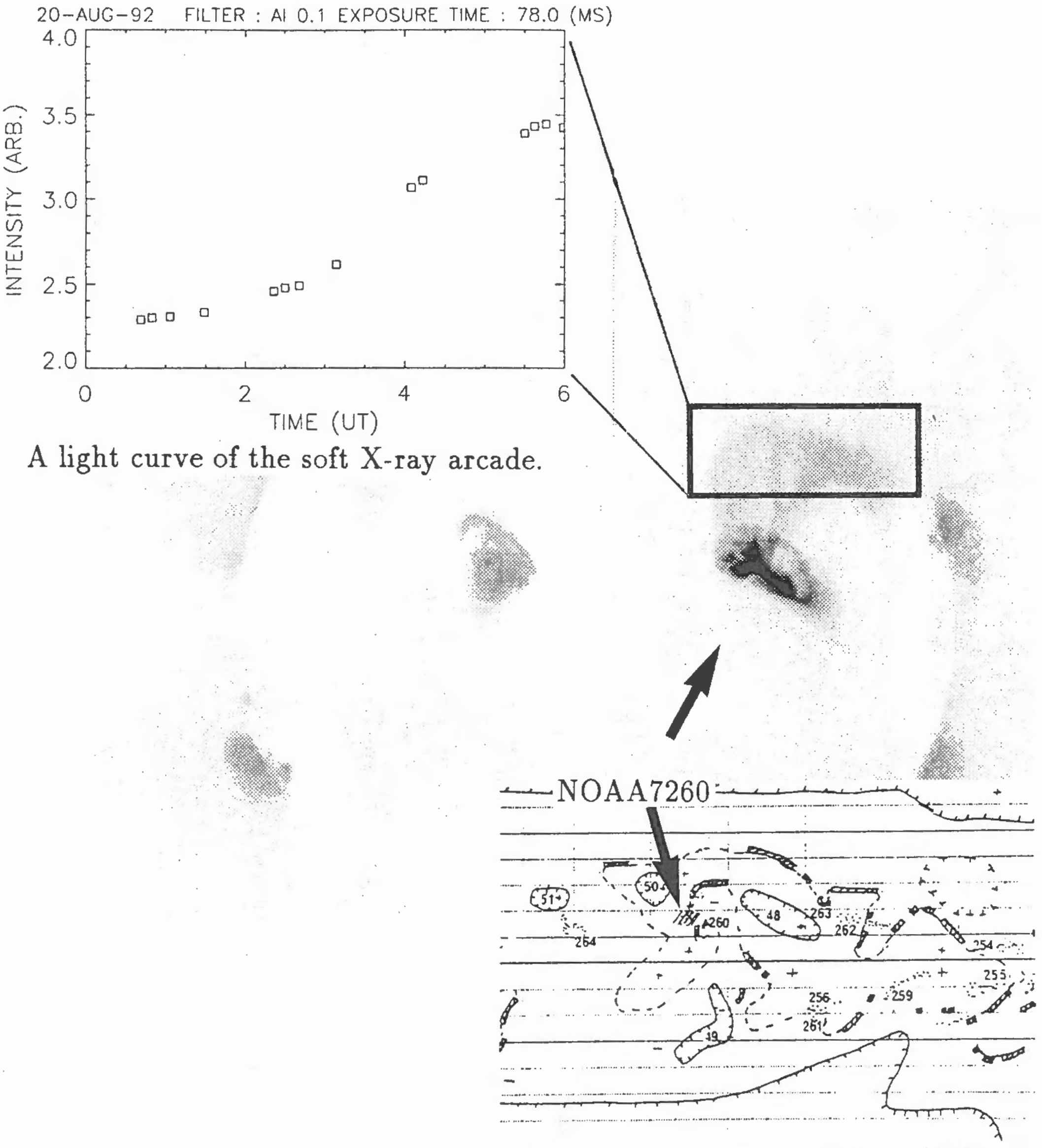

A light curve of the soft X-ray arcade.

Hα synoptic chart by NOAA/SESC.

Fig. 3. Soft X-ray arcade above NOAA7260 associated with the strong metric burst, a light curve of the soft X-ray arcade, and Hα synoptic chart by NOAA/SESC.

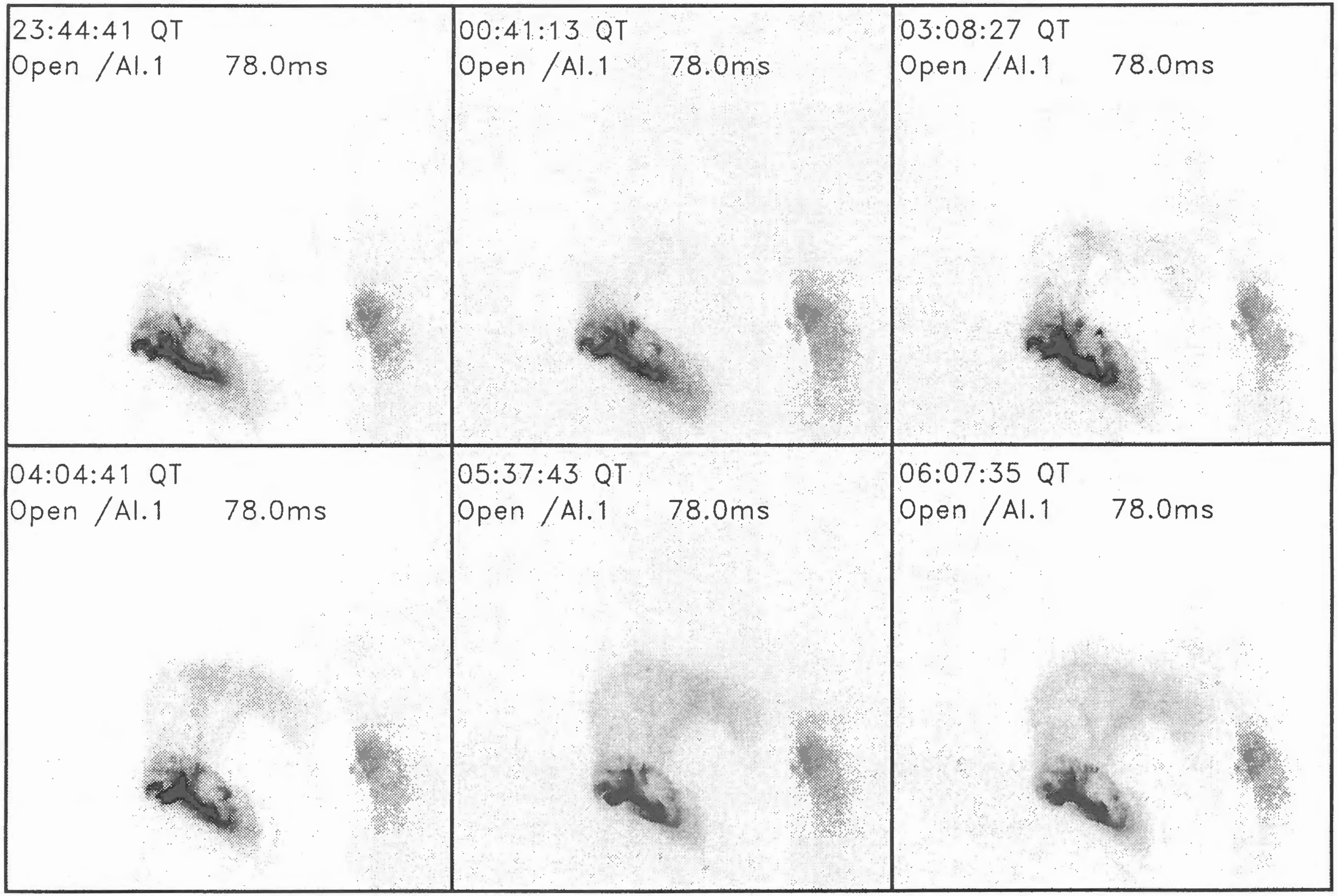

Fig. 4. Time evolution of soft X-ray arcade associated with the strong metric radio burst on 1992 August 20.

at 200 MHz and 100 MHz commenced at around 0300UT and 0330UT respectively. A weak microwave burst at 9500 MHz was observed at about 0450UT during meterwave continuum radiation. No remarkable impulsive burst was observed in both meter- and micro-wave range at the beginning of this event shown in Figure 1. Several C-class flares were observed by the American meteorological satellite, *GOES* (Figure 2). However, they weren't coincident with the beginning of this meterwave continuum radiation.

The soft X-ray bright arcade with large extension in the north side of the active region, NOAA7260(N16W28), was observed by the SXT on *Yohkoh* at the same time as this meterwave burst and continued for several hours shown in Figure 3. This arcade crossed over an inversion line and expanded along this, according to Hα synoptic chart (Figure 3) by NOAA/SESC. A light curve of the soft X-ray arcade above NOAA7260 (Figure 3) is similar to the time plot of the radio flux at 200 MHz shown in Figure 1. The similarity of these two time-profiles implies a close physical connection between the two phenomena. And height of the arcade is correspond with height responsible for plasma emission at around 200 MHz, according to Newkirk model. This suggests that meterwave emission occurred in the large arcade apart from the active region.

Time evolution of the arcade, formed above NOAA7260, is shown in Figure 4. At the beginning of this event, several large loops in the north side of NOAA7260 became brighter. They connected between small loops in NOAA7260 and area above it. There was a small filament along the top of the large loops. And then bright parts expanded both sides along the inversion line.

3. Discussion

As described above, frequent interactions between small and large loops may activate large loops along the inversion line and generate a intense metric continuum radiation, through continuous electron-acceleration, without remarkable impulsive bursts.

There are many loop-interactions in active regions according to *Yohkoh* observation. However, the observed number of intense metric events is not so many comparing with the number of observed loop-interactions. This implies that a large arcade may have an important role for intense and intense metric continuum radiation.

Gergely et al. (1979) pointed out that a long-lasting meterwave continuum emission on 1973 August 21 is associated with large white-light loops in the High Altitude Observatory's coronagraph. Lantos et al. (1981) analyzed the relationship between a soft X-ray long duration event and an intense metric noise storm and concluded that electrons of about 10 keV generate the radio emission inside a large expanding loop transient apart from an active region. Our observational result is in agreement with Gergely (1979) and Lantos (1981) and emphasizes that large loops activated by small loops in an active region have an important role for intense metric continuum emission.

4. Concluding Remarks

We may summarize the intense metric continuum event as follows :

(a) An intense metric continuum emission commenced at about 0300 UT without remarkable impulsive bursts (type II and type III bursts). This may suggest that impulsive bursts aren't necessary for this kind of continuum radiation. No flare was coincident with the beginning of this metric burst.

(b) The similarity of light curves of the soft X-ray arcade above NOAA7260 and 200 MHz radio flux implies that these events were physically linked.

(c) Small loops in an active region (NOAA7260) frequently interacted with a filament, which lay along an inversion line, through several large loops. As a result, a large bright arcade was developed. This activity seems to have generated the strong metric radiation. Large soft X-ray arcade or loops may have an important role for the strong metric continuum radiation.

References

Gergely, T.E., Kundu, M.R., Munro, R.H., and Poland, A.I., 1979, Astrophys.J., **230**, 575.

Lantos, P., Kerdraon, A., Rapley, G.G., and Bentley, R.D., 1981, Astron.Astrophys., **101**, 33.

BCS Spectra from Flares on 6th September 1992

T. Kato and T. Fujiwara* , BCS Group

National Institute for Fusion Science, Nagoya, 464-01,Japan
*Dep. of Education, Aichi University of Education, Kariya, 448, Japan

Abstract

We have studied time evolution of BCS spectra of He like S XV, Ca XIX and Fe XXV ions observed by the Yohkoh satellite for two flares on 6th September 1992 at 05:05 (M2.4 class) and 08:59(M3.3 class). Electron temperatures for S XV, Ca XIX and Fe XXV ions are derived through synthetic spectra mainly from the intensity ratios of the satellite lines to the resonance line. Apparent ion temperatures are derived from the line width of S XV and Ca XIX spectra. The blue shifted components in the rising phase are separated from the main component in Ca XIX spectra. The emission measures and other parameters derived from the spectra are compared with HXT and radio data. The ion ratios derived from the ratios of line intensities are studied relating to the ionization equilibrium.

1. Plasma parameters from BCS spectra

We can obtain the following plasma parameters from BCS spectra ;
i) electron temperature from the intensity ratios of the satellite lines to the resonance line, ii) ion temperature from the line broadening, iii) volume emission measure from the absolute line intensity, iv) ion ratios from the intensity ratios among the lines produced by the inner-shell excitation. These values for each ion are derived as a function of time.

2. Time evolution of the BCS spectra

The light curves of the integrated intensities are shown in Fig.1. The intensity of the Fe XXV increases very rapidly comparing to that of S XV. The maximum temperature from Fe XXV ions is about 2 keV(2.3×10^7K) at 1 - 2 min. before the period when the counting rates are maximum. The Time dependence of the electron temperature derived from BCS spectra of S XV, Ca XIX and Fe XXV (He-like ions) are shown in Fig.2. The error for the electron temperatures is estimated to be within 20% in the later phases.

Time dependent spectra are classified into four phases as follows,

1) Initial phase (05:10 - 05:13)... Counting rates are very low, almost constant and increases gradually with time. The Ca XIX spectra show the electron temperature around 1 keV and larger line broadening than that in the later phases indicating a turbulence. Apparent ion temperatures of the main component are about 2 - 3 keV for Ca XIX and S XV. This indicates that the turbulence begins before the increase of the X-ray flux.

2) Rising phase (05:13 - 05:16)... Counting rate begins to increase very rapidly. The electron temperatures increase following the increase of the counting rate. Line widths become broader than those in the initial phase and the blue shifted component appears obviously at the beginning of the rising phase. The apparent ion temperature of the blue shifted component is about 10 keV and the relative velocity to the main component is

about 200 km/s. The apparent ion temperature including main component and blue shifted component reaches the maximum value at the beginning of the rising phase (05:14) and decreases towards the maximum phase. The blue shifted component is shown in Fig.3.(2).

3) Maximum phase (05:16 - 05:18) ... Counting rates and the electron temperatures for Ca XIX and S XV reach the maximum. The maximum electron temperature from Fe XXV is about 2 keV just before the maximum phase. Line widths of the main component become narrow indicating no turbulence. The blue shifted component is still seen but the ratio to the main component is small (about 20%). The ion temperature from Ca XIX goes down and reaches the values lower than the electron temperatures to be around 1.5 keV.

4) Decay phase (05:18 - 05:25)... The electron temperature decreases from 2 keV to 1 keV as well as the counting rates. The ion temperature becomes a little larger that in the maximum phase to be around 1.5 - 2 keV.

3. The blue shifted component in the rising phase

Ca XIX spectra in the initial and rising phase show broad line width which indicate more than two blue shifted components1) as shown in Fig.3. We tentatively tried to fit the spectra with two components; the main component and the blue shifted component as shown in Fig.3(b). The wavelength of the main component is fixed from those in the initial phase and the decay phase. During the rising phase the apparent ion temperature of the main component is about 4 keV whereas that of the blue shifted component is around 10 keV which indicate the turbulence of 140 km/s and 220 km/s respectively. The relative velocity of the two components is derived to be 180 km/s from the wavelength shift of $1.9\text{x}10^{-3}$A in Ca spectra. This component goes down to 100 km/s towards the maximum phase. It seems that the intensity of the blue shifted component reaches the maximum before the maximum phase and only the main component increases afterwards. The ratio of the blue shifted component to the main component is about 20 - 30 % at the beginning and increases up to 100%. But this ratio decreases from the end of the rising phase.

It is interesting to compare HXT data and radio data in the rising phase. In the initial phase when Ca XIX line begin to be observed, HXT(13.9 - 22.7 keV)2) is not detected whereas SXT and radio emission (17GHz) are detected. In the rising phase when the blue shifted component reaches 100% of the main component, HXT begins to increase and HXT reaches the maximum value when the blue shifted component stops to increases. HXT begins to decay earlier than BCS flux. Time behavior of radio heliograph peak brightness temperature and the polarization degree at 17 GHz obtained in Nobeyama Observatory3) is similar to HXT flux after the rising phase. The polarization degree from radio is about 50 % in the initial phase, decreases down very rapidly to 20 % until the maximum phase and then increases again slowly up to 30 % in the decay phase. The time behaiviour of the polarization degree is very similar to that of the apparent ion temperature obtained from Ca XIX. It indicates that the turbulence from BCS data and the acceleration of electron from radio data are correlated to the strength of the magnetic field.

4. Volume emission measure

The volume emission measures n_e^2V are derived from the intensity of the resonance line of He-like ions. The observed line intensity is written as

$$I_w = \varepsilon_v(n(He)/n(Z))(n(Z)/n_H)(n_H/n_e)n_e^2V/(4\pi r^2)$$

$$\text{photons cm}^{-2}\ \text{s}^{-1}\ \text{sr}^{-1},$$

where ε_v is the emissivity of the line in $cm^3\ s^{-1}$, V is the volume in cm^3, r is the distance from the earth to the Sun in cm, n(He), n(Z), n_H and n_e are the density of the He-like ions, element Z, atomic hydrogen and electron respectively. We have used electron temperature derived from BCS spectra to obtain the emissivity ε_v. The value of He-like ion abundance, n(He)/n(Z), is assumed in ionization equilibrium. The solar abundance are assumed as $n(S)/n(H) = 2 \times 10^{-5}$, $n(Ca)/n(H) = 5 \times 10^{-6}$ 4), $n(Fe)/n(H) = 5 \times 10^{-5}$. The emission measure from S and Fe ions is about $1 - 2 \times 10^{49}\ cm^{-3}$ at maximum for both two flares. The emission measure derived from Fe XXV is always smaller by about factor of two than those from Ca and S ions.

Total energy assuming solar abundance is estimated to be $2 \times 10^{26}\ erg\ s^{-1}$ at maximum phase with the value of cooling rate $2 \times 10^{-23}\ erg\ s^{-1}\ cm^3$. The electron density is obtained to be $7 \times 10^{10} cm^{-3}$ at maximum phase using the value for $V = 2 \times 10^{27}\ cm^3$ from a SXT 5) image.

5. Ion abundance

The ion abundance ratios n(Li)/n(He) derived from Fe XXV spectra are always larger than those in the ionization equilibrium, where n(Li) is the ion densities of Li-like ions. We had the same results for the flare on January 21st 1992 6). This result indicates that the ionization balance is not in ionization equilibrium in solar flares although this problem has to be discussed more carefully with the atomic data. The emission measure from Fe spectra assuming the derived ion abundance in non equilibrium ionization is increases by about 80%.

References

1) G. A. Doschek, J.T. Mariska, T. Watanabe et al., PASJ, **44**, L95 (1992)
2) The Yohkoh HXT Databook (I), NAO, Mitaka (1993)
3) Y. Hanaoka and Nakajima, private communication(1993)
4) A.C. Sterling, G.A. Doschek and U. Feldman, Ap. J., **404**, 394 (1993)
5) K. Shibata, private communication (1993)
6) T. Kato, K. Masai, K. Sakimoto, Y. Itikawa, T. Watanabe, BCS group, Proceedings of the Fourth International Conference on Plasma Physics and Controlled Nuclear Fusion, esa sp-351,199 (1993)

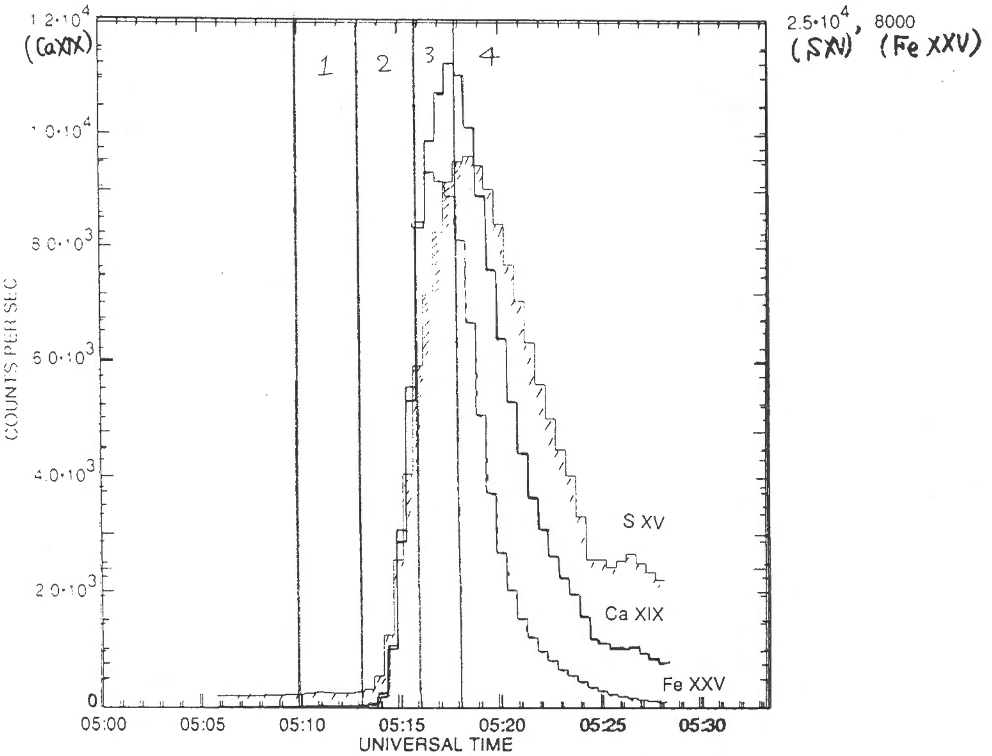

Fig.1. The light curves of the integrated intensities of S XV, Ca XIX and Fe XXV.

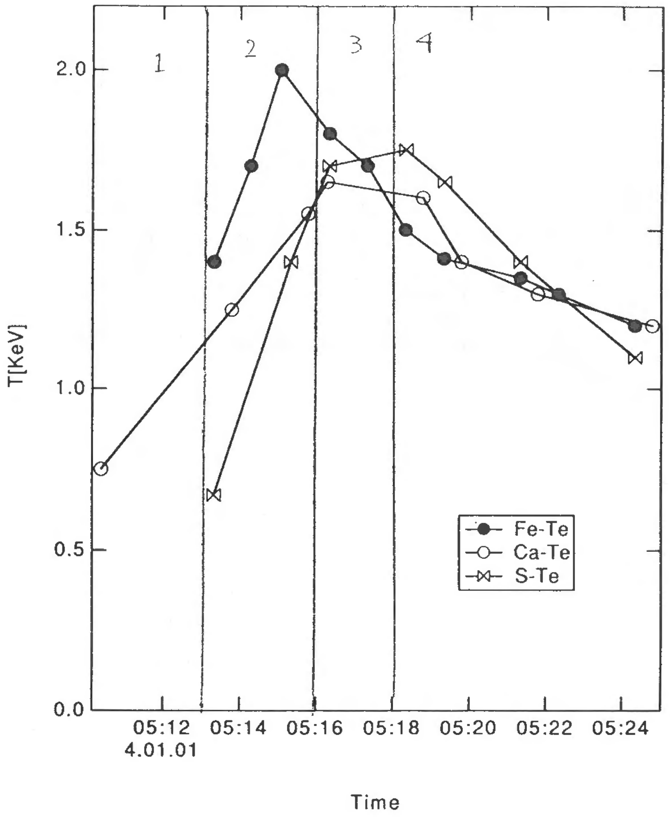

Fig.2 The Time evolution of the electron temperature derived from BCS spectra of S XV, Ca XIX and Fe XXV (He-like ions).

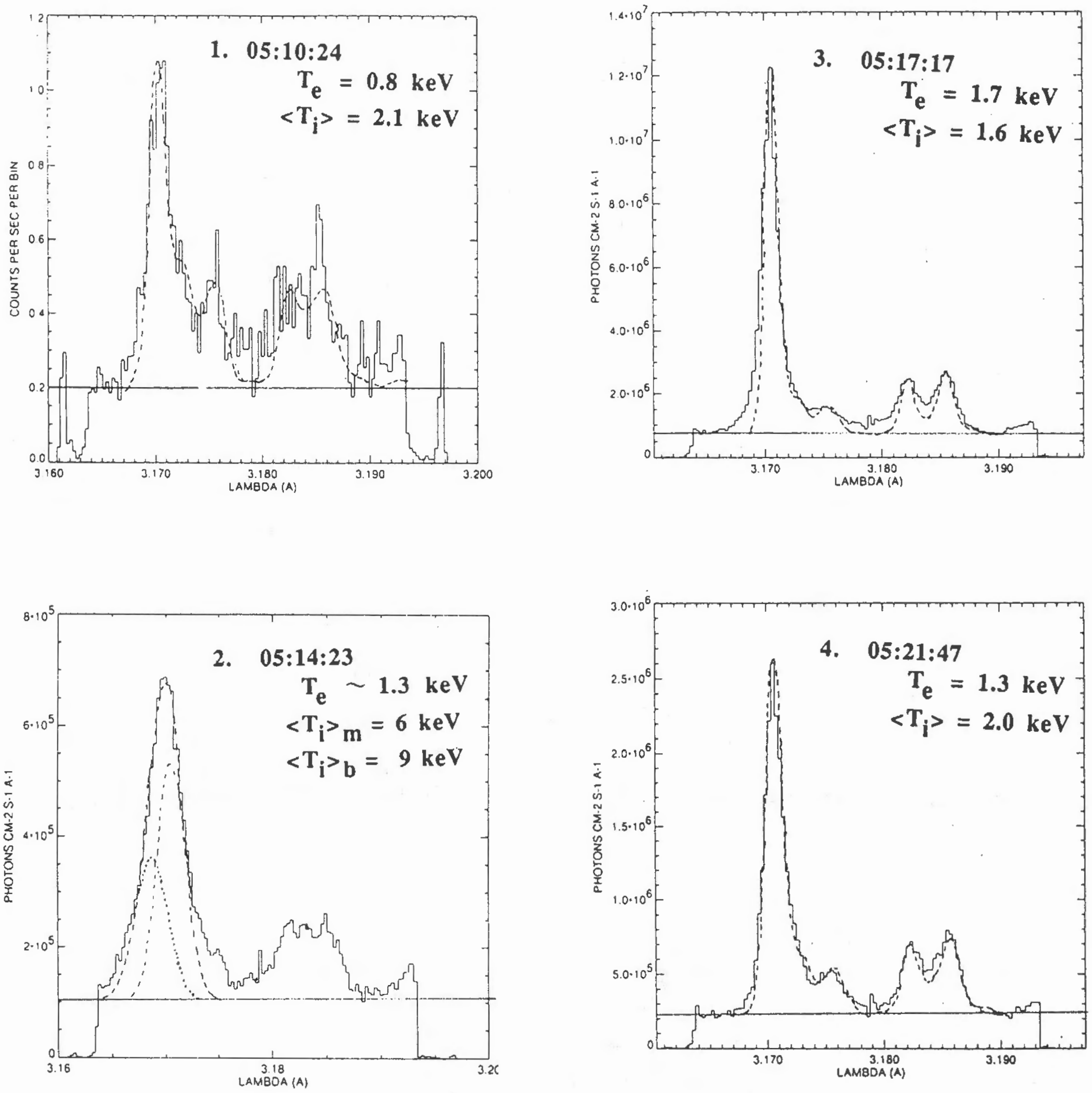

Fig.3 The Ca XIX spectra in four phases. $<T_i>$ indicates the apparant ion temperature. 1)Initial phase. 2)Rising phase. The main ($<T_i>_m$) and the blue shifted ($<T_i>_b$) components are fitted saparately. 3) Maximum phase. 4) Decay phase.

Epilogue: A Poem by Jingxiu Wang

客居鈴蘭小屋，書贈日本友人

山川藏秀色，礼仪悦賓朋。
酒暖客貪杯，饈珍主多情。
鈴蘭自幽香，小屋生雅風。
月流泉聲里，曉至鳥鳴中。

景琇　一九九三年七月九日晨，
于乘鞍高原鈴蘭小屋白樺居。

List of Participants

AI, Guoxiang
Beijing Astronomical Observatory

DENG, Yuanyong
Beijing Astronomical Observatory

ENOME, Shinzo
Nobeyama Radio Observatory
National Astronomical Observatory

FUJIWARA, Tomoko
Department of Earth Sciences
Aichi University of Education

GAO, Jing
Academia Sinica

HANAOKA, Yoichiro
Nobeyama Radio Observatory
National Astronomical Observatory

HARA, Hirohisa
Institute of Astronomy
The University of Tokyo

HASHIMOTO, Shizuyo
Department of Physics
Tokai University

HAYASHI, Keiji
Department of Astronomy
The University of Tokyo

HIEI, Eijiro
Meisei University

HIRAYAMA, Tadashi
Solar Physics Division
National Astronomical Observatory

ICHIMOTO, Kiyoshi
Solar Physics Division
National Astronomical Observatory

ISHIDO, Yoshinori
Solar Terrestrial Environment Research
Laboratory
Nagoya University

KATO, Takako
National Institute for Fusion Science

KAWAKAMI, Shingo
Osaka Museum of Science

KITAI, Reizaburo
Hida Observatory
Kyoto University

KOSUGI, Takeo
Radio Astronomy Division
National Astronomical Observatory

KUNDU, Mukul R.
Nobeyama Radio Observatory
National Astronomical Observatory

KUROKAWA, Hiroki
Hida Observatory
Kyoto University

LAN, Wenlung
Astronomy Institute
National Central University
Taiwan

LI, Ting
Nanjing Astronomical Instruments
Research Center

MAKITA, Mitsugu
Kwasan Observatory
Kyoto University

MARUBASHI, Katsuhide
Communications Research Laboratory

MASUDA, Satoshi
Radio Astronomy Division
National Astronomical Observatory

MIYAZAKI, Hideaki
Norikura Solar Observatory
National Astronomical Observatory

NAKAJIMA, Hiroshi
Nobeyama Radio Observatory
National Astronomical Observatory

NISHIO, Masanori
Nobeyama Radio Observatory
National Astronomical Observatory

OGAWARA, Yoshiaki
Institute for Space and Astronautical
Science

OKAMOTO, Tomizo
Norikura Solar Observatory
National Astronomical Observatory

SAKAO, Taro
Solar Physics Division
National Astronomical Observatory

SAKURAI, Takashi
Solar Physics Division
National Astronomical Observatory

SHIBASAKI, Kiyoto
Nobeyama Radio Observatory
National Astronomical Observatory

SHIBATA, Kazunari
Solar Physics Division
National Astronomical Observatory

SHIMIZU, Toshifumi
Institute of Astronomy
The University of Tokyo

STERLING, Alphonse C.
Computational Physics, Inc.

SUEMATSU, Yoshinori
Solar Physics Division
National Astronomical Observatory

TAKAHASHI, Masaaki
Department of Physics
Tokai Univewrsity

TAKAKURA, Tatsuo
Department of Astronomy
The University of Tokyo

UCHIDA, Yutaka
Department of Astronomy
The University of Tokyo

UGAI, Masayuki
Department of Electrical Engineering
Ehime University

WANG, Haimin
Big Bear Solar Observatory
California Institute of Technology

WANG, Jialong
Beijing Astronomical Observatory

WANG, Jingxiu
Beijing Astronomical Observatory

WATANABE, Takashi
Department of Earth Science
Ibaraki University

WATANABE, Tetsuya
Solar Physics Division
National Astronomical Observatory

WATARI, Shin-ichi
Hiraiso Solar Terrestrial Research Center
Communications Research Laboratory

WU, Mingchan
Yunnan Observatory

WU, Zhigang
Nick Enterprise, Co.Ltd.
Taipei, Taiwan

XIA, Zhiguo
Yunnan Observatory

XU, Aoao
Department of Astronomy
Nanjing University

YAJI, Kentaro
The Graduate University for Advanced
Studies
National Astronomical Observatory

YAMAGUCHI, Asami
Solar Physics Division
National Astronomical Observatory

YANG, Yongtian
Academia Sinica

YOSHIMURA, Hirokazu
Department of Astronomy
The University of Tokyo

YOU, Jianqi
Purple Mountain Observatory

ZHANG, Bairong
Yunnan Observatory

ZHANG, Caicheng
Academia Sinica

ZHANG, Heqi
Purple Mountain Observatory

ZHANG, Hongqi
Beijing Astronomical Observatory

ZHAO, Jie
Department of Electronics and Engineering
Toyama University

ZHAO, Renyang
Beijing Astronomical Observatory